Raman Spectroscopy of Nanoparticle-laden Evaporating Sessile Droplets

By

Sujay Paul

Roll No. 186122105

A Thesis

Submitted in Partial Fulfilment of the Requirements for the Degree of

DOCTOR OF PHILOSOPHY

at the

Indian Institute of Technology Guwahati

Department of Chemistry

Indian Institute of Technology Guwahati

Guwahati – 781039, Assam, India

March, 2025

TH_3719_186122105

Raman Spectroscopy of Nanoparticle-laden Evaporating Sessile Droplets

A thesis by ***Sujay Paul***

Thesis Supervisor, ***Prof Arun Chattopadhyay***

Department of Chemistry

Indian Institute of Technology Guwahati

Guwahati – 781039, Assam, India

TH_3719_186122105

DECLARATION

I hereby declare that the results and discussions incorporated in the thesis titled "***Raman Spectroscopy of Nanoparticle-laden Evaporating Sessile Droplets***" is the outcome of research work carried out by me under the supervision of ***Prof. Arun Chattopadhyay,*** **Department of Chemistry, Indian Institute of Technology Guwahati, Assam, India** for the award of the degree of Doctor of Philosophy. To the best of my knowledge and belief, the present thesis has not been submitted, partially or fully, for any degree, diploma, associateship etc. of any institute or university elsewhere. I also declare that the research works mentioned in the thesis are solely the results of original findings. **Assistance from any kinds of artificial intelligence has also not been taken while writing the thesis**.

Sujay Paul

Department of Chemistry

Indian Institute of Technology Guwahati

Guwahati – 781039, Assam, India

Date: 06/03/2025

Place: Guwahati

TH_3719_186122105

भारतीय प्रौद्योगिकी संस्थान गुवाहाटी
INDIAN INSTITUTE OF TECHNOLOGY GUWAHATI

CERTIFICATE

This is to certify that the thesis entitled "***Raman Spectroscopy of Nanoparticle-laden Evaporating Sessile Droplets***" being submitted to the **Indian Institute of Technology Guwahati** by ***Sujay Paul*** (Roll No. 186122105) for the award of the degree Doctor of Philosophy in Chemistry is a bona fide record of research work carried by him. The information and data reported by him are solely the results of original findings. He has meticulously carried out the investigations and followed the guideline of the laboratory. This work has not been submitted elsewhere for any degree or diploma.

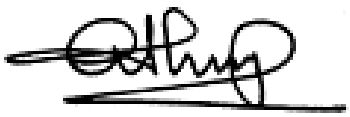

Prof. Arun Chattopadhyay **Date:** 06/03/2025

Thesis Supervisor **Place:** Guwahati

Department of Chemistry
Indian Institute of Technology Guwahati
Guwahati – 781039, Assam, India

Dedicated to my Parents

TH_3719_186122105

ACKNOWLEDGEMENTS

As it says, at one point all beautiful things come to an end. It is very difficult to put in words all the enriching experiences and learning of all these years in IIT Guwahati. For me, it is been a long association with IIT Guwahati, as I joined IIT Guwahati as a Junior Research Fellow (JRF) in Jan, 2019. From the beginning of this journey, I met many people whose encouragement and support have really helped me in my progress as a research scholar. I always believe that there is a lot to learn from every individual and each one of them has in some or the other way contributed in growing me as an individual. This journey would have been difficult without the support of these lovely people around me.

Firstly, I would like to convey my sincere gratitude to my supervisor, Prof. Arun Chattopadhyay for giving me this wonderful opportunity to be a part of his group. I am highly obliged for the support, encouragement, knowledgeable discussions, constructive criticism, and indispensable advices which really helped me to improve my research works. Since the beginning, my supervisor always used to ask "Anything New?". For the first two to three years I struggled to find out a new result and I used to reply "No Sir, Nothing New Yet". Then he came up with some innovative ideas which motivated me to think out of the box and I realized that all ideas can be implemented with sincerity, passion and hard work. After so many tries and failures, my first publication has boosted my confidence to finish the remaining works of this thesis with patience.

I extend my thank to my doctoral committee members, Prof. Uttam Manna (Chairperson) and to the other committee members Prof. A. S. Achalkumar and Dr. Partho Sarathi Gooh Pattader for their evaluation of my thesis work and giving valuable suggestions for improvement.

I would like to thank Department of Chemistry for selecting me after the interview and giving me an opportunity to admission in IIT Guwahati. I would also like to thank Centre for Nanotechnology and Central Instrument Facility for providing me with the much-needed instrument facilities. I would like to acknowledge all the staff members of Department of Chemistry for helping me with the official annual procedures of this course. Special thanks to Mrs. Emlin Elsa Abraham and Ms. Reena Dey for their guidance, suggestions and help to operate the Raman spectrometer instrument in Centre for Nanotechnology.

TH_3719_186122105

Next, I take this opportunity to thank Dr. Srimanta Pal, Dr. Mihir Manna and Dr. Manideepa Paul for teaching me all the basic techniques of research with so much ease and patience. Thank you Srimanta Da for all your guidance and support throughout and for being a supportive senior. I also thank my other seniors Dr. Ayan Pal, Dr. Srestha Basu, Dr. Shilaj Roy, Dr. Uday Narayan Pan and Dr. Chirantan Gayen whom I met in first year.

I have also been fortunate to work with Dr. Tushar Debnath and it's been a wonderful learning opportunity in his expertise.

I sincerely thank my group members Dr. Mihir, Dr. Anitha, Dr. Srimanta, Dr. Kasturi, Dr. Debashree, Dr. Manideepa, Dr. Priya, Dr. Arin, Dr. Archismita, Ujjala, Santanu, Shamim, Sawna, Subarna, Debjyoti and Ashmita for providing me a healthy environment.

I am greatly thankful to Council of Scientific & Industrial Research (CSIR) for fellowship during the first 5 years of PhD tenure.

Beside research, IITG have given me a friend for a lifetime- Mrinmoy. This wouldn't have been possible without his support. He has been a constant support and has helped me in keeping my fun and natural side alive with timeless discussions, help, encouragement and care. At the same time, I would like to thank my other friends from IITG, Prangobinda, Monuranjan and Mongoli for their support.

Next, I would like to thank my best friend Dipanwita for always being there. She has been my constant support in every ups and downs. I express my gratitude to my family for all their love and support.

Last but not the least; I thank my parents for all their encouragement, love, support and comfort. I thank them for giving me the best education. Many thanks to my sister Moumita for her love and encouragement. I thank almighty for gifting me with such wonderful people.

It will be incomplete without mentioning the beautiful green campus of IIT Guwahati. This is a nature's gift and a wonderful place. I feel refreshed every time I walked through the pleasant roads of this green campus.

Sujay Paul

TH_3719_186122105

TABLE OF CONTENTS

TH_3719_186122105

TH_3719_186122105

Thesis Abstract

Evaporation of a sessile droplet having dispersed particles on solid surface is technologically significant mainly due to the various kinds of pattern formation upon complete evaporation of solvent. The major outcome of substantial development in nanoscience and nanotechnology is the supremacy of nanoparticles in various kinds of applications in chemistry, biology, electronics and devices. The utilization of evaporation driven pattern formation of nanoparticles has become routine procedures for inkjet and 3D printing applications. Besides finding applications of the evaporation induced pattern formations, the understanding of deposition mechanism is also similarly crucial for the newer technology. In the present thesis, the ability of nanoparticles to enhance the Raman signature has been utilized to unravel the overall deposition process of nanoparticles from evaporating sessile droplets, which is otherwise not possible easily by other spectroscopic techniques.

The present thesis is primarily focused on the mechanistic insight of the deposition process of metal nanoparticles (Au and Ag) and molecular interactions on the surface of nanoparticles during the course of evaporation of solvent from sessile droplet containing the particles. This has further pursued for molecular systems leading to the generation of 2D crystals. The thesis is divided into six chapters.

Chapter 1 of the thesis is on the introduction of nanoparticles and their basic synthesis method, localized surface plasmon resonance (LSPR) properties and applications mainly in biology and photocatalysis. This chapter also elaborates the enhancement of Raman signal on the surface of metal nanoparticles. Further, basic concepts of evaporation induced particle deposition, primarily the novel 'coffee-ring' effect, has been discussed briefly. Moreover, the common factors, which can alter the deposition mechanisms, have also been introduced. After the assessment of reported literatures, the scope and salient features of the current research work have been described. C**hapter 2** of the thesis reports on the basic deposition kinetics of dispersed spherical nanoparticles at the contact line of an evaporating sessile droplet as probed by time dependent surface-enhanced Raman spectroscopy (SERS). In this chapter, the nanoparticles are functionalized with non-reacting molecules so that only the deposition behavior can be monitored. Unlike for the microparticle systems in which particles deposit linearly with time, our studies discovered that the deposition of nanoparticles followed phase transition from dispersion to deposit within a short window of time. Furthermore, particle size and concentration dependent deposition kinetics of nanoparticles have also been studied.

TH_3719_186122105

Chapter 3 of the thesis introduces unique and important utilization of nanoparticle deposition in an evaporating sessile droplet to distinguish the intrananoparticle and internanoparticle chemical reactions on the surface of nanoparticles, which has not been reported. The time-dependent SERS measurements were carried out to monitor the photochemical dimerization reaction of 4-aminothiophenol (4-ATP) on the surface of silver nanoparticles (AgNPs). Role of isotope effect of solvent, H_2O and D_2O, on the rates of intrananoparticle and internanoparticle reactions have also been reported. However, the 4-ATP dimerization as well as the AgNPs dispersibility in water are dependent on the pH of dispersion. The effect of pH on the overall deposition process of nanoparticles, having reacting molecules on the surface, is described in the **Chapter 4** of the thesis. Herein, the similar time-dependent SERS measurements were performed on sessile droplets of 4-ATP functionalized AgNPs at pH values of 7.0, 8.4 and 9.4. At pH 7.0 and 9.4, only one phase transition of nanoparticle deposition has been observed. However, at pH 8.4, multiple steps of phase transitions and 4-ATP dimerization have been monitored. The results were also supported by the atomic force microscopic (AFM) measurements of the deposits. The **Chapter 5** of the thesis illustrates the studies of Raman measurements of the deposits for similar sessile droplets having soluble organic molecules (methyl orange and methylene), which were crystallized by evaporation induced deposition technique. However, the nature of crystals formed in the deposit phase were found to be completely different from the bulk or 3D crystals. Powder X-ray diffraction measurements revealed the formation of 2D crystals of methyl orange and methylene blue molecules. Most importantly, the different vibrational characteristics of the surface and interior of the molecular crystals have also been discovered from Raman measurements studies. Finally, in **Chapter 6** of the thesis the essential conclusions and future prospects of the research works are included.

TH_3719_186122105

Glossary of Acronyms

4-ATP	4-Aminothiophenol
4-MBA	4-Mercaptobenzoic acid
Ag	Silver
Au	Gold
AgNPs	Silver nanoparticles
AuNPs	Gold nanoparticles
AFM	Atomic Force Microscopy
DFT	Density Functional Theory
FESEM	Field Emission Scanning Electron Microscopy
FETEM	Field Emission Transmission Electron Microscopy
GGA	Generalized Gradient Approximation
LSPR	Localized surface plasmon resonance
NaMBA	Sodium 4-mercaptobenzoate
MO	Methyl orange
MB	Methylene blue
NP	Nanoparticle
ONCV	Optimized norm-conserving Vanderbilt
PBE	Perdew-Burke-Ernzerhof
PXRD	Powder X-Ray Diffraction
SERS	Surface-enhanced Raman spectroscopy
SPR	Surface plasmon resonance
TPCL	Three-phase contact line

TH_3719_186122105

Chapter-1

Introduction and Literature Review

Chapter 1 *presents introduction of nanoparticles and their basic synthesis method, localized surface plasmon resonance (LSPR) properties and applications mainly in biology and photocatalysis. This chapter also elaborates the enhancement of Raman signal on the surface of metal nanoparticles. Further, basic concepts of evaporation induced particle deposition, primarily the novel 'coffee-ring' effect, has been discussed briefly.*

TH_3719_186122105

1.1. Introduction

Nanoscale particles, which have size between 1 to 100 nm, are of great scientific importance in chemistry,[1] biology,[2] medicine[3] and optoelectronics,[4] which cannot be achieved by bulk macroscopic materials. Innumerable research has been done on nanoscale particles and still many to do to get better efficiency, more eco-friendliness and less costly materials. As particles in nanometer-range have dimension - dependent special properties,[5] scientists are pursuing investigations to organize nanoscale particles in one, two, and three dimensions. Metal nanoparticles have unique abilities to support localized surface plasmons,[6] which in turn enhance light-driven electromagnetic field strength in the vicinity of nanoparticle surface thus providing opportunities for applications in heterogeneous plasmonic catalysis[7] and surface enhanced Raman spectroscopy (SERS).[8] Various organic carboxylic acids and thiols on specially prepared metal surfaces have been investigated by SERS.[8]

1.2. Nanoparticles

The 'nano' word came from Greek word 'dwarf'.[9] In general, nanoparticles are very small particles of size ranging from 1 to 100 nm i.e., they are far smaller that everyday objects but bigger than atoms.[9] Richard Feynman introduced the concept of 'nanotechnology' in 1959.[10] Due to the very tiny size, the surface area to volume ratio of nanoparticle is very high compared to bulk counterpart. In spite of its tiny size, a nanoparticle acts as a whole single component with respect to its properties. Metallic nanoparticles possess different chemical and physical properties from bulk metals such as different melting points, mechanical strength, optical and magnetic properties, which are appealing in numerous industrial applications.[11] Of crucial significance, the optical property is the fundamental characteristic of nanoparticles. In general, ~25 nm gold nanoparticles (AuNPs) show wine-red color[12] whereas silver nanoparticles (AgNPs) of the same size exhibit yellow-gray color.[13]

1.3. History and Developments of Nanoparticles

Without knowing any in-depth physical and chemical properties, the NP sol were used for coating and painting of ancient sculptures. AuNPs were found on archeological ivory during detailed study of an Egyptian ivory, with carving at the end of 9th century BC to the beginning of 8th century BC, discovered from the Louvre collection from Arslan Tash, Syria.[14] The Lycurgus cup, made around 4th century AD, is very famous for having a dichroic glass, which alters color depending on the way light is shown.[15] External light makes the cup green and

TH_3719_186122105

when light is shone internally, it turns red. It has been found that the cup contains 70 nm AgNPs and AuNPs in molar ratio of 14:1, which gives the extraordinary unusual optical phenomenon. 'Purple of Cassius', a colorant of glasses, a colloid of tin dioxide and gold particle mixture, was very popular in 17th century.[16] In 1857, reported by Faraday, the formation of deep red colloid of gold was synthesized by the reduction of aqueous solution of chloroaurate ($AuCl_4^-$) using phosphorus in CS_2.[17] Investigation of optical properties of the thin film of synthesized AuNPs were done by him and it was found that mechanical pressure changed the color from purple to green. Later, in 1861, 'colloid' term was given by Graham.[18] The first synthesis of AgNPs was reported by M. C. Lea in 1889.[19] The diameter of synthesized citrate-stabilized AgNPs was 7-9 nm. Also, protein stabilized AgNPs was described in 1902.[20] AgNPs has been commercialized as "Collargol" and utilized for medical purposes.[21] Numerous methods for the synthesis of colloidal NPs were reported in the 20th century. A very long history of rational invention of many synthetic techniques and their utilization in catalysis, sensing, biotechnology and energy have resulted in great knowledge over the past 100 years.

1.4. Synthetic Techniques

There are two types of techniques that are used for the synthesis of nanoparticles. Those are 'Top-Down' and 'Bottom-Up' approaches.[22] In the 'Top-Down' approach, AuNPs or AgNPs are synthesized from their bulk Au or Ag materials by physically cleaving the bulk matter into powder and very small fragments, which are later exfoliated into nanoparticles. Physical methods, which are used in the 'Top-Down' approach, are laser ablation, ball milling, physical vapour deposition and lithography. In contrast, nanoparticles that are synthesized in 'Bottom-Up' approach starts from atomic metals, which then nucleate and grow into nanoparticles. In a typical 'Bottom-Up' synthesis, at first, commercially available metal ions are reduced into metal atoms in zero oxidation in a suitable solvent. Therefore, most of the 'Bottom-Up' synthesis methods are chemical in nature and pretty straightforward for a chemist to do in laboratory. In my thesis, nanoparticles were synthesized chemically utilizing 'Bottom-Up' approach. A few common chemical methods for the nanoparticle synthesis are given below.

(i) Turkevich Method:

The Turkevich method, discovered in 1951, is the simplest and widely used chemical 'Bottom-Up' technique for AuNP synthesis by the reduction of a gold precursor, chloroauric acid ($HAuCl_4$), using trisodium citrate, which acts as both the reducing agent as well as stabilizer.[23] In the boiling aqueous solution, Au^{3+} ions are reduced by citrate ions into Au atoms (Au^0),

TH_3719_186122105

which nucleate into AuNPs. To synthesize AuNPs of different sizes, the Turkevich method was modified and refined by Frens in 1972.[24] By varying the ratio of precursor and citrate ions, AuNPs of different sizes from 16 nm to 147 nm were produced. The color of the colloid depends on the size of AuNPs. In 1982, Lee and Meisel introduced the Turkevich method for $AgNO_3$ to synthesize aqueous colloidal citrate capped AgNPs.[25] However, in contrast to AuNPs, the size of AgNPs were much larger with a high polydispersity and several morphologies. In order to obtain aqueous, monodisperse AgNPs, along with trisodium citrate, a polyphenolic compound tannic acid was added as reducing agent for $AgNO_3$ by Sivaraman *et* al.[26] By varying the tannic acid to $AgNO_3$ ratio, uniform 18-30 nm AgNPs were prepared by Dadosh.[27] These methods were followed for AgNP synthesis in the thesis work.

(ii) The Brust Method:

To synthesize AuNPs in organic solvent, Brust *et al* introduced two-phase liquid-liquid system in which one solvent is water and the other is organic.[28] The Au^{3+} ions in water are transferred into organic solvent by a phase transfer agent, as for example, tetraoctylammonium bromide. The organic layer consists of stabilizing molecules, such as alkanethiol, soluble in organic solvent. Therefore, upon reduction of Au^{3+} into AuNPs and stabilization by alkanethiol, the AuNPs are completely dispersible into organic solvent and stable for a longer period of time. The progress of the AuNP formation was monitored by color change of organic layer from orange to brown.

(iii) Seed-Mediated Growth:

This method is utilized to prepare nanoparticle of larger size using smaller nanoparticles. Smaller nanoparticles are called seed on which additional metal atoms grow into larger one. The major advantages of this method over other techniques are significant levels of control over the size, shape and structure of nanoparticles. In the beginning of 21st century, Catherine J. Murphy and coworkers developed the seed-mediated growth of plasmonic nanoparticles and nanorods.[29] At first very small nanoparticles are prepared using strong reducing agent and then they were incubated in the metal salt solution and reduced by weak reducing agent for control growth. In this way both the nanorod and spherical nanoparticles of different sizes have been synthesized.

TH_3719_186122105

(iv): Other Methods:

Photochemical processes utilize a photosensitizer that absorbs specific radiation leading to the formation of radial, which in turn reduce the metal ions to form metal nanoparticles. As for example, Marin *et al* synthesized AuNPs from Au^{3+} and Au^{+} using aromatic ketone molecule as photosensitizer.[30] Photochemical synthesis of decahedral AgNPs with excellent monodispersity has been reported.[31] Microorganisms' reductase enzymes secreted out by the cell can carry out the reduction process outside the bacterial cell.[32] Electron transfer from NADH transported by NADH-dependent enzyme initiate the reduction of Au^{3+} to Au^{0} resulting in the formation of AuNPs. Greener methods have been reported using plants. Various plant extract such as lignans,[34] flavonoids,[35] alkaloids,[36] steroids[37] and terpenoids[38] present in the leaves have also been reported for the synthesis of AuNPs and AgNPs.

1.5. Properties of Nanoparticles

The properties of nanoscale particles are substantially different from those of their bulk counterparts and some physical properties can also be easily distinguished visually by naked eye. Effect of size and shape become more dominant at nanoscale level.[5] As for example, bulk gold appears as golden yellow while AuNP dispersion typically exhibits red or purple under visible light.[12] Bulk silver is bright grey in color; however, AgNP dispersion appears as yellowish green.[13] The color of the nanoparticle dispersion can also be tuned by varying the size and shape.[38,39] As mentioned earlier, because of the size dependent color change, the nanoparticles were being used as paint for historical artefacts as mentioned before. All the properties of nanoparticles that arise from the size-dependent confinement effect are explained by using quantum mechanics. Faraday's work on AuNPs in 1852 inspired the theoretical scientist, Gustav Mie in early 20th century to explain the results,[40] which is described briefly in the next section.

(i) Localized surface plasmon resonance (LSPR):

On decreasing the size of the material, the surface area increases gradually relative to the volume of the material. Therefore, at the nanoscale level the surface area to volume ratio is so huge that electron density on the surface of the particle becomes very large. The collective oscillation of electrons on a material is commonly known as 'plasmons'.[41] Fermi liquid model described the plasmons as negative electron cloud, oscillations of which resonate at a particle frequency and at that moment the electrons are coherently displaced around a positively

TH_3719_186122105

charged lattice.[41] As the electron density around the surface of nanoparticles is very high, to achieve such coherently oscillating electron on the surface, external electric field from electromagnetic radiation is the best choice. Also, the size of NP is smaller than the wavelength of incident radiation that the electric field of the incident light penetrates the metal NP and polarize the electrons all over the surface creating positive and negative charge separation on the surface of NP as shown in the **Figure 1.1A**. The separated charge or polarized electrons, thereby, oscillate all over the surface of NP along the wave of the radiation. As the polarized electron cloud cannot leave or propagate from the nanoparticle surface, the coherently oscillating of electron cloud on the surface is known as localized surface plasmons (LSP). At a certain wavelength of the incident radiation, all the electron clouds are coherently displaced from their equilibrium position and the oscillation frequency is maximum. This is termed as localized surface plasmon resonance (LSPR).[6] In other words, the LSP couple with the incident electromagnetic radiation and get excited by absorbing the energy at a certain wavelength. Therefore, the occurrence of LSPR can be easily detected by ultraviolet-visible (UV-vis) spectroscopy.

In order to gain conceptual understandings about LSPR, simple model of mass-on-a-spring damped oscillator was considered in which the electron density represents the mass of the oscillator and the restoring Coulombic force in between the electrons and lattice atoms sets the spring constant. According to the model, deformation of the electron cloud by the incident electric field is given by the polarizability (α) of the metal.[41, 42]

$$\alpha(\omega) = 3\varepsilon_m(\omega)V\frac{\varepsilon(\omega) - \varepsilon_m(\omega)}{\varepsilon(\omega) + \chi\varepsilon_m(\omega)}$$

In this equation, ω, V and χ are the frequency of incident radiation, volume of NP and geometrical factor, respectively. χ is 2 for spherical shape NP. ε_m and ε are dielectric constants of surrounding non-absorbing medium and NP, respectively. The frequency dependent ε of NP is a complex function and $\varepsilon(\omega) = Re[\varepsilon(\omega)] + iIm[\varepsilon(\omega)]$.[6] At the resonant condition, the polarizability is maximum and the denominator in equation 1 should be minimum. In case of slowly varying $Im[\varepsilon(\omega)]$ as compared to the $Re[\varepsilon(\omega)]$, such as the case of Au and Ag, the resonant condition is simplified to

$$Re[\varepsilon(\omega)] = -\chi\,\varepsilon_m$$

This relationship is known as Fröhlich condition, which defines the LSPR.[6] In other words, the nanomaterials, which has negative real part of the dielectric function, are plasmonic in nature.

TH_3719_186122105

The frequency of SPR depends on ε_m of the surrounding medium and LSPR can be tuned by changing the outside environment around the NPs. The LSPR red-shifts when ε_m of the surrounding medium is increased.[43] While the real part of ε indicates the resonance condition, the imaginary part of ε express the loss.[6] Losses are mainly due to confinement of electron gas,

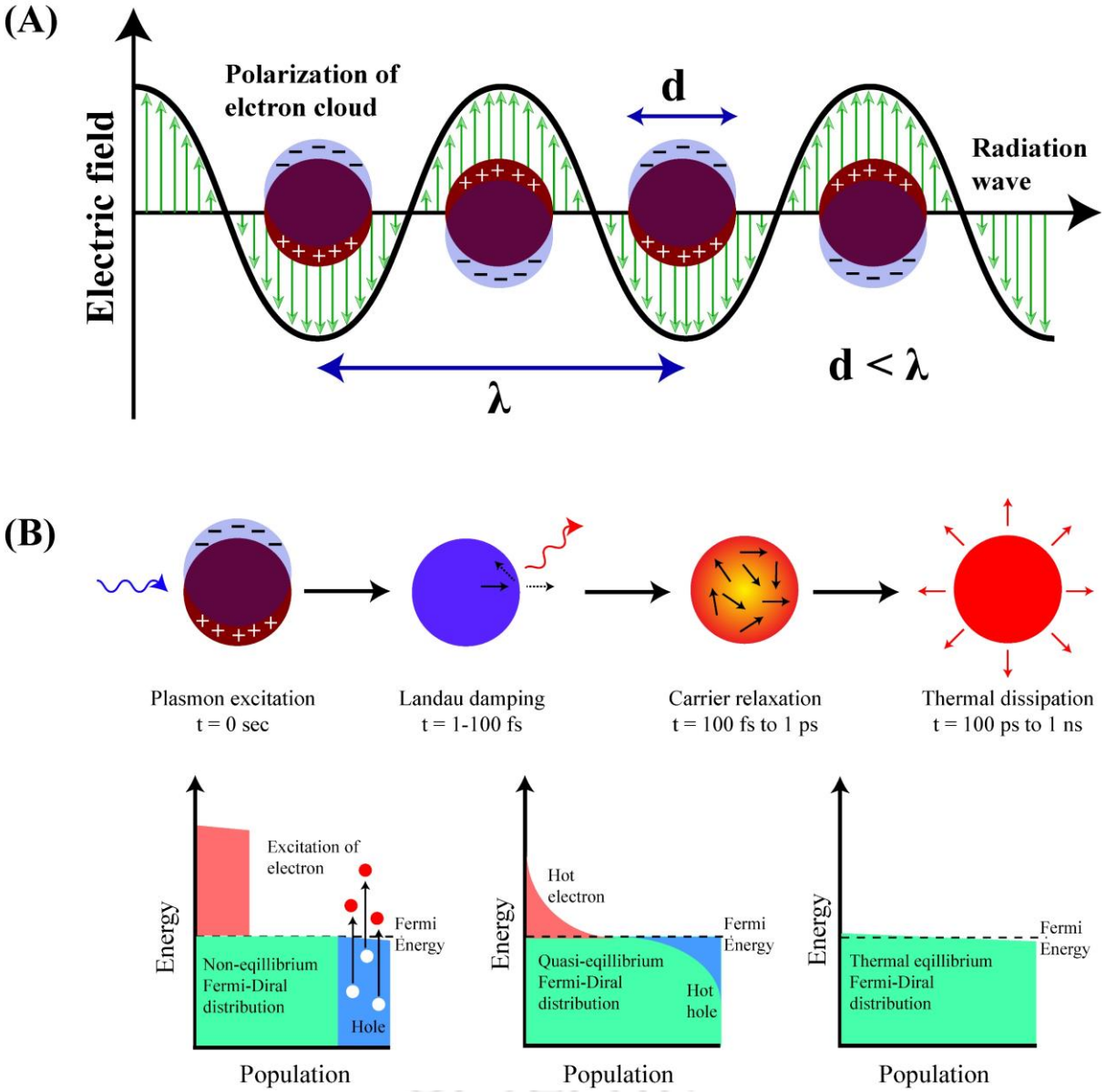

Figure 1.1: (A) Generation of LSPR on the surface of nanoparticles in presence of electromagnetic radiation. (B) Decay process of relaxation of LSPR.

radiative damping, metal heating, structural defects and intraband transitions from valance d band to conductive s-p band. Au possess higher loss in visible region. Moreover, there is more overlap between the intraband transition and LSPR for Au than that of Ag.[6] LSP cannot decay for Ag into intraband transition. Therefore, Ag shows sharp and enhanced LSPR compared to Au. The faster loss of coherence in electron oscillation for Au is also reflected in the broader plasmon bandwidth in the UV-vis spectrum compared to the sharp signal coming from AgNPs.

TH_3719_186122105

However, in real applications Au is preferred for its higher chemical stability and better biocompatibility. Majority of other properties of metal NPs come form the phenomenon of LSPR.

Other factors such as size and shape alter the position and quality of LSPR band. The SPR band in the UV-vis spectrum arises from the sum of absorption and scattering photons.[6] The ratio of these two depends on particle size. In order to theoretically understand the color of colloidal AuNPs, Mie in 1908 developed a theory of absorption and scattering of the electromagnetic radiation by spherical NPs.[40] For NPs of size much less than the wavelength of incident radiation, absorption is the dominating factor over scattering. However, with increasing the size of NPs, the scattering effect become pronounced. For AuNPs above 70 to 100 nm, scattering prevails.[6] Moreover, when the particle size is increasing, the coherent oscillation of electrons on the surface of NPs become non-uniform and multiple coherent oscillations exists, which is reflected in a broad and red-shift of SPR band in spectrum. When the size of NP is below the mean free path of conducting electron, the free electron scattering and the effect of Im[ε(ω)] decrease the SPR quality and LSPR band decreases. LSPR is almost quenched when particle size is about 2 nm.[6]

Due to the advancement of synthetic techniques over the years, NPs of different shapes such as rod,[44] wire,[45] star,[46] cube,[47] triangle,[48] cone,[49] prism[50] and shell[51] have been prepared. With the reduction of particle symmetry from spherical to other shapes, the number, position and intensity of LSPR are modified. In all the cases, the position of additional band is always red-shifted from the band of spherical NPs. As for example, spherical AuNPs of 2-50 nm only show one plasmonic band at about 515-540 nm, while cylindrical Au nanorods (AuNRs) exhibit two plasmon bands, which are called transverse band at shorter wavelength and longitudinal band at higher wavelength.[52] The position of the longitudinal band linearly varies with aspect ratio of AuNRs. Moreover, the LSPR modes are also dependent on the assembly of NPs. In an assembly, plasmon of each NP can influence the adjacent particle generating a new hybrid plasmon mode. The simplest example of assembly is dimer of NPs.[53] Recent result suggested that coupling of plasmon in a dimer red-shifted the plasmon mode of spherical AuNPs. Most importantly, the dimer assembly led to high enhancement of local electric field at the junction of the AuNPs, which is termed as plasmonic 'hot-spot'.[53] Plasmonic 'hot-spot' formation in an assembly of NPs has been applied to photocatalytic dimerization reaction in an end-to-end assembly of AuNRs.[44] Upon assembly formation a new hybrid LSPR peak appears at higher wavelength nearly at 600-650 nm for spherical AuNPs and AgNPs.[54]

TH_3719_186122105

(ii) Relaxation or Decay of LSPR:[6]

The complete decay process of LSPR is schematically represented in the **Figure 1.1B**. After the LSPR excitation, electron-hole pair formation is observed, which results in a non-equilibrium Fermi-Dirac distribution of negative electron and positive hole as shown in **Figure 1.1B**. Then the electron-hole pair releases energy in radiative or nonradiative way in 1 to 100 fs, which is known as Landau damping. The energy of hot carriers is rearranged by electron-electron scattering in the next 100 fs to 1 ps forming quasi-equilibrium Fermi-Dirac distribution (**Figure 1.1B**). After that, the energy is released to surrounding by electron-phonon scattering during the next 1 to 5 ps and finally the released energy is dissipated in the surrounding medium by phonon-phonon and phonon-surrounding scattering in 100 ps to nanosecond time range. The released energy can be utilized as heat source for photothermal applications or activation energy for chemical reaction at the surface of NPs.

1.6. Applications of Nanoparticles

In the modern age of technology, plasmonic nanoparticles have been majorly utilized in biomedical applications such as cancer therapy,[55] drug delivery,[56] diagnostics,[57] as antimicrobial agents[58] and in sensing.[59] Moreover, they are also used in color engineering,[60] plasmonic solar sell,[61] photocatalysis[62] and enhanced spectroscopy.[63] AuNP and AgNP colloids were used in biomedical applications as mentioned before. Because of the local heating effect caused by the LSPR of plasmonic NPs, they have been used for targeted drug delivery and photothermal therapy.[64] Due to strong light scattering of NPs, the NPs can also act as contrast agents in imaging owing to the presence of high electron density.[65] Upon irradiation of light, hot electrons and holes are generated owing to LSPR effect. The hot carriers, then, can be transferred to the adsorbed molecules thereby excite the vibrational or electronic states of the molecule. This will accelerate the chemical reaction of the substrate molecule significantly.[52] Therefore, the plasmonic NPs have been used as efficient photocatalyst, such as CO_2 reduction[66] and water splitting.[67] Another important chemical reaction, heterogeneous surface plasmon catalysis, which is applied for the oxidation of 4-aminothiophenol (4-ATP) to 4,4´-dimercaptoazobenzene (DMAB) on the surface of any plasmonic materials.[52] Since the discovery of this reaction, the 4-ATP dimerization became the model reaction for plasmonic substrates. The photon absorption cross section is high for smaller nanoparticles. The hot carriers can also be transferred to the nearby semiconductor resulting in the separation of charge or the harvesting of solar energy into electrical properties in solar cell.[61] Plasmon

TH_3719_186122105

enhanced extinction[68] and fluorescence[69] are two important spectroscopic techniques. If the LSPR peak is close to the excitation wavelength, the excitation radiation is confined and excitation efficiency of highest order is expected. However, if the LSPR is close to the emission wavelength, efficient emission can occur depending on the distance between plasmonic NP and fluorophore. By utilizing plasmonic nanorod structures, which has two LSPR bands, enhancements of both the excitation and emission are possible as reported.[70] Out of all these applications, the most important advantage of LSPR is the enhancement of Raman signal also termed as surface-enhanced Raman spectroscopy (SERS).[8]

1.7. Surface-Enhanced Raman Spectroscopy (SERS)

The discovery of Raman scattering enhancement of molecule attached on plasmonic nanostructure surface is one of the greatest breakthroughs in spectroscopic techniques. In 1974, Fleischmann and co-workers discovered the enhanced Raman scattering when intense Raman signal of pyridine on rough surface of silver electrode was observed.[71] In 1977, this incident was also identified by Jeanmaire and Richard P. Van Duyne and also by Albrecht and Creighton.[72,73] Both the groups calculated the Raman enhancement factors of 10^5-10^6. Albrecht and Creighton also suggested that there was connection between surface plasmon and enhanced Raman effect which was later put forward by Moskovits in 1978.[74] Subsequently, the enhancement effect was termed as surface-enhanced Raman scattering (SERS) by Richard P. Van Duyne in 1979.[75] Since its discovery, tens of thousands research papers related to SERS have been reported so far. Because of rich vibrational information obtained by SERS techniques, SERS has been applied in several fields such as catalysis,[52] electrochemistry,[76] biology,[77] material science,[78] medicine[79] and others. Moreover, recent reports suggested that SERS has potential in single-molecule level detection also.[80]

(i) Electromagnetic mechanism (EM):

There are two types of mechanisms that explain the enhancement during the SERS measurements, which are electromagnetic mechanism (EM)[81] and chemical mechanism (CM)[82]. EM depends on the local electric field strength enhanced by LSPR or assembly of NPs. When a molecule is placed at the surface of NP or at the junction of two NPs in an assembly, the analyte molecule experiences enhanced electric field, $E(\omega)$, at the LSPR frequency of ω in the presence of an incoming electromagnetic radiation. At the junction of two nanoparticles electric field enhancement is higher than that on the surface of single nanoparticle. The junction of two nanoparticles in assembly is called plasmonic 'hot-spot' as

TH_3719_186122105

shown in **Figure 1.2A(i)**. Due to the this, the polarizability changes greatly, which is reflected in the intense Raman spectrum as shown in the **Figure 1.2A(ii)**. SERS enhancement at the plasmonic 'hot-spot' is significantly higher than that in the absence of 'hot-spot' environment. The SERS enhancement factor (EF) calculated by EM theory is $|E(\omega)|^4/ |E_0|^4$ where E_0 is the electric field amplitude of incident radiation.[8, 83] EF through EM pathway can reach as high as 10^9.

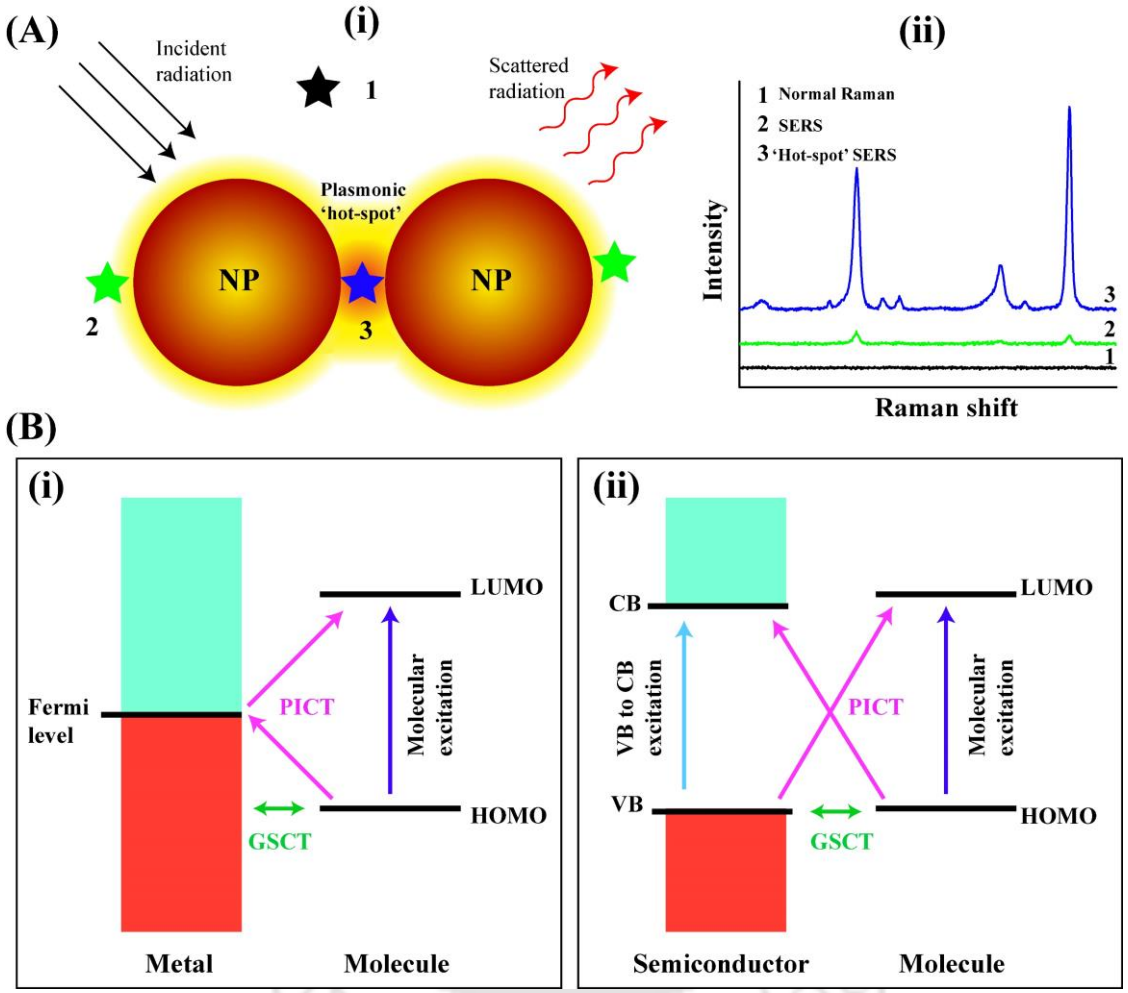

Figure 1.2: (A) Schematic representations of (i) plasmonic 'hot-spot' generation at the junction of two nanoparticles due to LSPR and (ii) Raman spectra corresponding to the position of analyte molecules. (B) Schematic energy profile diagram showing charge transfer processes involved in the chemical enhancement mechanism of SERS for (i) metal-molecule and (ii) semiconductor-molecule systems.

(ii) Chemical mechanism (CM):

Although the EM pathway comes up with possible explanation of the intense Raman signal, it fails to provide possible reason for different magnitude of enhancement observed for dissimilar vibrational modes. In this regard, CM pathway invokes charge transfer (CT) process in between

TH_3719_186122105

the analyte molecule and the SERS substrate. The CT process alters the electron distribution of the analyte molecule thereby changing the polarizability of specific vibrational modes, which have higher SERS signal intensity.[82] There are two types of CT processes that are possible for a substrate-molecule system, which are ground state charge transfer (GSCT) and photo-induced charge transfer (PICT) as schematically given in the **Figure 1.2B**. For metal-molecule system, the EF for CM pathway has been found to be on the order of 10^3. Raman enhancement by CM route is often specific to substrate-molecule of choice because CT depends on the energy of valence band, conduction band of substrate and HOMO and LUMO of analyte molecule.

For analytical purpose, the following relation is used to calculate the SERS EF, which contains effect of both the EM and CM pathways.[84]

$$EF = \frac{I_{SERS}/N_{SERS}}{I_{Bulk}/N_{Bulk}}$$

where I_{SERS} and I_{Bulk} are the intensity of the analyte molecule with SERS substrates and without SERS substrate, respectively. N_{SERS} and N_{Bulk} are the number of analyte molecules in the Raman probe area attached with the SERS substrate and in absence of the SERS substrate, respectively.

(iii) Semiconductor SERS substrates:

Due to the widespread applications of SERS in probing reaction pathways and detecting molecules, new novel, less costly and easily fabricable substrates for SERS are being discovered. Apart from the conventional metal nanoparticles, non-noble metallic materials including graphene,[85] transition metal oxides,[86] chalcogenides,[87] nitrides,[88] MXenes,[89] metal organic frameworks[90] and pi-conjugated organic molecules[91] have also proven to boost SERS activity. Most of the substrates show SERS enhancement by CM pathway and are specific to analyte molecules. Recently, significant SERS enhancement has been reported for simple inorganic and organic molecular crystals. Microcrystal of copper(II) 8-hydroxyquinoline complex exhibits specific SERS enhancement of about 3×10^5 towards rhodamine 6g (R6G) in comparison to lower enhancement for other dye molecules.[92] SERS measurement on organic crystal of terephthalic acid (TA) has revealed moderately high EF of 1.5×10^6 for R6G and the same TA crystal also gave rise to cooperative SERS enhancement of rhodamine B (RhB) in presence of R6G.[93] SERS enhancement of the crystals are both the EM and CM in nature,

TH_3719_186122105

which have been reflected in the high EF. Therefore, for specific sensing purpose and selective probing of one vibrational band with respect to other, discovery of new semiconductor crystal materials for SERS is relevant.

1.8. Evaporation Induced Particle Deposition

Evaporation of a sessile droplet leading to deposition of the dissolved or dispersed solid on substrate surface continues to be technologically and scientifically significant in thin-film deposition,[94] printing[95] and self-assembly.[96] Therefore, understanding of droplet evaporation under different conditions such as droplet composition and viscosity,[97] evaporation temperature,[98] humidity[99] and nature and morphology of substrate surface[100] has been key to the progresses in technological applications. In general, droplet evaporation is a method to concentrate dispersed particles in a certain deposition pattern of choice. A common evaporation induced pattern formation is the 'coffee-ring' where the solid gets preferentially deposited on the surface in the form of a ring akin to coffee stain.[101]

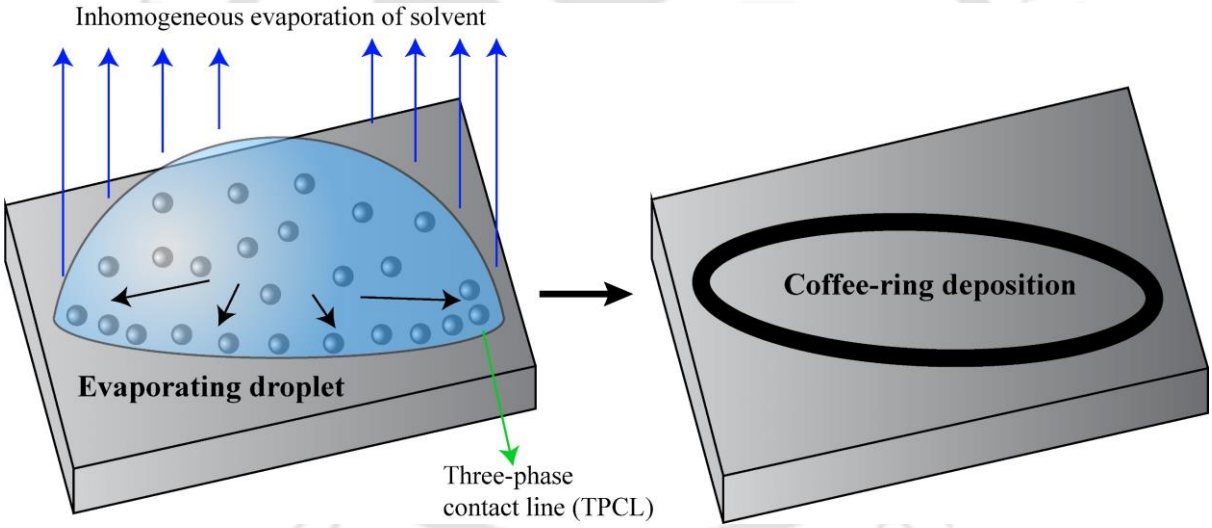

Figure 1.3: Schematic representation of 'coffee-ring' deposition formation at the TPCL due to inhomogeneous evaporation rate of solvent from the surface of a sessile droplet having dispersed particles.

(i) Coffee-ring effect:

When a liquid droplet having dispersed particles is placed on solid surface, it forms a cylindrical-cap shape object with circular base. Because of the unique shape of the sessile droplet the evaporation rate along the circular edge is higher than that from the centre of the surface. The particles inside the droplet tend to move towards the three-phase contact line (TPCL) or air-liquid-solid interface with the capillary flow of liquid induced by the

TH_3719_186122105

inhomogeneous evaporation rate along the surface of the droplet.[101] This leads to the formation of ring-like deposition at the circular base of the evaporating droplet, commonly known as 'coffee-ring' deposition (**Figure 1.3**). In spite of the ubiquitous nature of the 'coffee-ring' effect, it involves a complex dynamics and mechanism of solvent evaporation, particle movement and particle deposition. Mechanism of 'coffee-ring' formation using microparticle dispersion was reported for the first time by Deegan in 1997.[102] It was observed that microparticles deposited at TPCL linearly with time. However, the deposition rate is higher only at the final leg of drying. The complex mechanism and dynamics of deposition have been given in details separately by Deegan *et al* and Boulogne *et al*.[101, 103]

(ii) Factors affecting evaporation induced particle deposition:

The evaporation induced particle deposition pattern depends on many factors such as particle shape[104] and size,[100] temperature,[98] viscosity of the solvent,[97] humidity of environment,[99] roughness of the solid substrate[100] and addition of surfactant.[105] Yunker *et al.* revealed spherical microparticles formed coffee-ring whereas uniform deposition was produced by ellipsoidal microparticles.[104] Temperature-dependent pattern formation using silica microparticles by Zhang *et al.* unveiled ring pattern formation at room temperature and uniform precipitation on silicon and glass substrates at elevated temperature.[98] It was also reported that in a mixture of two different sized particles, deposition at the ring was formed by smaller ones.[100] This technique was later utilized to separate particles of different sizes through the formation of coffee ring.[106] It has been reported that the presence of surface roughness is a key factor for ring pattern formation. Addition of ionic surfactant (CTAB) in nanofluid minimize particles sticking probability and thereby uniform deposition was observed.[105] Another important factor opposing the capillary flow of particles is Marangoni flow, which hampers the coffee-ring deposition and often results in uniform pattern or deposition at the centre of circular base.[107]

(iii) Significance of evaporation induced particle deposition:

In the last two decades, evaporation induced particle deposition has been of great significance in inkjet printing technology, which is being applied in the fabrications of electronic devices,[108] chemical sensors,[109] display pixels,[110] solar cells,[111] stretchable and flexible devices,[112] wearables[113] and supercapacitors.[114] Moreover, similar principles of target moiety depositions are being used in healthcare applications such as tissue engineering,[115] printing of sensing elements,[116] cells,[117] DNA microarrays[118] and regenerative medicine.[115] Significant advancement in inkjet printing technology revolutionized healthcare by 3D printing of skins,[119]

TH_3719_186122105

artificial cartilage[120] and cellular structures.[121] Nanoscale and molecular materials printing by dip-pen lithography offers advancement in the various fields of technology.[122] Therefore, deep understanding of the fundamental processes of evaporation induced particle deposition is important and may bring about discovery of novel phenomena during the deposition process.

(iv) Nanoparticle deposition at TPCL:

Particle deposition studies using dispersions of nanoparticles have also been reported in which only the final deposition patterns were focused. As for example, effect of surfactant, CTAB, caused uniform deposition of 25 nm aluminum oxide nanoparticles, whereas coffee-ring deposition was noticed without surfactant.[105] Effect of temperature was also monitored for evaporating droplet containing alumina nanoparticles in a binary solvent mixture.[98] At higher temperatures, uniform depositions were observed. Moreover, spherical nanoparticles form coffee-ring deposition, whereas uniform deposition has been reported for rod shaped particles.[104]

1.9. Key Areas and Scopes

In all of the above-mentioned reported cases, evaporation of solvent, gradual precipitation of particles at the ring and final deposition patterns were probed by either video or fluorescent microscopy for microparticle systems only. Basic drawback using these methodologies is that these will fail to determine movement of nonfluorescent nanoparticles at TPCL during evaporation. On the other hand, Raman spectroscopy has the capability to detect molecular fingerprints.[123] This spectroscopic technique was previously employed to monitor droplet evaporation behavior of binary solvent mixture and to measure solvent temperature during evaporation.[124] Yet it has not been applied to keep track on the fate of dispersed nanoparticles during evaporation and kinetics of nanoparticles assembly is still unknown. Sample preparation using functionalized plasmonic nanoparticles utilizes coffee-ring effect to concentrate the particles at a specific position by simple drop-casting method.[125] Nanoscale particles have unique property of LSPR, which possesses remarkable ability to enhance Raman signal intensity as mentioned before. In this regard, SERS is highly efficient method to detect a certain substance at nearly single molecule level. Combined strategy of coffee-ring effect and SERS using plasmonic nanoparticles have shown advantages in heterogenous plasmon catalysis,[52] toxic dye detection,[126] accurate diagnosis of cancer,[127] biomolecule detection[128] etc. Therefore, the coffee-ring formation study during droplet evaporation consisting of nanoscale

TH_3719_186122105

nonfluorescent plasmonic particle is remarkably important and has not been experimented fully.

Moreover, heterogeneous surface plasmon catalysis on the surface of nanoparticles are often performed in solid state or in liquid medium. There are two types of reactions possible on the surface of nanoparticles. Those are intrananoparticle reaction on the surface of same nanoparticle and internanoparticle reaction in between two nanoparticles. Similar to the intramolecular and intermolecular reactions, intrananoparticle and internanoparticle reactions may consist of different kinetics, stereochemistry and product selectivity. However, due to lack of system to probe the process separately, those two pathways have not been observed so far. In this context, dynamic nature of nanoparticles during the evaporation of sessile droplet may bring about novel information of a chemical reaction on the surface of NPs at TPCL. Such chemical reactions may also alter the deposition mechanism of NPs, depending on the property such as pH of the medium.

Due to the recent growing applications of organic molecular crystals as SERS substrates[92, 93] and Moiré superlattices,[129, 130] easy fabrications of crystalline organic materials are emergent. Most common crystallization process of organic molecules is evaporation of solvent from a supersaturated solution, which often results in large three-dimensional crystals that are not so significant in nanoscale applications. However, droplet evaporation induced crystallization may bring about new novel crystalline, structure which are fundamentally important.

Therefore, the following scopes have been pointed out as potential areas of research.

- Discovery of mechanism of deposition process of plasmonic nanoparticles at TPCL forming 'coffee-ring' pattern owing to the evaporation of sessile droplets by SERS.
- Effect of nanoparticle size and concentration on the deposition kinetics.
- Discovery of new novel phenomenon at the TPCL upon evaporation of droplet containing nanoparticles functionalized with reacting molecules probed by SERS.
- Effect of pH of the dispersion on the deposition kinetics of nanoparticles.
- Monitoring the crystallization process and discovery of new type of common organic molecular crystals utilizing the evaporation induced deposition technique.

TH_3719_186122105

1.10. Significance and important reports of the present research work

The salient features of the present research work are briefly summarized below:

- Deposition of nanoparticles at the TPCL follows a phase transition behavior in a short window of time from dispersion to deposit. This is completely different from the reported linear time-dependent deposition for microparticle systems.
- All the nanoparticles deposit within the short window of time during phase transition.
- In order for the deposition, the nanoparticles at TPCL must reach a critical concentration. The critical concentration for phase transition depends on size of the nanoparticles.
- Increasing the initial particle concentration leads faster phase transition. However, with the increase of particle size, phase transition of nanoparticles at TPCL occurs earlier.
- When the nanoparticles were functionalized with reactive molecules, the similar phase transition process has been observed. However, the overall reaction followed two-step kinetics at neutral pH.
- Intrananoparticle and internanoparticle reactions have been successfully probed by SERS utilizing the droplet evaporation induced deposition method.
- The deposition kinetics depends on pH of the dispersion. At neutral and highly basic pH 9.4, only one major phase transition step has been identified. But, at intermediate pH 8.4, six steps of phase transitions have been observed.
- Common organic molecules, methyl orange and methylene blue form two-dimensional (2D) single crystals at the TPCL after evaporation of droplets of their aqueous solutions.
- Raman spectroscopic study on the deposited 2D crystals revealed that the surface of crystal is different from the interior of crystal in terms of molecular vibrational characteristics as applicable to both 2D and 3D crystals.

TH_3719_186122105

1.11. References

1. Daniel, M.-C.; Astruc D. Gold Nanoparticles: Assembly, Supramolecular Chemistry, Quantum-Size-Related Properties, and Applications toward Biology, Catalysis, and Nanotechnology. *Chem. Rev.* **2004**, *104*, 1, 293–346.
2. De, M.; Ghosh, P. S.; Rotello, V. M. Applications of Nanoparticles in Biology. *Adv. Mater.* **2008**, *20*, 4225–4241.
3. Marchesan, S.; Prato, M. Nanomaterials for (Nano)medicine. *ACS Med. Chem. Lett.* **2013**, *4*, 2, 147–149.
4. Lee, M.; Seung, H.; Kwon, J. I.; Choi, M. K.; Kim, D.-H.; Choi, C. Nanomaterial-Based Synaptic Optoelectronic Devices for In-Sensor Preprocessing of Image Data. *ACS Omega* **2023**, *8*, 6, 5209–5224.
5. Roduner, E. Size matters: why nanomaterials are different. *Chem. Soc. Rev.* **2006**, *35*, 583-592.
6. Amendola, V.; Pilot, R.; Frasconi, M.; Maragò, O. M.; Iatì, M. A. Surface plasmon resonance in gold nanoparticles: a review. *J. Phys.: Condens. Matter* **2017**, *29*, 203002.
7. Schauermann, S.; Nilius, N.; Shaikhutdinov, S.; Freund, H.-J. Nanoparticles for Heterogeneous Catalysis: New Mechanistic Insights. *Acc. Chem. Res.* **2013**, *46*, 8, 1673–1681.
8. Langer, J.; Jimenez de Aberasturi, D.; Aizpurua, J.; Alvarez-Puebla, R. A.; Auguié, B.; Baumberg, J. J.; Bazan, G. C.; Bell, S. E. J.; Boisen, A.; Brolo, A. G., et al. Present and Future of Surface-Enhanced Raman Scattering. *ACS Nano* **2020,** *14*, 28-117.
9. Bayda, S.; Adeel, M.; Tuccinardi, T.; Cordani, M.; Rizzolio, F. The History of Nanoscience and Nanotechnology: From Chemical–Physical Applications to Nanomedicine. *Molecules* **2020**, *25*, 112.
10. Feynman, R. P. There's plenty of room at the bottom. *Eng. Sci.* **1960**, *23*, 22–36.
11. Stark, W. J.; Stoessel, P. R.; Wohlleben, W.; Hafner, A. Industrial applications of nanoparticles. *Chem. Soc. Rev.* **2015**, *44*, 5793-5805.
12. Rivera, R. B. P.; Unabia, R. B.; Reazo, R. L. D.; Lapening, M. A.; Lumod, R. M.; Ruda, A. G. R.; Omping, J. L.; Magdadaro, M. R. D.; Sayson, N. L. B.; Latayada, F. S. et al. Influence of the Gold Nanoparticle Size on the Colorimetric Detection of Histamine. *ACS Omega* **2024**, *9*, 31, 33652–33661.
13. Alzahrani, E. Colorimetric Detection of Ammonia Using Synthesized Silver Nanoparticles from Durian Fruit Shell. *Journal of Chemistry*, **2020**, 4712130.

TH_3719_186122105

14. Spadavecchia, J.; Apchain, E.; Albéric, M.; Fontan, E.; Reiche, I. One-Step Synthesis of Collagen Hybrid Gold Nanoparticles and Formation on Egyptian-like Gold-Plated Archaeological Ivory. *Angew. Chem. Int. Ed.* **2014**, *53*, 8363-8366.
15. Freestone, I.; Meeks, N.; Sax, M.; Higgitt, C. The Lycurgus Cup — A Roman nanotechnology. *Gold Bull* **2007**, *40*, 270–277.
16. Hunt, L. B. The true story of Purple of Cassius. *Gold Bull* **1976**, *9*, 134–139.
17. Faraday, M. Experimental Relations of Gold (and other Metals) to Light. *Philos. Trans.* **1857**, *147*, 145-181.
18. Graham, T. Liquid Diffusion applied to Analysis. *Philos. Trans. R. Soc.* **1861**, *151*, 183-190.
19. Lea, M. C. On allotropic forms of silver *Am. J. Sci.* **1889**, *37*, 476– 491.
20. Paal, C. Über colloidales Silber Ber. *Dtsch. Chem. Ges.* **1902**, *35*, 2224– 2236.
21. Nowack, B.; Krug, H. F.; Height, M. 120 Years of Nanosilver History: Implications for Policy Makers. *Environ. Sci. Technol.* **2011**, *45*, 1177–1183.
22. Abid, N.; Khan, A. M.; Shujait, S.; Chaudhary, K.; Ikram, M.; Imran, M.; Haider, J.; Khan, M.; Khan, Q.; Maqbool, M. Synthesis of nanomaterials using various top-down and bottom-up approaches, influencing factors, advantages, and disadvantages: A review. *Advances in Colloid and Interface Science* **2002**, *300*, 102597.
23. Turkevitch, J.; Stevenson, P. C.; Hillier, J. Nucleation and Growth Process in the Synthesis of Colloidal Gold. *Discuss. Faraday Soc.* **1951**, *11*, 55-75.
24. Frens, G.; Controlled Nucleation for the Regulation of the Particle Size in Monodisperse Gold Suspensions. *Nature Physical Science* **1973**, *241*, 20-22.
25. Lee, P. C.; Meisel, D. Adsorption and Surface-Enhanced Raman of Dyes on Silver and Gold Sols. *J. Phys. Chem.* **1982**, *86*, 3391– 3395.
26. Sivaraman, S. K.; Elango, I.; Kumar, S.; Santhanam, V. A green protocol for room temperature synthesis of silver nanoparticles in seconds. *Current Science* **2009**, *97*, 1055-1059.
27. Dadosh, T. Synthesis of uniform silver nanoparticle with a controllable size. *Materials Letters* **2009,** *63*, 2236-2238.
28. Brust, M.; Walker, M.; Bethell, D.; Schiffrin, D. J.; Whyman, R. Synthesis of thiol-derivatised gold nanoparticles in a two-phase Liquid–Liquid system. *J. Chem. Soc., Chem. Commun.*, **1994**, 801-802.

TH_3719_186122105

29. Jana, N. R.; Gearheart, L.; Murphy, C. J. Seed-Mediated Growth Approach for Shape-Controlled Synthesis of Spheroidal and Rod-like Gold Nanoparticles Using a Surfactant Template. *Adv. Mater.* **2001**, *13*, 1389-1393.
30. Marin, M. L.; McGilvray, K. L.; Scaiano, J. C.; Photochemical Strategies for the Synthesis of Gold Nanoparticles from Au(III) and Au(I) Using Photoinduced Free Radical Generation. *J. Am. Chem. Soc.* **2008**, *130*, 49, 16572–16584.
31. Pietrobon, B.; Kitaev, V. Photochemical Synthesis of Monodisperse Size-Controlled Silver Decahedral Nanoparticles and Their Remarkable Optical Properties. *Chem. Mater.* **2008**, *20*, 16, 5186–5190.
32. Iravani, S. Bacteria in Nanoparticle Synthesis: Current Status and Future Prospects. *International Scholarly Research Notices* **2014**, 359316.
33. Han, G.; Wang, X.; Hamel, J.; Zhu, J.; Sun, R. Lignin-AuNPs liquid marble for remotely-controllable detection of Pb^{2+}. *Sci Rep* **2016**, *6*, 38164.
34. Das, M.; Bodroth, R. P. Green Synthesis of Silver Nanoparticles Using Flavonoids and Assessment of Their Antimicrobial Properties. *BioNanoSci.* **2023**, *13*, 186–193.
35. Chaachouay, N.; Azeroual, A.; Benkhnigue, O.; Zidane, L. (2023). Alkaloids: A Suitable Precursor for Nanomaterials Synthesis, and Their Various Applications. In: *Husen, A. (eds) Secondary Metabolites Based Green Synthesis of Nanomaterials and Their Applications. Smart Nanomaterials Technology.* Springer, Singapore, **2023**.
36. Dawadi, S.; Katuwal, S.; Gupta, A.; Lamichhane, U.; Thapa, R.; Jaisi, S.; Lamichhane, G.; Bhattarai, D. P.; Parajuli, N. Current Research on Silver Nanoparticles: Synthesis, Characterization, and Applications, *Journal of Nanomaterials*, **2021**, 6687290.
37. Mashwani, Z.; Khan, M. A.; Khan, T.; Nadhman, A. Applications of plant terpenoids in the synthesis of colloidal silver nanoparticles. *Advances in Colloid and Interface Science* **2016**, *234*, 132–141.
38. Dreaden, E. C.; Alkilany, A. M.; Huang, X.; Murphy, C. J.; El-Sayed, M. A. The golden age: gold nanoparticles for biomedicine. *Chem. Soc. Rev.* **2012**, *41*, 2740-2779.
39. González, A. L.; Noguez, C.; Beránek, J.; Barnard, A. S. Size, Shape, Stability, and Color of Plasmonic Silver Nanoparticles. *J. Phys. Chem. C* **2014**, *118*, 17, 9128–9136.
40. Mie, G. Beiträge zur Optik trüber Medien, speziell kolloidaler Metallösungen. *Ann. Phys.* **1908**, *330*, 377-445.
41. Maier, S. A. *Plasmonics: Fundamentals and Applications* (Springer) **2007.**
42. Bohren, C. F.; Huffman, D. R. *Absorption and Scattering of Light by Small Particles* (New York: Wiley-Interscience) 1983.

TH_3719_186122105

43. Mahmoud, M. A.; Chamanzar, M.; Adibi, A.; El-Sayed, M. A. Effect of the Dielectric Constant of the Surrounding Medium and the Substrate on the Surface Plasmon Resonance Spectrum and Sensitivity Factors of Highly Symmetric Systems: Silver Nanocubes. *J. Am. Chem. Soc.* **2012**, *134*, 6434–6442.
44. Pal, S.; Dutta, A.; Paul, M.; Chattopadhyay, A. Plasmon-Enhanced Chemical Reaction at the Hot Spots of End-to-End Assembled Gold Nanorods. *J. Phys. Chem. C* **2020**, *124*, 3204-3210.
45. Kiriy, A.; Minko, S.; Gorodyska, G.; Stamm, M.; Jaeger, W. Palladium Wire-Shaped Nanoparticles from Single Synthetic Polycation Molecules. *Nano Lett.* **2002**, *2*, 8, 881–885.
46. Cathcart, N.; Coombs, N.; Gourevich, I.; Kitaev, V. Synthesis and sensing properties of D_{5h} pentagonal silver star nanoparticles. *Nanoscale* 2016, *8*, 18282-18290.
47. Yu, D.; Yam, V. Controlled Synthesis of Monodisperse Silver Nanocubes in Water. *J. Am. Chem. Soc.* **2004**, *126*, 41, 13200–13201.
48. Chen, L.; Ji, F.; Xu, Y.; He, L.; Mi, Y.; Bao, F.; Sun, B.; Zhang, X.; Zhang, Q. High-Yield Seedless Synthesis of Triangular Gold Nanoplates through Oxidative Etching. *Nano Lett.* **2014**, *14*, 12, 7201–7206.
49. Shoyama, K.; Würthner, F. Synthesis of a Carbon Nanocone by Cascade Annulation. *J. Am. Chem. Soc.* **2019**, *141*, 33, 13008–13012.
50. Frank, A. J.; Cathcart, N.; Maly, K. E.; Kitaev, V. Synthesis of Silver Nanoprisms with Variable Size and Investigation of Their Optical Properties: A First-Year Undergraduate Experiment Exploring Plasmonic Nanoparticles. *J. Chem. Educ.* **2010**, *87*, 10, 1098–1101.
51. Chaudhuri, R. G.; Paria, S. Core/Shell Nanoparticles: Classes, Properties, Synthesis Mechanisms, Characterization, and Applications. *Chem. Rev.* **2012**, *112*, 4, 2373–2433.
52. Pal, S.; Paul, S.; Chattopadhyay, A. Enhanced solid-state plasmon catalyzed oxidation and SERS signal in the presence of transition metal cations at the surface of gold nanostructures. *Phys. Chem. Chem. Phys.* **2021**, *23*, 21808-21816.
53. Dutta, A.; Chattopadhyay, A. Surface and Tip-Enhanced Raman Spectroscopy at the Plasmonic Hot Spot of a Coordination Complex-Conjugated Gold Nanoparticle Dimer. *J. Phys. Chem. C* **2017**, *121*, 18854-18861.
54. Dong, F.; Valsami-Jones, E.; Kreft, J. U. New, rapid method to measure dissolved silver concentration in silver nanoparticle suspensions by aggregation combined with centrifugation. *J Nanopart Res* **2016**, *18*, 259.

TH_3719_186122105

55. Wang, P.; Tang, H.; Zhang, P. Plasmonic Nanoparticle-based Hybrid Photosensitizers with Broadened Excitation Profile for Photodynamic Therapy of Cancer Cells. *Sci Rep* **2016**, *6*, 34981.
56. Tomitaka, A.; Arami, H.; Ahmadivand, A. *et al.* Magneto-plasmonic nanostars for image-guided and NIR-triggered drug delivery. *Sci Rep* **2020**, *10*, 10115.
57. Sotiriou, G. A. Biomedical applications of multifunctional plasmonic nanoparticles. *WIREs Nanomed Nanobiotechnol* **2013**, *5*, 19-30.
58. Kubacka, A.; Cerrada, M. L.; Serrano, C.; Fernández-García, M.; Ferrer, M.; Fernández-Garcia, M. Plasmonic Nanoparticle/Polymer Nanocomposites with Enhanced Photocatalytic Antimicrobial Properties. *J. Phys. Chem. C* **2009**, *113*, 21, 9182–9190.
59. Vo-Dinh, T.; Dhawan, A.; Norton, S. J.; Khoury, C. G.; Wang, H.-N.; Misra, V,; Gerhold, M. D. Plasmonic Nanoparticles and Nanowires: Design, Fabrication and Application in Sensing. *J. Phys. Chem. C* **2010**, *114*, 16, 7480–7488.
60. Shao, L.; Zhou, X.; Wang, J. Advanced Plasmonic Materials for Dynamic Color Display. *Adv. Mater.* **2018**, *30*, 1704338.
61. Enrichi, F.; Quandt, A.; Righini, G. C. Plasmonic enhanced solar cells: Summary of possible strategies and recent results. *Renewable and Sustainable Energy Reviews* **2018**, *82*, 2433–2439.
62. Amirjani, A.; Amlashi, N. B.; Ahmadiani, Z. S. Plasmon-Enhanced Photocatalysis Based on Plasmonic Nanoparticles for Energy and Environmental Solutions: A Review. *ACS Appl. Nano Mater.* **2023**, *6*, 11, 9085–9123.
63. Liu, J.; He, H.; Xiao, D.; Yin, S.; Ji, W.; Jiang, S.; Lua, D.; Wang, B.; Liu, Y. Recent Advances of Plasmonic Nanoparticles and their Applications. *Materials* **2018**, *11*, 1833.
64. Huang, X.; Jain, P. K.; El-Sayed, I. H. *et al.* Plasmonic photothermal therapy (PPTT) using gold nanoparticles. *Lasers Med Sci* **2008**, *23*, 217–228.
65. Peng, Y.; Xiong, B.; Peng, L. Li, H.; He, Y.; Yeung, E. S. Recent Advances in Optical Imaging with Anisotropic Plasmonic Nanoparticles. *Anal. Chem.* **2015**, *87*, 1, 200–215.
66. Kumari, G.; Zhang, X.; Devasia, D.; Heo, J.; Jain, P. K. Watching Visible Light-Driven CO_2 Reduction on a Plasmonic Nanoparticle Catalyst. *ACS Nano* **2018**, *12*, 8, 8330–8340.
67. Warren, S. C.; Thimsen, E. Plasmonic solar water splitting. *Energy Environ. Sci.* **2012**, *5*, 5133-5146.
68. Yin, Z.; Li, H.; Xu, W.; Cui, S. B.; Zhou, D. L.; Chen, X.; Zhu, Y. S.; Qin, G. S.; Song, H. W. Local field modulation induced three-order upconversion enhancement: Combining surface plasmon effect and photonic crystal effect. Adv. Mater. **2016**, *28*, 2518–2525.

TH_3719_186122105

69. Zhang, H.; Li, Y. J.; Ivanov, I. A.; Qu, Y. Q.; Huang, Y.; Duan, X. F. Plasmonic modulation of the upconversion fluorescence in $NaYF_4$:Yb/Tm hexaplate nanocrystals using gold nanoparticles or nanoshells. *Angew. Chem. Int. Ed.* **2010**, *49*, 2865–2868.
70. Liu, X.; Yuan Lei, D. Simultaneous excitation and emission enhancements in upconversion luminescence using plasmonic double-resonant gold nanorods. *Sci Rep* **2015**, *5*, 15235.
71. Fleischmann, M.; Hendra, P. J.; McQuillan, A. J. Raman Spectra of Pyridine Adsorbed at a Silver Electrode. *Chem. Phys. Lett.* **1974**, *26*, 163– 166.
72. Jeanmaire, D. L.; Van Duyne, R. P. Surface Raman Spectroelectrochemistry Part I. Heterocyclic, Aromatic, and Aliphatic Amines Adsorbed on the Anodized Silver Electrode. *J. Electroanal. Chem. Interfacial Electrochem.* **1977**, *84*, 1– 20.
73. Albrecht, M. G.; Creighton, J. A. Anomalously Intense Raman Spectra of Pyridine at a Silver Electrode. *J. Am. Chem. Soc.* **1977**, *99*, 5215– 5217.
74. Moskovits, M. Surface Roughness and the Enhanced Intensity of Raman Scattering by Molecules Adsorbed on Metals. *J. Chem. Phys.* **1978**, *69*, 4159.
75. Allen, C. S.; Schatz, G. C.; P. Van Duyne, R. Tunable laser excitation profile of surface enhanced raman scattering from pyridine adsorbed on a copper electrode surface. *Chem. Phys. Lett.* **1980**, *75*, 201.
76. Zaleski, S.; Wilson, A. J.; Mattei, M.; Chen, X.; Goubert, G.; Cardinal, M. F.; Willets, K. A.; & Van Duyne, R. P. (2016). Investigating Nanoscale Electrochemistry with Surface- and Tip-Enhanced Raman Spectroscopy. *Acc. Chem. Res.* **2016**, *49*, 9, 2023-2030.
77. Baumberg, J.; Bell, S.; Bonifacio, A.; Chikkaraddy, R.; Chisanga, M.; Corsetto, S.; Delfino, I.; Eremina, O.; Fasolato, C.; Faulds, K. et al. SERS in biology/biomedical SERS: general discussion. *Faraday Discuss.* **2017**, *205*, 429-456.
78. Cardinal, M. F.; Ende, E. V.; Hackler, R. A.; McAnally, M. O.; Stair, P. C.; Schatz, G. C.; Van Duyne, R. P. Expanding applications of SERS through versatile nanomaterials engineering. *Chem. Soc. Rev.* **2017**, *46*, 3886-3903.
79. Vo-Dinh, T.; Liu, Y.; Fales, A. M.; Ngo H.; Wang, H.-N.; Register, J. K.; Yuan, H.; Norton, S. J.; Griffin, G. D. SERS Nanosensors and Nanoreporters: Golden Opportunities in Biomedical Applications. *WIREs Nanomed Nanobiotechnol* **2015**, *7*, 17-33.
80. Schmidt, M. M.; Brolo, A. G.; Lindquist, N. C. Single-Molecule Surface-Enhanced Raman Spectroscopy: Challenges, Opportunities, and Future Directions. *ACS Nano* **2024**, *18*, 38, 25930–25938.
81. Ding, S.-Y.; You, E.-M.; Tian, Z.-Q.; Moskovits, M. Electromagnetic theories of surface-enhanced Raman spectroscopy. *Chem. Soc. Rev.* **2017**, *46*, 4042-4076.

TH_3719_186122105

82. Cong, S.; Liu, X.; Jiang, Y.; Zhang, W.; Zhao, Z. Surface Enhanced Raman Scattering Revealed by Interfacial Charge-Transfer Transitions. *The Innovation* **2020**, *1*, 100051.
83. Ausman, L. K.; Schatz, G. C. On the Importance of Incorporating Dipole Reradiation in the Modeling of Surface Enhanced Raman Scattering from Spheres. *J. Chem. Phys.* **2009**, *131*, 084708.
84. Le Ru, E. C.; Blackie, E.; Meyer, M.; Etchegoin, P. G. Surface Enhanced Raman Scattering Enhancement Factors: A Comprehensive Study. *J. Phys. Chem. C* **2007**, *111*, 37, 13794–13803.
85. Ling, X.; Xie, L.; Fang, Y.; Xu, H.; Zhang, H.; Kong, J.; Dresselhaus, M. S.; Zhang, J.; Liu, Z. Can Graphene be used as a Substrate for Raman Enhancement?. *Nano Lett.* **2010**, *10*, 2, 553–561.
86. Hou, X.; Fan, X.; Wei, P.; Qiu, T. Planar transition metal oxides SERS chips: a general strategy. *J. Mater. Chem. C*, **2019**, *7*, 11134-11141.
87. Fraser, J. P.; Postnikov, P.; Miliutina, E.; Kolska, Z.; Valiev, R.; Švorčík, V.; Lyutakov, O.; Ganin, A. Y.; Guselnikova, O., Application of a 2D Molybdenum Telluride in SERS Detection of Biorelevant Molecules. *ACS Appl. Mater. Interfaces* **2020,** *12* (42), 47774-47783.
88. Liu, D.; Song, X.; Yi, W.; Li, Y.; Kong, Q.; Bai, H.; Zou, M.; Xi, G., General Microwave Route to Single-Crystal Porous Transition Metal Nitrides for Highly Sensitive and Stable Raman Scattering Substrates. *Nano Lett.* **2021,** *21* (18), 7724-7731.
89. Sarycheva, A.; Makaryan, T.; Maleski, K.; Satheeshkumar, E.; Melikyan, A.; Minassian, H.; Yoshimura, M.; Gogotsi, Y. Two-Dimensional Titanium Carbide (MXene) as Surface-Enhanced Raman Scattering Substrate. *J. Phys. Chem. C* **2017**, *121*, 36, 19983–19988.
90. Liu, Y.; Chui, K. K.; Fang, Y.; Wen, S.; Zhuo, X.; Wang, J. Metal–Organic Framework-Enabled Trapping of Volatile Organic Compounds into Plasmonic Nanogaps for Surface-Enhanced Raman Scattering Detection. *ACS Nano* **2024**, *18*, 17, 11234–11244.
91. Yilmaz, M.; Babur, E.; Ozdemir, M.; Gieseking, R. L.; Dede, Y.; Tamer, U.; Schatz, G. C.; Facchetti, A.; Usta, H.; Demirel, G., Nanostructured organic semiconductor films for molecular detection with surface-enhanced Raman spectroscopy. *Nat. Mater.* **2017,** *16* (9), 918-924.
92. Bhakat, A.; Paul, S.; Chattopadhyay, A. Molecular Specificity in the Intense Surface-Enhanced Raman Scattering on Copper(II) 8-Hydroxyquinoline Microcrystals. *J. Phys. Chem. C* **2023**, *127*, 10, 5169–5177.

TH_3719_186122105

93. Bhakat, A.; Chattopadhyay, A. Molecular Cooperativity in the Intense Raman Scattering on the Surface of an Organic Molecular Microcrystal. *Adv. Optical Mater.* **2024**, *12*, 2301776.
94. Zheng, C.; Xu, X.; He, F.; Li, L.; Wu, B.; Yu, G.; Liu, Y. Preparation of High-Quality Organic Semiconductor Nanoparticle Films by Solvent-Evaporation-Induced Self-Assembly. *Langmuir* **2010**, *26*, 22, 16730–16736.
95. Deng, R.; Yang, L.; Bain, C. D. Combining Inkjet Printing with Emulsion Solvent Evaporation to Pattern Polymeric Particles. *ACS Appl. Mater. Interfaces* **2018**, *10*, 15, 12317–12322.
96. Hoeven, J. E. S. v. d.; Shneidman, A. V.; Nicolas, N. J.; Aizenberg, J. Evaporation-Induced Self-Assembly of Metal Oxide Inverse Opals: From Synthesis to Applications. *Acc. Chem. Res.* **2022**, *55*, 13, 1809–1820.
97. Wilkinson, J.; Tam, C.; Askounis, A.; Qi, S. Suppression of the coffee-ring effect by tailoring the viscosity of pharmaceutical sessile drops. *Colloids and Surfaces A: Physicochemical and Engineering Aspects* **2021**, *614*, 126144.
98. Zhang, W.; Yu, T.; Liao, L.; Cao, Z. Ring formation from a drying sessile colloidal droplet. *AIP Advances* **2013**, *3*, 102109.
99. Brutin, D. Influence of relative humidity and nano-particle concentration on pattern formation and evaporation rate of pinned drying drops of nanofluids. *Colloids and Surfaces A: Physicochemical and Engineering Aspects* **2013**, *429*, 112-120.
100. Lohani, D.; Basavaraj, M. G.; Satapathy, D. K.; Sarkar, S. Coupled effect of concentration, particle size and substrate morphology on the formation of coffee rings. *Colloids and Surfaces A: Physicochemical and Engineering Aspects* **2020**, *589* 124387.
101. Deegan, R. D.; Bakajin, O.; Dupont, T. F.; Huber, G.; Nagel, S. R.; Witten, T. A. Contact line deposits in an evaporating drop. *Phys. Rev. E* **2000**, *62*, 756-765.
102. Deegan, R. D.; Bakajin, O.; Dupont, T. F.; Huber, G.; Nagel, S. R.; Witten, T. A. Capillary flow as the cause of ring stains from dried liquid drops. *Nature* **1997**, *389*, 827-829.
103. Boulonge, F.; Ingremeau, F.; Stone, H. A. Coffee-stain growth dynamics on dry and wet surfaces. *J. Phys.: Condens. Matter* **2017**, *29*, 074001.
104. Yunker, P. J.; Still, T.; Lohr, M. A.; Yodh, A. G. Suppression of the coffee-ring effect by shape-dependent capillary interactions. *Nature* **2011**, *476*, 308-311.
105. Crivoi, A.; Duan, F. Effect of Surfactant on the Drying Patterns of Graphite Nanofluid Droplets. *J. Phys. Chem. B* **2013**, *117*, 5932-5938.

TH_3719_186122105

106. Wong, T.-S.; Chen, T.-H.; Shen, X.; Ho, C.-M. Nanochromatography Driven by the Coffee Ring Effect. *Anal. Chem.* **2011**, *83*, 6, 1871–1873.

107. Hu, H.; Larson, R. G. Marangoni Effect Reverses Coffee-Ring Depositions. *J. Phys. Chem. B* **2006**, *110*, 14, 7090–7094.

108. Torrisi, F.; Hasan, T.; Wu, W.; Sun, Z.; Lombardo, A.; Kulmala, T. S.; Haieh, G.-W.; Jung, S.; Bonaccorso, F.; Paul, P. J.; *et al.* Inkjet-Printed Graphene Electronics. *ACS Nano* **2012**, *6*, 2992-3006.

109. Ye, X.; Ge, L.; Jiang, T.; Guo H.; Chen, B.; Liu, C.; Hayashi, K. Fully Inkjet-Printed Chemiresistive Sensor Array Based on Molecularly Imprinted Sol–Gel Active Materials. *ACS Sens.* **2022**, *7*, 1819-1828.

110. Xuan, T.; Shi, S.; Wang, L.; Kuo, H.-C.; Xie, R.-J. Inkjet-Printed Quantum Dot Color Conversion Films for High-Resolution and Full-Color Micro Light-Emitting Diode Displays. *J. Phys. Chem. Lett.* **2020**, *11*, 5184-5191.

111. Pendyala, N. K.; Magdassi, S.; Etgar, L. Fabrication of Perovskite Solar Cells with Digital Control of Transparency by Inkjet Printing. *ACS Appl. Mater. Interfaces* **2021**, *13*, 30524-30532.

112. Molina-Lopez, F.; Gao, T. Z.; Kraft, U.; Zhu, C.; Öhlund T.; Pfattner, R.; Feig, V. R.; Kim, Y.; Wang, S.; Yun, Y.; *et al.* Inkjet-printed stretchable and low voltage synaptic transistor array. *Nat Commun* **2019**, *10*, 2676.

113. Gao, M.; Li, L.; Song, Y. Inkjet printing wearable electronic devices. *J. Mater. Chem. C* **2017**, *5*, 2971-2993.

114. Sajedi-Moghaddam, A.; Rahmanian, E.; Naseri, N. Inkjet-Printing Technology for Supercapacitor Application: Current State and Perspectives. *ACS Appl. Mater. Interfaces* **2020**, *12*, 34487-34504.

115. Gao, G.; Chu, X. Three-dimensional bioprinting in tissue engineering and regenerative medicine. *Biotechnol Lett.* **2016**, *38*, 203-211.

116. Hussain, A.; Abbas, N.; Ali, A. Inkjet Printing: A Viable Technology for Biosensor Fabrication. *Chemosensors* **2022**, *10*, 103.

117. Derby, B. Bioprinting: inkjet printing proteins and hybrid cell-containing materials and structures. *J. Mater. Chem.* **2008**, *18*, 5717-5721.

118. Bietsch, A.; Henger, M.; Lang, H. P.; Gerber, C. Inkjet Deposition of Alkanethiolate Monolayers and DNA Oligonucleotides on Gold: Evaluation of Spot Uniformity by Wet Etching. *Langmuir* **2004**, *20*, 5119-5122.

TH_3719_186122105

119. Olejnik, A.; Semba, J. A.; Kulpa, A.; Dańczak-Pazdrowska A.; Rybka, J. D.; Gornowicz-Porowska J. 3D Bioprinting in Skin Related Research: Recent Achievements and Application Perspectives. *ACS Synth. Biol.* **2022**, *11*, 26-38.

120. Meng, Y.; Cao, J.; Chen, Y.; Yu, Y.; Ye, L. 3D printing of a poly(vinyl alcohol)-based nano-composite hydrogel as an artificial cartilage replacement and the improvement mechanism of printing accuracy. *J. Mater. Chem. B* **2020**, *8*, 677-690.

121. Kim, S.; Handler, J. J.; Cho, Y. T.; Barbastathis, G.; Fang, N. X. Scalable 3D printing of aperiodic cellular structures by rotational stacking of integral image formation. *Sci. Adv.* **2021**, *7*, eabh1200.

122. Hadibrata, W.; Wei, H.; Krishnaswamy, S.; Aydin, K. Inverse Design and 3D Printing of a Metalens on an Optical Fiber Tip for Direct Laser Lithography. *Nano Lett.* **2021**, *21*, 2422-2428.

123. Zhang, S.; Qi, Y.; Tan, S. P. H.; Bi, R.; Olivo, M. Molecular Fingerprint Detection Using Raman and Infrared Spectroscopy Technologies for Cancer Detection: A Progress Review. *Biosensors* **2023**, *13*, 557.

124. Quiño, J.; Hellwig, T.; Griesing, M.; Pauer, W.; Moritz, H.-U.; Will, S.; Braeuer, A. One-dimensional Raman spectroscopy and shadowgraphy for the analysis of the evaporation behavior of acetone/water drops. *International Journal of Heat and Mass Transfer* **2015**, *89*, 406–413.

125. Zargartalebi, H.; Hejazi, S. H.; Sanati-Nezhad, A. Self-assembly of highly ordered micro- and nanoparticle deposits. *Nat Commun* **2022**, *13*, 3085.

126. Ramos, R. M. C. R.; Jiang, W.; Heng, J. Z. X.; Ko, H. Y. Y.; Ye, E.; Regulacio, M. D. Hyperbranched Au Nanocorals for SERS Detection of Dye Pollutants. *ACS Appl. Nano Mater.* **2023**, *6*, 5, 3963–3973.

127. Gao, S.; Lin, Y.; Zhao, X.; Gao, J.; Xie, S.; Gong, W.; Yu, Y.; Lin, J. Label-free surface enhanced Raman spectroscopy analysis of blood serum via coffee ring effect for accurate diagnosis of cancers. *Spectrochimica Acta Part A: Molecular and Biomolecular Spectroscopy* **2022**, *267*, 120605.

128. Tahir, M. A.; Dina, N. E.; Cheng, H.; Valev, V. K.; Zhang, L. Surface-enhanced Raman spectroscopy for bioanalysis and diagnosis. *Nanoscale*, **2021**, *13*, 11593-11634.

129. Dey, U.; Chattopadhyay, A. Two-dimensional molecular moiré superlattices of tryptophan with visible photoluminescence for photo-activatable CO_2 sensing and storage. *J. Mater. Chem. C* **2024**, *12*, 5506-5516.

TH_3719_186122105

130. Hajra, A.; Chattopadhyay, A. Chemically Reversible Translational Moiré Superlattice Formations in the Two-Dimensional Films of the Zinc Phthalate Complex. *J. Phys. Chem. Lett.* **2024**, *15*, 39, 10046–10053.

TH_3719_186122105

Chapter-2

Single Phase Transition Leads to the Nanoparticle Deposition in an Evaporating Sessile Droplet

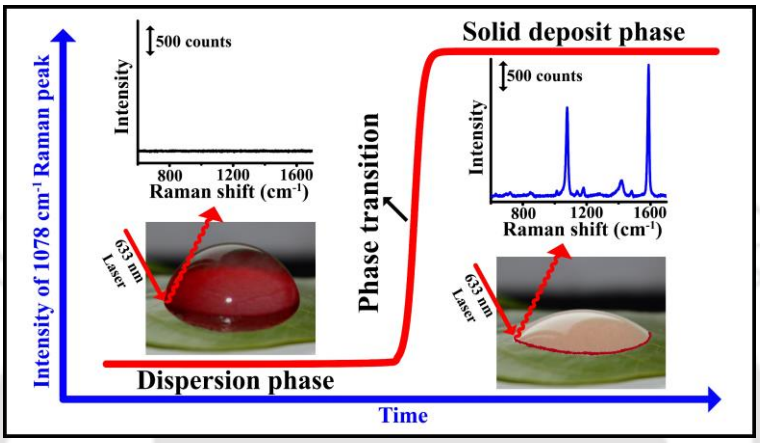

Chapter 2 *reports the basic deposition kinetics of dispersed spherical nanoparticles at the contact line of an evaporating sessile droplet probed by time dependent surface-enhanced Raman spectroscopy (SERS). We have utilized SERS when aqueous droplets of sodium 4-marcaptobenoate-stabilized nanomolar plasmonic gold nanoparticles (NaMBA-AuNPs) were evaporated under ambient conditions. The Raman signal of the molecules were observed to have sharply increased in a short window of time that matched well with simultaneous digital photographing of the deposition. Higher initial AuNP concentrations led to faster phase transitions; however, the final concentration at the TPCL was about 13 μM for 25 nm AuNPs, irrespective of the initial concentrations studied. The time for phase transitions were decreasing with increasing particle size at a fixed initial AuNPs concentration.*

The content of Chapter 2 has been published in *The Journal of Physical Chemistry C*, a journal of the American Chemical Society (ACS). *J. Phys. Chem. C* **2023,** *127*, 45, 22401–22411

https://pubs.acs.org/doi/full/10.1021/acs.jpcc.3c06029

TH_3719_186122105

2.1. Introduction

Evaporation of a sessile droplet leading to deposition of the dissolved or dispersed solid on substrate surface continues to be technologically significant and scientifically intriguing. For example, inkjet printing of liquid droplets drives technology such as printed electronics[1], solar cells[2], chemical sensors[3], supercapacitors[4], display pixels[5], wearable[6], flexible and stretchable devices[7]. In healthcare applications such as printing of biomolecular sensing elements[8], DNA microarrays[9] and cells (including stem cells)[10], tissue engineering[11] and regenerative medicine[12], similar principles are used for depositions of target moieties. Further, advancement in technology for inkjet printing promises to revolutionize healthcare through personalized medicine that takes recourse of 3D printing of artificial cartilage[13], skins[14] and cellular structures[15] as applicable for transplantation therapies. On the other hand, dip-pen lithography-based printing of molecular and nanoscale matters offers promises of advancement in all of the aforementioned fields through deposition of materials of interests at the highest resolution.[16] Thus, notwithstanding the apparent maturity of field in understanding the fundamental processes of printed structures, the versatility of applications may spring surprises in discovering novel phenomena.

Understanding of droplet evaporation under different conditions such as droplet composition and viscosity[17], evaporation temperature[18], humidity[19] and nature and morphology of substrate surface[20] has been key to the progresses in technological applications. In general, droplet evaporation is a method to concentrate dispersed particles in a certain deposition pattern of choice. A common evaporation induced pattern formation is the 'coffee-ring' effect where the solid gets preferentially deposited on the surface in the form of a ring akin to coffee stain.[21] Thus, when a sessile droplet is placed with a non-zero contact angle on a substrate surface, the three-phase pinned contact line and inhomogeneous solvent evaporation from the liquid-vapor interface cooperatively initiate an outward advective motion of the liquid carrying the dispersed particles towards the periphery.[21] The height of the droplet decreases linearly with time.[18] The particles get deposited in the form of a ring primarily along the perimeter. The mass of the ring has a power law dependent growth with time.[21] Importantly, the models predict continuous deposition of the dispersed particles at the pinned contact line with capillary flow carrying the particles from the bulk to the periphery and little role of diffusion opposing that.[21,22]

The progress in experimental techniques has helped improve the understanding of particle motions and deposition characteristics and also in modulating the desired deposition patterns.

TH_3719_186122105

For example, videography and fluorescence microscopy revealed the advective motion of micron-sized particles from the center to the pinned contact line.[21-23] Advanced analytical methods have also been used to pursue the details of profiles of the patterns following deposition of the analyte and drying of the solvent.[24] Means of changing the patterns of deposition have also been applied in order to have uniform deposition across the liquid-solid interface.[20,25] However, it is also important to probe the depositions as the particles get settled to the substrate surface. This would be especially important for deposition of nanoparticles that have important consequences in applications such as in biomolecular sensing.[26] A well-established method that could be utilized in order to pursue the particles being deposition at the pinned contact line is surface enhanced Raman spectroscopy (SERS).[27] This is based on the extraordinary enhancement of Raman scattering intensity of molecular bonds when being on the surface of Ag and Au nanoparticles (NPs).[27] The plasmon fields on such metal NP surfaces make Raman scattering easy to probe. In addition, hot-spot generation in between the metal NPs further enhances the signal intensity.[28] It is thus plausible that such a technique could be used in order to probe the time-dependent particle deposition on the substrate surface. This would be facile for the deposition of metal NPs (such as those of Au or Ag) at the pinned periphery of the droplet laden with NPs and molecules as probe.

2.2. Outline of the Present Work

We report herein the observation of phase transition in the evaporation of NP-laden sessile water droplets, leading to the ring pattern formation at the pinned three-phase boundary. We used a dispersion of plasmonic Au NPs mixed with sodium 4-mercaptobenzoate (NaMBA). The droplets of less than 2 mm in radius were placed on glass surfaces and were allowed to evaporate at 22 °C and room humidity of about 65-70% unless otherwise mentioned. Time-depended SERS spectra of 4-MBA on the surface of the Au NPs were recorded at the pinned contact lines of the evaporating droplets. Interestingly, the agglomerated AuNPs -when deposited as ring- also helped obtain high quality spectra possibly through the contributions of the plasmonic fields at the hot-spots. Importantly, we observed either no or weak signal due to 4-MBA at the pinned contact line, even though the droplet height and contact angle were decreasing linearly. However, much before the droplet evaporated completely, there was sudden increase in intensity of the Raman signals due to 4-MBA, which remained nearly constant till the droplet was dry. We also observed through videography using the Raman microscope sudden deposition of solid concurrent with the change in signal intensity. The plot

TH_3719_186122105

of Raman signal of a characteristic peak due to 4-MBA indicated a sharp change in intensity at the point of deposition, akin to a phase transition. Further, we observed that the lower was the concentration of the dispersed particles in the medium the longer was the phase transition time. Our observations also indicated that for the same sized particles, the concentration at the pinned periphery at the time of phase transition was nearly the same for all initial concentrations. Particle size dependent experiments revealed, for same initial particle concentration, larger nanoparticles underwent phase transition earlier than the smaller nanoparticles.

2.3. Experimental Section

2.3.1. Materials:

Gold(III) chloride solution ($HAuCl_4$), and 4-mercaptobenzoic acid, 99% (4-MBA) were bought from Sigma-Aldrich India. Trisodium citrate dihydrate, sodium hydroxide and acetone were purchased from Merck India. All the chemicals were used as such and without further purification. Milli-Q grade water was used for all experiments and washing purposes. Rectangular borosilicate glass slides were precleaned sequentially using fresh aqua regia, Milli-Q water and acetone.

2.3.2. Instruments and Characterizations:

UV-Vis absorbance spectra were recorded using PerkinElmer® Lambda 365+ UV-Vis spectrometer. Malvern Zetasizer Nano ZS-90 instrument was used to measure zeta potential. Transmission electron microscopic (TEM) images and selected-area electron diffractions (SAED) were obtained from JEOL JEM-2100F Field Emission Transmission Electron Microscope (FETEM) instrument having acceleration voltage of 200 kV. FETEM samples were prepared by drop-casting 7 µL of AuNP dispersions on carbon-coated copper grids. Raman spectra were recorded using Horiba LabRAM HR Evolution Raman spectrometer attached with 633 nm laser source. Field emission scanning electron microscopic (FESEM) images were captured from Carl Zeiss JSM-7610F FESEM instrument. Atomic force microscopic (AFM) measurements were done using Oxford Asylum Research Model: MFP-3D instrument. Optical images were obtained using microscope system attached to Raman spectrometer and Nikon D3200 DSLR camera. All the captured images were post-processed using ImageJ software[29] to obtain contact angle, height, thickness of coffee-ring and droplet radius on glass substrate. All the graphs were plotted in Origin 9.0 pro software and variations

TH_3719_186122105

of Raman signal intensity with time were fitted as sigmoidal growth using the Boltzmann fitting in Origin 9.0. Fitting parameters are given in **Table A2.4** in Supporting Information.

2.3.3. Synthesis of Gold Nanoparticles (AuNPs) of Different Size:

Citrate capped gold nanoparticles was synthesized by the method reported by Frens *et al.* after slight modification.[30] 10 µL of 1.4453 (M) gold(III) chloride solution was added in 25 mL Milli-Q water and heated at 110 °C for 30 min. Then, 38.7 (mM) trisodium citrate solution were added at a time to the boiling solution and boiling was continued for another 15 min. For the synthesis of nanoparticles of different size, volume of the trisodium citrate solution was varied. 1000 µL citrate solution yielded reddish dispersion of small AuNP (AuNP-1) used in our experiment. 800 µL citrate solution gave rise to wine-red dispersion of AuNP (AuNP-2) and 500 µL of citrate solution produced purple dispersion of big AuNP (AuNP-3). The dispersions were cooled to room temperature. To purify, 4 mL AuNP dispersions were centrifuged at 15000 rpm, 12,000 rpm and 8000 rpm for small, medium and big AuNPs respectively for 10 min at 10 °C and were then redispersed in 400 µL, 400 µL and 250 µL Milli-Q water respectively. Formation of AuNPs of different size was confirmed from UV-Vis spectroscopic measurement and sizes of the particles were calculated from FETEM images.

2.3.4. Preparation of Sodium 4-mercaptobenzoate (NaMBA) Capped AuNP Dispersions (NaMBA-AuNP):

4.5 mg 4-MBA was completely dissolved in 1 mL Milli-Q water using minimum volume of 1 (M) aqueous sodium hydroxide solution. A diluted stock was made using 20 µL of previous sodium 4-mercaptobenzoate (NaMBA) solution in 200 µL water. From this, 50 µL of NaMBA diluted solutions was added in each 400 µL centrifuged AuNP-1, AuNP-2 and 250 µL centrifuged AuNP-3 dispersions. The mixture was ultrasonicated for 1 h for complete surface functionalization of AuNP with 4-mercaptobenzoate (MBA). These were the highest concentrated NaMBA capped AuNP dispersions abbreviated as NaMBA-AuNP-1, NaMBA-AuNP-2 and NaMBA-AuNP-3 for nanoparticles of three different sizes. For nanoparticle concentration dependent experiment, NaMBA-AuNP-2 was subsequently diluted four and eight-times using Milli-Q water to maintain the same ratio of NaMBA to AuNP for all three concentrations. For nanoparticle size dependent experiments at a fixed nanoparticle initial concentration, 92 µL NaMBA-AuNP-1 and 400 µL NaMBA-AuNP-2 were both diluted to 800 uL in order to obtain 5 nM NaMBA-AuNP dispersions. Diluted dispersions were also ultrasonicated for 1 h in order to avoid agglomeration before further experiments. Those

TH_3719_186122105

colloidal dispersions of NaMBA-AuNP were directly used for UV-Vis spectroscopy, zeta potential measurements, drop casting for TEM images, formation of coffee-ring and Raman measurements.

2.3.5. Coffee-ring Formation and Raman Measurement:

5 µL of NaMBA attached AuNP (NaMBA-AuNP) was dropped - using a micropipette - on a cleaned glass slide to make a tiny spherical-cap droplet. The slide was then placed on Raman sample holder to record Raman spectra while the droplet was evaporating. A DSLR camera was placed in front of the droplet to capture pictures of the droplet horizontally in order to measure contact angle and height. An optical microscope attached with the Raman spectrometer was used to obtain droplet images vertically. Spectra and images were taken after every 2.5 min, which included Raman scan time till complete evaporation of the droplet. Details of the experimental setup have been presented in **Figure 2.1c** of the Chapter 2. This experiment was done in an air-conditioned room at temperature ~22 °C. Raman spectra were recorded at a fixed spot on the circular edge of the pinned droplet using 1% power of 633 nm laser (16 mW) at 600 gr/mm diffraction grating with acquisition time of 5 s and accumulation of 5 under 50× long distance objective lens. Baseline corrections for all recorded spectra were performed in LabSpec 6 software.

2.3.6. Atomic force microscopic (AFM) analysis:

In order to probe the depositions at different times during the phase-transition time window, we prepared different samples by following Raman signal intensities of different evaporating droplets (of similar sizes) at the same initial AuNP concentration. Similar to the other Raman measurement experiments, 5 µL of NaMBA attached AuNP-2 (NaMBA-AuNP-2) was dropped on a cleaned glass slide. The slide was then placed on Raman sample holder to record Raman spectra while the droplet was evaporating. During evaporation, as soon as we got desired Raman signal intensity at the TPCL, the remaining dispersion was dried very carefully with a tissue paper without disturbing the deposition at the TPCL. Three different samples were prepared at different times of deposition by observing Raman signal intensities and one sample was left to dry completely while recording Raman spectrum with time in order to get maximum deposition and thus the maximum Raman signal intensity. One at very low Raman signal intensity; another one was prepared following complete deposition, which gave maximum signal intensity and another two samples were prepared where the signal intensities of the depositions were in between the lowest and maximum intensities. The four samples were dried

TH_3719_186122105

and then AFM images were obtained by scanning the sample in tapping mode using gold coated AFM tip. For topographic analysis, 50 µm × 50 µm area containing deposited NaMBA-AuNP-2 and for observing gold nanoparticle assembly, 500 nm × 500 nm area on the deposition were scanned.

2.4. Results and Discussions

2.4.1. Characterization of NaMBA-AuNP-2:

For the results reported herein, AuNPs of three sizes, namely, 15.4 nm (AuNP-1), 25.3 nm (AuNP-2) and 36.4 nm (AuNP-3) were used. For the nanoparticle concentration dependent experiments leading to coffee-ring formation, dispersions having three different concentrations i.e., 10 nM, 2.5 nM and 1.25 nM of 25.3 nm AuNPs (AuNP-2) were used. However, the results and discussions of the measurements using 2.5 nM NP dispersion are detailed below. The remainder of the results are included in the Appendix of Chapter 2 (A2). UV-Vis spectrum of NaMBA-AuNP-2 in **Figure 2.1a** shows surface plasmon resonance peak at 530 nm, which was

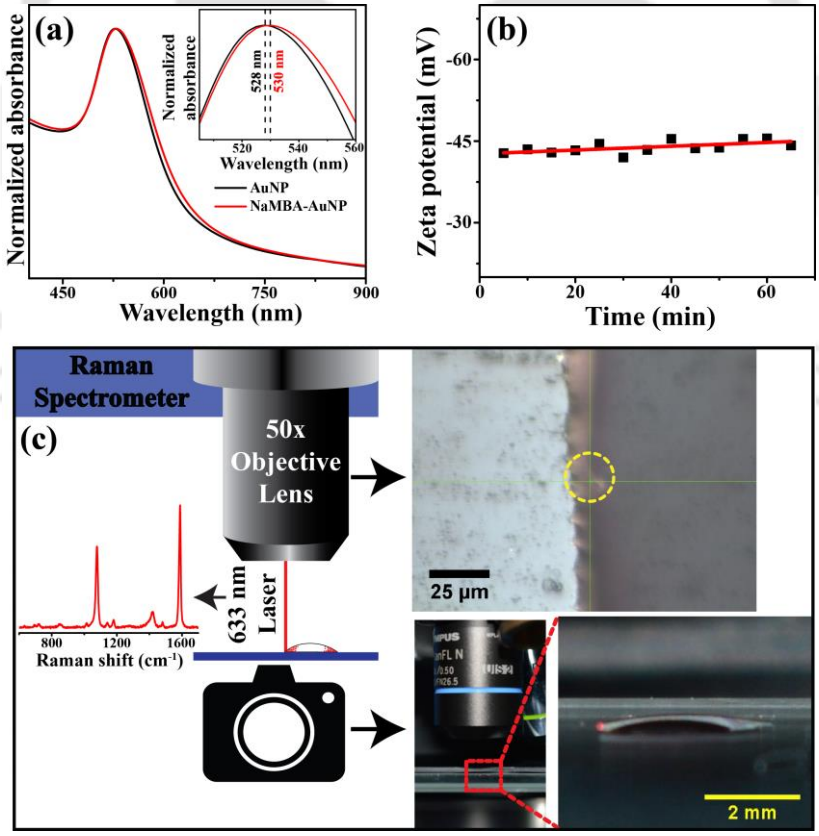

Figure 2.1: (a) UV-Vis spectra of the AuNP-2 and NaMBA-AuNP-2 dispersions. Inset is the zoomed spectra of the same. (b) Plot of zeta potential of NaMBA-AuNP-2 with time. (c) Pictorial illustration of the experimental set up for measuring coffee-ring formation and related Raman scattering.

TH_3719_186122105

2 nm red-shifted with respect to that at 528 nm for only AuNP. The shift of SPR peak signified the attachment of NaMBA with AuNP through soft sulfur atom.[31] The constancy of the zeta potential of the dispersion with time (**Figure 2.1b**) revealed stability of the medium for more than an hour that was sufficient to carry out other experiments.[32] Furthermore, the negative zeta potential value of −43.9±1.0 mV confirmed the presence of free COO^- group of MBA on the surface of NaMBA-AuNP-2 particles. Also, no major aggregations were observed in the TEM image of NaMBA-AuNP-2 (**Figure A2.1**). Average diameter of spherical AuNP calculated from TEM image was 25.3±4.2 nm. UV-Vis spectra and zeta potential variation with time for other two initial concentrations were given in **Figure A2.2** in the Appendix A2. Because of high dispersion stability, factors for nanoparticles aggregation such as hydrogen bonding or hydrophobic interactions between surface attached molecules of nearby nanoparticles could be neglected. However, NaMBA-AuNP-2 particles will eventually be deposited as solid aggregates during the formation of coffee-ring. The NaMBA-AuNP-2 dispersion was dropped on a cleaned glass slide for following the evaporation using SERS. Schematic illustration of the experimental setup is given in **Figure 2.1c**.

2.4.2. Coffee-ring Formation:

Here, the radii of the droplets were kept less than the capillary length of water (~2 mm) so that the effect of gravity to flatten the drop was minimized and surface tension always kept the droplet cap spherical. **Figure 2.2** illustrates typical real-time images of the drying droplet on the glass slide. Side-view images were captured while recording Raman spectra and red dots of 633 nm laser were visible. These images were correlated with the changes in the Raman signals as the droplet evaporated. Particles were transported to the edge of the droplet and started to deposit as solid with dark reddish-black hue on the glass substrate beginning at 27.5 min (**Figure 2.2d(ii)**). The deposition appeared to have been complete within 7.5 min time window and the coffee-ring pattern was clearly visible when water was still present at 35.0 min. Results of atomic force microscopic (AFM) measurements, shown in **Figure 2.4**, indicated gradual deposition in the form of assemblies of Au nanoparticles, the height of which increased significantly during the transition. It is clear that TPCL was pinned throughout the whole drying process and evaporation followed constant contact radius (CCR) mode.[33] During evaporation, the droplet with contact angle could be imaged till 42.5 min (**Figure 2.2h**), whereas the sessile droplet took around 45.0 min for complete drying (**Figure 2.2i**). A thick ring pattern was clearly visible after complete drying (**Figure 2.2i,j**). The small segment of the whole ring pattern was representative of the ring deposition as similar depositions were

TH_3719_186122105

observed at other locations at the TPCL, shown in **Figure A2.3**. Optical images corresponding to the time-dependent evaporation of NaMBA-AuNP colloidal droplet dispersions at 10 nM and 1.25 nM initial concentrations were presented in **Figure A2.4** and **Figure A2.5** respectively.

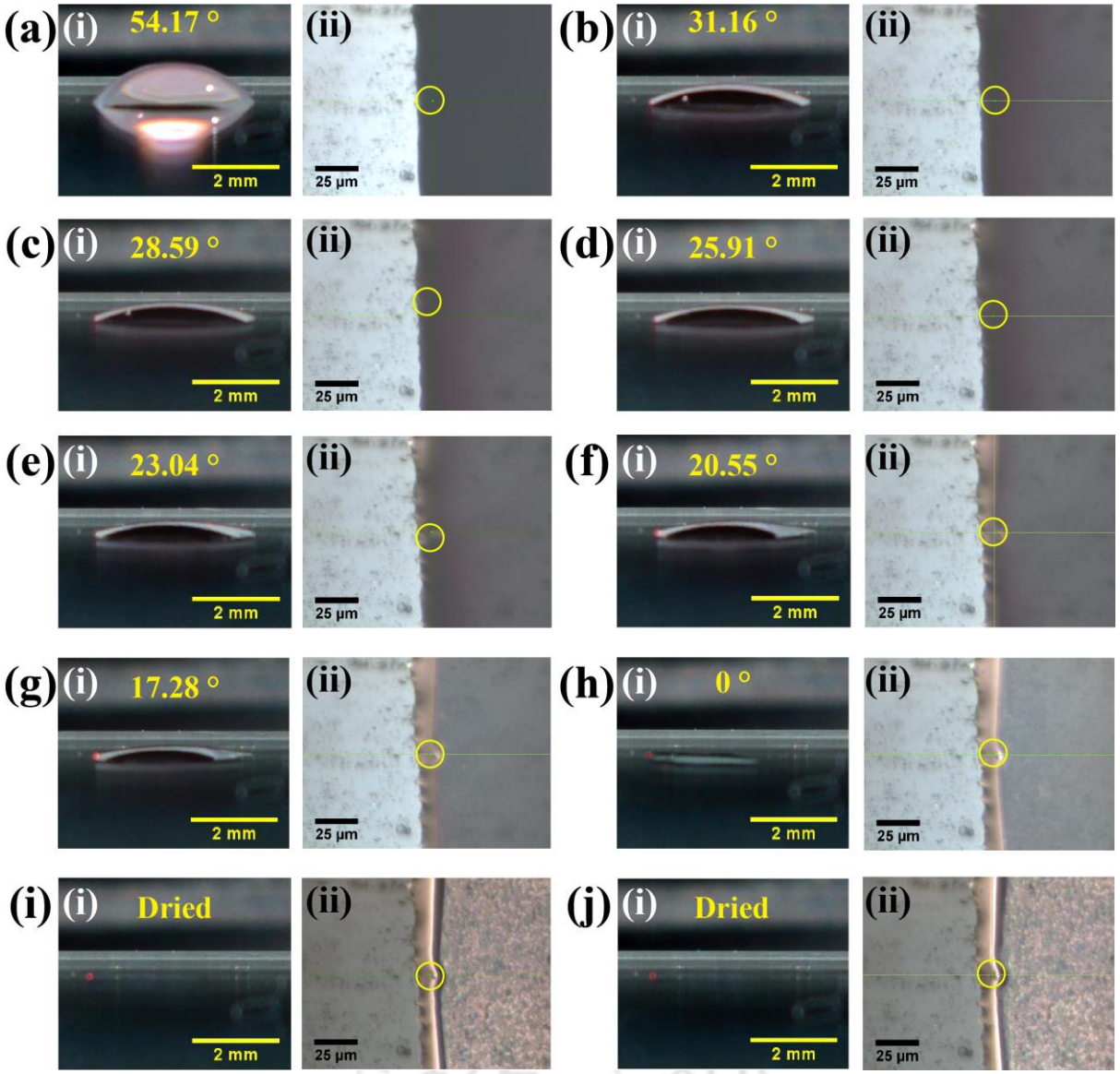

Figure 2.2: Optical images of evaporating droplet containing 2.5 nM NaMBA-AuNP-2 at (a) 0 min, (b) 22.5 min, (c) 25.0 min, (d) 27.5 min, (e) 30.0 min, (f) 32.5 min, (g) 35.0 min, (h) 42.5 min, (i) 45.0 min and (j) 52.5 min. The images in (i) were captured horizontally using DSLR camera and and their corresponding images in (ii) were recorded vertically using camera attached to the Raman microscope. Contact angles are mentioned on top side of each horizontal images and Raman probe areas are identified with yellow circles.

TH_3719_186122105

2.4.3. SERS Measurements at TPCL:

As shown in **Figure 2.3a**, the evaporation of the sessile droplet was accompanied by the decrease in the contact angle and height linearly with time. This is consistent with the literature reports for CCR mode of evaporation.[18,33] On the other hand, the recording of Raman spectra with time at a fixed spot near the pinned contact line revealed novel results. The spectra were recorded at an interval of 2.5 min. Time-dependent Raman spectra corresponding to the droplet images of **Figure 2.2** are shown in **Figure 2.3b** and detailed assignments of Raman peaks are given in **Table A2.1** in **A2**. As is clear from the figure, during the evaporation till 25 min,

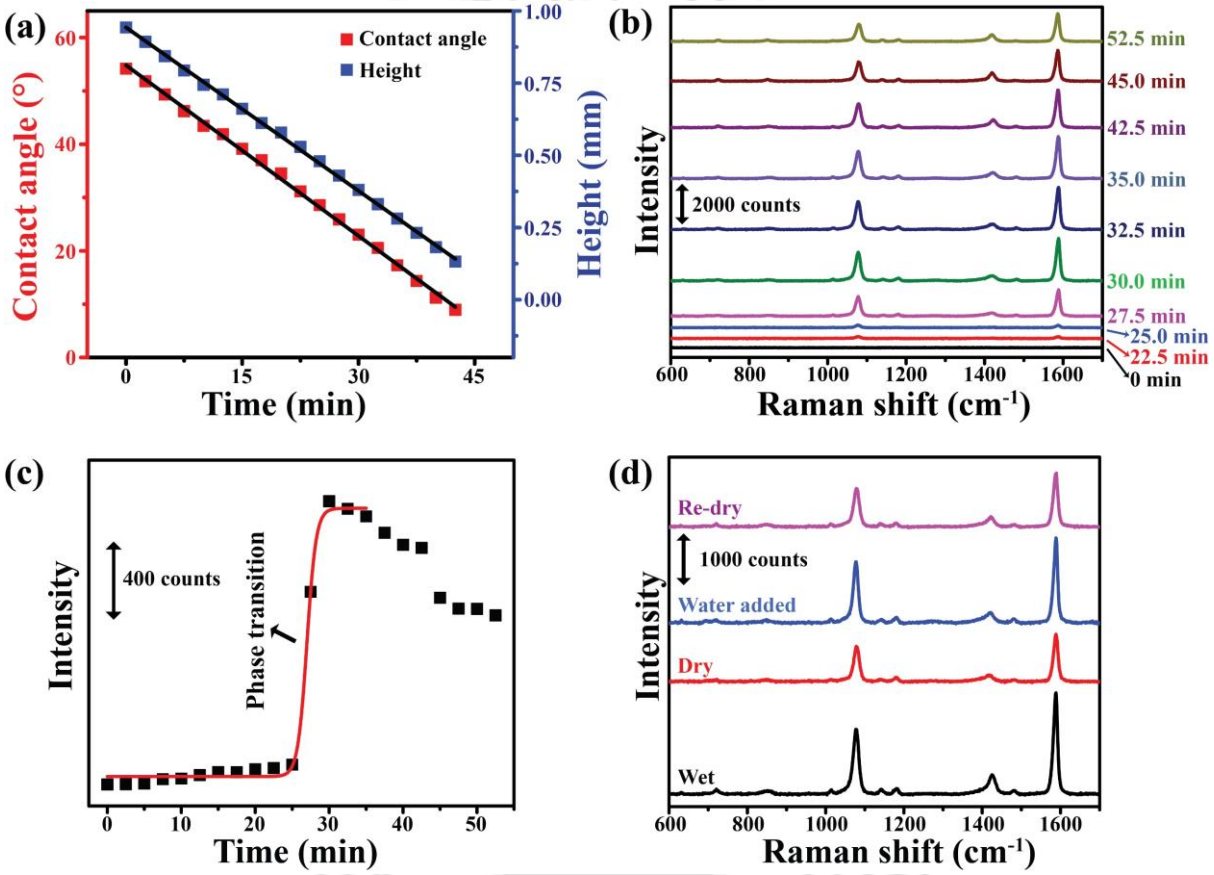

Figure 2.3: (a) Plot of variation of contact angle and droplet height with time. Black lines are linear fits. (b) Raman spectra of evaporating droplet containing NaMBA-AuNP-2 at the fixed spot on three-phase contact tine recorded at different times. (c) Plot of intensity of 1078 cm^{-1} Raman peak vs. time and red curve is Boltzmann fitting of sigmoidal growth. (d) SERS spectra of NaMBA-AuNP-2 in wet, dry and subsequent addition of water and re-dried conditions respectively. The spectra were recorded on the same spot of a coffee ring.

Raman signal intensities (if any) were negligibly small. However, at 27.5 min, the peak intensities increased significantly. The intensities continued to increase till 30 min. Then the peak intensities decreased slowly till 42.5 min that was followed by significant decline upon

TH_3719_186122105

complete evaporation at 45.0 min of the droplet. The Raman peak at 1078 cm^{-1}, corresponding to combined aromatic C=C ring breathing and C−S stretching vibrations,[28] was chosen to monitor the intensity variation of Raman signal with time. As is evident from **Figure 2.3c**, Raman signal intensity initially was very low and after sometimes intensity went up drastically within a short period of time and then after reaching a maxima intensity dropped. After complete drying, no significant change in intensity was observed. Further, analysis of the photographic images in **Figure 2.2** revealed that solid particle depositions occurred in concurrence with the increase in signal intensity. For example, till 25.0 min, Raman signal intensity was very weak as there was no deposition of AuNP at that spot (**Figure 2.2c(ii)**). Starting of AuNP deposition from 27.5 min, as shown in **Figure 2.2d(ii)**, was reflected in increase of Raman signal intensity. Then at 30 min, maximum Raman signal intensity was correlated to the solid deposition at the probing area in **Figure 2.2e(ii)**. It was observed that upon drying there were apparently more particles deposited on the inner side of TPCL, as is clear from **Figures 2.2i** and **2.2j**. However, this was probably due to the presence of water droplet at the phase transition time preventing a clearer imaging of the deposits. Thus, when water was removed using a tissue paper carefully, without disturbing the ring pattern after maximum Raman signal intensity, inner NP deposit was observed as shown in **Figure A2.6**. NP deposits indeed were there similar to naturally dried droplets. Further, it appears that the majority of particles were deposited during 25.0 to 30.0 min. The decrease in signal intensity from 32.5 min was probably due to loss of water as that could be observed starting with **Figure 2.2g**.

A chemical dispersion starts deposition once the concentration reaches beyond saturation. Similarly, when the concentration of the AuNP dispersion at the TPCL reached a certain value, it is plausible that larger particles were formed due to ion-dipole interactions involving the stabilizing NaMBA molecules that lead to deposition into a ring. This was followed by complete evaporation of the droplet. It is important to note here that the Raman signal intensity decreased gradually with time following the maximum at the phase transition (**Figure 2.3c**). The diminishing signal intensity could be correlated with the loss of water as that is established as a better dielectric for SERS as compared to air.[34] In order to ascertain this, in a separate experiment, Raman spectrum on the same spot (at the TPCL of the original droplet) was measured again following addition of water to the dried ring. As is clear from **Figure 2.3d**, the signal intensities indeed went back to the original high values after water was added to the dried ring, which again went down following drying.

TH_3719_186122105

Intensity of Raman signal of a molecular vibration generally increases with increasing change of polarizability,[35] surging radiation source power,[36] rising concentration of analyte molecule[37] and nature and magnitude of the surrounding plasmonic field (whenever applicable)[38]. Here, NaMBA molecules were attached to the surface of AuNPs. Hence, SERS would contribute significantly to the Raman signal of the molecules. In addition, the change in polarizability will be the same for all surface attached molecules in the presence of plasmonic field. Laser power remained constant during the whole evaporation process. Hence, it might have been the change in concentration and the plasmonic environment of NaMBA on the molecule-laden NPs at the point of the probe that was altering the intensity. As soon as a droplet with dispersed particles is placed on a planer substrate, particles tend to move towards the TPCL due to capillary flow. Because of lower experimental temperature, the effect of Marangoni flow could be neglected here.[18] As suggested by earlier models, therefore, the concentration of the NaMBA attached particles would increase gradually at TPCL. That would mean that a monotonous increase in the signal intensity at the probe point should have been observed. However, it is plausible that even if particle concentration had increased, the intensity of the Raman signal in the dispersion medium would be low as compared to that when the particles are deposited as solid. Further, not only is the concentration of the particles increased in solid deposition but also plasmonic 'hot spots' were generated in between the aggregated particles that greatly increase the Raman signal intensity. The nanoparticles assembly, which resulted in the formation of 'hot-spots' in the deposition can be observed in field emission scanning electron microscopic image shown in **Figure A2.7**. This was further supported by the observed AFM images of the depositions at the TPCL shown in **Figure 2.4b**. Raman signal intensity change with time for four different droplets evaporation are shown in **Figure A2.8**. Also, from **Figure 2.4c** and **Figure 2.4e**, it is clear that the height of the deposition also increased drastically, which generated more and more hot-spots of NaMBA-AuNP-2 assembly in the depositions during the short span of time when the Raman signal intensity had increased sharply as shown in **Figure 2.4d** and **Figure 2.4f**. For example, the average height, at the beginning of deposition i.e., at the lowest Raman signal intensity, was 120±26 nm at 22.5 min (65% humidity in **Figure A2.8(i)**). The height of deposition had increased to 216±14 nm and 354±11 nm with rise in intensity corresponding to **Figure 2.4d(ii)** at 25.0 min (65% humidity in **Figure A2.8(ii)**) and **Figure 2.4d(iii)** at 35 min (72% humidity in **Figure A2.8(iii)**), respectively. Finally, the height had increased to 755±41 nm when the Raman signal intensity was maximum (**Figure 2.4d(iv)**) at 35 min (65% humidity in **Figure**

TH_3719_186122105

A2.8(iv)). It is worth mentioning here that higher humidity led to the increase in time for Raman signal intensity change. The increase in Raman

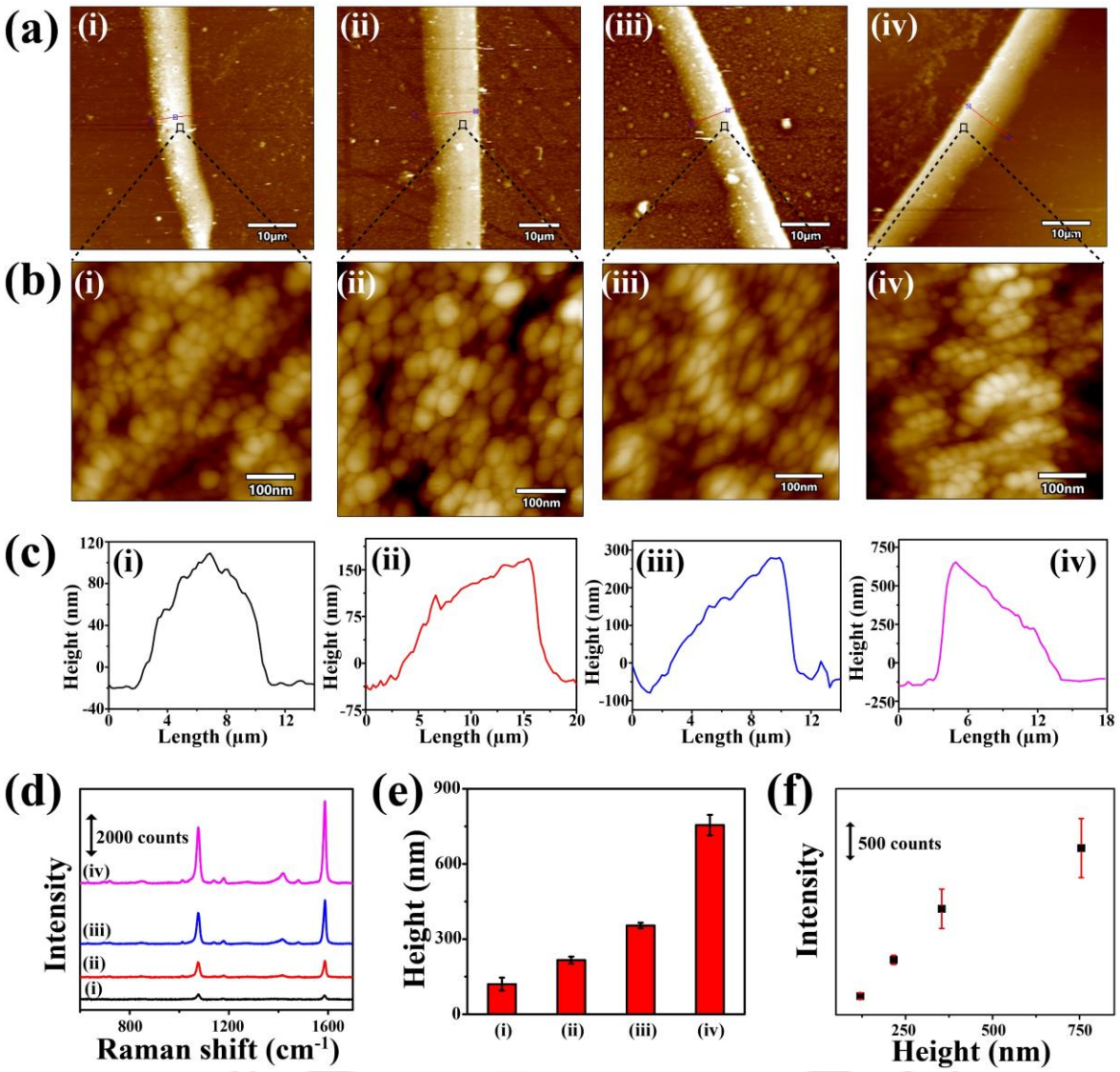

Figure 2.4: (a) AFM images of the depositions at TPCL, (b) AFM images of gold nanoparticles (AuNP-2) assembly at TPCL and (c) height profile of the depositions corresponding to the Raman signals of (i), (ii), (iii) and (iv) in (d) respectively. (e) Average maximum heights of the depositions for Raman signal intensity (i), (ii), (iii) and (iv) respectively during the short period of time when phase transition was occurring. Average maximum heights were calculated by measuring maximum heights at seven different locations on the deposition for different samples. (f) Correlation plot of 1078 cm^{-1} Raman peak intensity with respect to measured height of the deposition.

signal intensity in **Figure 2.4d** was similar to the observed sudden rise in the intensity in **Figure 2.3c**. The lack of observable signal for the first 25 min in **Figure 2.3c** as well as in **Figure A2.8(iv)** indicated no significant depositions of the particles and deposition of the particles was

TH_3719_186122105

correlated to the Raman signal intensity as shown in **Figure 2.4e** based on the time when particles were depositing depending on external humidity. Thus, while deposition, the number of molecules and plasmonic 'hot-spots' increased with time. In other words, the increase in Raman signal intensity with time reflected the increasing number of molecules deposited at TPCL as well as the plasmonic 'hot-spots'. On the other hand, a sudden surge in the signal indicated depositions of the particles at the TPCL within a narrow window of time. Thus, the current observations suggest a phase transition of the concentrated dispersed NPs at the TPCL leading to deposition into a "coffee ring". For the dispersion with initial AuNP concentration of 2.5 nM, the phase transition occurred at the inflection point 27.0 min, as obtained from Boltzmann fitting (**Figure 2.3c**). The evaporation of the droplet occurred under ambient conditions of 22 °C and 65% relative humidity. In brief, the phase transition behavior as measured through SERS was indeed a measure of sudden depositions of molecules along with the plasmonic particles at the TPCL.

2.4.4. AuNP-2 Concentration Dependent Phase Transition:

Further experiments with initial AuNP concentration-dependent evaporation of droplets revealed similar phase transitions the occurrence time of which decreased with increased NP concentration. The experiments were pursued with 10 nM and 1.25 nM of AuNP-2. Results of changes in contact angle, height, Raman signal intensity with time at these initial concentrations of AuNP were included in **Figure A2.9**. For both the concentrations of AuNP-2, similar sudden changes in Raman signal intensities were observed. **Figure 2.5a** shows the plot of time-dependent Raman signal intensities at 1078 cm^{-1} of three sessile droplets with initial AuNP-2 concentrations of 10 nM, 2.5 nM and 1.25 nM, respectively. As is clear from the figure, for initial AuNP concentrations of 10 nM, 2.5 nM and 1.25 nM, respectively, the occurrence of maximum intensity i.e., the phase transition times were at 24.0 min, 32.9 min and 41.5 min, respectively. The results indicated that it is plausible that upon evaporation of the droplet, once a critical concentration of the AuNPs is reached at the TPCL, phase transition occurs. This critical concentrations of the AuNP-2 at the TPCL may be the same for droplets with similar-sized droplets. Thus, with higher initial concentration, the time taken for phase transition was shorter than that at intermediate concentration and which was shorter than that at the lowest concentration. Variation of contact angle, height with time and time dependent Raman spectra of this set of experiment are given in **Figure A2.10**.

TH_3719_186122105

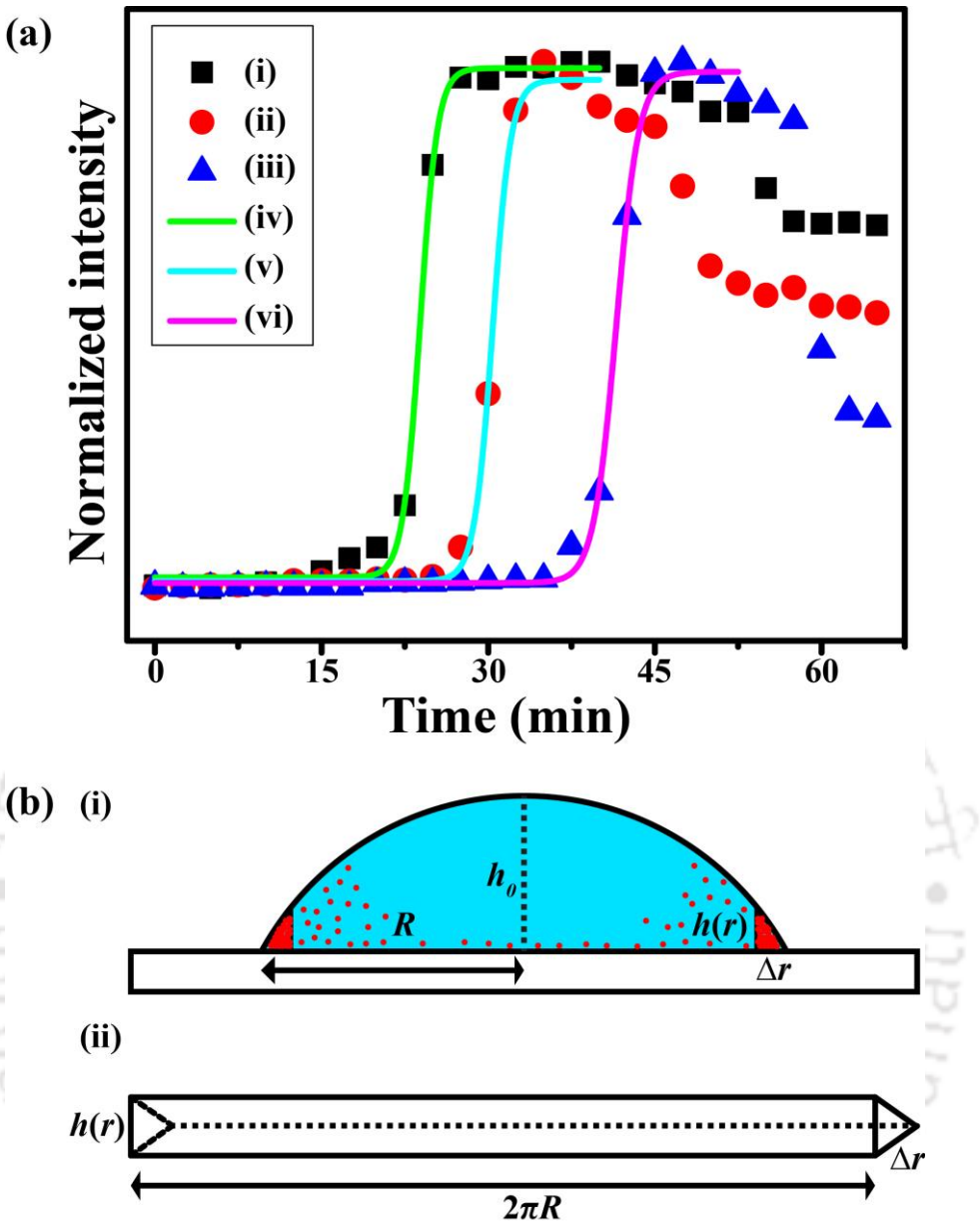

Figure 2.5: (a) Time-dependent intensity variation of 1078 cm^{-1} Raman peak of evaporating droplets containing AuNP at (i) 10 nM, (ii) 2.5 nM, (iii) 1.25 nM initial concentrations, respectively and corresponding fitted curves marking phase transition regions, (iv), (v) and (vi) respectively. (b) Schematic illustrations of (i) spherical cap droplet on a substrate where red dots represent AuNPs and (ii) stretched ring as a triangular prism (not to scale).

The results of the Raman spectroscopic measurements of the evaporating sessile droplet containing NaMBA_AuNP-2 demonstrated that when the concentration of the colloidal nanoparticles at the TPCL reaches a certain value they deposited out of the medium into an aggregated solid that is akin to a phase transition. A question may be raised about the concentrations of the NPs at the TPCL for the observed phase transitions and their correlations for the three different initial concentrations.

TH_3719_186122105

2.4.5. Calculation of AuNP-2 Concentration for Phase Transition:

The concentration of NaMBA_AuNP, $C(r,t)$, can be calculated from the expression given below-

$$C(r,t) = \frac{N(t)\times 10^{15}}{N_A \times v(r,t)}\ \mu M \qquad (2.1)$$

where N_A and $N(t)$ are Avogadro's number and number of particles reached at the TPCL in time t, respectively and $v(r,t)$ is volume of the coffee ring in nL. Total number of AuNPs (N_0) and initial volume (V_0) were known. Contact angle $\theta(t)$, droplet height at the center at different time $h(0,t)$, ring width (Δr) and droplet radius on the substrate (R) were found out from droplet images. Phase transition time was obtained from time-dependent Raman measurements. Number of particles accumulating at TPCL with time, $N(t)$, can be calculated using the following expression[22]

$$N(t) = 2\pi C_0 h_0 R^2 \left(\frac{1}{4} - \frac{r_0(t)^2}{2R^2} + \frac{r_0(t)^4}{4R^4}\right) \qquad (2.2)$$

where C_0 is number of particles per unit volume at 0 min, i.e., $C_0 = N_0/V_0$, h_0 is height at the center of the droplet at t = 0 min. $r_0(t)$ is the position of a particle at t = 0 min and t is the time the particles take to reach the contact line. $r_0(t)/R$ depends on total drying time (τ) by the relation given below[22]

$$\frac{r_0(t)}{R} = \sqrt{1 - \left\{1 - \left(1 - \frac{t}{\tau}\right)^{\frac{3}{4}}\right\}^{2/3}} \qquad (2.3)$$

Following phase transition, the probability of arrival of more particles on top of the formed ring could be ignored because Raman signal intensity for all the three concentrations did not increase following the transition and also the accumulated particles were piled up to the maximum height possible at that moment, which was thus fixed.[21] In our experiment also, following the observation of the maximum Raman signal intensity at 27.5 min as shown in **Figure A2.11a**, the inner-side deposition at TPCL of excess AuNPs was observed at 32.5 min (**Figure A2.11c**), due to nanoparticles being already piled up to the maximum height at the Raman probing spot. It should be noted that changes in droplet's parameters, external temperature, humidity and air flow would alter the phase transition time (t) and drying time (τ) leading to different number of AuNP at TPCL for different set of experiments at a specific initial concentration. The evaporation time follows the relation, $\tau = \frac{\rho h_0 R\pi}{8D(c_s - c_\infty)}$, where ρ is

TH_3719_186122105

density of solvent, D is diffusion coefficient. c_s and c_∞ are vapor concentrations at droplet-air interface and surrounding, respectively. So, the drying time took care of the effects of droplet's internal and external parameters. Spherical cap droplet of small contact angle (**Figure 2.5b(i)**) has height profile $h(r,t) = h(0,t)\left(1 - \frac{r^2}{R^2}\right)$, where r is the radial distance from the center to the edge. During droplet evaporation in CCR mode, evaporated liquid from the edge is replaced by the liquid coming through capillary flow. Therefore, volume and height change at the edge are very small. The surface meniscus in the extremely small region at the edge can be considered as plane surface tilted at θ rather than a convex lens type surface. Therefore, the ring can be approximated to a prism of height equals to circumference ($2\pi R$) with right triangle edges of sides $h(r)$ and Δr as illustrated in **Figure 2.5b(ii)**. So, the approximated volume at time t i.e., $v(r,t)$, at the ring where particles were accumulated is $\pi R h(r,t)\Delta r$. When the sideway deposition observed as shown in **Figure A2.11**, Δr was considered to be the width of deposition without taking into account of excess deposition width for a more reliable calculation.

Table 2.1: Calculated concentration of AuNP-2 at the TPCL during phase transition leading to coffee-ring formation.

Initial conc. (nM)	Experiment	Phase transition time (min)	τ (min)	$N(t)$	$v(r,t)$ (nL)	$C(r,t)$ (µM)	Average $C(r,t)$ (µM)	Average conc. (µM)
10	1	24.3	45.0	1.09×10^{10}	1.22	14.87	**11.18±2.86**	**12.93±3.17**
	2	24.0	57.5	5.94×10^{9}	1.25	7.89		
	3	23.8	47.5	7.93×10^{9}	1.22	10.79		
2.5	1	27.0	45.0	2.88×10^{9}	0.38	12.60	**12.23±0.27**	
	2	30.4	57.5	2.09×10^{9}	0.29	11.98		
	3	30.2	50	2.84×10^{9}	0.39	12.11		
1.25	1	32.3	50	1.30×10^{9}	0.17	12.66	**15.37±3.52**	
	2	41.5	60.0	1.59×10^{9}	0.13	20.35		
	3	32.8	45.0	1.98×10^{9}	0.25	13.12		

Based on the above, concentrations of AuNP-2 at the time of phase transition at TPCL with starting dispersion concentrations 10 nM, 2.5 nM and 1.25 nM were calculated using **Equation (2.1)** and are given in **Table 2.1**. In order to reproduce the data, three different sets of experiments were performed. Experiment-1 was the set described earlier in details. Experiment-2 corresponds to the phase transitions results of which are presented in **Figure 2.5a**. Time-dependent Raman spectra, variation of Raman signal intensity with time and phase transition plots of the other set of experiment (Experiment-3) are shown in **Figure A2.12**.

TH_3719_186122105

Images of all the dried circular drops were presented in **Figure A2.13** and values of R and Δr after analysis of dried droplets of every experiment were given in **Table A2.2**. $v(r,t)$ values at phase transition time were obtained from linear fitted plots of calculated volume at different times as shown in **Figure A2.14**. Difference in the observed τ was because of slightly different humidity of the surrounding medium at different days of experiments. As different phase transition times were observed for different initial AuNP-2 concentration and there were significant time gaps between the phase transition time and drying time, the depositions of AuNP in our case was not taking place due to the 'last stage rush-hour' effect reported in earlier models.[21,22] The so-calculated AuNP-2 concentrations for phase transition at the coffee-ring using experimentally obtained parameters were within a short range of values. For three different initial AuNP-2 concentrations of 10 nM, 2.5 nM and 1.25 nM phase transition concentrations were calculated to be 11.18±2.86 µM, 12.23±0.27 µM and 15.37±3.52 µM, respectively. Finally, the average concentration for phase transition of AuNP-2 from dispersed phase to solid phase was found to be 12.93±3.17 µM.

2.4.6. AuNP Size Dependent Phase Transition:

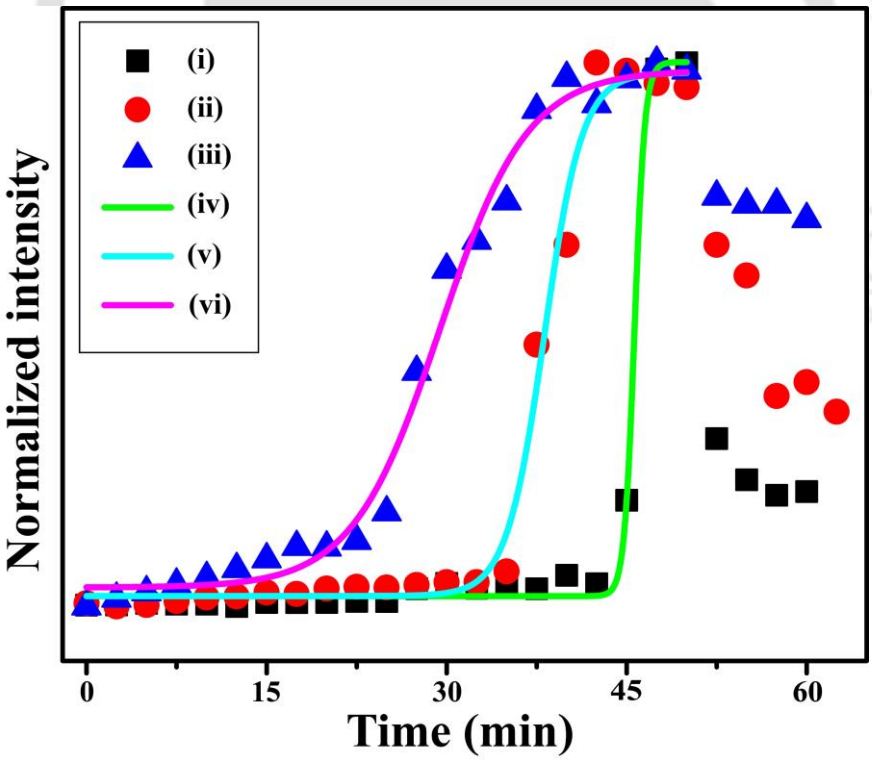

Figure 2.6: Time-dependent intensity variation of 1078 cm^{-1} Raman peak of evaporating droplets containing 5 nM each of NaMBA capped (i) AuNP-1, (ii) AuNP-2 and (iii) AuNP-3, respectively and corresponding Boltzmann fitted curves marking phase transition regions (iv), (v) and (vi), respectively.

TH_3719_186122105

For the AuNP size-dependent phase transition experiments, initial particle concentration of 5 nM in the evaporating droplets containing NaMBA capped AuNPs of three different sizes were used. Absorption maxima at 524 nm, 528 nm and 536 nm for AuNP-1, AuNP-2 and AuNP-3, respectively in UV-Vis spectra indicated the formation of AuNPs of different sizes, which was confirmed from FETEM images in **Figure A2.15**. When the droplet containing the NPs at that fixed concentration were evaporated at 72-75% humidity, typical phase transitions were observed in all the cases as shown in **Figure 2.6**. Phase transition at the TPCL for droplet containing 15.4 nm AuNPs (AuNP-1) was observed at 45.7 min while that for 36.4 nm particles (AuNP-3), was observed at 29.4 min. Evaporating droplet containing 25.3 nm AuNPs (AuNP-2) led to phase transition at 38.2 min. It may be mentioned here that the higher phase transition time for AuNP-2 at 5 nM initial concentration as compared to that at 2.5 nM initial concentration in Table-1 was due to the higher humidity during the measurements. The different times for phase transition of nanoparticles of different sizes might be because of particle size dependent diffusion behavior and packing fraction in solid deposit. Packing fraction of spherical particles decreases with increasing diameter.[39] Diffusion coefficient (D) depends on the particle size according to the Einstein-Stokes relation $D = k_BT/6\pi\eta r$ where k_B, T, η and r are the Boltzmann constant, temperature, liquid viscosity and particle radius, respectively.[40] So, the larger particle has lower D compared to that for smaller particles. Therefore, during evaporation, strong diffusion in case of smaller particles led to increase in the time for the particles to have the required concentration at the TPCL before being deposited as solid. Also, for the larger particles, lower number of particles are needed compared to smaller one to reach a certain packing fraction until they deposit as solid from the dispersed medium. The particles were moving to the TPCL due to capillary flow while the droplets were evaporating. Therefore, AuNP-3 reached the critical concentration for phase transition earlier than AuNP-2, which in turn was deposited as solid earlier than AuNP-1. It is worth mentioning here that the 'last-stage rush-hour' effect and strong diffusion might have been present for 14.3 nm AuNPs (AuNP-1) because phase transition for the dispersion containing AuNP-1 was observed close to the complete drying of water (55.0 min). The concentrations of AuNPs at the phase transition times were calculated from **Equation (2.1)** and are given in **Table-2.2**. Variation of contact angle, height and Raman signal with time of the evaporating droplets leading to phase transitions as shown in **Figure 2.6** (Experiment-4) are given in **Figure A2.16**.

TH_3719_186122105

Table 2.2: Calculated concentration of AuNP-1, AuNP-2 and AuNP-3 at the TPCL during phase transition leading to coffee-ring formation at 5 nM initial concentration:

AuNP diameter (nm)	Experiments	Phase transition time (min)	τ (min)	$N(t)$	$v(r,t)$ (nL)	$C(r,t)$ (μM)	Average $C(r,t)$ (μM)
15.4	4	45.7	55.0	9.75×10^9	0.097	166.90	**146.10±20.99**
	5	44.3	60.0	6.93×10^9	0.075	154.04	
	6	48.3	60.0	8.99×10^9	0.127	117.36	
25.3	4	38.2	57.5	6.93×10^9	0.888	12.96	**14.84±1.33**
	5	38.5	55.0	7.52×10^9	0.795	15.70	
	6	38.0	52.5	6.88×10^9	0.720	15.86	
36.4	4	29.4	52.5	5.03×10^9	2.514	3.32	**3.21±0.12**
	5	29.4	55.0	4.50×10^9	2.287	3.27	
	6	28.7	52.5	4.93×10^9	2.683	3.05	

For each concentration, three different trials of experiments were performed. Raman signal with time and phase transition for Experiment-5 and Experiment-6 were plotted in **Figure A2.17(i)** and **Figure A2.17(ii)**, respectively. Deposited ring widths and droplet radii were given in **Table A2.3**. $v(r,t)$ values were obtained from linear fitted plots of calculated volume at different times as shown in **Figure A2.18**. For AuNP-1 and AuNP-3, phase transitions were observed at 146.10±20.99 μM and 3.21±0.12 μM NP concentrations, respectively. At 5 nM initial NP concentration, AuNP-2 resulted in phase transition at 14.84±1.33 μM NP concentration, which is consistent with the results reported above (**Table 2.1**).

2.5. Conclusions

In brief, we have for the first time reported the observation of phase transition in the evaporation of water droplets containing probe molecule-laden colloidal AuNPs based on SERS of the deposited solid. Although the AuNPs from the whole droplet volume might have moved earlier to TPCL; however, they were deposited on substrate surface only after reaching a certain concentration within a very short window of time even when water was still present. The initial AuNP concentration-depended studies revealed that higher was the concentration faster was the time of phase transition. Importantly, for all the initial AuNP concentrations of 25.3 nm diameter studied here, the results indicated that phase transitions occurred only when the particle concentration at the TPCL was same for all, which was about 13 μM. The particle size dependent studies revealed that at same initial particle concentration, larger nanoparticles changed phase at TPCL from dispersion to deposition occurred much earlier at lower

TH_3719_186122105

concentration compared to smaller nanoparticles. Phase transitions at TPCL for 15.4 nm and 36.4 nm AuNPs were observed at 146.10±20.99 µM and 3.21±0.12 µM NPs concentrations, respectively. The observation of phase transition leading to the 'coffee ring' deposition in a sessile droplet may usher new discoveries that may have important consequences in liquid-based printing technology, agriculture, forensics and disease diagnostics.

2.6. References

1. Torrisi, F.; Hasan, T.; Wu, W.; Sun, Z.; Lombardo, A.; Kulmala, T. S.; Haieh, G.-W.; Jung, S.; Bonaccorso, F.; Paul, P. J.; *et al.* Inkjet-Printed Graphene Electronics. *ACS Nano* **2012**, *6*, 2992-3006.
2. Pendyala, N. K.; Magdassi, S.; Etgar, L. Fabrication of Perovskite Solar Cells with Digital Control of Transparency by Inkjet Printing. *ACS Appl. Mater. Interfaces* **2021**, *13*, 30524-30532.
3. Ye, X.; Ge, L.; Jiang, T.; Guo H.; Chen, B.; Liu, C.; Hayashi, K. Fully Inkjet-Printed Chemiresistive Sensor Array Based on Molecularly Imprinted Sol–Gel Active Materials. *ACS Sens.* **2022**, *7*, 1819-1828.
4. Sajedi-Moghaddam, A.; Rahmanian, E.; Naseri, N. Inkjet-Printing Technology for Supercapacitor Application: Current State and Perspectives. *ACS Appl. Mater. Interfaces* **2020**, *12*, 34487-34504.
5. Xuan, T.; Shi, S.; Wang, L.; Kuo, H.-C.; Xie, R.-J. Inkjet-Printed Quantum Dot Color Conversion Films for High-Resolution and Full-Color Micro Light-Emitting Diode Displays. *J. Phys. Chem. Lett.* **2020**, *11*, 5184-5191.
6. Gao, M.; Li, L.; Song, Y. Inkjet printing wearable electronic devices. *J. Mater. Chem. C* **2017**, *5*, 2971-2993.
7. Molina-Lopez, F.; Gao, T. Z.; Kraft, U.; Zhu, C.; Öhlund T.; Pfattner, R.; Feig, V. R.; Kim, Y.; Wang, S.; Yun, Y.; *et al.* Inkjet-printed stretchable and low voltage synaptic transistor array. *Nat Commun* **2019**, *10*, 2676.
8. Hussain, A.; Abbas, N.; Ali, A. Inkjet Printing: A Viable Technology for Biosensor Fabrication. *Chemosensors* **2022**, *10*, 103.
9. Bietsch, A.; Henger, M.; Lang, H. P.; Gerber, C. Inkjet Deposition of Alkanethiolate Monolayers and DNA Oligonucleotides on Gold: Evaluation of Spot Uniformity by Wet Etching. *Langmuir* **2004**, *20*, 5119-5122.

TH_3719_186122105

10. Derby, B. Bioprinting: inkjet printing proteins and hybrid cell-containing materials and structures. *J. Mater. Chem.* **2008**, *18*, 5717-5721.
11. Li, X.; Liu, B.; Pei, B.; Chen, J.; Zhou, D.; Peng, J.; Zhang, X.; Jia, W.; Xu, T. Inkjet Bioprinting of Biomaterials. *Chem. Rev.* **2020**, *19*, 10793-10833.
12. Gao, G.; Chu, X. Three-dimensional bioprinting in tissue engineering and regenerative medicine. *Biotechnol Lett.* **2016**, *38*, 203-211.
13. Meng, Y.; Cao, J.; Chen, Y.; Yu, Y.; Ye, L. 3D printing of a poly(vinyl alcohol)-based nano-composite hydrogel as an artificial cartilage replacement and the improvement mechanism of printing accuracy. *J. Mater. Chem. B* **2020**, *8*, 677-690.
14. Olejnik, A.; Semba, J. A.; Kulpa, A.; Dańczak-Pazdrowska A.; Rybka, J. D.; Gornowicz-Porowska J. 3D Bioprinting in Skin Related Research: Recent Achievements and Application Perspectives. *ACS Synth. Biol.* **2022**, *11*, 26-38.
15. Kim, S.; Handler, J. J.; Cho, Y. T.; Barbastathis, G.; Fang, N. X. Scalable 3D printing of aperiodic cellular structures by rotational stacking of integral image formation. *Sci. Adv.* **2021**, *7*, eabh1200.
16. Hadibrata, W.; Wei, H.; Krishnaswamy, S.; Aydin, K. Inverse Design and 3D Printing of a Metalens on an Optical Fiber Tip for Direct Laser Lithography. *Nano Lett.* **2021**, *21*, 2422-2428.
17. Wilkinson, J.; Tam, C.; Askounis, A.; Qi, S. Suppression of the coffee-ring effect by tailoring the viscosity of pharmaceutical sessile drops. *Colloids and Surfaces A: Physicochemical and Engineering Aspects* **2021**, *614*, 126144.
18. Zhang, W.; Yu, T.; Liao, L.; Cao, Z. Ring formation from a drying sessile colloidal droplet. *AIP Advances* **2013**, *3*, 102109.
19. Brutin, D. Influence of relative humidity and nano-particle concentration on pattern formation and evaporation rate of pinned drying drops of nanofluids. *Colloids and Surfaces A: Physicochemical and Engineering Aspects* **2013**, *429*, 112-120.
20. Lohani, D.; Basavaraj, M. G.; Satapathy, D. K.; Sarkar, S. Coupled effect of concentration, particle size and substrate morphology on the formation of coffee rings. *Colloids and Surfaces A: Physicochemical and Engineering Aspects* **2020**, *589* 124387.
21. Deegan, R. D.; Bakajin, O.; Dupont, T. F.; Huber, G.; Nagel, S. R.; Witten, T. A. Contact line deposits in an evaporating drop. *Phys. Rev. E* **2000**, *62*, 756-765.
22. Boulonge, F.; Ingremeau, F.; Stone, H. A. Coffee-stain growth dynamics on dry and wet surfaces. *J. Phys.: Condens. Matter* **2017**, *29*, 074001.

TH_3719_186122105

23. Shaw, M.; Bella, A.; Ryadnov, M. G.; CREIM: Coffee Ring Effect Imaging Model for Monitoring Protein Self-Assembly *in Situ*. *J. Phys. Chem. Lett.* **2017**, *8*, 4846-4851.
24. Acuña, C.; Mier y Terán, A.; Kokornaczyk, M. O.; Baumgartner, S.; Castelán, M. Deep learning applied to analyze patterns from evaporated droplets of *Viscum album* extracts. *Sci Rep* **2022**, *12*, 15332.
25. Crivoi, A.; Duan, F. Effect of Surfactant on the Drying Patterns of Graphite Nanofluid Droplets. *J. Phys. Chem. B* **2013**, *117*, 5932-5938.
26. Devineau, S.; Anyfantakis, M.; Marichal, L.; Kiger, L.; Morel, M.; Rudiuk, S.; Baigl, D. Protein Adsorption and Reorganization on Nanoparticles Probed by the Coffee-Ring Effect: Application to Single Point Mutation Detection. *J. Am. Chem. Soc.* **2016**, *138*, 11623-11632.
27. Langer, J.; Jimenez de Aberasturi, D.; Aizpurua, J.; Alvarez-Puebla, R. A.; Auguié, B.; Baumberg, J. J.; Bazan, G. C.; Bell, S. E. J.; Boisen, A.; Brolo, A. G., et al. Present and Future of Surface-Enhanced Raman Scattering. *ACS Nano* **2020,** *14*, 28-117.
28. Marques, F. C.; Alves, R. S.; dos Santos, D. P.; Andrade, G. F. S. Surface-enhanced Raman spectroscopy of one and a few molecules of acid 4-mercaptobenzoic in AgNP enabled by hot spots generated by hydrogen bonding. *Phys. Chem. Chem. Phys.* **2022**, *24*, 27449-27458.
29. Schneider, C.; Rasband, W.; Eliceiri, K. NIH Image to ImageJ: 25 years of image analysis. *Nat Methods* **2012**, *9*, 671-675.
30. Frens, G.; Controlled Nucleation for the Regulation of the Particle Size in Monodisperse Gold Suspensions. *Nature Physical Science* **1973**, *241*, 20-22.
31. Pandey, P.; Singh, S. P.; Arya, S. K.; Gupta, V.; Datta, M.; Singh, S.; Malhotra, B. D. Application of Thiolated Gold Nanoparticles for the Enhancement of Glucose Oxidase Activity. *Langmuir*, **2007**, *23*, 3333-3337.
32. Midekessa, G.; Godakumara, K.; Ord, J.; Viil, J.; Lättekivi, F.; Dissanayake, K.; Kopanchuk, S.; Rinken, A.; Andronowska, A.; Bhattacharjee, S.; *et al.* Zeta Potential of Extracellular Vesicles: Toward Understanding the Attributes that Determine Colloidal Stability. *ACS Omega* **2020**, *5*, 16701-16710.
33. Gelderblom, H.; Diddens, C.; Marin, A. Evaporation-driven liquid flow in sessile droplets. *Soft Matter* **2022**, *18*, 8535-8553.
34. de Barros, A.; Shimizu, F. M.; de Oliveira, C. S.; Sigoli, F. A.; dos Santos, D. P.; Mazali, I. O. Dynamic Behavior of Surface-Enhanced Raman Spectra for Rhodamine

TH_3719_186122105

6G Interacting with Gold Nanorods: Implication for Analyses under Wet versus Dry Conditions. *ACS Appl. Nano Mater.* **2020**, *3*, 8138-8147.

35. Yoon, D.; Moon, H.; Son, Y.-W.; Samsonidze, G.; Park, B. H.; Kim, J. B.; Lee, Y.; Cheong, H. Strong Polarization Dependence of Double-Resonant Raman Intensities in Graphene. *Nano Lett.* **2008**, *8*, 4270-4274.
36. Su, L.; Zhang, Y. Temperature coefficients of phonon frequencies and thermal conductivity in thin black phosphorus layers. *Appl. Phys. Lett.* **2015**, *107*, 071905.
37. Das, S.; Saxena, K.; Mehta, D. S. A highly sensitive SERS substrate based on a mesoporous Ag–TiO_2 thin film for the detection of dye molecules. *Mater. Adv.* **2022**, *3*, 5337-5343.
38. Yu, H.; Peng, Y.; Yang, Y.; Li, Z.-Y. Plasmon-enhanced light-matter interactions and applications. *npj Comput Mater* **2019**, *5*, 45.
39. Bansal, L.; Seth, P.; Murugappan, B.; Basu, S. Suppression of coffee ring: (Particle) size matters. *Appl. Phys. Lett.* **2018**, *112*, 211605.
40. Ahumada-Lazo, J. A.; Chen, R.-H. Effects of nanoparticle concentration and peclet number on nanofluid droplet evaporation behavior. *International Journal of Thermal Sciences* **2022**, *178*, 107582.

TH_3719_186122105

Appendix of Chapter 2 (A2):

A2.1. Calculations of number and concentration of AuNPs at three different sizes:[1]

A2.1.1. Calculation of number of synthesized citrate capped AuNPs:

10 µL of 1.4453 (M) gold(III) chloride solution contains Au atoms

$= 8.71\times10^{18}$

Radius of one Au atom in AuNP is 0.144 nm. Packing fraction of face-centered cubic (FCC) AuNP = 0.74.

AuNPs of average diameter 15.4 nm (AuNP-1), 25.3 nm (AuNP-2) and 36.4 nm (AuNP-3) were synthesized.

For AuNP-1, total volume of reaction mixture was 26.0 mL.

Number of Au atoms in one AuNP-1

$= 0.74\times\left(\frac{15.4}{0.144\times2}\right)^3$

$= 1.136\times10^5$

Number of AuNP-1 in 26.0 mL reaction mixture

$= \frac{8.71\times10^{18}}{1.136\times10^5}$

$= 7.67\times10^{13}$

For AuNP-2, Total volume of reaction mixture was 25.8 mL.

Number of Au atoms in one AuNP-2

$= 0.74\times\left(\frac{25.3}{0.144\times2}\right)^3$

$= 5.02\times10^5$

Number of AuNP-2 in 25.8 mL reaction mixture

$= \frac{8.71\times10^{18}}{5.02\times10^5}$

$= 1.74\times10^{13}$

TH_3719_186122105

For, AuNP-3, Total volume of reaction mixture was 25.5 mL.

Number of Au atoms in one AuNP-3

$= 0.74\times \left(\frac{36.4}{0.144\times 2}\right)^3$

$= 1.494\times 10^6$

Number of AuNP in 25.8 mL reaction mixture

$= \frac{8.71\times 10^{18}}{1.494\times 10^6}$

$= 5.83\times 10^{12}$

A2.1.2. Total number of AuNPs (N_0) for coffee-ring formation experiment at three different initial concentrations of AuNP-2:

Each of 4 mL synthesized AuNP-2 was centrifuged and redispersed in 400 µL water. This was chosen as very highly concentrated AuNP-2 dispersion for coffee-ring formation experiment.

Therefore, after centrifugation 400 µL AuNP-2 dispersion contains NP

$= \frac{4\times 1.74\times 10^{13}}{25.8}$

$= 2.70\times 10^{12}$

As mentioned in the experimental section, 50 µL of NaMBA solution was added into 400 µL centrifuged AuNP-2 dispersion. Therefore, total volume became 450 µL or 0.45 mL. So, AuNP-2 concentration in this dispersion = $\frac{1000\times 2.70\times 10^{12}}{0.45\times 6.023\times 10^{23}}$ (M) = 10 nM

Then after treatment with NaMBA, 5 µL of 10 nM dispersion was dropped on the glass slide. So, number of particles for 10 nM initial NaMBA-AuNP-2 dispersion for coffee-ring experiment, N_0, was = $\frac{5\times 2.70\times 10^{12}}{450} = 3.0\times 10^{10}$

NP concentrations of four-times and eight-times diluted NaMBA-AuNP-2 were 2.5 nM and 1.25 nM respectively.

Therefore, for 2.5 nM starting NaMBA-AuNP-2 dispersion, total number of AuNP (N_0) was = 7.5×10^9

For 1.25 nM starting NaMBA-AuNP-2 dispersion, total number of AuNP (N_0) was = 3.75×10^9

TH_3719_186122105

A2.1.3. Preparation of 5 nM NaMBA-AuNP dispersions of different size:

In order to obtain 5 nM NaMBA-AuNP-2, 10 nM dispersion was diluted two times.

Therefore, for each of 5 µL of 5 nM starting NP dispersions, total number of AuNP (N_0) was $= 1.5\times10^{10}$

For AuNP-1, 4 mL as synthesized NPs was centrifuged and redispersed in 400 µL. Then 50 µL of NaMBA solution was added. Therefore, 450 µL of NaMBA-AuNP-1 initially contained NPs

$$= \frac{4\times7.67\times10^{13}}{26.0}$$

$$= 1.179\times10^{13}$$

Particle concentration of this dispersion was 43.5 nM.

Therefore, in order to obtain 5 nM dispersion, 92 µL of the 43.5 nM NaMBA-AuNP-1 dispersion was added to 708 µL water.

For AuNP-3, 4 mL as synthesized NPs was centrifuged and redispersed in 250 µL. Then 50 µL of NaMBA solution was added. Therefore, 300 µL of NaMBA-AuNP-3 initially contained NPs

$$= \frac{4\times5.83\times10^{12}}{25.5}$$

$$= 9.145\times10^{11}$$

Particle concentration of this dispersion was 5 nM.

TH_3719_186122105

A2.2. TEM images and SAED patterns of AuNP-2 and NaMBA-AuNP-2:

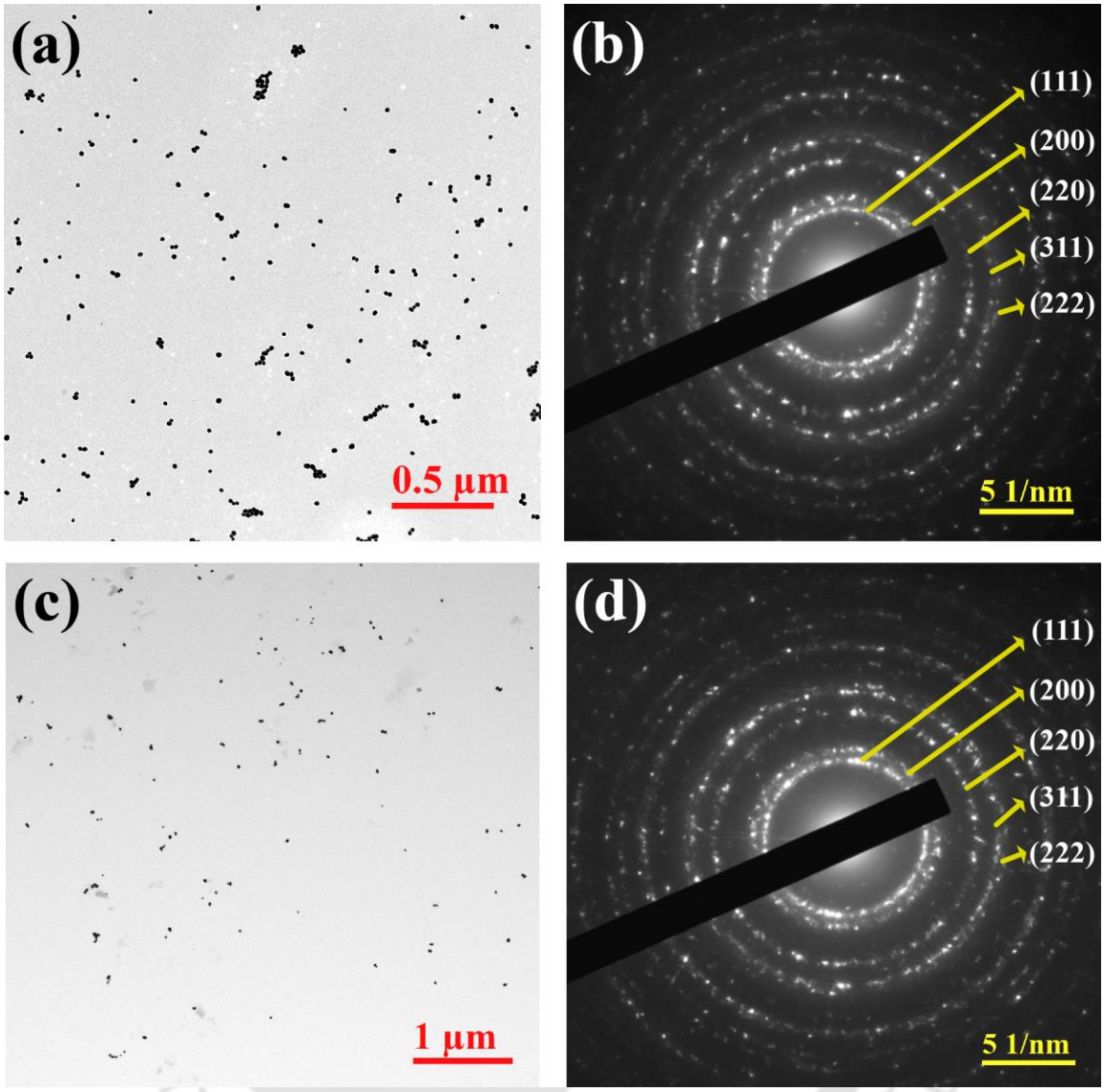

Figure A2.1: TEM image (a) and SAED pattern (b) of AuNP-2, TEM image (c) and SAED pattern (d) of NaMBA-AuNP-2.

TH_3719_186122105

A2.3. UV-Vis spectra and Zeta potential variation of 10 nM and 1.25 nM AuNP-2 dispersions:

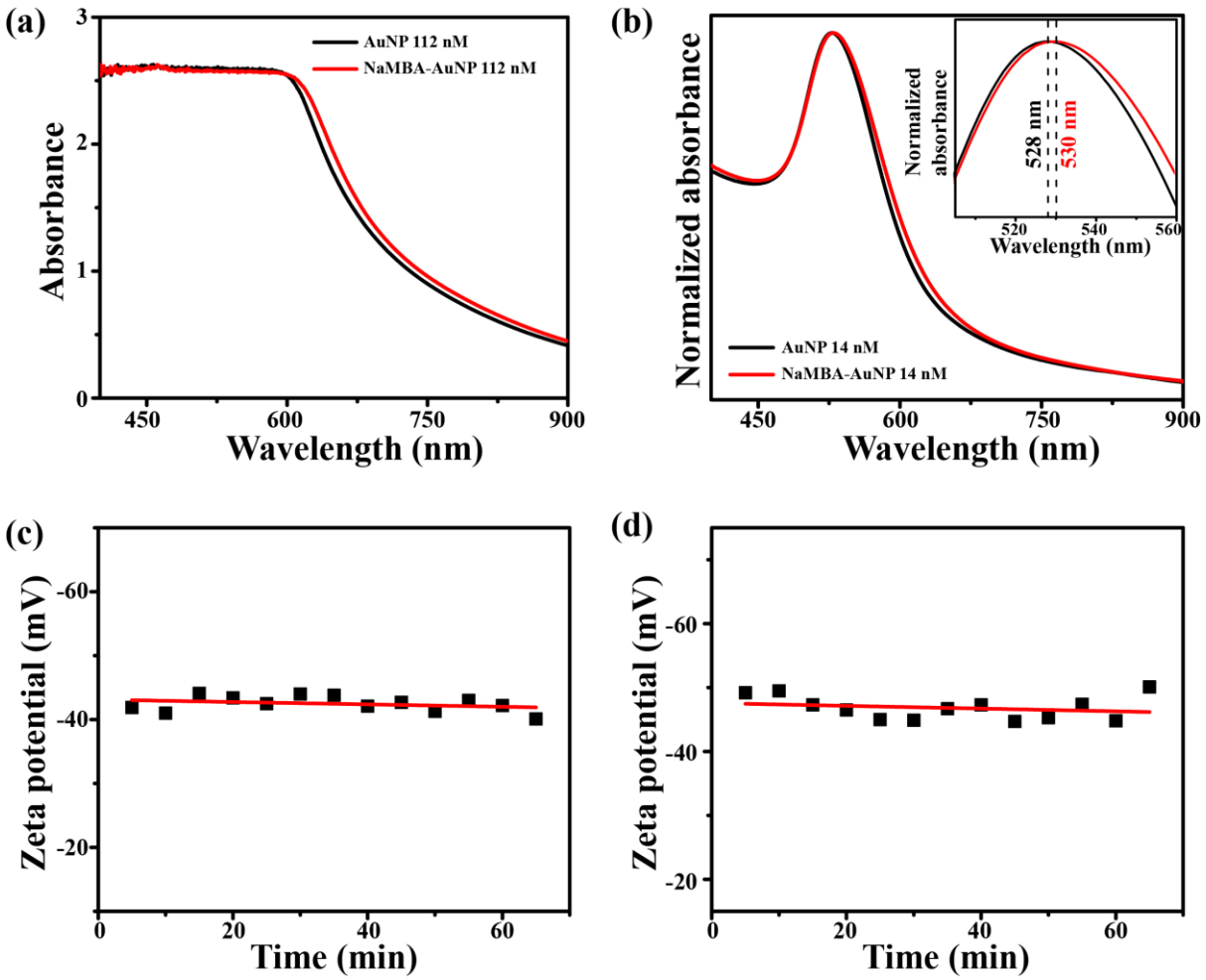

Figure A2.2: (a) UV-Vis absorbance spectra of AuNP-2 and NaMBA-AuNP-2 at 10 nM initial concentrations. Parts of spectra were flattened due to instrument limit at this very high concentration. (b) UV-Vis absorbance spectra of AuNP-2 and NaMBA-AuNP-2 at 1.25 nM initial concentrations. Inset is the zoomed view near peak position. Variation of Zeta potential with time of NaMBA-AuNP-2 dispersions at 10 nM (c) and 1.25 nM (d) initial concentrations respectively. Red lines are linearly fitted curves.

TH_3719_186122105

A2.4. Optical images at other locations of the ring pattern taken from Raman microscope:

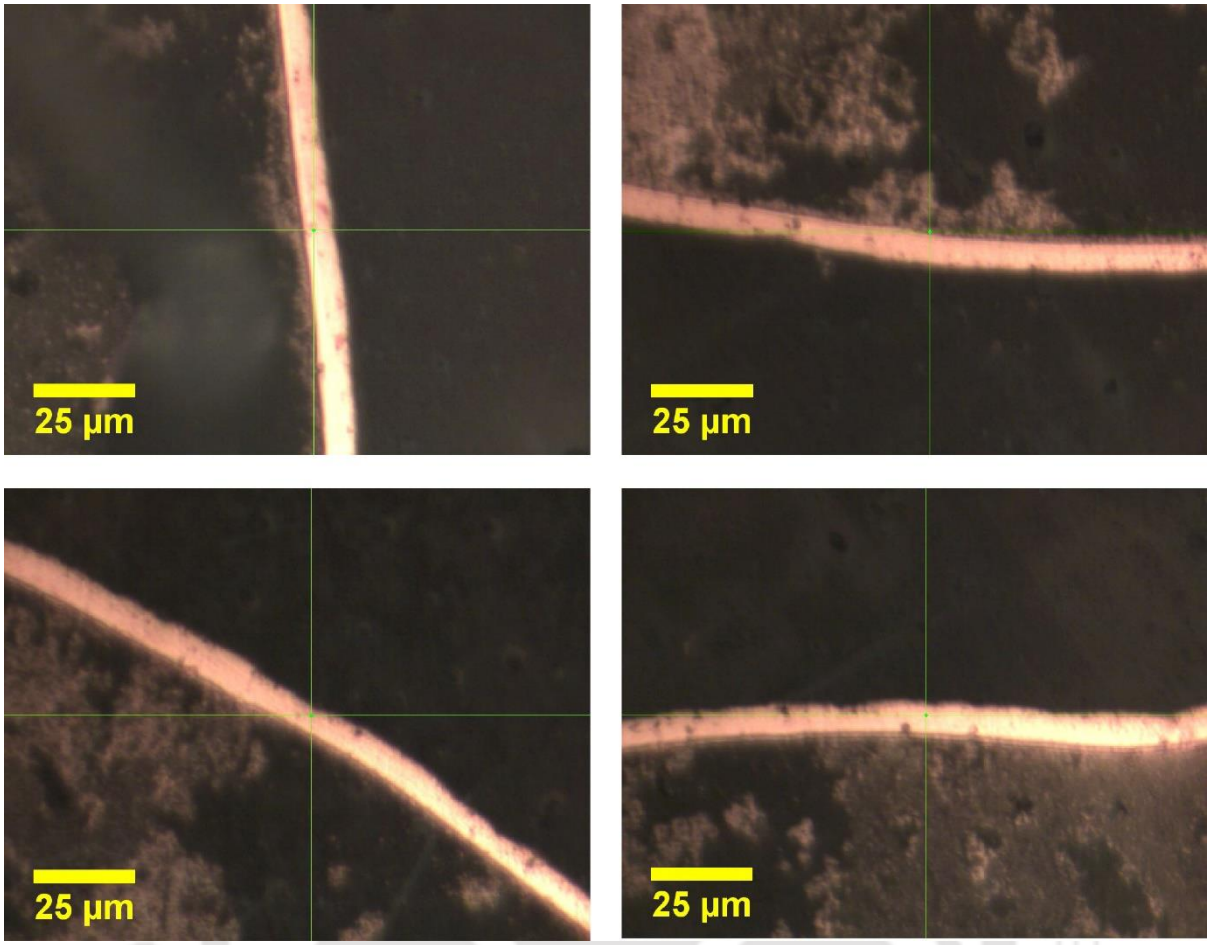

Figure A2.3: Representative images of the ring deposition of NaMBA-AuNPs at other locations of TPCL after complete drying the droplet containing 2.5 nM initial NaMBA-AuNP-2 dispersion.

TH_3719_186122105

A2.5. Optical images of evaporating droplet containing 10 nM initial NaMBA-AuNP-2 dispersion of Experiment-1 in the Chapter 2:

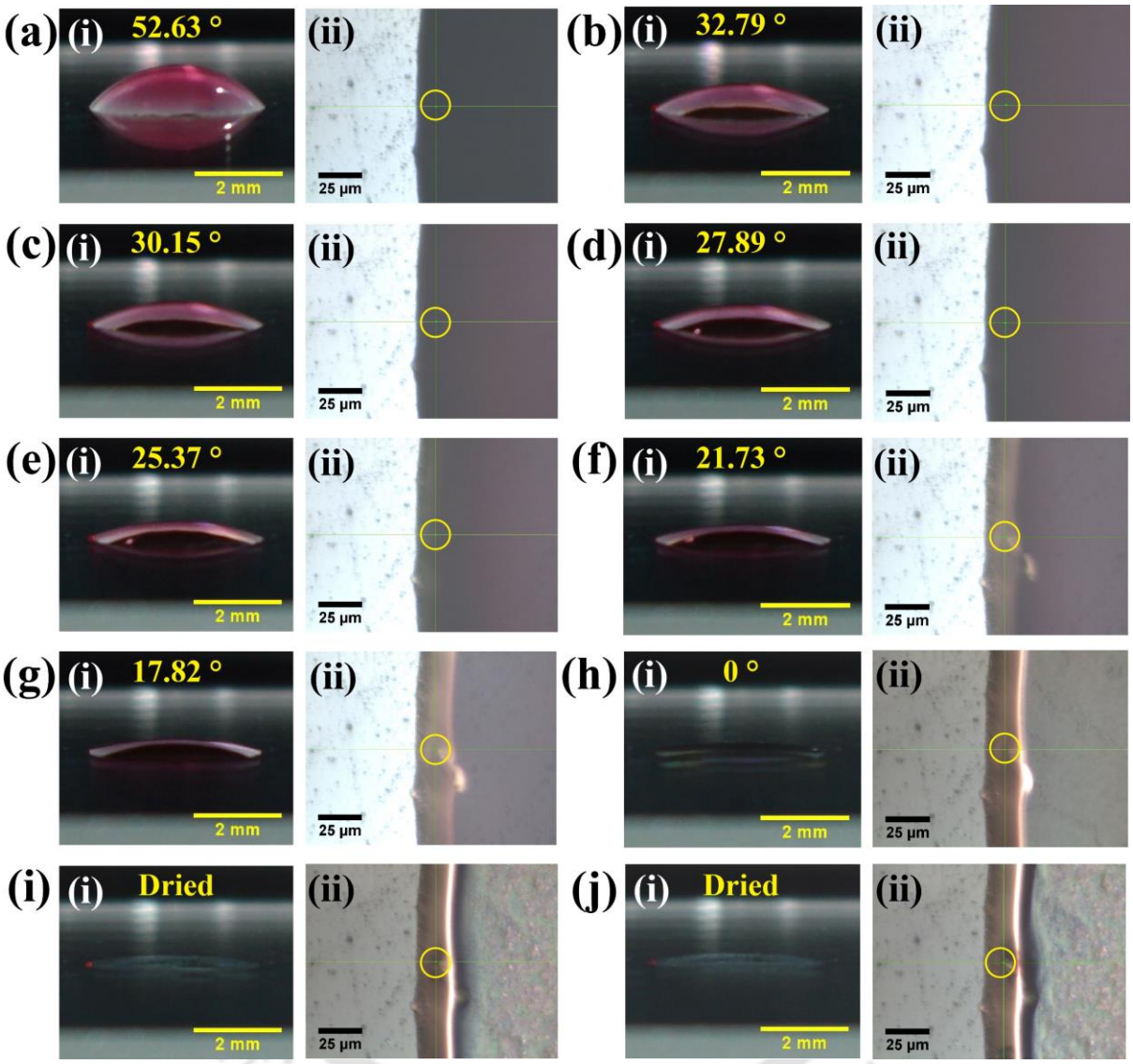

Figure A2.4: Optical images of evaporating droplet containing 10 nM initial NaMBA-AuNP-2 at (a) 0 min, (b) 17.5 min, (c) 20.0 min, (d) 22.5 min, (e) 25.0 min, (f) 27.5 min, (g) 30.0 min, (h) 42.5 min, (i) 45.0 min and (j) 52.5 min, The images in (i) were captured horizontally using DSLR camera and the corresponding images in (ii) were recorded vertically using camera attached to the Raman microscope. Contact angles are mentioned on top side of each horizontal images and the Raman probe areas are identified with yellow circles.

TH_3719_186122105

A2.6. Optical images of evaporating droplet containing 1.25 nM initial NaMBA-AuNP-2 dispersion of Experiment-1 in the Chapter 2:

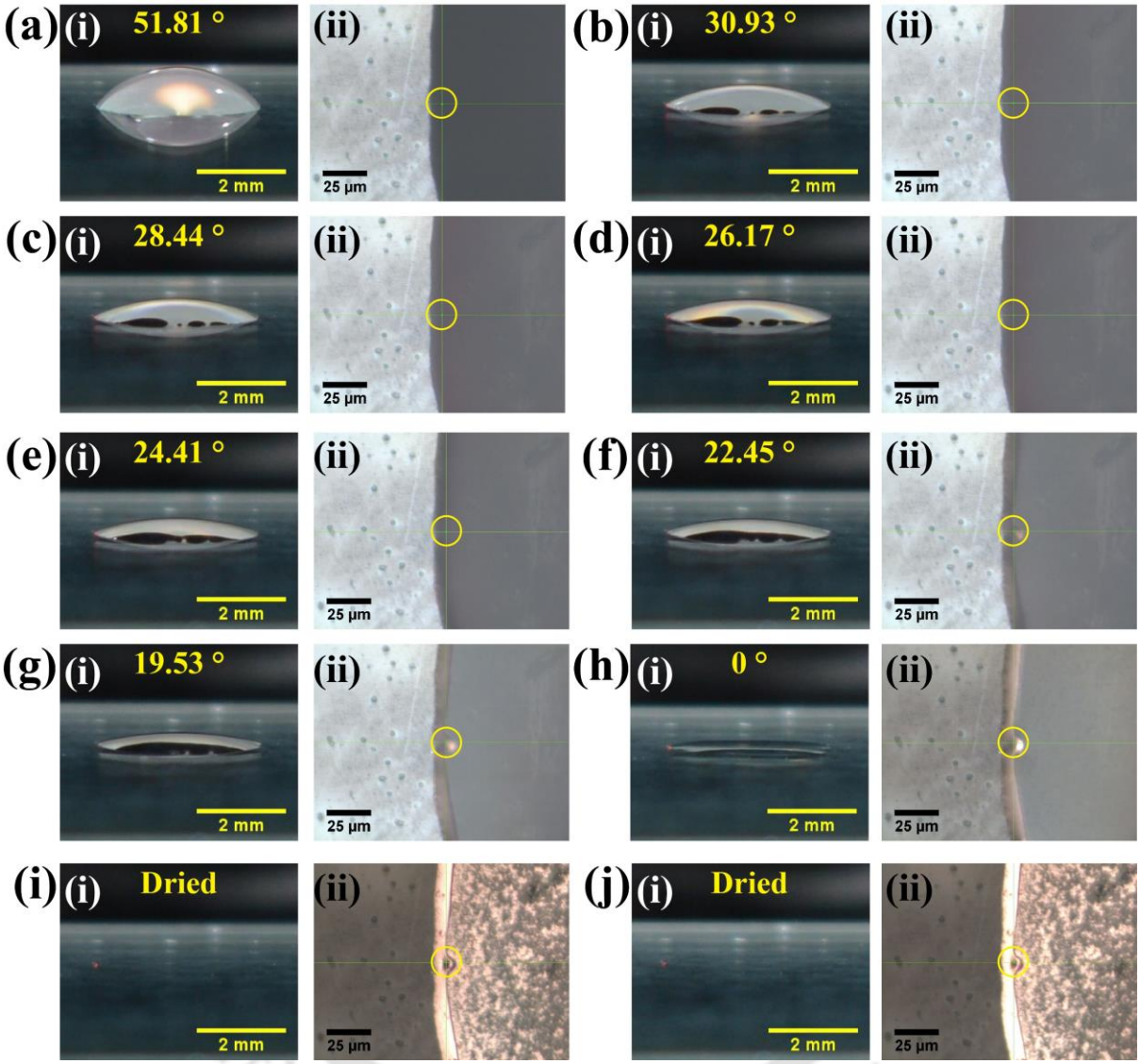

Figure A2.5: Optical images of evaporating droplet containing 1.25 nM initial NaMBA-AuNP-2 at (a) 0 min, (b) 25.0 min, (c) 27.5 min, (d) 30.0 min, (e) 32.5 min, (f) 35.0 min, (g) 37.5 min, (h) 47.5 min, (i) 50.0 min and (j) 57.5 min, The images in (i) were captured horizontally using DSLR camera and the corresponding images in (ii) were recorded vertically using camera attached to the Raman microscope. Contact angles are mentioned on top side of each horizontal images and Raman probe areas are identified with yellow circles.

TH_3719_186122105

A2.7. Table A2.1: Raman peak assignments of NaMBA attached to AuNP.[2-4]

Peak positions (cm^{-1})	Vibrations
631.4	δ(CCC)
720.5	τ(CCCC) + δ(OCO)
850.7	δ(OCO)
1014.9	$\delta(CCC)_{ring}$ + $\nu(C{=}C)_{ring}$
1078.0	$\nu(C{=}C)_{ring}$ + $\nu(C{-}S)$
1141.8	$\nu(C{-}H)$
1180.8	$\nu(C{-}COO)$
1425.3	$\nu(COO^{-})$
1481.9	$\nu(C{=}C)_{ring}$ + $\delta(C{-}H)_{ring}$
1588.2	$\nu(C{=}C)_{ring}$

where, ν = stretching vibration, δ = in-plane deformation, τ = twisting vibration**.**

TH_3719_186122105

A2.8. Results of experiments involving removal of water after phase transition:

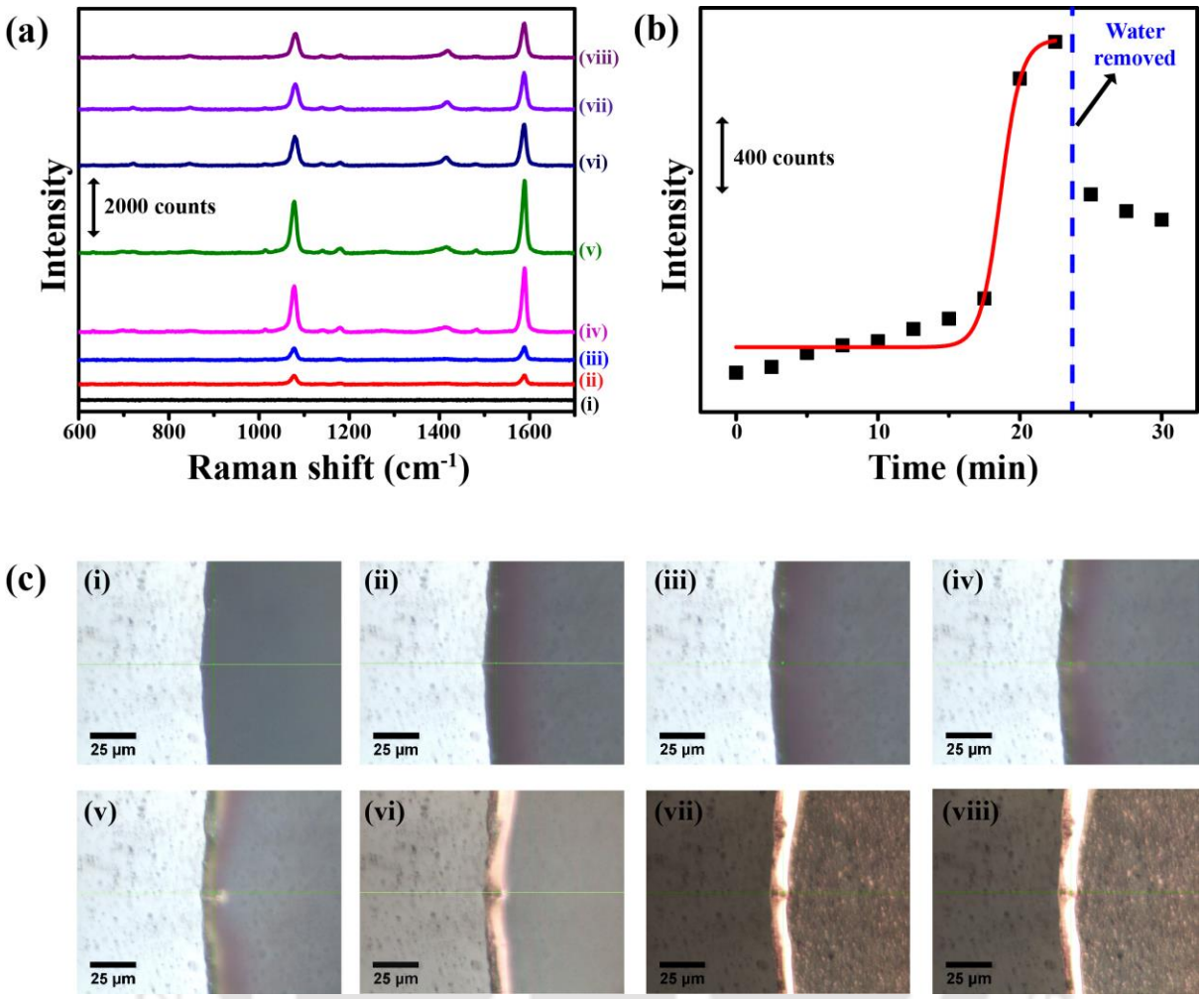

Figure A2.6: (a) Raman spectra of evaporating NaMBA-AuNP-2 dispersion at (i) 0 min, (ii) 15.0 min, (iii) 17.5 min, (iv) 20.0 min, and at (v) 22.5 min. Water was then removed from the remaining droplet using a tissue paper and the spectra were again recorded at (vi) 25.0 min after wiped out water, (vii) 27.5 min and (viii) 30.0 min. (b) 1078 cm^{-1} Raman peak intensity variation with time corresponding to 1078 cm^{-1} peak. Red curve is the Boltzmann fitted plot. (c) Microscopic images of the droplet edge at (i) 0 min, (ii) 15.0 min, (iii) 17.5 min, (iv) 20.0 min, (v) 22.5 min, (vi) 25.0 min (following removal of water), (vii) 27.5 min and (viii) 30.0 min.

TH_3719_186122105

A2.9. FESEM image of the NaMBA-AuNP-2 deposit:

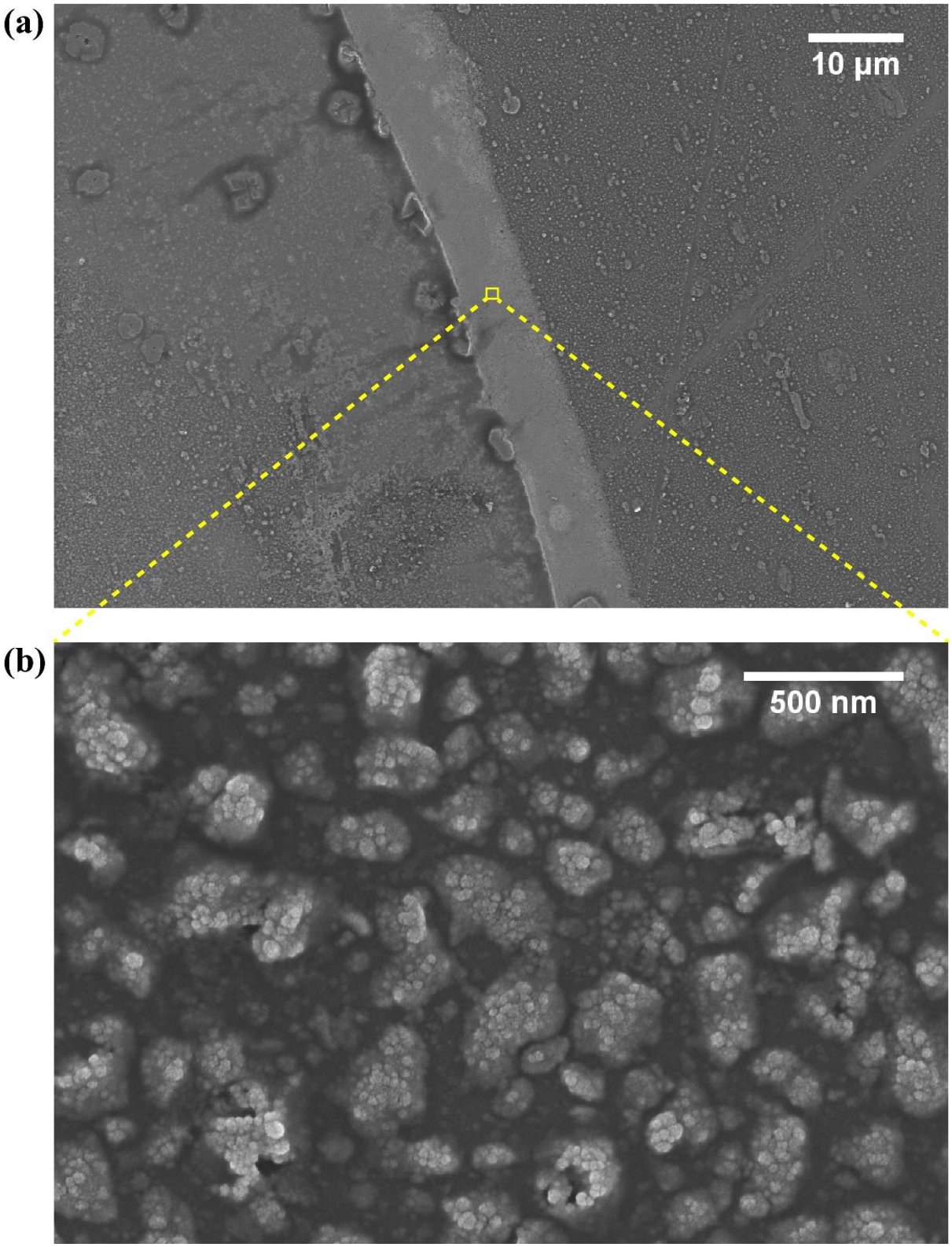

Figure A2.7: (a) FESEM image of NaMBA-AuNP-2 deposit at TPCL recorded after complete deposition and drying and (b) zoomed view of the deposit showing the assembly of NaMBA-AuNPs.

The ring depositions for different times at the TPCL were further probed by AFM.

TH_3719_186122105

A2.10. Variation of Raman signal intensity with time for evaporating droplets used to prepare samples for AFM measurements (corresponding to Figure 2.4 in the Chapter 2):

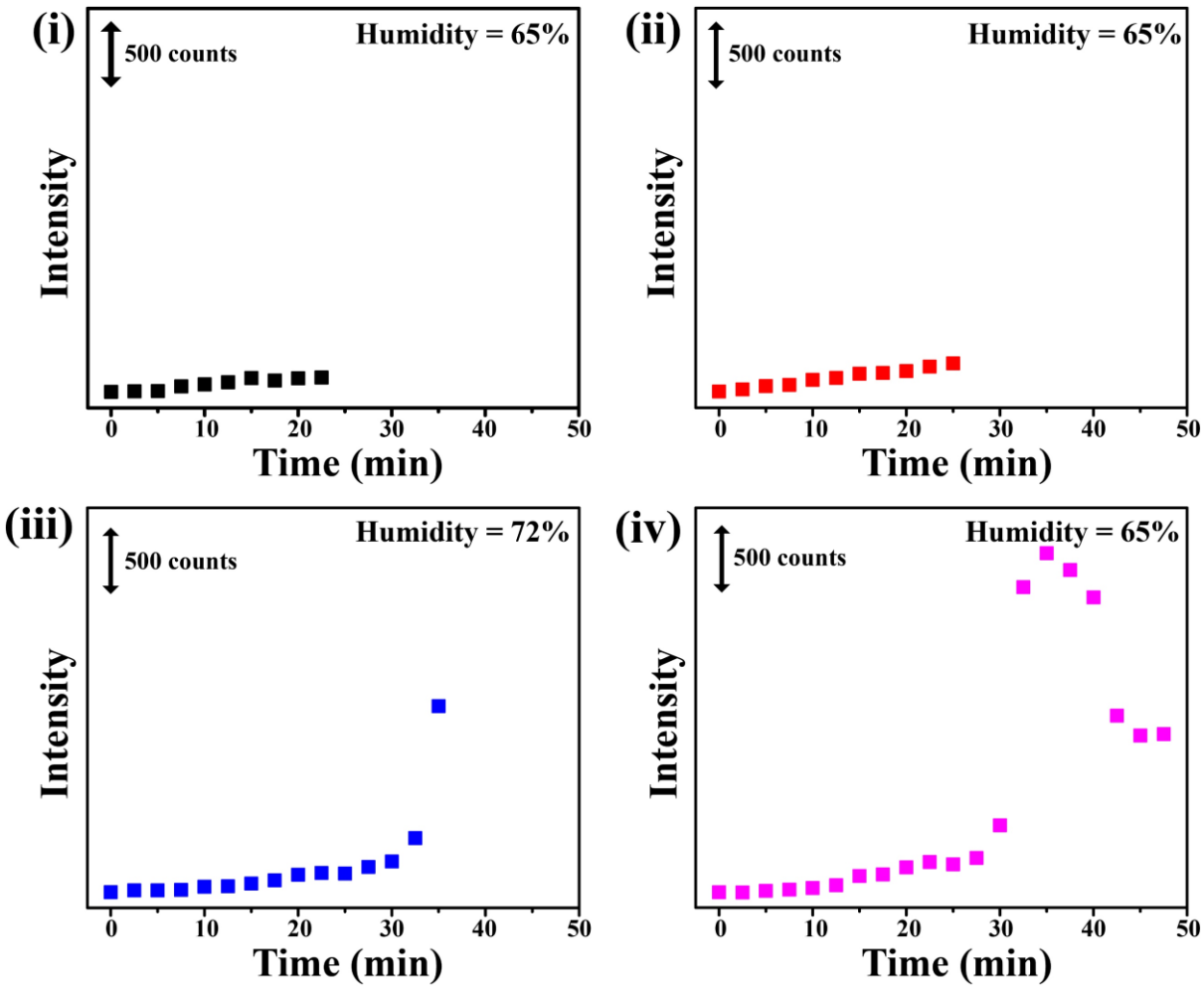

Figure A2.8: Raman peak intensity (for 1078 cm^{-1} peak) variation with time of evaporating droplets containing 2.5 nM NaMBA-AuNP-2 dispersions corresponding to (i), (ii), (iii) and (iv) in the Figure 2.4 in the Chapter 2, respectively. During evaporation, the remaining dispersions were wiped dry with tissue paper at 22.5 min, 25 min and 35 min for (i), (ii) and (iii), respectively.

TH_3719_186122105

A2.11. Phase transition study of 10 nM and 1.25 nM initial NaMBA-AuNP-2 dispersions of Experiment-1 in the Chapter 2:

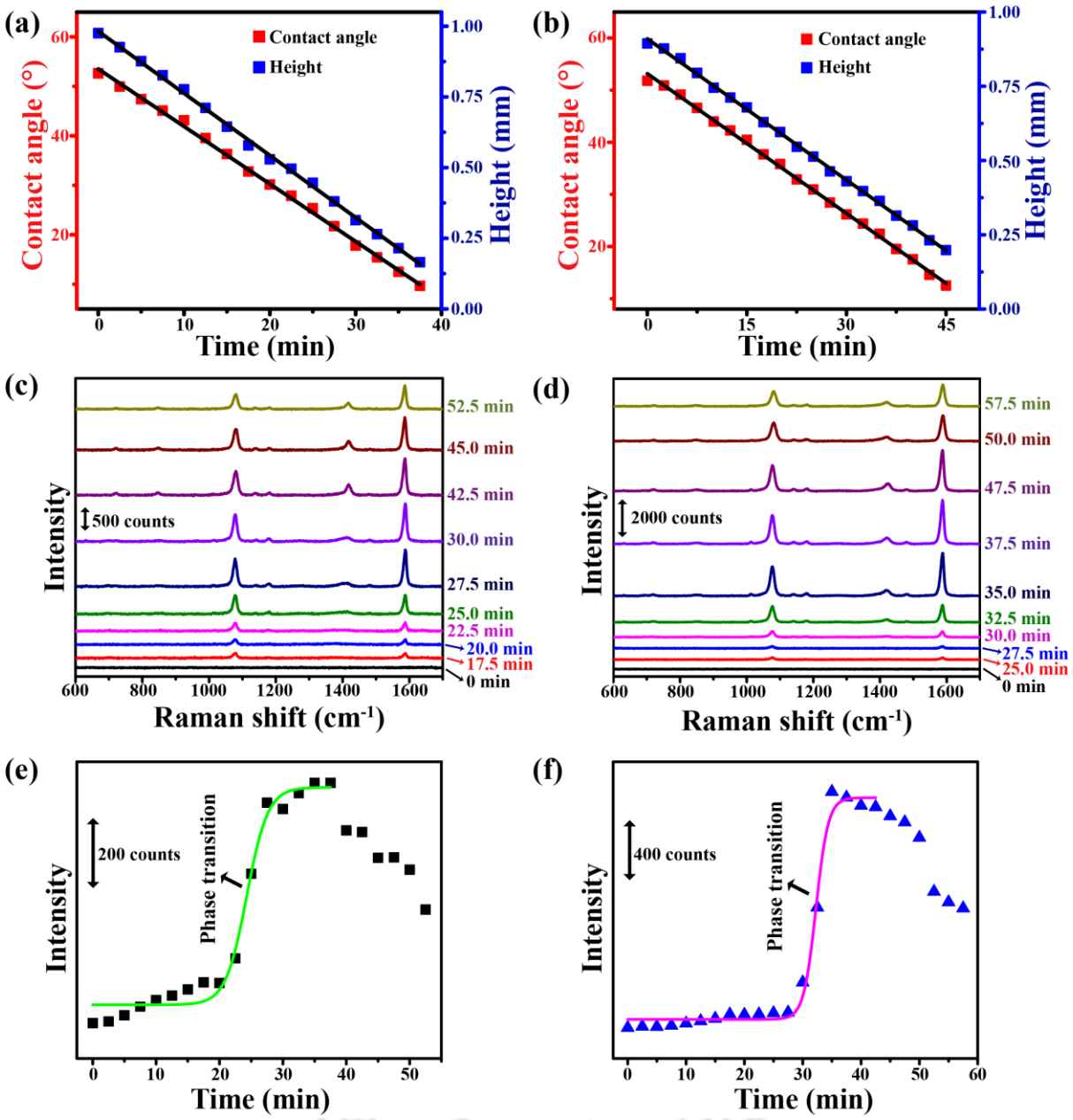

Figure A2.9: Plots of contact angle, droplet height variation with time for evaporating droplet containing (a) 10 nM and (b) 1.25 nM initial NaMBA-AuNP-2 dispersions, respectively. Black lines are linear fits. (c) and (d): Time-dependent Raman spectra of the droplets containing 10 nM and 1.25 nM initial NaMBA-AuNP-2 dispersions, respectively. (e) and (f): Raman peak intensity (for 1078 cm^{-1} peak) variation with time for 10 nM and 1.25 nM initial NaMBA-AuNP-2 dispersions, respectively. Green and purple plots are Boltzmann fittings up to phase transition regions respectively.

TH_3719_186122105

A2.12. Variation of contact angle, height and time dependent Raman spectra of Experiment-2 (Corresponding to Figure 2.5a in the Chapter 2):

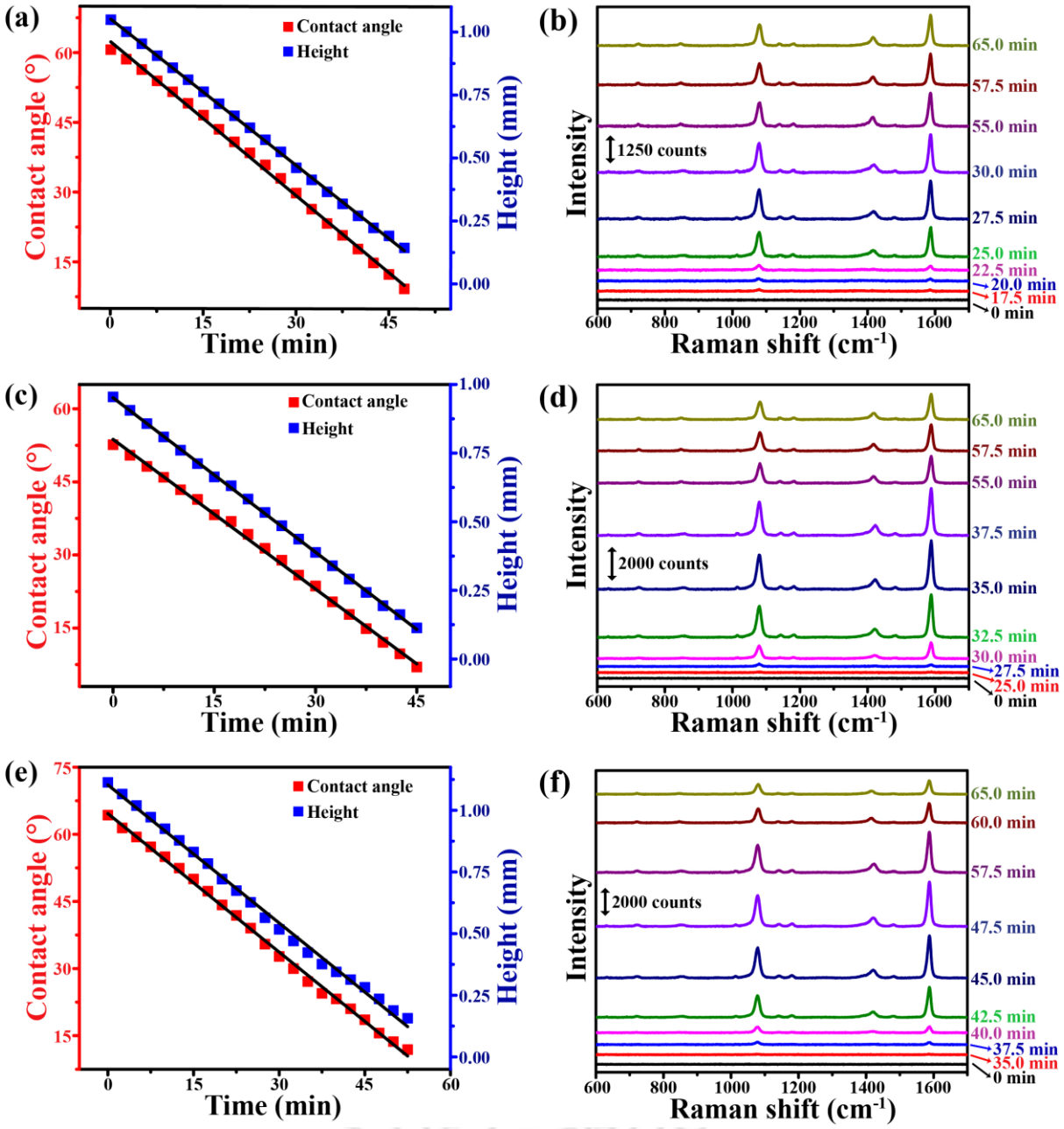

Figure A2.10: Plots of variation of contact angle, height with time and time-dependent Raman spectra of evaporating droplets containing (a) and (b): 10 nM, (c) and (d): 2.5 nM, and (e) and (f): 1.25 nM initial NaMBA-AuNP-2 dispersions, respectively.

TH_3719_186122105

A2.13. Sidewise deposition of excess particles after pileup of nanoparticles deposition at TPCL:

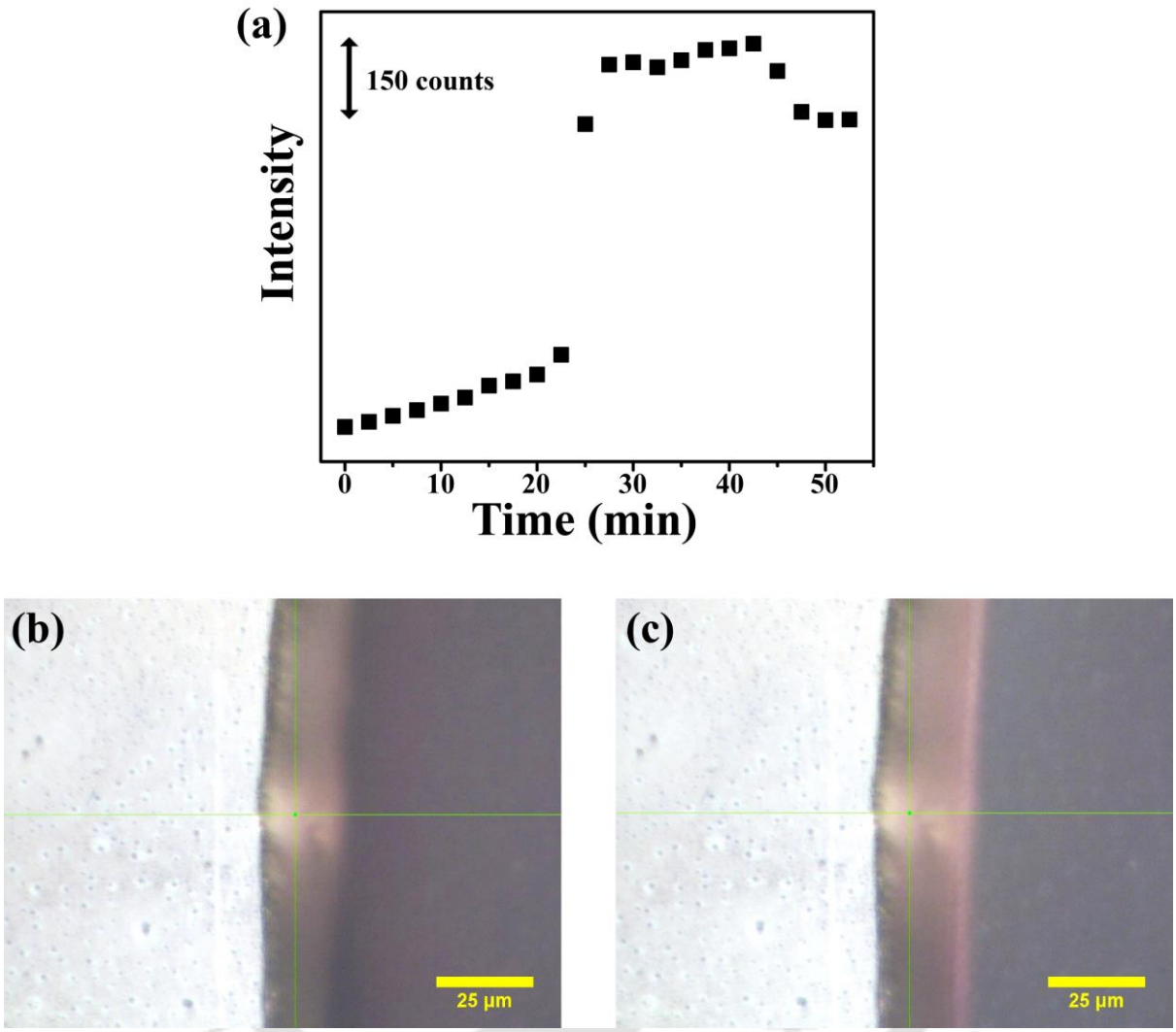

Figure A2.11: (a) Raman peak intensity (for 1078 cm^{-1} peak) variation with time of evaporating droplets containing 10 nM NaMBA-AuNP-2 dispersions. (b) and (c) optical images of the depositions at 30.0 min and 32.5 min respectively. Beyond the time when the maximum Raman intensity was observed, the excess nanoparticles were depositing at the inner side of the deposition as observed (b) at 30.0 min versus that (c) at 32.5 min.

TH_3719_186122105

A2.14. Time dependent Raman spectra, Raman peak (at 1078 cm^{-1}) intensity variations with time and phase transitions of evaporating NaMBA-AuNP-2 dispersions at 10 nM, 2.5 nM and 1.25 nM initial concentrations (corresponding to Experiment-3 of the Chapter 2):

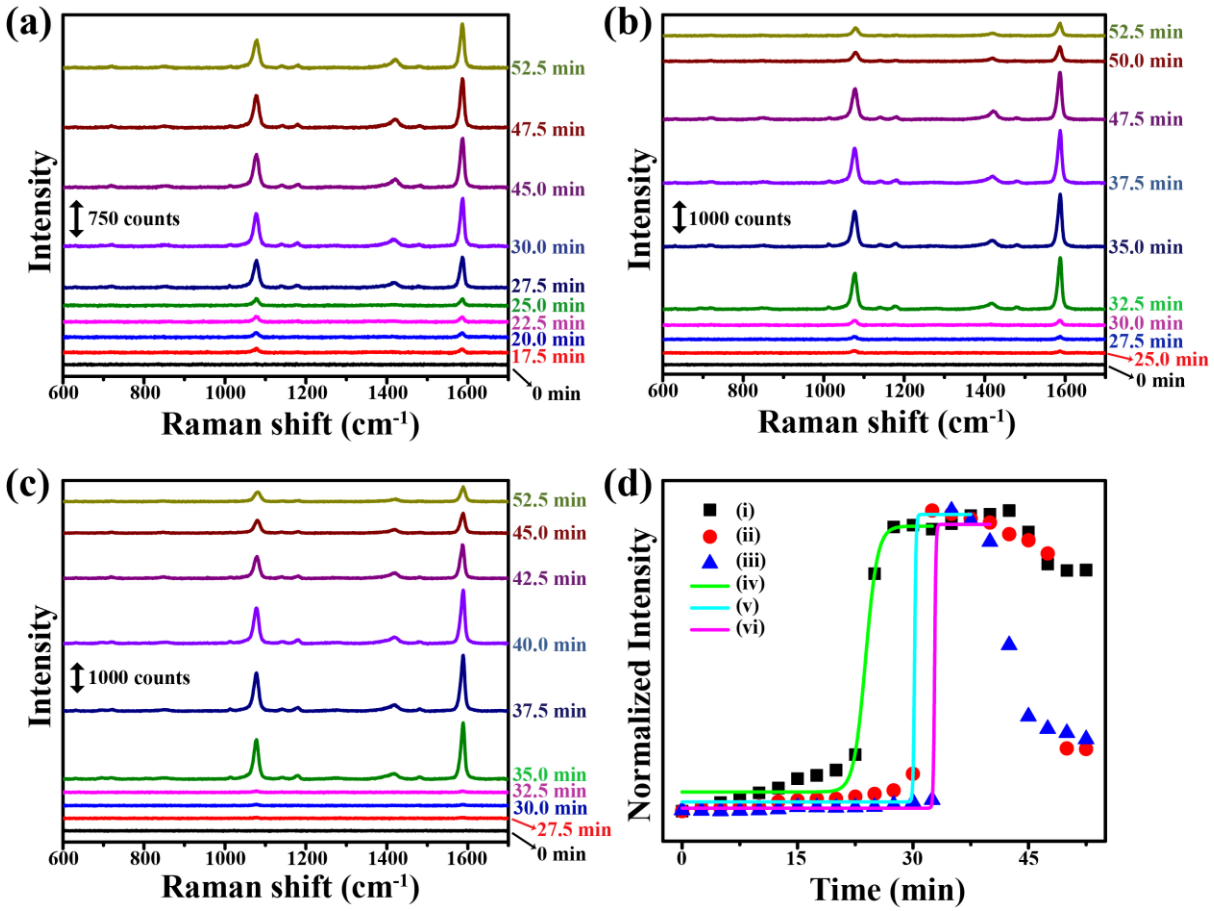

Figure A2.12: Time-dependent Raman spectra of evaporating droplets containing (a) 10 nM, (b) 2.5 nM and (c) 1.25 nM NaMBA-AuNP-2 initial dispersions, respectively. (d) Raman peak (at 1078 cm^{-1}) intensity variation with time of the evaporating droplets containing NaMBA-AuNP-2 at (i) 10 nM, (ii) 2.5 nM, (iii) 1.25 nM initial concentrations respectively and corresponding fitted curves marking phase transition regions in (iv), (v) and (vi) respectively.

TH_3719_186122105

A2.15. Images of dried ring deposits of all AuNP-2 initial concentration dependent experiments:

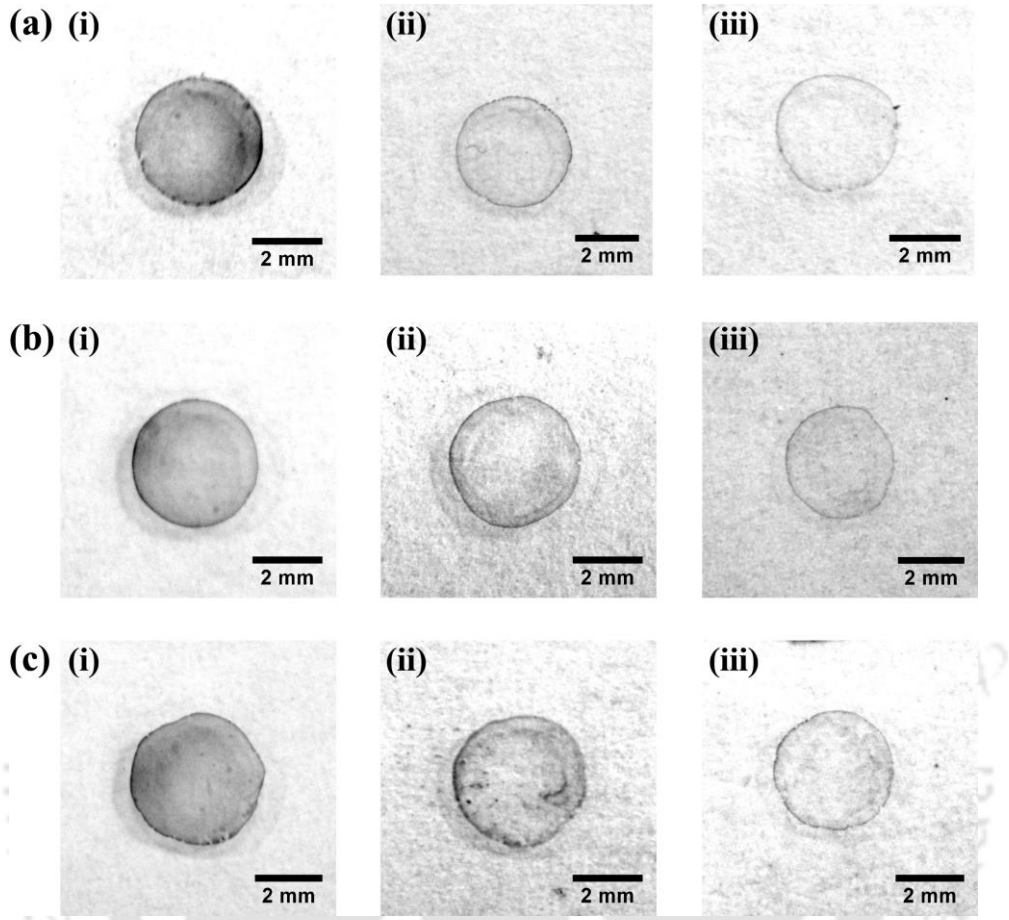

Figure A2.13: Optical images of dried ring depositions of (a) Experiment-1, (b) Experiment-2 and (iii) Experiment-3 of the Chapter 2 recorded after complete evaporation of the droplets containing (i) 10 nM, (ii) 2.5 nM and (iii) 1.25 nM initial NaMBA-AuNP-2 dispersions, respectively.

A2.16. Table A2.2: Droplet radius (*R*) and deposited ring width (Δ*r*) for all AuNP-2 initial concentration dependent experiments:

Experiment	NaMBA-AuNP initial conc. (nM)	*R* (mm)	Δ*r* (μm)
1	10	1.881	21.0
	2.5	1.818	11.9
	1.25	1.672	8.3
2	10	1.615	18.5
	2.5	1.690	11.0
	1.25	1.573	8.0
3	10	1.956	20.0
	2.5	1.876	12.0
	1.25	1.805	11.0

TH_3719_186122105

A2.17. Variation of volume at TPCL with time for all AuNP-2 initial concentration dependent experiments:

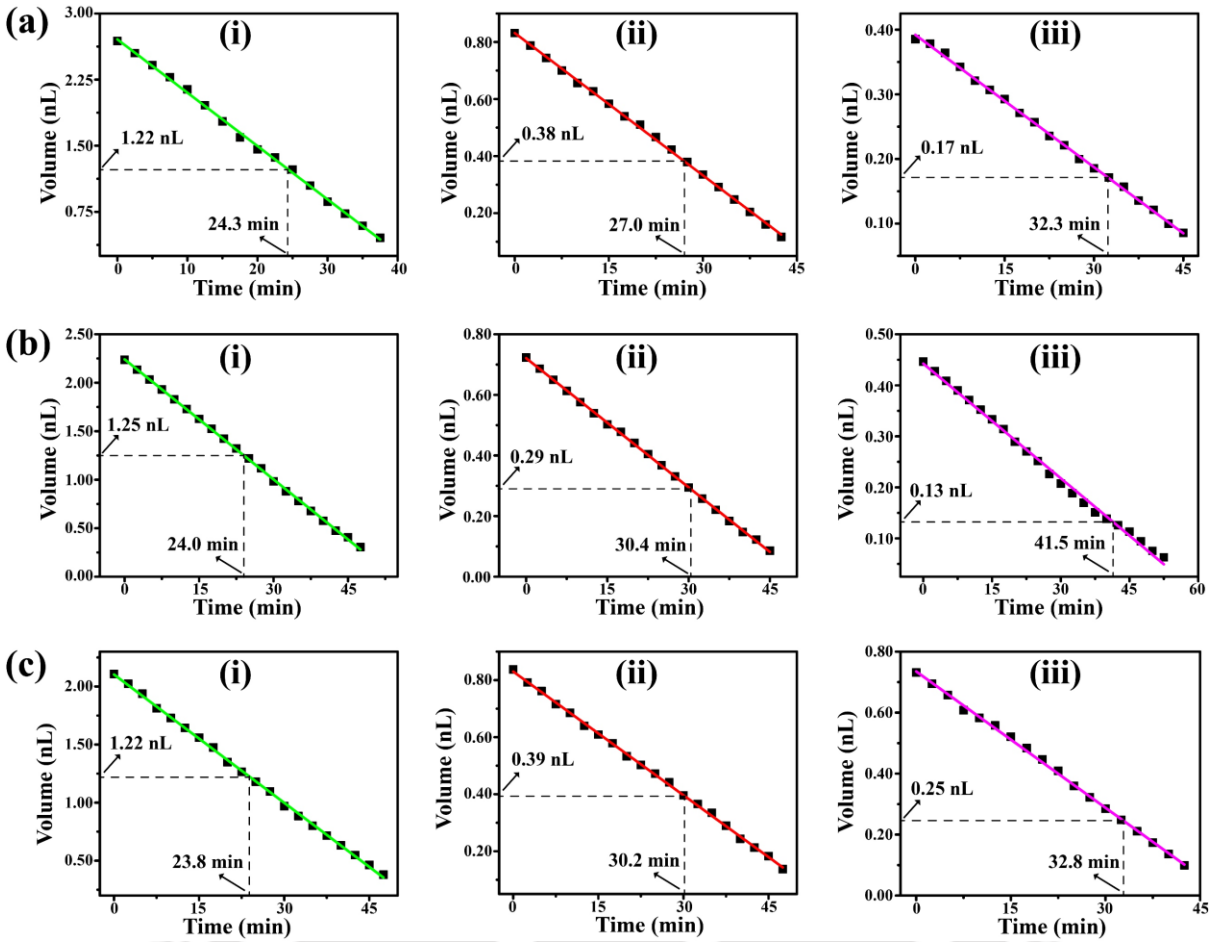

Figure A2.14: Plots of variation of volume at TPCL with time of the evaporating droplets for (a) Experiment-1, (b) Experiment-2 and (c) Experiment-3 of the Chapter 2, containing (i) 10 nM, (ii) 2.5 nM and (iii) 1.25 nM initial NaMBA-AuNP-2 dispersions, respectively.

TH_3719_186122105

A2.18. Characterization of AuNPs of three different size by UV-Vis spectroscopy and FETEM measurements:

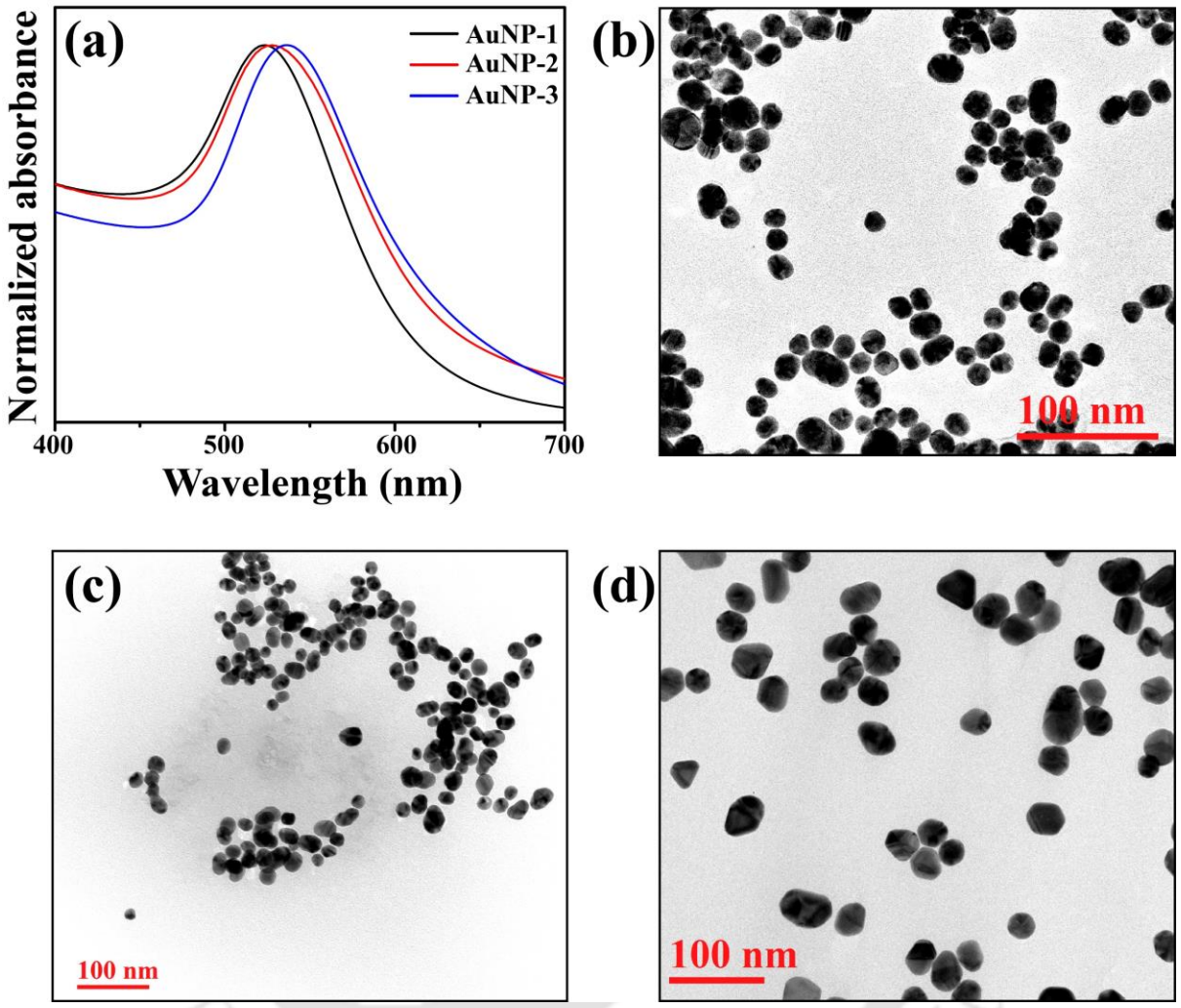

Figure A2.15: (a) UV-Vis spectra of AuNP-1 (15.4 nm), AuNP-2 (25.3 nm) and AuNP-3 (36.4 nm) dispersions, respectively. (b), (c) and (d) are FETEM images of AuNP-1, AuNP-2 and AuNP-3, respectively.

TH_3719_186122105

A2.19. Variation of contact angle, height and time dependent Raman spectra of Experiment-4 for AuNPs of three different sizes (Corresponding to Figure 2.6 in the Chapter 2):

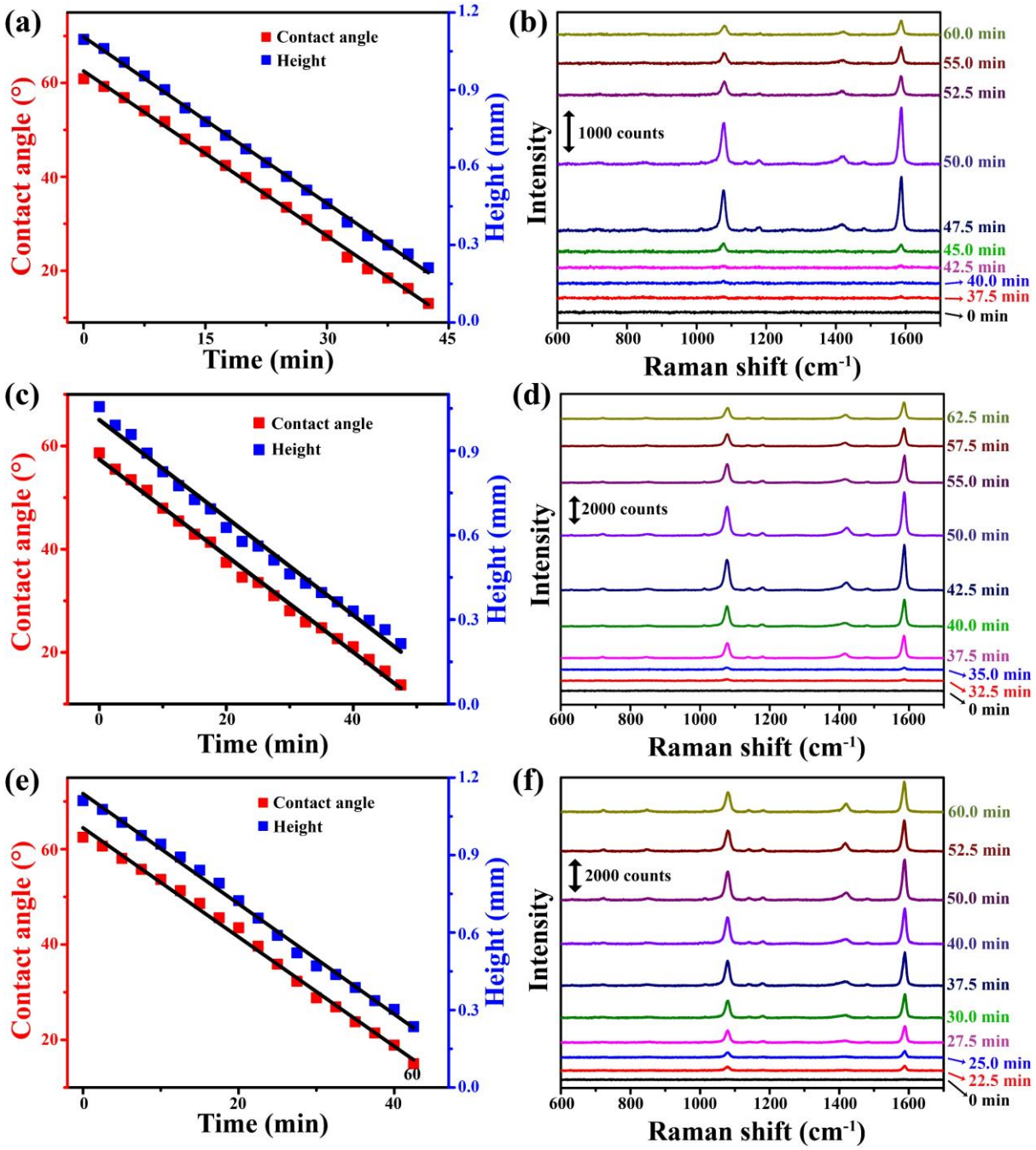

Figure A2.16: Plots of variation of contact angle, height with time and time-dependent Raman spectra of evaporating droplets containing 5 nM of NaMBA attached (a) and (b): AuNP-1, (c) and (d): AuNP-2, and (e) and (f): AuNP-3 dispersions, respectively.

TH_3719_186122105

A2.20. Time dependent Raman spectra, Raman peak (at 1078 cm^{-1}) intensity variations with time and phase transitions of evaporating NaMBA attached AuNP-1, AuNP-2 and AuNP-3 dispersions (corresponding to Experiment-5 and Experiment-6 of the Chapter 2):

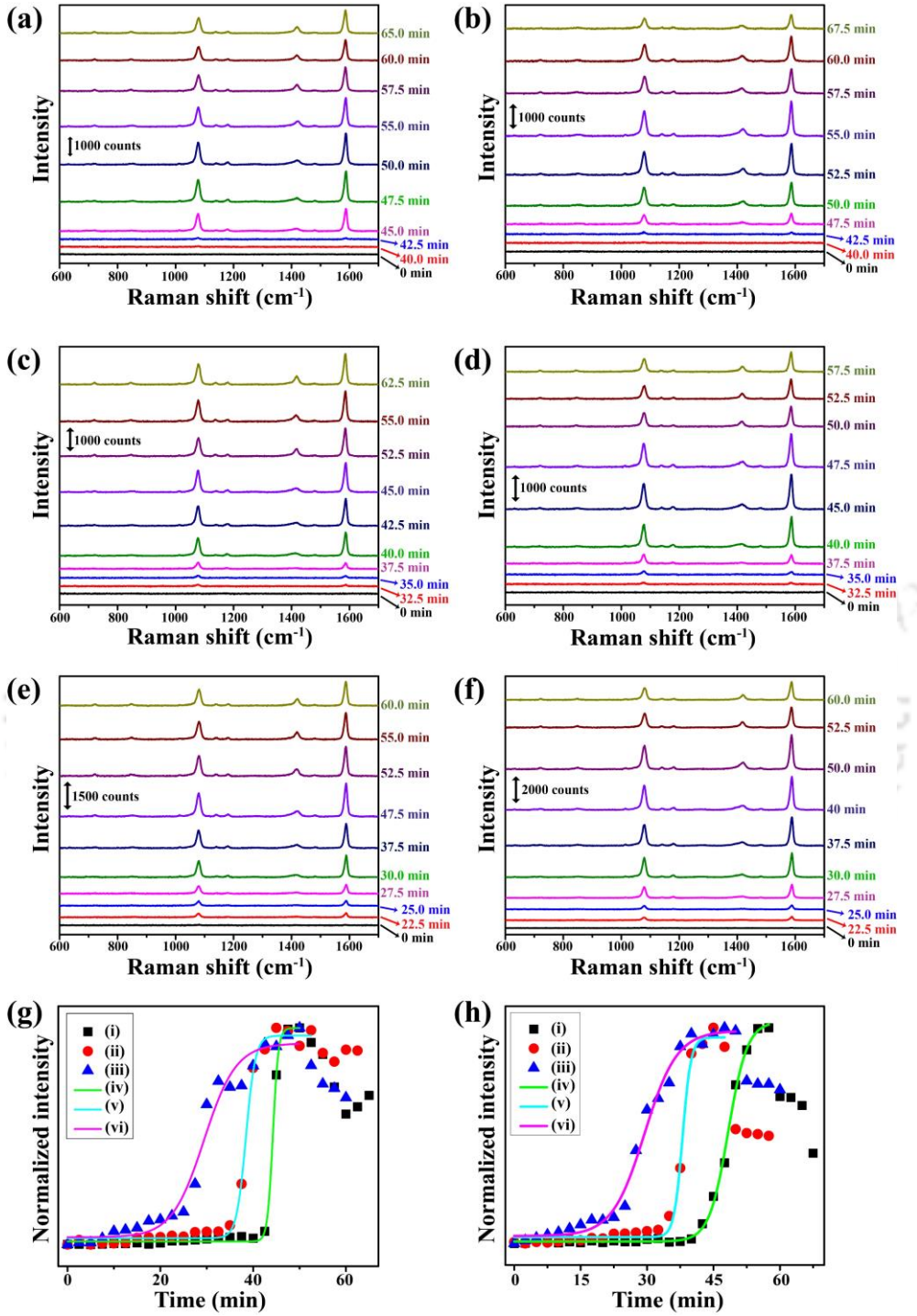

Figure A2.17: Time-dependent Raman spectra of evaporating droplets containing 5 nM of NaMBA attached (a) and (b) AuNP-1, (c) and (d) AuNP-2, (e) and (f) AuNP-3, in Experiment-5 and Experiment-6, respectively. (g) and (h) Raman peak (at 1078 cm^{-1}) intensity variation with time of the evaporating droplets containing 5 nM of NaMBA attached (i) AuNP-1, (ii) AuNP-2, (iii) AuNP-3, corresponding fitted curves marking phase transition regions in (iv), (v), (vi) in Experiment-5 and Experiment-6, respectively.

TH_3719_186122105

A2.21. Table A2.3: Droplet radius (*R*) and deposited ring width (Δ*r*) for all particle size dependent phase transition experiments:

AuNP diameter (nm)	Experiment	*R* (mm)	Δ*r* (μm)
15.4	4	1.683	11.1
	5	1.648	9.2
	6	1.668	9.5
25.3	4	1.737	20.2
	5	1.815	21.4
	6	1.688	20.3
36.4	4	1.641	28.1
	5	1.650	27.1
	6	1.654	27.9

A2.22. Variation of volume at TPCL with time for all particle size dependent phase transition experiments:

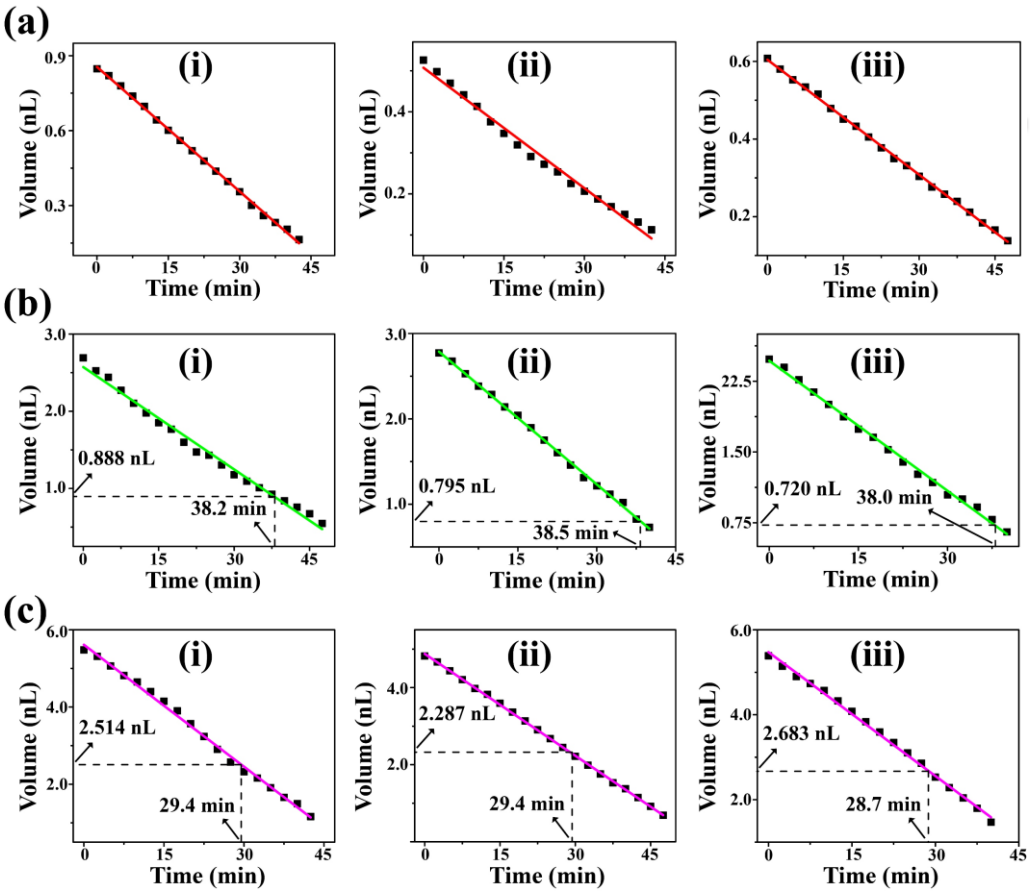

Figure A2.18: Plots of variation of volume at TPCL with time of the evaporating droplets containing 5 nM of NaMBA attached (a) AuNP-1, (b) AuNP-2, (c) AuNP-3 for (i) Experiment-4, (ii) Experiment-5 and (iii) Experiment-6 in the Chapter 2, respectively. For AuNP-1, volumes at TPCL at phase transition times were calculated manually from the linear equations obtained after fitting.

TH_3719_186122105

A2.23. Table A2.4: Boltzmann Fitting Parameters of the sigmoidal growth.

Equation	$y = A_2 + \frac{(A_1 - A_2)}{(1 + e^{\frac{x - x_0}{dx}})}$					
Experiment	**Figure**	A_1	A_2	x_0	dx	**Adj. R-Square**
1	Figure A2.9e	53.71 ± 13.12	676.69 ± 19.98	24.30 ± 0.34	1.66 ± 0.29	0.983
	Figure 2.3c	53.30 ± 11.08	1449.56 ± 20.72	27.00 ± 0.11	0.62 ± 0.11	0.996
	Figure A2.9f	63.31 ± 18.84	1557.25 ± 36.92	32.27 ± 0.18	1.057 ± 0.18	0.989
2	Figure 2.5a(iv)	2.07 ± 0.73	98.79 ± 0.91	24.01 ± 0.09	0.79 ± 0.06	0.998
	Figure 2.5a(v)	1.35 ± 0.63	96.56 ± 1.26	30.40 ± 0.09	0.83 ± 0.09	0.997
	Figure 2.5a(vi)	0.99 ± 0.47	98.08 ± 1.00	41.52 ± 0.08	1.02 ± 0.07	0.997
3	Figure A2.12d(iv)	6.39 ± 1.43	94.84 ± 2.54	23.84 ± 0.21	0.77 ± 0.12	0.988
	Figure A2.12d(v)	3.09 ± 0.61	98.73 ± 0.01	30.21	0.09	0.996
	Figure A2.12d(vi)	1.02 ± 0.62	95.42 ± 5.43	32.81	0.09	0.996
4	Figure 2.6(iv)	1.90 ± 0.43	100.11 ± 1.83	45.70 ± 0.23	0.43 ± 0.14	0.996
	Figure 2.6(v)	1.94 ± 1.12	98.18 ± 2.40	38.15 ± 0.24	1.58 ± 0.21	0.989
	Figure 2.6(vi)	3.50 ± 1.61	98.61 ± 2.26	29.44 ± 0.43	3.66 ± 0.39	0.989
5	Figure A2.17g(iv)	1.43 ± 0.31	99.93 ± 0.92	44.31 ± 0.06	0.59 ± 0.04	0.998
	Figure A2.17g(v)	2.94 ± 0.74	96.46 ± 1.32	38.45 ± 0.13	1.02 ± 0.10	0.995
	Figure A2.17g(vi)	3.35 ± 2.45	92.85 ± 3.39	29.41 ± 0.68	3.46 ± 0.61	0.972
6	Figure A2.17h(iv)	0.93 ± 0.40	102.90 ± 1.49	48.34 ± 0.13	2.15 ± 0.11	0.997
	Figure A2.17h(v)	2.97 ± 0.82	95.55 ± 1.87	38.01 ± 0.14	0.96 ± 0.13	0.993
	Figure A2.17h(vi)	3.50 ± 1.61	98.61 ± 2.27	29.45 ± 0.44	3.66 ± 0.39	0.989

A2.24. References:

1. Pal, S; Paul, S.; Chattopadhyay, A. Dual Role of Au nanoparticles in the Catalytic Formation of an Amorphous Polynuclear Peroxo Complex and Surface Enhanced Resonance Raman Scattering. *ChemistrySelect* **2022**, *7*, e202201569
2. Dutta, A.; Chattopadhyay, A. Surface and Tip-Enhanced Raman Spectroscopy at the Plasmonic Hot Spot of a Coordination Complex-Conjugated Gold Nanoparticle Dimer. *J. Phys. Chem. C* **2017**, *121*, 18854-18861.
3. Marques, F. C.; Alves, R. S.; dos Santos, D. P.; Andrade, G. F. S. Surface-enhanced Raman spectroscopy of one and a few molecules of acid 4-mercaptobenzoic in AgNP enabled by hot spots generated by hydrogen bonding. *Phys. Chem. Chem. Phys.* **2022**, *24*, 27449-27458.
4. Li, P.; Wang, X.; Li, H.; Yang, X.; Zhang, X.; Zhang, L.; Ozaki, Y.; Liu, B.; Zhao, B.; *Chem. Commun.* **2018**, *54*, 6280-6283.

TH_3719_186122105

Chapter-3

Distinction of Plasmonic Intrananoparticle and Internanoparticle Molecular Reaction Rates at the Three-Phase Contact Line of an Evaporating Sessile Droplet

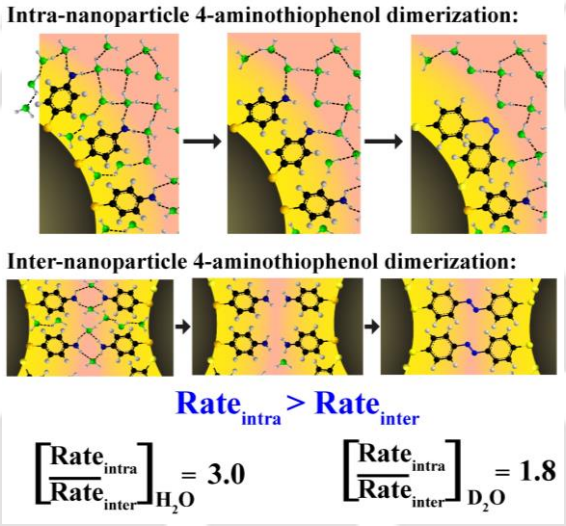

Chapter 3 *of the thesis introduces that the difficulty in distinguishing the kinetics of intranaoparticle and internanoparticle reactions in a dispersion medium could be overcome by probing the reactions at the three-phase contact line (TPCL) of an evaporating sessile droplet using surface enhanced Raman spectroscopy (SERS). Thus, when an evaporating aqueous droplet on glass, containing 4-aminothiophenol (4-ATP)-stabilized Ag nanoparticles, was monitored by SERS at the TPCL, dimerization into 4,4´-dimercaptoazobenzene followed two steps, each preceded by the loss of H-bonded water accordingly. Based on the results, we assigned the first step with higher relative kinetic rate (~3 times) to be intrananoparticle and the second one as internanoparticle reactions. In D_2O medium, the ratio of the rates was ~1.8. The observed vibrational signatures of the losses of water molecules before reactions and product formations were accounted for using density functional theoretical calculations.*

The content of Chapter 3 has been published in *The Journal of Physical Chemistry Letters*, a journal of the American Chemical Society (ACS). *J. Phys. Chem. Lett.* **2024,** *15*, 26, 6812–6817

https://pubs.acs.org/doi/full/10.1021/acs.jpclett.4c01055

TH_3719_186122105

3.1. Introduction

In chemistry, intramolecular and intermolecular reactions present contrasts in kinetics[1,2], dynamics[3] and product selectivity[4] with stereochemistry[5] in action. This has helped industrial productions of chemicals especially those involving multistep reactions[6,7]. What if similar studies could be pursued on the surface and in between nanoparticles? Nanoparticles are typically functionalized with molecules on the surfaces for their stability and utilization. Inter-nanoparticle bond formation through chemical reaction is a potent mean for the formation of well-defined assembly[8,9]. It is plausible that intra-nanoparticle and inter-nanoparticle reactions involving the surface species would be nearly identical in molecular context. However, the nature of nanoparticles and role of solvent molecules may contribute significantly in their differing reaction kinetics or pathways[10]. For example, reactions involving plasmonic Ag, Au or similar nanoparticles may differ in rates and product selectivity aided by surface plasmons of individual nanoparticles and hot-spots in between the nanoparticles[11,12].

While the differing products make it easier to follow intramolecular and intermolecular reactions simultaneously in the same reaction mixture, the nearly identical nature of the molecular products makes it rather difficult to probe the product molecules on the nanoparticle surfaces. The conventional spectroscopic probes, especially in the dispersion medium or in the solid state, are not necessarily sufficient to establish the differences – if any – in such reactions. Our recent results suggest that an evaporating sessile droplet may offer an alternative way of probing such reactions. Thus, sodium 4-marcaptobenzoate (NaMBA) – stabilized Au nanoparticles in aqueous dispersion, when evaporated as sessile droplets and probed by SERS at the TPCL, a phase transition signifying the depositions of the nanoparticles all at once occurs[13]. Now, a chemical reaction occurring at the TPCL following deposition and in the presence of plasmonic hot spots and evaporating water may reveal new information about the nature of reactions especially by distinguishing the rates of intra-nanoparticle and inter-nanoparticle reactions. In this respect, the photochemical oxidative dimerization of 4-ATP on nanoparticle surface is a versatile and well-studied reaction that can occur between two molecules attached to a single nanoparticle or two nanoparticles[14]. The most common dimerization product is DMAB[15], formed through the coupling of the two aromatic rings via a N=N bond. Recently, interparticle reaction of 4-ATP to DMAB in an end-to-end assembly of gold nanorod has been reported[9].

TH_3719_186122105

3.2. Outline of the Present Work

We report that evaporation of the aqueous droplet containing 4-ATP functionalized spherical (~25 nm) silver nanoparticles (AgNPs) when probed at the TPCL by SERS photochemical dimerization into DMAB was observed in two steps following deposition of the nanoparticles. The rate for the first step was 3 times as high as that for the second step. Interestingly, this ratio was 1.5 in D_2O medium. The Raman peak at 946 cm^{-1} - due to the collective vibration of water molecules bonded with 4-ATP attached with Ag nanoparticles as supported by density functional theory (DFT) calculations– diminished in two steps each preceding the reaction. This indicated the loss of water bonded to the intra-nanoparticle 4-ATP molecules first followed by those bonded to inter-nanoparticle molecules leading to the dimerization reactions accordingly.

3.3. Experimental Section

3.3.1. Materials:

Silver nitrate, 99% ($AgNO_3$), deuterium oxide (D_2O), 4-aminothiophenol, 97% (4-ATP) and tannic acid were purchased from Sigma Aldrich. Trisodium citrate dihydrate, sodium hydroxide, methanol, acetone, hydrochloric acid (35%) and nitric acid (98%) were bought from Merck India. All the chemicals were used without further purification. For all experimental and washing purpose, Milli-Q grade water was used. Commercial rectangular glass slides were precleaned using aqua regia followed by sonication in Milli-Q water and acetone.

3.3.2. Instruments and Characterizations:

UV-Vis absorbance spectra were recorded using PerkinElmer® Lambda 365+ UV-Vis spectrometer. Transmission electron microscopic (TEM) images and selected-area electron diffractions (SAED) were obtained from JEOL JEM-2100F Field Emission Transmission Electron Microscope (FETEM) instrument having acceleration voltage of 200 kV. FETEM samples were prepared by drop-casting 7 μL of AuNP dispersions on carbon-coated copper grids. Raman spectra were recorded using Horiba LabRAM HR Evolution Raman spectrometer attached with 633 nm laser source. Atomic force microscopic (AFM) measurements on the dried deposits were done using Oxford Asylum Research Model: MFP-3D instrument. Optical images were obtained using microscope system attached to Raman spectrometer and Nikon D3200 DSLR camera. All the graphs were plotted and fitted in Origin 9.0 pro software.

TH_3719_186122105

3.3.3. Synthesis of citrate capped silver nanoparticles (Cit@AgNPs): Cit@AgNPs were synthesized using previously reported method.[16] Briefly, 40 mg of trisodium citrate dihydrate and 10 mg of $AgNO_3$ were dissolved in 20 mL and 80 mL Milli-Q water in two separate round bottom flasks. 20 µL aqueous solution of 3.0 (mM) tannic acid was added in the trisodium citrate solution. The two flasks were stirred and heated up to 65 °C. Then the hot mixture of trisodium citrate and tannic acid was added at a time to the stirring solution of $AgNO_3$ at 65 °C and stirred vigorously. When the color of the solution became yellowish nearly after 5 min, the mixture was boiled for 20 min. Appearance of dark reddish green color dispersion confirmed the completion of Cit@AgNPs synthesis. The mixture was then cooled to room temperature and stored at 4 °C in a refrigerator before further experiments. 10 mL of as synthesized Cit@AgNP was centrifuged first at 4000 rpm for 10 min at 10 °C to remove relatively larger particles and agglomerates. Then the supernatant was divided into two parts (each of 5 mL) and centrifuged at 15,000 rpm for 10 min at 10 °C and the precipitates of the two parts were re-dispersed in 1 mL H_2O and 1 mL D_2O, respectively. 500 µL of the dispersion in H_2O was used to characterize as synthesized AgNP by UV-vis spectroscopy and TEM measurements. Another 500 µL was used for 4-ATP functionalization.

3.3.4. AgNPs functionalization with 4-ATP:

Separate solutions of 4-ATP and NaOH were made in H_2O and D_2O. 2.2 µL of each 0.01 (M) NaOH solution in H_2O and D_2O were added in the 500 µL centrifuged dispersion of Cit@AgNPs in H_2O and D_2O, respectively to make the 7.0 pH of each AgNP dispersion. Then 4 µL of 34 µM 4-ATP solution either in 1:1 methanol-H_2O or in 1:1 methanol-D_2O mixtures was added to the 500 µL centrifuged dispersion of Cit@AgNPs in H_2O or D_2O. Then the mixtures were ultrasonicated for 30 min to obtain homogeneous dispersion of 4-ATP functionalized AgNPs (ATP@AgNPs). After ultrasonication, the 4-ATP@AgNPs dispersions were centrifuged at 4000 rpm for 10 min at 10 °C to remove relatively larger agglomerates, which was confirmed by UV-vis spectroscopy.

3.3.5. Raman measurements and 4-ATP dimerization on AgNPs surface:

5 µL of ATP@AgNPs dispersion was carefully dropped on cleaned glass slide to obtain a sessile droplet of circular base. Raman measurements were carried out at every 30 sec on a fixed spot of three-phase contact line (TPCL) while the sessile droplet was evaporating at 22 °C and 68% relative humidity. Raman spectra were recorded using 633 nm laser source at 600 gr/mm diffraction grating for 5 s acquisition time and accumulation number of 3 at the fixed

TH_3719_186122105

spot of TPCL focused using 50x long distance objective lens. Baseline corrections of all the spectra were done in the LabSpec 6.0 software equipped with the instrument. The 633 nm laser source was also acted as photon source for the dimerization of 4-ATP into 4,4´-dimercaptoazobenzene (DMAB) over time. Recording of Raman spectra was carried out till the droplet was completely evaporated.

3.3.6. Density functional theory (DFT) calculation:

DFT calculations were done using Gaussian 16.0 suit[17]. For drawing and visualization of all the chemical structures, GaussView 6.0 software[18] was used. Two layers of Ag atomic cluster obtained from Ag crystal structure was used for intraparticle calculations. On top of the Ag slab, two 4-ATP molecules were connected with Ag slab through Ag−S bonds ($AgATP_{intra}$). For interparticle calculations, two 4-ATP molecules connected separately to two different Ag_5 clusters ($AgATP_{inter}$), was used. Two types of H_2O or D_2O molecules were chosen. In between 4-ATP molecules, four water molecules were directly hydrogen bonded (H-bonded) through the amine groups (Water-H). Another four water molecules were used as bulk water, which were not directly H-bonded to 4-ATP (Water-B). Control calculations were done using Ag-DMAB-Ag and Ag-ATP structures (connected by Ag−S bonds). All the Ag atoms were kept frozen in all the calculations. All calculations were done through DFT using PW91PW91 functional[19], 6-31G(d,p) basis set[20] for C, H, O, N and S atoms and LANL2DZ basis set[21] for Ag atoms. For simplification of all calculations, a larger number of Ag atoms were not used. Obtained input files were modified using text editor for the calculation using D atoms. At first, ground state geometry was optimized. Then, from the optimized structures, Raman spectra and ground state energies were calculated. Interaction energies were calculated using the following equations-

$$(E_{interaction})_{intra} = E_{intra} - \left(E_{AgATP_{intra}} + E_{Water-H} + E_{Water-B}\right)$$

$$(E_{interaction})_{inter} = E_{inter} - \left(E_{AgATP_{inter}} + E_{Water-H} + E_{Water-B}\right)$$

In order to confirm the isotope exchange between H and D at the amine group of 4-ATP, H atoms at the amine group was replaced one by one in the optimized Ag-ATP structure and Raman spectra were calculated using same level of DFT. Then the calculated spectra were compared with the experimentally obtained data. No D atom substituted, one D atom substituted and two D atoms substituted molecules were denoted as Ag-ATP(NH_2), Ag-ATP(NHD) and Ag-ATP(ND_2), respectively.

TH_3719_186122105

3.4. Results and Discussions

3.4.1. SERS Measurements at TPCL:

Experimentally, when 2.4 nM of citrate-capped 25 nm AgNPs were surface functionalized with 34 µM solution of 4-ATP (ATP@AgNP) there was no significant shift in the plasmon peak of the NPs at 397 nm (**Figure A3.1** in the Appendix of Chapter 3 (A3)). The absence of an additional plasmon peak in UV-vis spectra for both of the above NPs indicated lack of agglomeration in the medium which was further confirmed by transmission electron microscopy (TEM) investigations in **Figure A3.2** in SI. TEM measurements further supported the presence of ~28 nm particles in the dispersion of ATP@AgNP.

When a 3.5 mm (diameter) aqueous droplet of ATP@AgNP dispersion was evaporated on glass slide at 22 °C and 68% relative humidity (typical values) (Experiment-1), and the Raman laser probe was being shone at the TPCL, no signal could be observed till 39.0 min (**Figure A3.3** in A3). However, a peak at 1078 cm^{-1} (due to the combined C=C and C-S stretching vibration mode) started appearing right after and at 41.5 min a sudden increase in the peak intensity – representing a transition from dispersion to deposition phase of the NPs as reported earlier[13] - was observed (**Figure 3.1a,c**). Within a short time lag, there was the appearance of the characteristic vibrational peak of the dimerization product DMAB at 1434 cm^{-1} due to N=N stretching mode, which at first increased till 41.5 min (**Figure 3.1a,c**). As is evident from **Figure 3.1c**, there was 1.0 min time gap in the increase of 1434 cm^{-1} peak or the starting of DMAB formation compared to increase of 1078 cm^{-1} Raman peak or phase transition. In order words, the DMAB formation was occurring after 'hot-spot' generations due to the phase transition. Following this, there was decrease in the Raman signal intensity till 43.5 min as shown in **Figure 3.1c** caused by the change in dielectric environment from water to air as discussed in details in later section.[22] Then again from 44.0 min Raman signal intensity of the peak at 1434 cm^{-1} was gradually increasing till 46.0 min as shown **Figure 3.1b,c**. This was followed by gradual loss of the signal intensity accompanying drying of the droplet.

In case of evaporating droplet containing D_2O (instead of H_2O) (Experiment-2), similar phase transition behavior (**Figure A3.4** in A3) i.e., increasing of 1078 cm^{-1} peak started at 45.0 min (**Figure 3.1d,f**). On the other hand, a 1.0 min time lag was also noticed in the appearance of 1434 cm^{-1} Raman peak or DMAB formation, the signal intensity of which increased till 48.5 min (**Figure 3.1f**). After that there was no significant intensity change till 51.0 min as shown in Figure 1f. Then again rise in intensity of 1434 cm^{-1} Raman peak till 55.0 min was noticed as shown in **Figure 3.1e,f**. Thus, the results indicated that there were two sequential increases in

TH_3719_186122105

the product peak intensity at 1434 cm^{-1} that were separated by a decrease in the same in between.

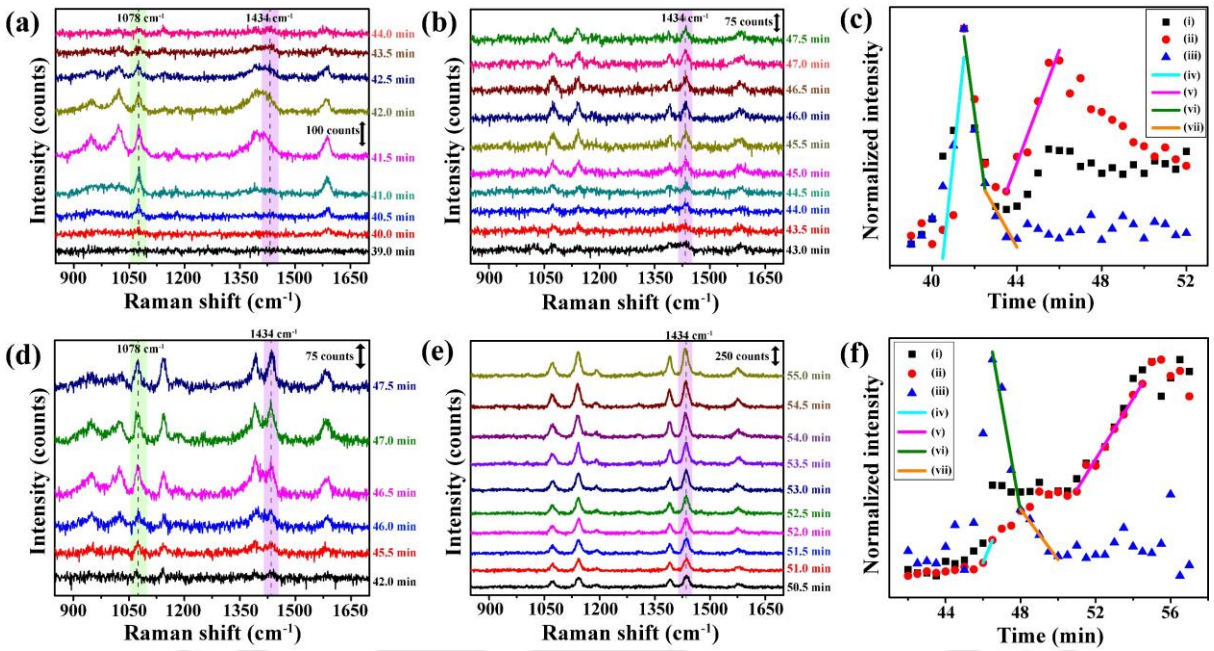

Figure 3.1: For ATP@AgNP dispersion in H_2O, (a), (b) Raman spectra at TPCL of evaporating droplet at different times, (c) variation of (i) 1078 cm^{-1}, (ii) 1434 cm^{-1} and (iii) 946 cm^{-1} Raman peak intensities with time, (iv), (v) and (vi), (vii) are linear fittings of the variations of intensities with time of 1434 cm^{-1} and 946 cm^{-1} peaks, respectively. For ATP@AgNP dispersion in D_2O, (d), (e) Raman spectra at TPCL of evaporating droplet at different times, (f) variations of (i) 1078 cm^{-1}, (ii) 1434 cm^{-1} and (iii) 949 cm^{-1} Raman peak intensities with time, (iv), (v) and (vi), (vii) are linear fittings of the variation of intensities with time of 1434 cm^{-1} and 949 cm^{-1} peaks, respectively Intensity values in (c) and (f) were obtained from Lorentzian fitting of the Raman spectra as shown in **Figure A3.5** in A3.

3.4.2. Water evaporation and DFT calculated results:

Interestingly, we also observed the appearance and then disappearance of a peak at 946 cm^{-1} in H_2O as shown in **Figure 3.2a**. Also, as is evident in **Figure 3.1c(iii)**, the intensity of the peak increased sharply starting at 39.5 min in parallel with the phase transition time window and after reaching maximum at 40.5 min, that went down in two steps as shown by the linear fittings in **Figure 3.1c(vi)** and **Figure 3.1c(vii)**, respectively. The sudden jump in intensity was possibly due to the plasmonic 'hot-spot' generation during phase transition from dispersion to deposit state[13]. The peak at 946 cm^{-1} account for structures having intraparticle (**Figure 3.2e**) and interparticle (**Figure 3.2f**) 4-ATP molecules H-bonded to H_2O molecules on the surface of AgNP, with the calculated peaks appearing 959 cm^{-1} for both (**Figure 3.2b**). For the D_2O

TH_3719_186122105

medium, the results were similar in nature i.e., a sudden increase during phase transition followed by two-step decrease (**Figure 3.1f**), with the peak appearing instead at 949 cm^{-1} (**Figure 3.2c**). Likewise, simulations indicated the corresponding vibrational peaks for D_2O bonded to intraparticle (**Figure 3.2e**) and interparticle (**Figure 3.2f**) 4-ATP molecules on AgNP surface appeared at 952 cm^{-1} and 969 cm^{-1} as shown in **Figure 3.2d(ii)** and **Figure 3.2d(iii)**, respectively. Interestingly, these peaks were absent for both the Ag-ATP and Ag-DMAB complexes in vacuum or in the dry phase as shown in **Figure 3.2b** and **Figure 3.2d**. Therefore, the experimentally observed peaks at 946 cm^{-1} in H_2O and at 949 cm^{-1} in D_2O were because of the H-bonded solvent framework shell around 4-ATP@AgNP in plasmonic 'hot-spot' environment and gradual movement of solvent molecules from AgNP surface to the bulk during evaporation was causing the decrease of the intensity of these peaks till solvent molecules moved from the plasmonic 'hot-spot' environment to the bulk.

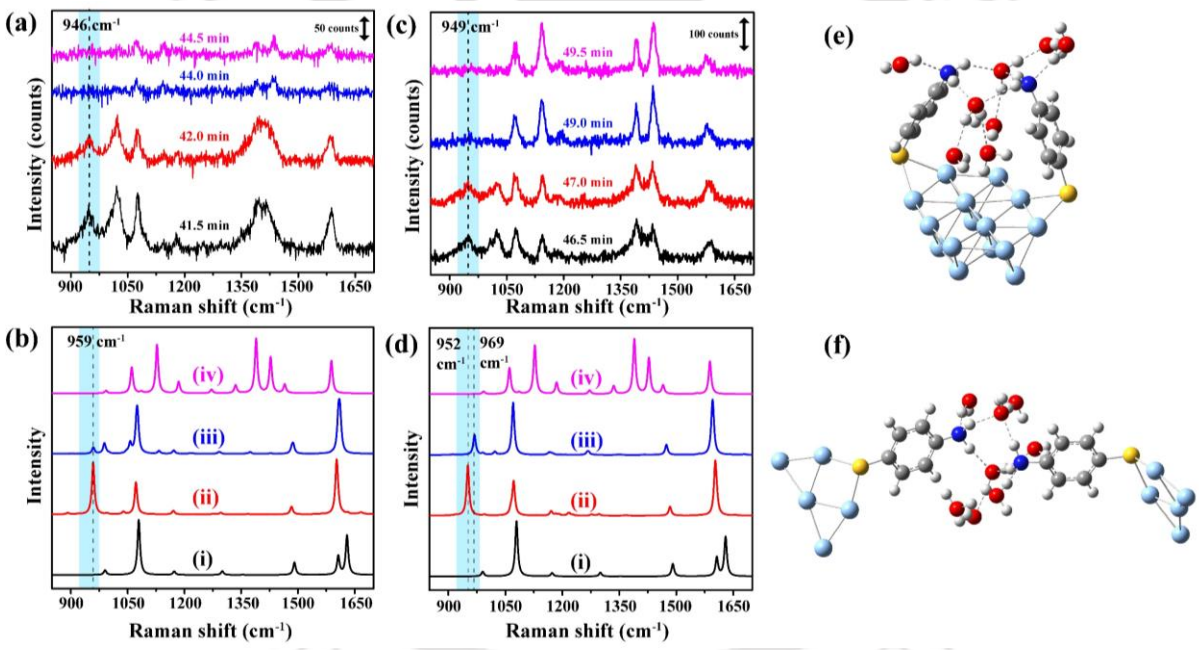

Figure 3.2: Raman spectra at the TPCL, of the evaporating droplet containing ATP@AgNP dispersion, at different times with highlighted (a) 946 cm^{-1} peak in H_2O and (c) 949 cm^{-1} peak in D_2O. (b) Calculated Raman spectra of (i) Ag-ATP in vacuum, (ii) intra-nanoparticle 4-ATP in H_2O, (iii) inter-nanoparticle 4-ATP in H_2O and (iv) Ag-DMAB in vacuum. (d) Calculated Raman spectra of (i) Ag-ATP in vacuum, (ii) intra-nanoparticle 4-ATP in D_2O, (iii) inter-nanoparticle 4-ATP in D_2O having and (iv) Ag-DMAB in vacuum. (e) DFT calculated structure of intra-nanoparticle 4-ATP H-bonded with H_2O/D_2O. (f) DFT calculated structure of inter-nanoparticle 4-ATP H-bonded with H_2O/D_2O. Red, blue, gray, yellow, cyan and white atoms in (e) and (f) are O, N, C, S, Ag and H or D, respectively.

TH_3719_186122105

However, optical image in **Figure A3.6** in A3 at 46.0 min showed the presence of bulk water when 946 cm^{-1} peak was absent in the spectrum shown in **Figure 3.1b**. Eigenvectors or displacement vectors due to the vibration of H-bonded H_2O and D_2O molecules with 4-ATP on silver surface are shown in **Figure A3.7**. Moreover, linear fittings in **Figure 3.1c** and **Figure 3.1f** suggested that the decreasing of 946 cm^{-1} peak in H_2O in both the steps were faster than the lowering of 949 cm^{-1} peak in D_2O due to its slower evaporation rate. Slower evaporation rate of ATP@AgNP in D_2O compared to ATP@AgNP in H_2O was confirmed from simultaneous observation of both the droplets evaporation with time as shown in **Figure A3.8** in A3. H_2O and D_2O containing ATP@AgNP were evaporated completely by 50 min and 58 min, respectively (**Figure A3.8**). Therefore, around ATP@AgNP, dielectric environment change in D_2O was slower than that in H_2O and the DMAB formation in second step occurring simultaneously with the change in D_2O environment without extraordinary increase and then decrease in the 1434 cm^{-1} peak in **Figure 3.1f(ii)**. It is worth mentioning here that release of energy in the surrounding environment following plasmonic heating of the deposited AgNPs might have been accelerating the rapture of H-bonded networks around 4-ATP molecules.

3.4.3. Two-step DMAB formation rates:

The above results point to three important phenomena associated with the evaporation of ATP@AgNP containing H_2O or D_2O droplets. Firstly, following enhanced evaporation of water there was deposition of ATP@AgNP at the TPCL, occurring through a phase transition in a short span of time. This led to easy observation of Raman peaks due to ATP and H_2O (D_2O) that increased with the depositions of the NPs. Secondly, this step was followed by the lowering of peak due to H_2O (D_2O) in two steps. Finally, nearly simultaneously, there was product (DMAB) formation in two steps that followed the losses of peaks due to H_2O (D_2O). Further analysis revealed that the rate of product formation in the first step was higher than the second step for both the solvents. For the H_2O droplet (Experiment-1), the ratio of the two rates was measured to have been 3.56 (**Table A3.2**) while that for D_2O medium (Experiment-2) was 1.48 (**Table A3.3**). Now, in the dispersion medium, ATP molecules of ATP@AgNP were bonded to H_2O (D_2O) through hydrogen bonding. Following depositions of a large number of ATP@AgNP at the TPCL plasmonic hot-spots would have been generated that led to easy detection of peaks due to ATP and H_2O (D_2O) through SERS. There could be two types of solvent molecules in the 'hot-spot' environment that were bonded to ATP molecules through hydrogen bonding: intrananoparticle and internanoparticles H_2O (D_2O) as shown in **Figure 3.2e** and **Figure 3.2f**. Computer simulations on the optimized structures suggested that

TH_3719_186122105

interaction energy for the intraparticle 4-ATP on Ag surface with H_2O (489.5 kJ/mol) or D_2O (487.1 kJ/mol) was lower than that for the interparticle 4-ATP of Ag surface with H_2O (502.1 kJ/mol) or D_2O (503.0 kJ/mol). Therefore, it was easy to break the H-bonds of the intraparticle solvent rather than interparticle solvent in the plasmonic 'hot-spot' environment. This would mean intra-particle solvent molecules would break and move first to the bulk. As, the plasmonic dimerization of 4-ATP could occur only after breaking the H-bonds of attached solvent molecules, the first step of the DMAB formation was mostly intraparticle in nature following the loss of solvent molecules attached to the interparticle 4-ATP molecules. Surprisingly, as evidenced from **Figure 3.1c** and **Figure 3.1f**, the second step of rise of 1434 cm^{-1} peak intensity with time or 4-ATP dimerization in both the solvent occurred only after complete vanishing of the 946 cm^{-1} and at 949 cm^{-1} peaks in H_2O and D_2O solvents, respectively. Hence the second step of DMAB formation was inter-particle in nature. Four more experiments for each solvent (Experiment-3, 4, 5 and 6 for H_2O and Experiments-7, 8, 9 and 10 for D_2O) were performed. Detailed results of Experiment-3, 4, 7 and 8 were given **Figure A3.11**, **Figure A3.12**, **Figure A3.13** and **Figure A3.14**. The results from five experiments for each solvent and rates of DMAB formation are given in **Table A3.2** and **Table A3.3**. Absolute rate at two steps might vary in different experiment depending on slight changes in temperature, pressure, air flow, humidity, droplet size and droplet diameter. Yet, the intra-particle dimerization was always faster than the inter-particle dimerization. For droplets having H_2O, the ratio of the two rates was measured to have been 3.04 ± 0.38 (**Table A3.2**) while that for D_2O medium was 1.75 ± 0.37 (**Table A3.3**). The intraparticle as well as interparticle reaction of 4-ATP occurred in absence of any H-bonded solvent molecules. There was also a possibility of H/D exchange at amine group of 4-ATP, which might have slowed the N=N bond formation compared to H_2O. As shown in the **Figure A3.8**, the D_2O having ATP@AgNP evaporated completely by 58 min, much earlier than the only D_2O which dried fully by 64 min. Difference in evaporation rate of D_2O containing AgNP@ATP compared to only D_2O in **Figure A3.8** might be because of the H/D isotope exchange of 4-ATP with D_2O resulted in the formation of H_2O or HOD evaporated earlier that D_2O.[23] Moreover, at the earlier stage of drying, red-shift of 1590 cm^{-1} peak of ATP@AgNP in H_2O to 1584 cm^{-1} for ATP@AgNP in D_2O was noticed as shown in **Figure A3.9**. The DFT calculated spectra shown in **Figure A3.9(d)** confirmed that the red-shift could be accounted for H/D exchange between the hydrogen atoms of amine groups and D atoms of D_2O. Therefore, slower movement of H-bonded D_2O to bulk and isotope effect might have lowered the rate of both intraparticle and interparticle reactions in D_2O medium. The difference could be attributed to differing nature of

TH_3719_186122105

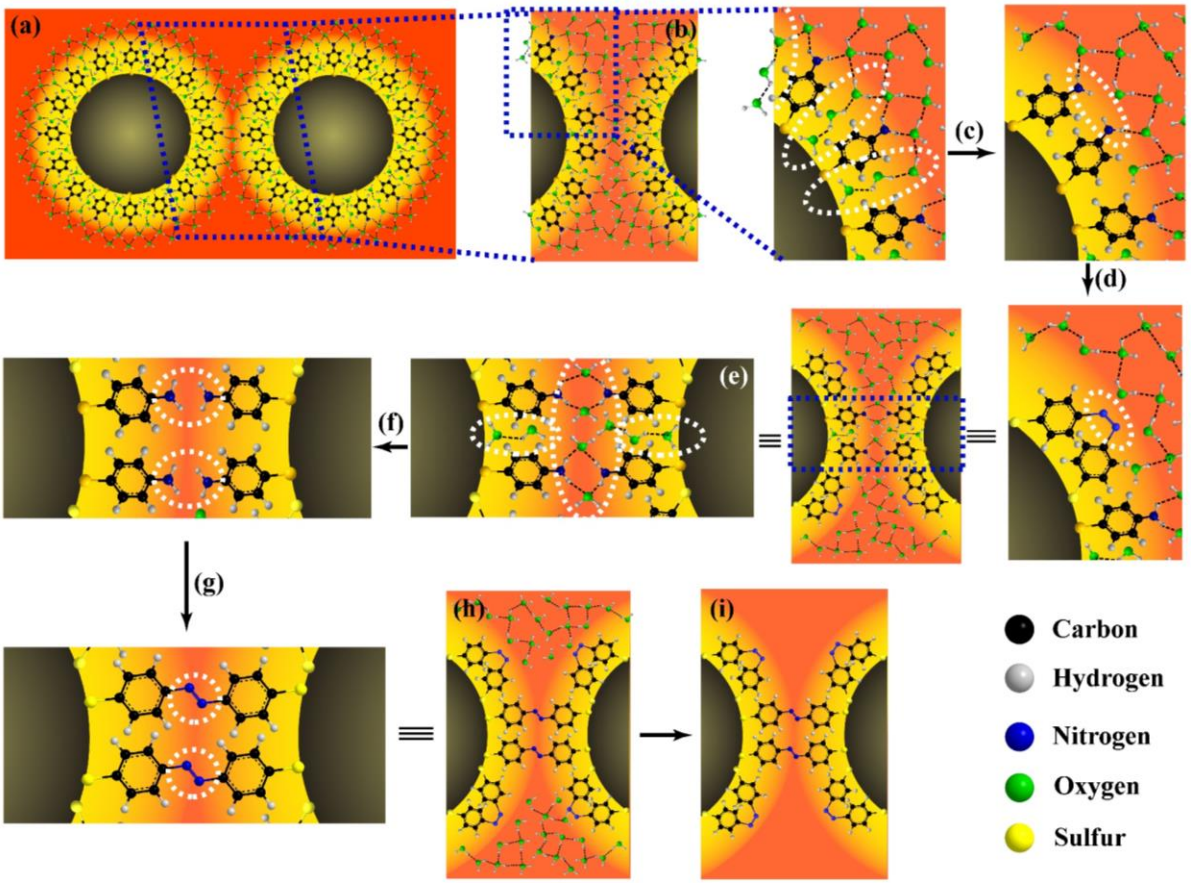

Figure 3.3: (a) Two-dimensional schematic representation of two ATP@AgNP having solvent shell connected through H-bonds, (b) that of the indicated cross-section area in (a) showing solvent network attached with 4-ATP in between the two AgNPs, (c) loss of intra-nanoparticle solvent molecules (marked) in between 4-ATP molecules closest to the NP surface. (d) intra-nanoparticle DMAB formation, (e) cross-section area showing inter-nanoparticle solvent molecules attached with 4-ATP through H-bonds, (f) loss of inter-nanoparticle solvent molecules (marked), (g) inter-nanoparticle DMAB formation, (h) representation of DMAB@AgNP having bulk solvent molecules in the surroundings and (i) fully dried DMAB@AgNP.

H-bonded environment and the dielectric constant in the immediate vicinity of reaction centers. Moreover, atomic force microscopy (AFM) measurements shown in **Figure A3.10**, for both H_2O and D_2O, revealed that the nature of AgNP aggregates and morphology in the deposits at the laser probe area (where DMAB formation took place) were similar to the area where no laser radiation was shone. The laser power and reaction energy were unable to provide sufficient energy for reorganization of AgNPs upon DMAB formation. On the other hand, the dimensions of the aggregated AgNPs - both before and after reactions - were larger in the

TH_3719_186122105

deposits from D_2O dispersions (95 ± 20 nm) as compared to those obtained from H_2O dispersions (54 ± 5 nm).

3.4.4. Mechanism of inrananoparticle and internanoparticle reactions:

Finally, based on the above experimental results and DFT calculations we propose the following mechanism of two step DMAB formation at TPCL as shown in **Figure 3.3** when the liquid droplet was evaporating on a glass surface. At first, there was phase change of ATP@AgNPs from dispersion to deposit where each nanoparticle came close to each other with solvent molecule shell (**Figure 3.3a**). During the droplet evaporation, solvent molecules in between and H-bonded to intraparticle 4-ATP molecules on each AgNP surface move to the bulk (**Figure 3.3c**) followed by intraparticle DMAB formation (**Figure 3.3d**) leaving behind interparticle solvent molecules in plasmonic 'hot-spot' (**Figure 3.3e**). Then, the interparticle solvent moved to the bulk (**Figure 3.3f**) that was followed by interparticle DMAB formation (**Figure 3.3g**). After this, only bulk solvent molecules were present (**Figure 3.3h**) which then completely dried as shown in **Figure 3.3i**.

3.5. Conclusions

In summary, distinction of the plasmon catalyzed differing and sequential intra-nanoparticle and inter-nanoparticle reactions (with a ratio of rates of about 3) was achieved at the TPCL of an evaporating water droplet. The two-step reactions were preceded by a phase-transition leading to the deposition of the NPs. Elimination of water molecules H-bonded to 4-ATP for each step occurred before the reaction leading to the product formation. In D_2O medium, the ratio was about 1.8. DFT calculations accounted for the Raman signatures of the two-step reactions following loss of H-bonded water for each step. The results presented here may bring novel ways of carrying out plasmon-catalyzed chemical reactions especially those involving assembly formations.

3.6. References

1. Bender, M. L.; Neveu, M. C. Intramolecular Catalysis of Hydrolytic Reactions. IV. A Comparison of Intramolecular and Intermolecular Catalysis[1,2]. *J. Am. Chem. Soc.* **1958**, *20*, 5388-5391.
2. Ishizu, K.; Nunomura, M.; Fukutomi T. Kinetics of crosslinking reactions. 2. Reaction rates of intermolecular and intramolecular crosslinkings by using a soluble microgel. *J. Polym. Sci. A Polym. Chem.* **1987**, *25*, 1163-1175.

TH_3719_186122105

3. Nagy, P. I. Competing Intramolecular vs. Intermolecular Hydrogen Bonds in Solution. *Int. J. Mol. Sci.* **2014**, *15*, 19562-19633.
4. Wang, J.; Zheng, K.; Lin, B.; Weng, Y. A comparative study of inter- and intramolecular C-H aminations: mechanism and site selectivity. *RSC Adv.* **2017**, *7*, 34783-34794.
5. Tschaen, D. M.; Turos, E.; Weinreb, S. M. Stereochemical Studies of Thermal Intermolecular and Intramolecular *N*-Sulfonylimine Ene Reactions. *J. Org. Chem.* **1984**, *49*, 5058-5064.
6. Reber, K. P.; Tilley, S. D.; Sorensen, E. J. Bond formations by intermolecular and intramolecular trapping of acylketens and their applications in natural product synthesis. *Chem. Soc. Rev.* **2009**, *38*, 3022-3034.
7. Nalivela, K. S.; Rudolph, M.; Baeissa, E. S.; Alhogbi, B. G.; Mkhalid, I. A. I.; Hashmi, A. S. K. Sequential Au/Cu Catalysis: A Two Catalyst One-Pot Protocol for the Enantioselective Synthesis of Oxazole α-Hydroxy Esters *via* Intramolecular Cyclization/Intermolecular Alder-Ene Reaction. *Adv. Synth. Catal.* **2018**, *360*, 2183-2190.
8. Maneeprakorn, W.; Malik, M. A.; O'Brien, P. Developing Chemical Strategies for the Assembly of Nanoparticles into Mesoscopic Objects. *J. Am. Chem. Soc.* **2010**, *132*, 1780-1781.
9. Pal, S.; Dutta, A.; Paul, M.; Chattopadhyay, A. Plasmon-Enhanced Chemical Reaction at the Hot Spots of End-to-End Assembled Gold Nanorods. *J. Phys. Chem. C* **2020**, *124*, 3204-3210.
10. Liu, Y.; Yang, D.; Zhao, Y.; Yang, Y.; Wu, S.; Wang, J.; Xia, L.; Song, P. Solvent-controlled plasmon-assisted surface catalysis reaction of 4-aminothiophenol dimerizing to p,p´-dimercaptoazobenzene on Ag nanoparticles. *Heliyon* **2019**, *5*, e01545.
11. Zhang, Z.; Zhang, C.; Zheng, H.; Xu, H. Plasmon-Driven Catalysis on Molecules and Nanomaterials. *Acc. Chem. Res.* **2019**, *52*, 2506-2515.
12. Alekseeva, S.; Nedrygailov, I. I.; Langhammer, C. Single Particle Plasmonics for Materials Science and Single Particle Catalysis. *ACS Photonics* **2019**, *6*, 1319-1330.
13. Paul, S.; Chattopadhyay, A. Single Phase Transition Leads to the Nanoparticle Deposition in an Evaporating Sessile Droplet. *J. Phys. Chem. C* **2023**, *45*, 22401-22411.
14. Sheng, S.; Ji, Y.; Yan, X.; Wei, H.; Luo, Y.; Xu, H. Azo-Dimerization Mechanisms of *p*-Aminothiophenol and *p*-Nitrothiophenol Molecules on Plasmonic Metal Surfaces

TH_3719_186122105

Revealed by Tip-/Surface-Enhanced Raman Spectroscopy. *J. Phys. Chem. C* **2020**, *124*, 11586-11594.

15. Pal, S.; Paul, S.; Chattopadhyay, A. Enhanced solid-state plasmon catalyzed oxidation and SERS signal in the presence of transition metal cations at the surface of gold nanostructures. *Phys. Chem. Chem. Phys.* **2021**, *23*, 21808-21816.
16. Dadosh, T. Synthesis of uniform silver nanoparticle with a controllable size. *Materials Letters* **2009,** *63*, 2236-2238.
17. Frisch, M. J.; Trucks, G. W.; Schlegel, H. B.; Scuseria, G. E.; Robb, M. A.; Cheeseman, J. R.; Scalmani, G.; Barone, V.; Mennucci, B.; Petersson, G. A.; *et al*. *Gaussian 16*, Revision C.01; Gaussian, Inc.: Wallingford CT, **2016**.
18. Dennington, R.; Keith, T. A.; Millam, J. M. *GaussView*, Version 6.1; Semichem Inc., Shawnee Mission, KS, **2016**.
19. Perdew, J. P.; Burke, K.; Wang, Y. Generalized gradient approximation for the exchange-correlation hole of a many-electron system. *Phys. Rev. B* **1998**, *54*, 16533.
20. Ditchfield, R.; Hehre, W. J.; Pople, J. A. Self-Consistent Molecular Orbital Methods. 9. Extended Gaussian-type basis for molecular-orbital studies of organic molecules. *J. Chem. Phys.* **1971**, *54*, 724.
21. Hay, P. J.; Wadt, W. R.; *Ab initio* effective core potentials for molecular calculations. Potentials for the transition metal atoms Sc to Hg. *J. Chem. Phys.* **1985**, *82*, 270-283.
22. de Barros, A.; Shimizu, F. M.; de Oliveira, C. S.; Sigoli, F. A.; dos Santos, D. P.; Mazali, I. O. Dynamic Behavior of Surface-Enhanced Raman Spectra for Rhodamine 6G Interacting with Gold Nanorods: Implication for Analyses under Wet versus Dry Conditions. *ACS Appl. Nano Mater.* **2020**, *3*, 8138-8147.
23. Ojea-Jiménez, I.; Romero, F. M.; Bastús, N. G.; Puntes, V. Small Gold Nanoparticles Synthesized with Sodium Citrate and Heavy Water: Insights into the Reaction Mechanism. *J. Phys. Chem. C* **2010**, *114*, 1800-1804.

TH_3719_186122105

Appendix of Chapter 3 (A3):

A3.1. UV-vis spectra of Cit@AgNPs and ATP@AgNPs:

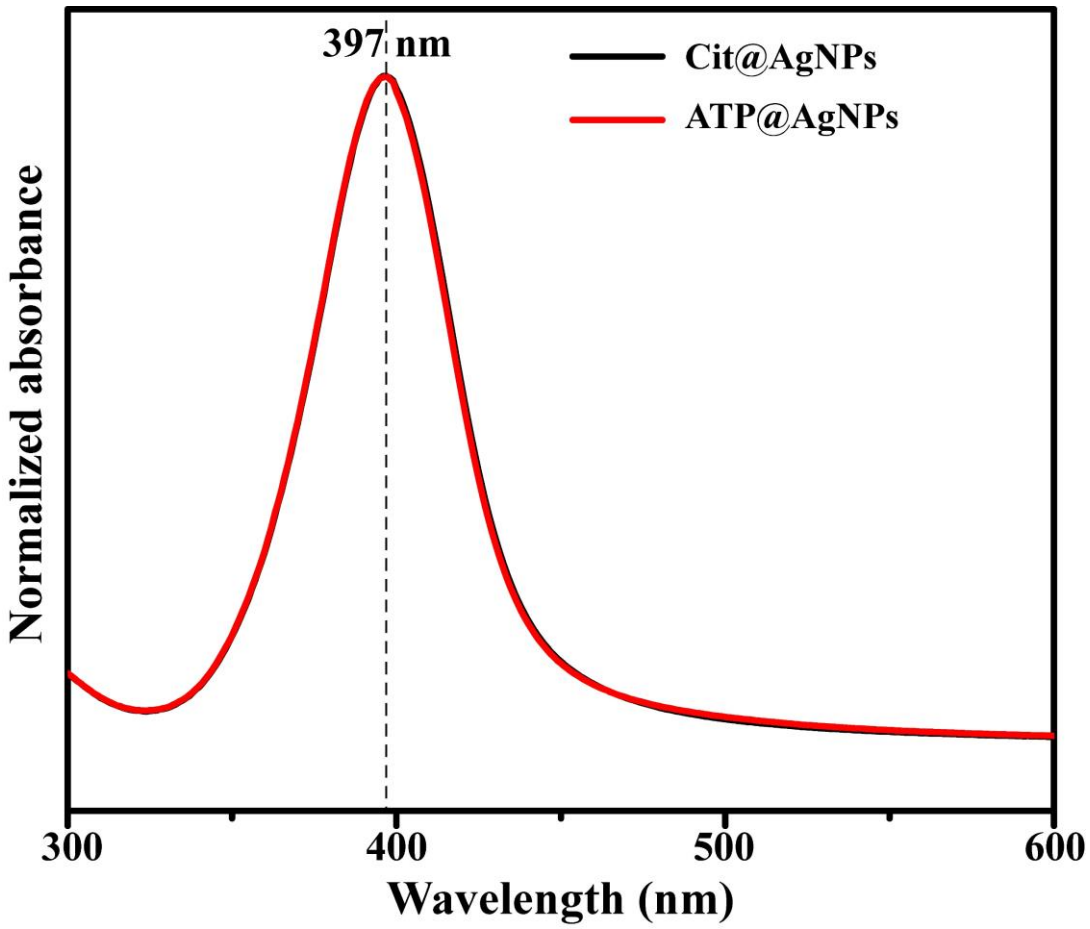

Figure A3.1: UV-vis spectra of Cit@AgNPs and ATP@AgNPs dispersions.

TH_3719_186122105

A3.2. TEM images and SAED of Cit@AgNPs and ATP@AgNPs:

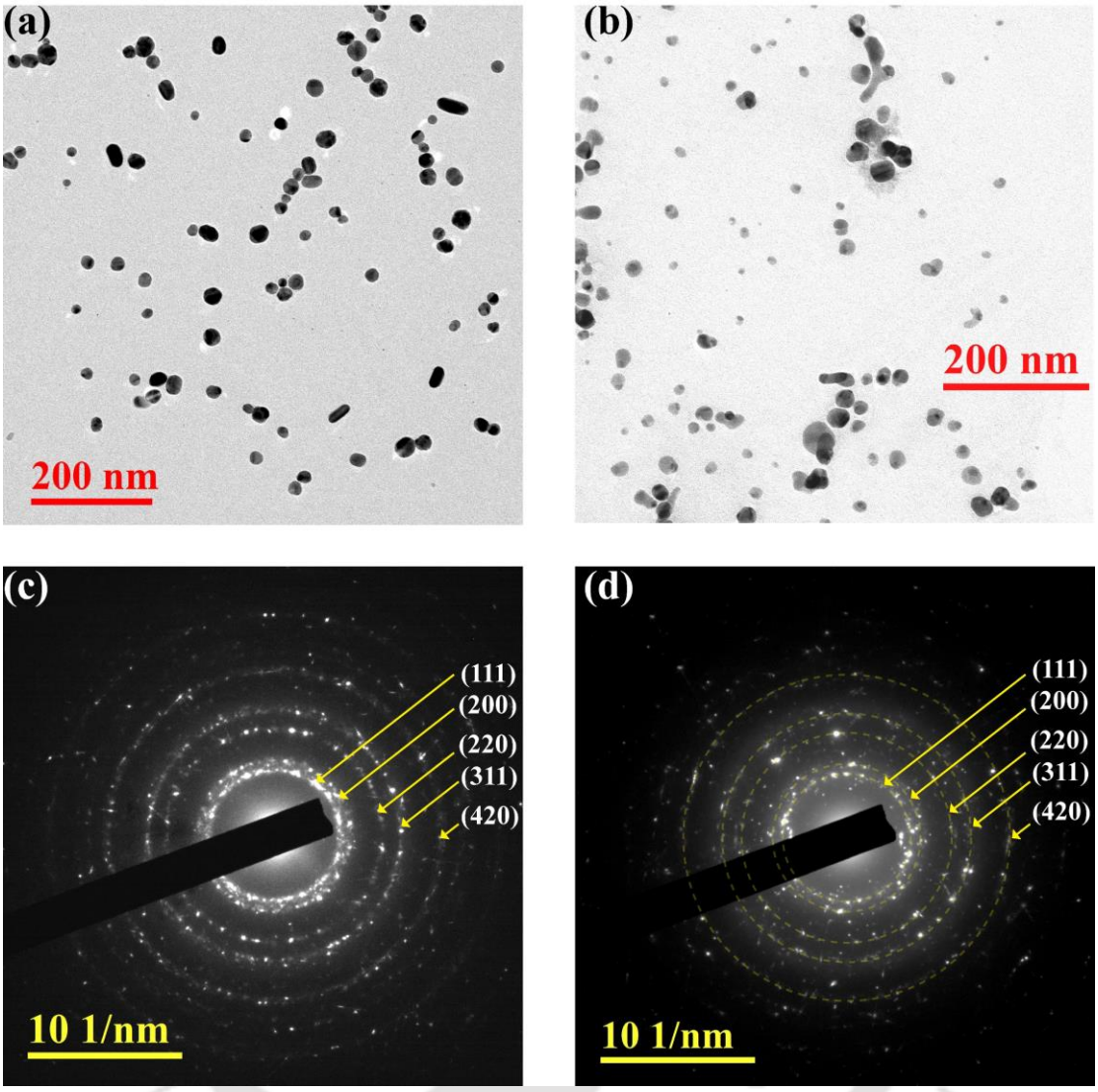

Figure A3.2: (a) and (b) TEM images of Cit@AgNPs and ATP@AgNPs, respectively. (c) and (d) SAED of Cit@AgNPs and ATP@AgNPs, respectively.

TH_3719_186122105

A3.3. Time dependent variation of experimentally obtained Raman peak intensities in H_2O:

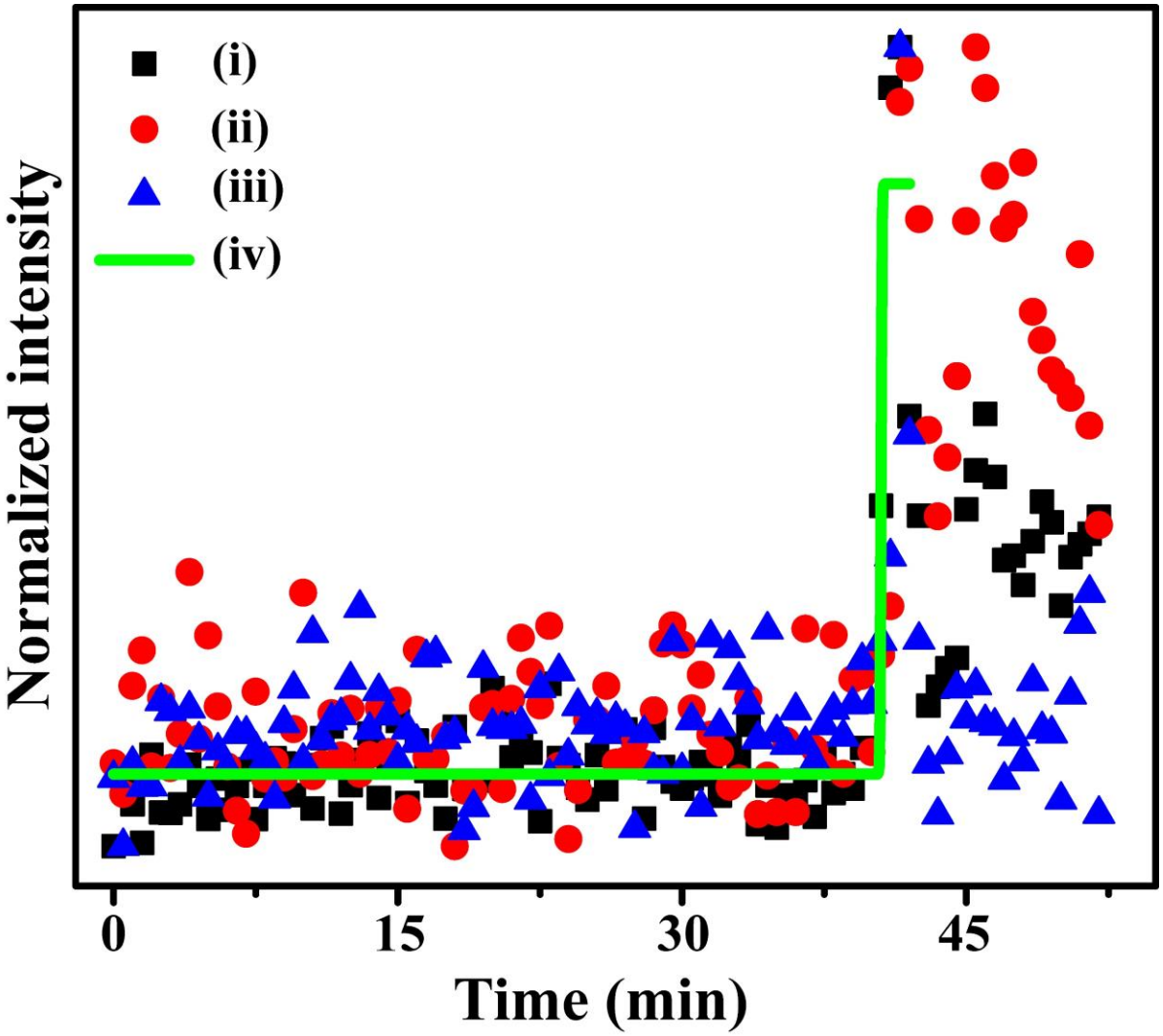

Figure A3.3: Variation of (i) 1078 cm^{-1}, (ii) 1434 cm^{-1} and (iii) 946 cm^{-1} Raman peak intensities with time of experimentally obtained Raman spectra at the TPCL, of the evaporating droplet containing ATP@AgNPs dispersion in H_2O. (iv) Boltzmann fitting of the variation of 1078 cm^{-1} peak intensity with time showing phase transition.

TH_3719_186122105

A3.4. Time dependent variation of experimentally obtained Raman peak intensities in D_2O:

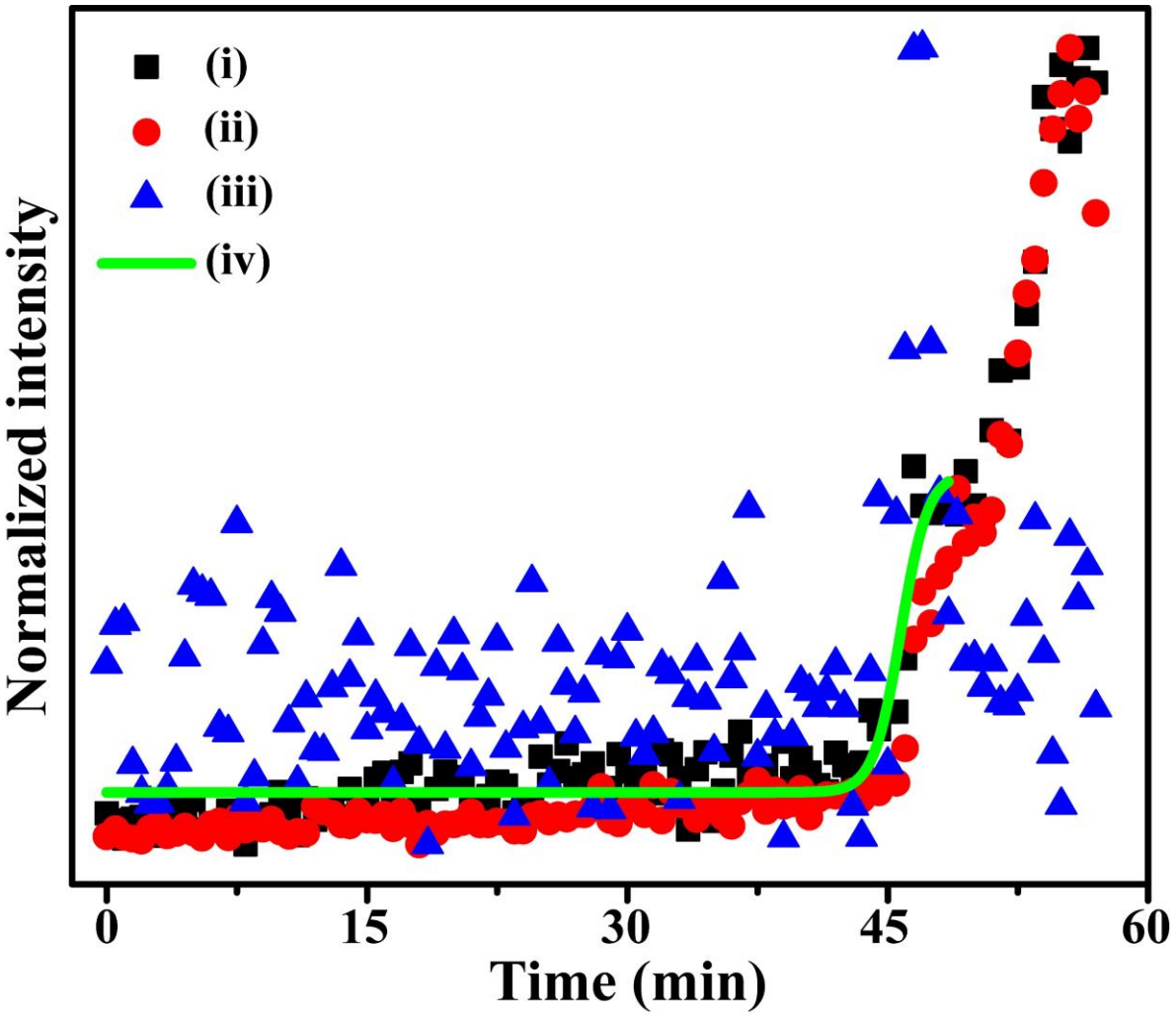

Figure A3.4: Variation of (i) 1078 cm^{-1}, (ii) 1434 cm^{-1} and (iii) 949 cm^{-1} Raman peak intensities with time of experimentally obtained Raman spectra at the TPCL of the evaporating droplet containing ATP@AgNPs dispersion in D_2O. (iv) Boltzmann fitting of the variation of 1078 cm^{-1} peak intensity with time showing phase transition.

TH_3719_186122105

A3.5. Table A3.1: Vibration assignment of major Raman peaks of 4-ATP and DMAB on AgNP surface:[1]

Raman peaks of 4-ATP (cm^{-1})	Raman peaks of DMAB (cm^{-1})	Vibration
946	–	$\nu(C=C)_{ring} + \nu(O-H)$ (This work)
949	–	$\nu(C=C)_{ring} + \nu(O-D)$ (This work)
1078	1078	$\nu(C=C)_{ring} + \nu(C-S)$
–	1140	$\nu(C=N) + \beta(C-H)$
–	1390	$\nu(N=N) + \nu(C=N)$
–	1434	$\nu(N=N) + \beta(C-H)$
–	1581	$\nu(C=C)_{ring}$
1590	–	$\nu(C=C)_{ring} + \delta NH_2$

TH_3719_186122105

A3.6. Lorentzian fittings of the experimentally obtained Raman spectrum:

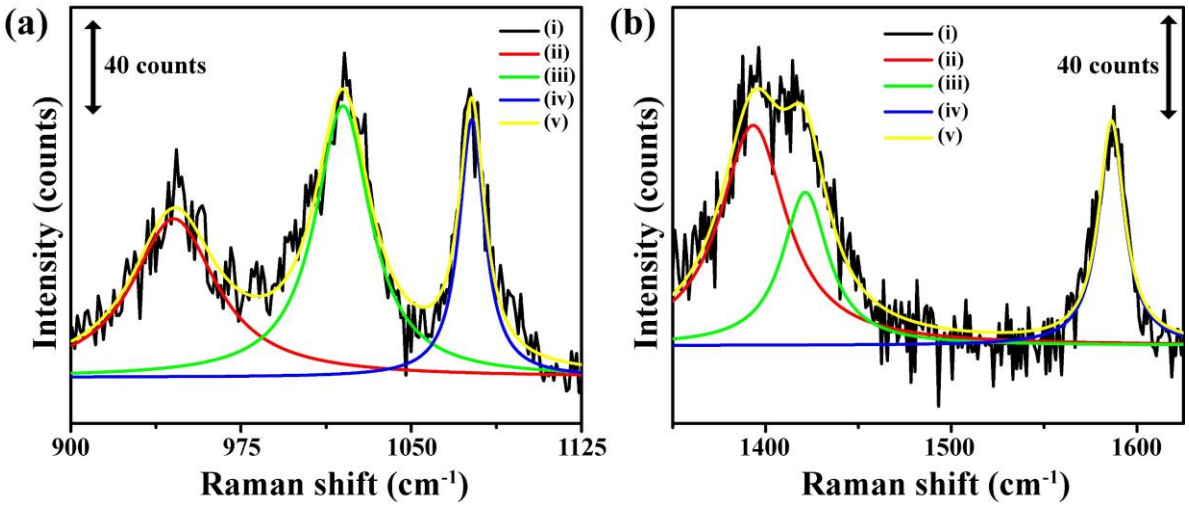

Figure A3.5: Lorentzian fittings of experimentally obtained Raman spectrum (a) from 900 - 1125 cm^{-1} and (b) from 1350 - 1625 cm^{-1} ranges recorded at 41.5 min (**Figure 3.1a** in Chapter-3). (a), (i) Experimental spectrum, (ii) fitted peak at 946 cm^{-1}, (iii) fitted peak at 1020 cm^{-1}, (iv) fitted peak at 1078 cm^{-1} and (v) cumulative fit (adj. R-square: 0.89). (b), (i) Experimental spectrum, (ii) fitted peak at 1393 cm^{-1}, (iii) fitted peak at 1421 cm^{-1}, (iv) fitted peak at 1590 cm^{-1} and (v) cumulative fit (adj. R-square: 0.92). The shift in the 1434 cm^{-1} to 1421 cm^{-1} was due to the presence of H-bonded H_2O molecules.

Other experimentally obtained spectra were also fitted similarly.

A3.7. Presence of bulk water after completion of DMAB formation in second step:

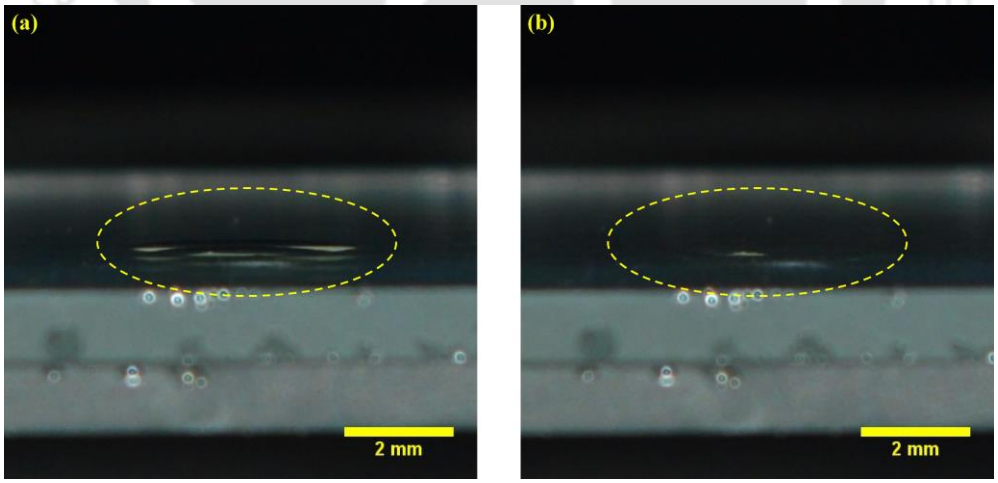

Figure A3.6: (a) Image of the droplet at 46.0 min showing presence of bulk water after complete DMAB formation in second step. (**Figure 3.1c** in Chapter 3). (b) Image of the fully dried deposit at 52 min.

TH_3719_186122105

A3.8. Eigenvector (or displacement vector) of the vibrations of 4-ATP with H_2O or D_2O on Ag surface:

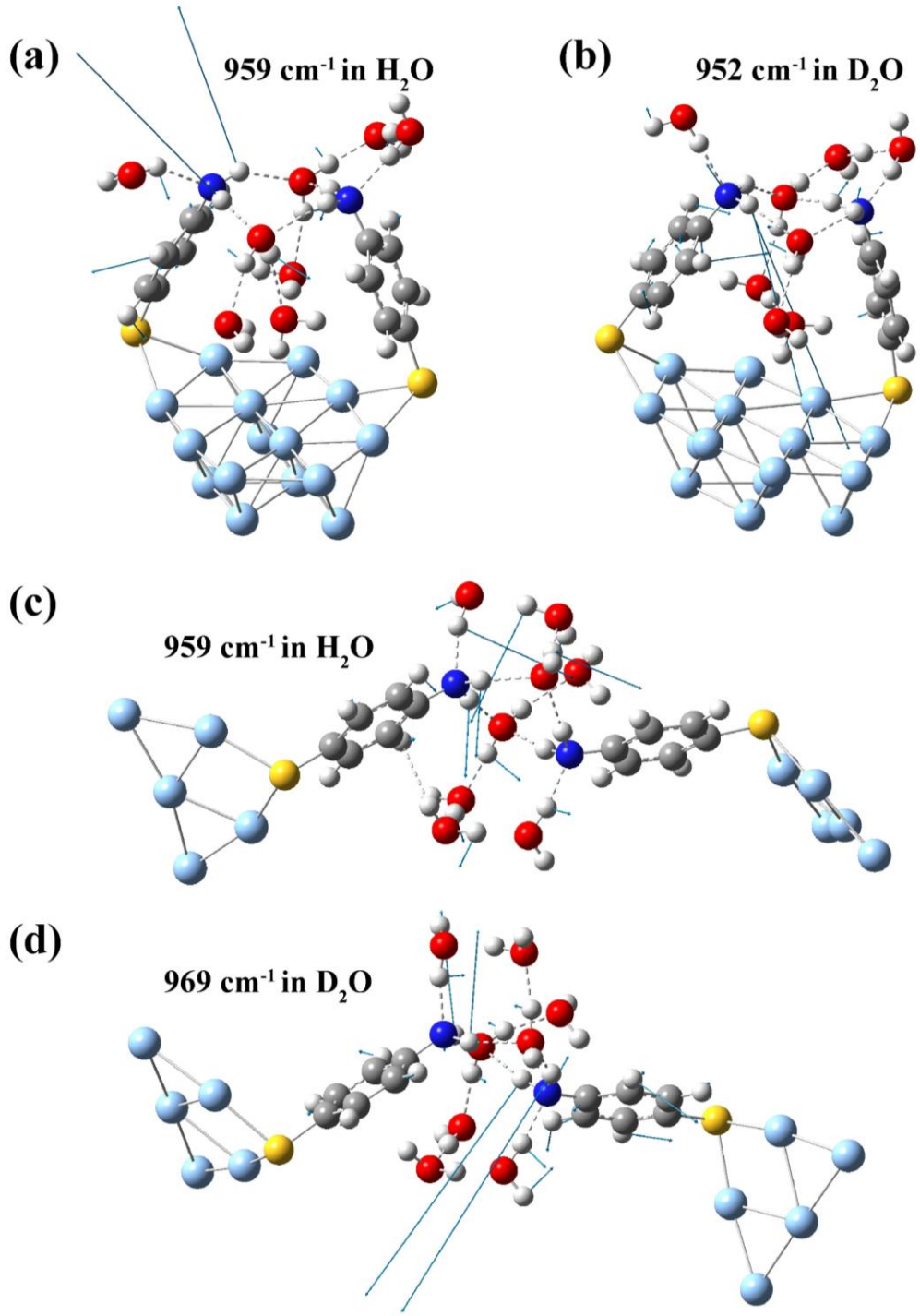

Figure A3.7: Eigenvectors or displacement vectors of the collective vibrations of 4-ATP and solvent for (a) intraparticle H_2O, (b) intraparticle D_2O, (c) interparticle H_2O and (d) interparticle D_2O, respectively, corresponding to the Raman peaks. Red, blue, gray, yellow, cyan and white atoms are O, N, C, S, Ag and H or D, respectively.

TH_3719_186122105

A3.9. Optical images of droplets evaporation at different times:

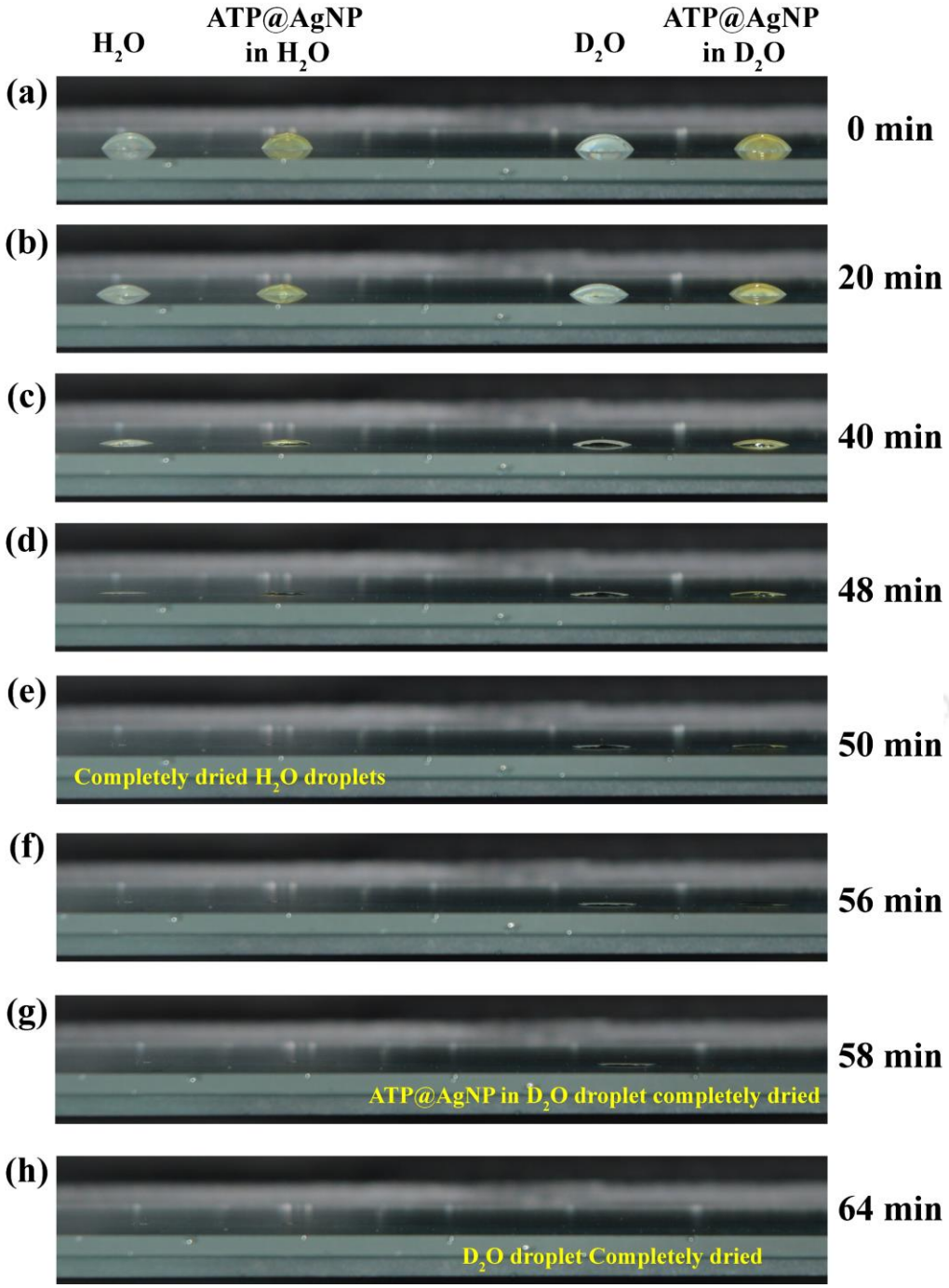

Figure A3.8: Optical images of evaporating 5 µL droplets of H_2O, H_2O containing ATP@, D_2O and D_2O containing ATP@AgNP recorded at (a) 0 min, (b) 20 min, (c) 40 min, (d) 48 min, (e) 50 min, (f) 56 min, (g) 58 min and (h) 64 min, respectively. Droplets were evaporated at 22 °C and 68% relative humidity. Both H_2O and H_2O containing ATP@AgNP droplets evaporated completely by 50 min. The droplet containing ATP@AgNP in D_2O had evaporated by 58 min. Interestingly, only D_2O droplet evaporated fully at 64 min.

TH_3719_186122105

A3.10. H/D exchange at the amine group of 4-ATP in D_2O solvent:

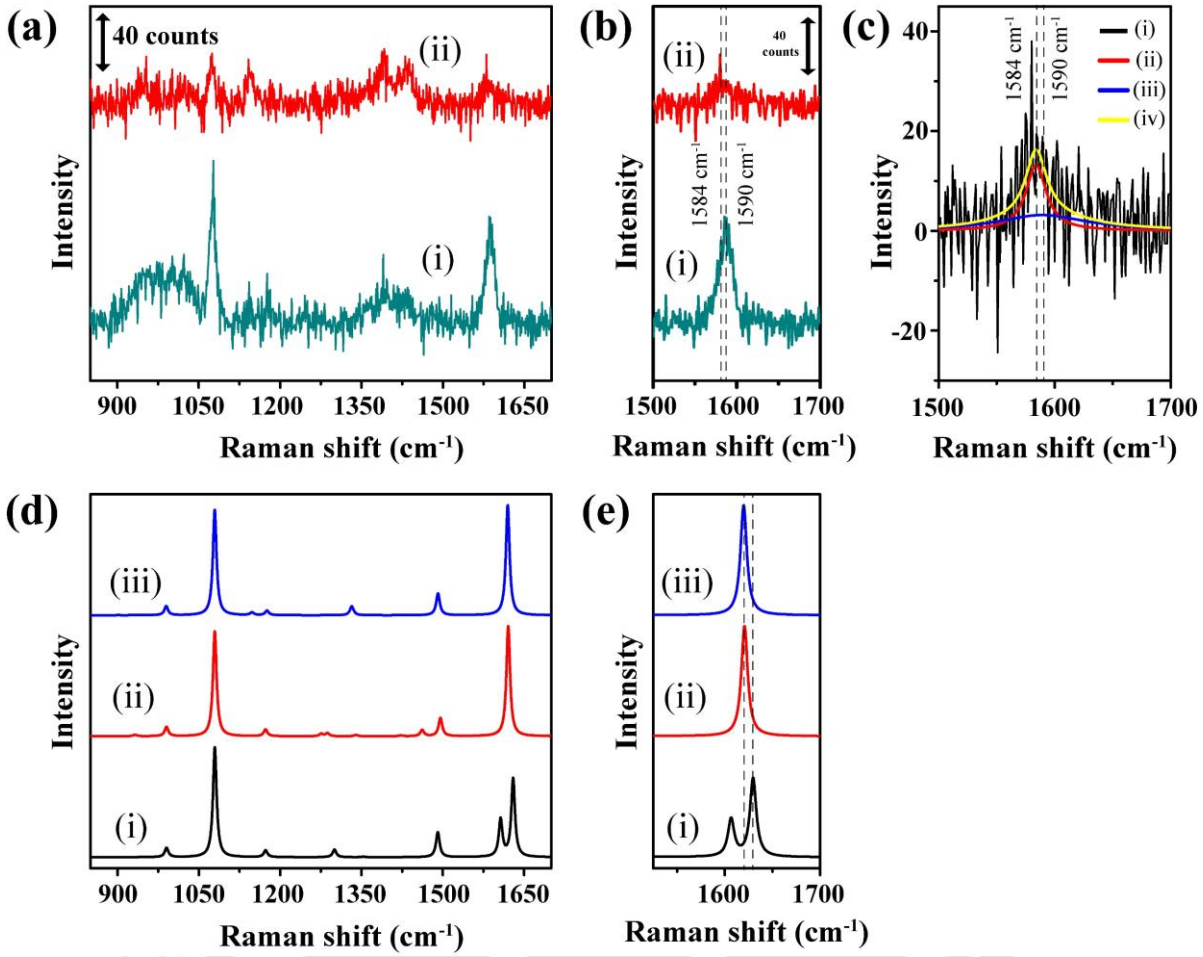

Figure A3.9: (a) Raman spectra at TPCL of evaporating droplets containing ATP@AgNP (i) in H_2O at 40.5 min (**Figure 3.1(a)** in the Chapter 3) and (ii) in D_2O at 45.5 min (**Figure 3.1(d)** in the Chapter 3). (b) Expanded Raman spectra of (a) from 1500 cm^{-1} to 1700 cm^{-1} showing red-shift of peak position from 1590 cm^{-1} to 1584 cm^{-1} as in (i) and (ii), respectively. (c) (i) Experimental Raman spectrum, (ii) fitted plot having peak at 1584 cm^{-1}, (iii) fitted plot having peak at 1590 cm^{-1} and (iv) cumulative fitted spectrum of b(ii). (d) Calculated Raman spectra of (i) Ag-ATP(NH_2), (ii) Ag-ATP(NHD) and (iii) Ag-ATP(ND_2), respectively. (e) Expanded spectra from 1525 cm^{-1} to 1700 cm^{-1} of (d) showing red-shifting of the peak position from (i) to (iii).

As evidenced from **Table A3.1**, the Raman peak at 1590 cm^{-1} for ATP@AgNP in water was due to collective stretching C=C bond and NH_2 bending vibrations. At the earlier stages of drying, when there were appearances of noticeable Raman signal of 4-ATP on AgNP surface at 40.5 min in H_2O and 45.5 min in D_2O (**Figure 3.1** in Chapter 3), red-shift of the vibrational signature from 1590 cm^{-1} to 1584 cm^{-1} was observed in D_2O medium. As shown in **Figure A3.9(c)**, this broad peak consisted of mostly 1584 cm^{-1} peak and contribution of 1590 cm^{-1} peak was low. DFT calculated Raman spectra in **Figure A3.9(d)** and **Figure A3.9(e)** suggested similar red-shift of the peak because of H/D exchange. Hence, H/D exchange was the key factor for the experimentally observed red-shift of the same vibrational signature in D_2O medium. These results confirmed the H/D isotope exchange at the amine group of 4-ATP in D_2O solvent,

TH_3719_186122105

which resulted in early evaporation of D_2O containing ATP@AgNP compared to only D_2O as shown in **Figure A3.8**.

A3.11. AFM images of the AgNPs deposited in H_2O and D_2O:

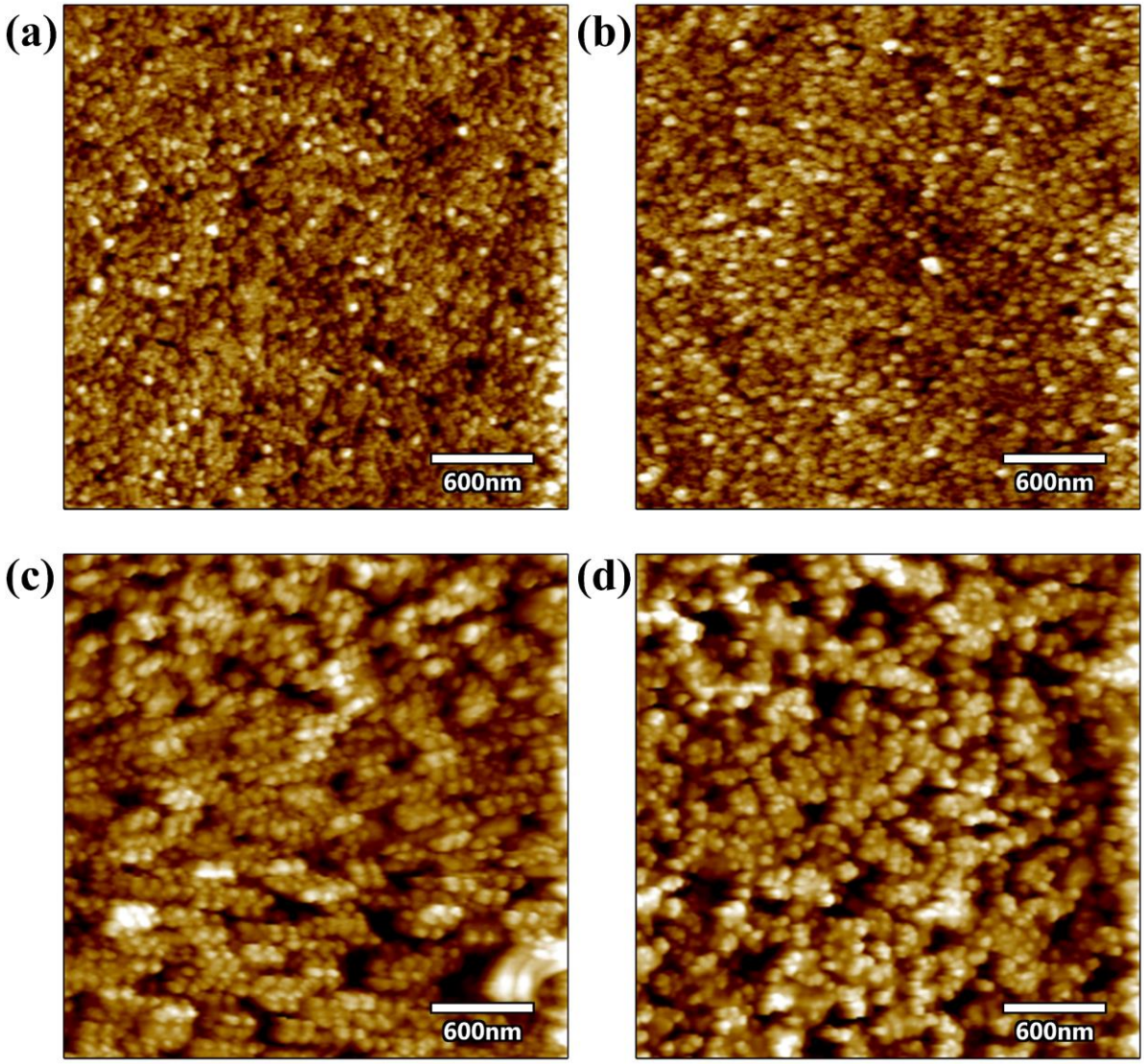

Figure A3.10: AFM images of the AgNPs depositions (a) at the laser probe area where DMAB formation took place following evaporation of H_2O, (b) at the area, which was not irradiated with laser light following evaporation of H_2O, (c) at the laser probe area where DMAB formation took place following evaporation of D_2O, and (b) at the area, which was not irradiated with laser light following evaporation of D_2O. The average size of AgNP aggregates were 54 ± 5 nm and 95 ± 20 nm in H_2O and D_2O, respectively.

TH_3719_186122105

A3.12. Experiment-3: Reproduction of results of the two-step DMAB formation at TPCL in H_2O

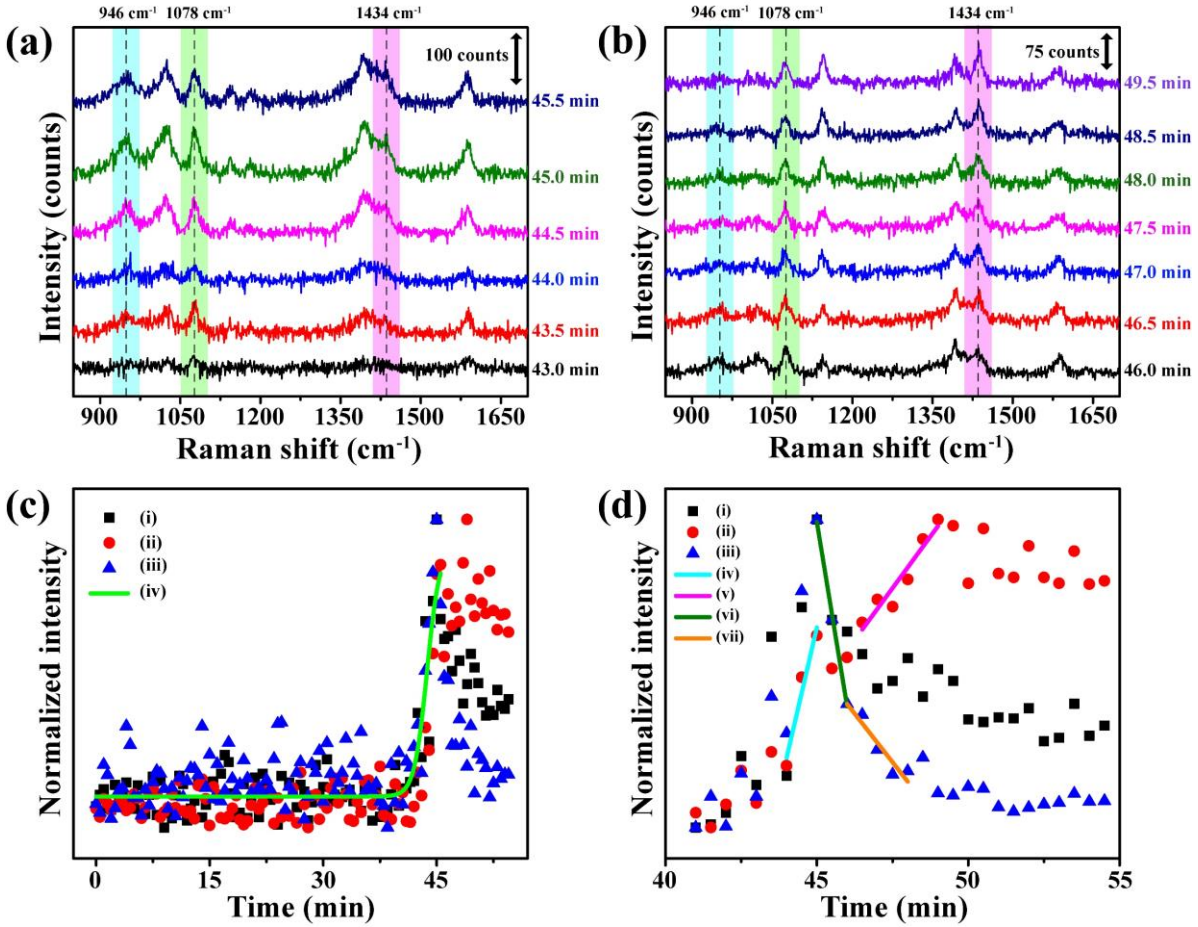

Figure A3.11: (a), (b) Raman spectra at TPCL of evaporating droplet at different times, (c) variation of (i) 1078 cm^{-1}, (ii) 1434 cm^{-1} and (iii) 946 cm^{-1} Raman peak intensities with time from experimentally obtained Raman spectra, (iv) Boltzmann fitting of the variation of 1078 cm^{-1} peak with time, (d) variation of (i) 1078 cm^{-1}, (ii) 1434 cm^{-1} and (iii) 946 cm^{-1} Raman peak intensities (from Lorentzian fittings of experimental spectra) with time, (iv), (v) and (vi), (vii) are linear fittings of the variations of intensities with time of 1434 cm^{-1} and 946 cm^{-1} peaks, respectively.

TH_3719_186122105

A3.13. Experiment-4: Reproduction of results of the two-step DMAB formation at TPCL in H_2O

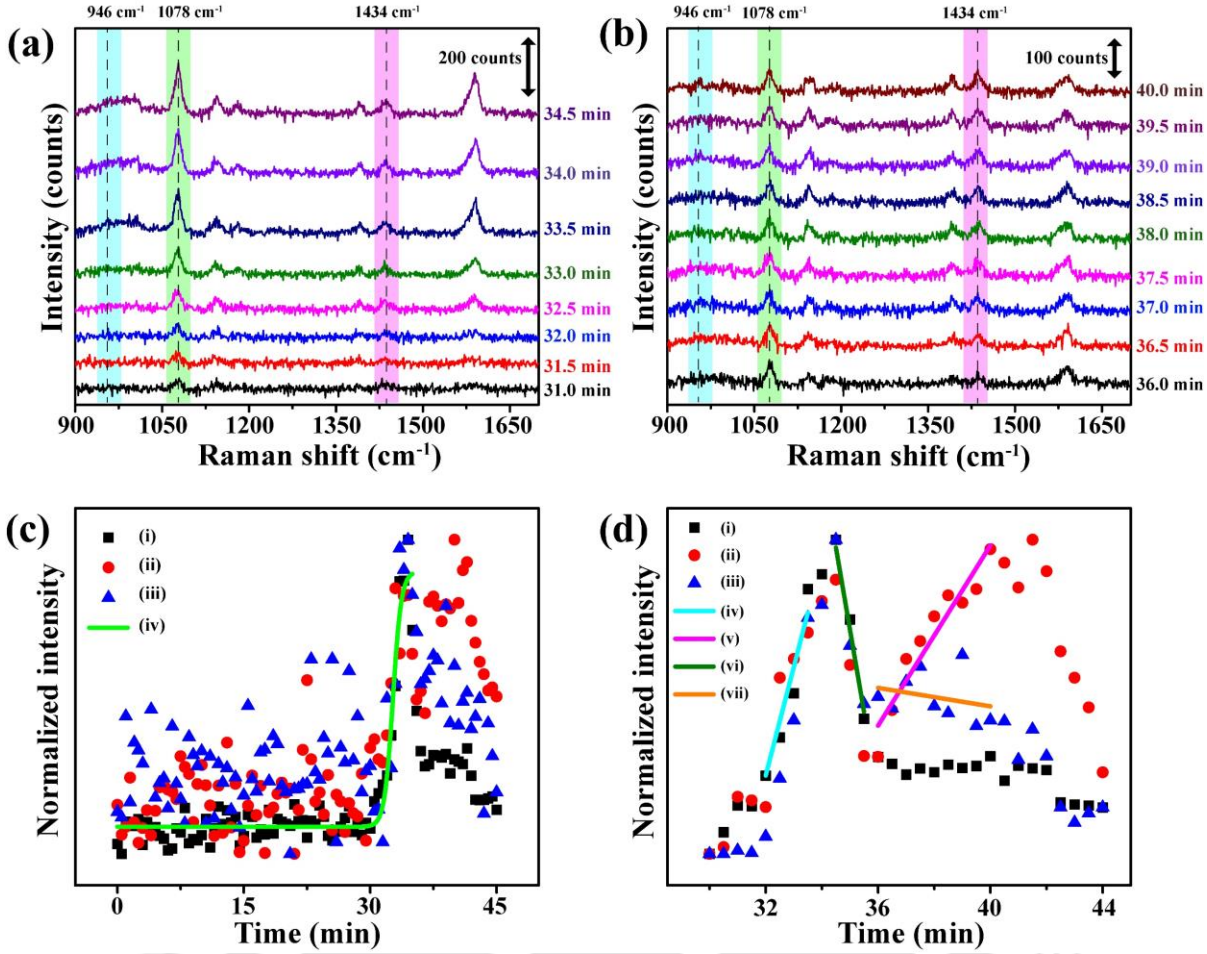

Figure A3.12: (a), (b) Raman spectra at TPCL of evaporating droplet at different times, (c) variation of (i) 1078 cm^{-1}, (ii) 1434 cm^{-1} and (iii) 946 cm^{-1} Raman peak intensities with time from experimentally obtained Raman spectra, (iv) Boltzmann fitting of the variation of 1078 cm^{-1} peak with time, (d) variation of (i) 1078 cm^{-1}, (ii) 1434 cm^{-1} and (iii) 946 cm^{-1} Raman peak intensities (from Lorentzian fittings of experimental spectra) with time, (iv), (v) and (vi), (vii) are linear fittings of the variations of intensities with time of 1434 cm^{-1} and 946 cm^{-1} peaks, respectively.

TH_3719_186122105

A3.14. Experiment-7: Reproduction of results of the two-step DMAB formation at TPCL in D_2O

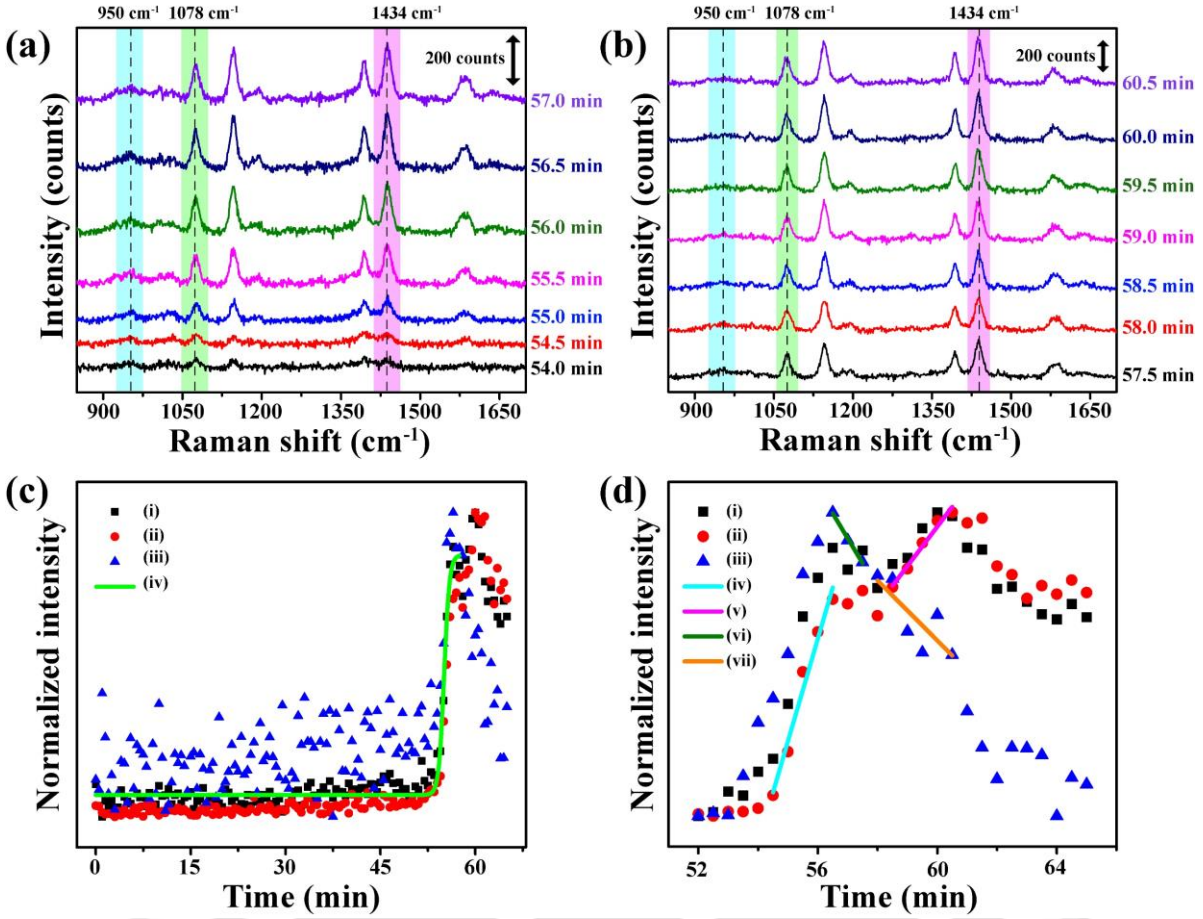

Figure A3.13: (a), (b) Raman spectra at TPCL of evaporating droplet at different times, (c) variation of (i) 1078 cm^{-1}, (ii) 1434 cm^{-1} and (iii) 950 cm^{-1} Raman peak intensities with time from experimentally obtained Raman spectra, (iv) Boltzmann fitting of the variation of 1078 cm^{-1} peak with time, (d) variation of (i) 1078 cm^{-1}, (ii) 1434 cm^{-1} and (iii) 950 cm^{-1} Raman peak intensities (from Lorentzian fittings of experimental spectra) with time, (iv), (v) and (vi), (vii) are linear fittings of the variations of intensities with time of 1434 cm^{-1} and 950 cm^{-1} peaks, respectively.

TH_3719_186122105

A3.15. Experiment-8: Reproduction of results of the two-step DMAB formation at TPCL in D_2O

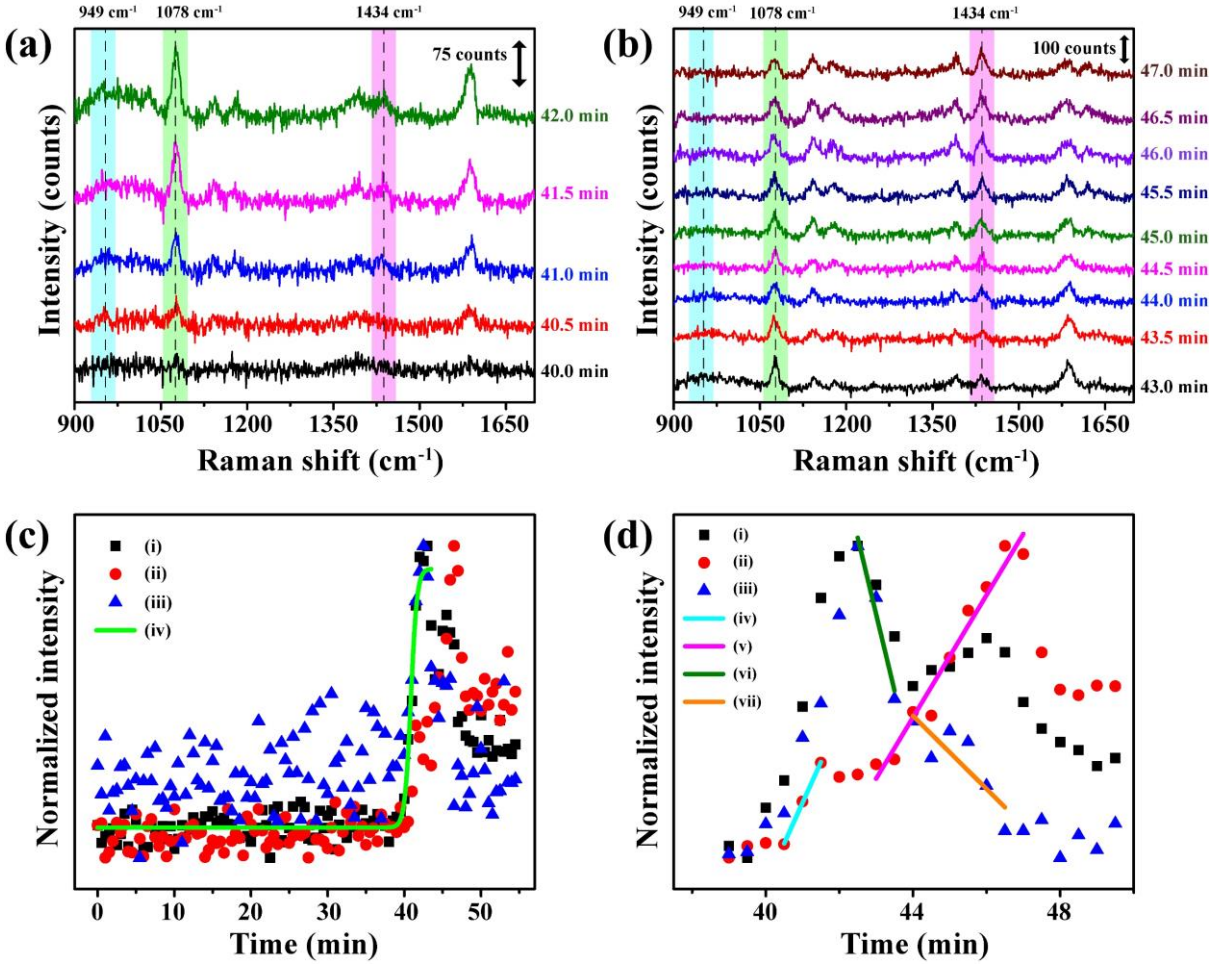

Figure A3.14: (a), (b) Raman spectra at TPCL of evaporating droplet at different times, (c) variation of (i) 1078 cm^{-1}, (ii) 1434 cm^{-1} and (iii) 949 cm^{-1} Raman peak intensities with time from experimentally obtained Raman spectra, (iv) Boltzmann fitting of the variation of 1078 cm^{-1} peak with time, (d) variation of (i) 1078 cm^{-1}, (ii) 1434 cm^{-1} and (iii) 949 cm^{-1} Raman peak intensities (from Lorentzian fittings of experimental spectra) with time, (iv), (v) and (vi), (vii) are linear fittings of the variations of intensities with time of 1434 cm^{-1} and 949 cm^{-1} peaks, respectively.

TH_3719_186122105

A3.16. Table A3.2: Rate of DMAB formation in two steps at TPCL on evaporating droplets containing H_2O:

Experiments	Rate of intraparticle DMAB formation (R_1) (a. u.)	Rate of interparticle DMAB formation (R_2) (a. u.)	R_1/R_2	Average R_1/R_2
Experiment-1	93.3	26.2	3.56	**3.04 ± 0.38**
Experiment-3	42.3	13.4	3.16	
Experiment-4	34.5	14.3	2.41	
Experiment-5	19.2	6.0	3.20	
Experiment-6	16.3	5.7	2.86	

A3.17. Table A3.3: Rate of DMAB formation in two steps at TPCL on evaporating droplets containing D_2O:

Experiments	Rate of intraparticle DMAB formation (R_1) (a. u.)	Rate of interparticle DMAB formation (R_2) (a. u.)	R_1/R_2	Average R_1/R_2
Experiment-2	20.9	14.1	1.48	**1.75 ± 0.37**
Experiment-7	33.7	15.4	2.19	
Experiment-8	26.5	19.1	1.39	
Experiment-9	45.0	20.4	2.21	
Experiment-10	43.7	29.5	1.48	

19. References:

1. Huang, Y.-F.; Wu, D.-Y.; Zhu, H.-P., Zhao, L.-B.; Liu, G.-K.; Ren, B.; Tian, Z.-Q. Surface-enhanced Raman spectroscopic study of p-aminothiophenol. *Phys. Chem. Chem. Phys.* **2012**, *14*, 8485–8497.

TH_3719_186122105

Chapter-4

Multistep Phase Transition and Molecular Reaction of Plasmonic Nanoparticles at the Three-Phase Contact Line of an Evaporating Sessile Droplet

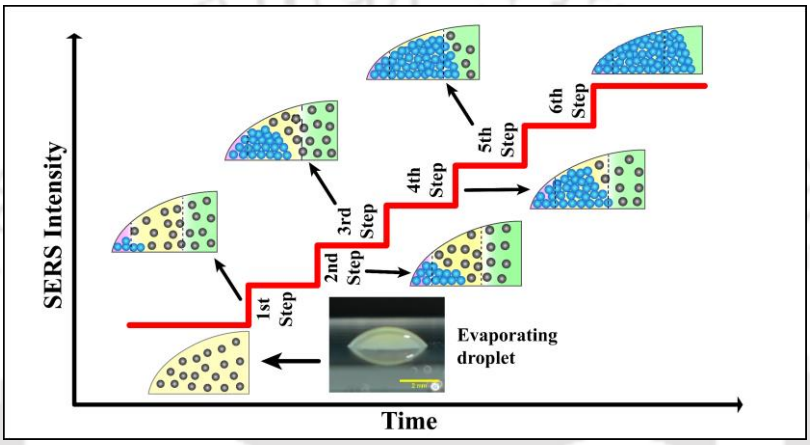

Chapter 4 *illustrates the pH dependent phase transition and reaction in an aqueous droplet of 4-aminothiophenol (ATP) functionalized Ag nanoparticles (AgNPs) dispersion at the three-phase contact line (TPCL) using surface-enhanced Raman spectroscopy (SERS) and atomic force microscopy (AFM). The results indicated that at pH 7.0, single phase transition led deposition followed by photochemical reaction occurred at the outer, middle and inner boundaries of the deposited ring. On the other hand, at pH 9.4, the dominant observation was the product formation of 4,4´-dimercaptoazobenzene (DMAB) preceding phase transition led depositions at all the three positions of the ring. Importantly, at pH 8.4, several steps of simultaneous product formation and depositions were the most prominent at the centre of the deposited ring, while smaller number of steps or single-step similar events were observed to have occurred at the inner and outer peripheries of the ring. AFM images evidenced the step-wise depositions leading the changes in the height and width of the ring with time.*

The content of Chapter 4 has been published in *The Journal of Physical Chemistry C,* a journal of the American Chemical Society (ACS). *J. Phys. Chem. C* **2025**, *129*, 8, 4250–4260

https://pubs.acs.org/doi/full/10.1021/acs.jpcc.4c08222

TH_3719_186122105

4.1. Introduction

Evaporation of sessile droplets leading to depositions of the dispersed solids in the form of ring[1], a seemingly well-understood phenomenon, continues to reveal important results about the nature of particle settlement that are relevant to the latest printing technology[2]. For example, our recent studies had shown that nanoscale particle deposition at the three-phase contact line (TPCL) occurs through a phase transition as opposed to the well-known model of continuous deposition.[3] Further experiments also unraveled the difference in intrananoparticle and internanoparticle plasmon-catalyzed reaction kinetics that is possibly not addressable in ordinary liquid dispersion.[4] Interestingly, the study also revealed that water molecules that are H-bonded to the reactant molecules on the surface of the same nanoparticle leave the deposited particle before the water molecules that are bonded to two different nanoparticles. This forms the basis of differing kinetics of reactions mentioned above.[4]

In application such as printed electronics[5], chemical sensors[6], solar cells[7], display pixels[8], supercapacitors [9], and wearable[10], flexible and stretchable devices[11], the speed and quality of inkjet printing of liquid droplets drives the technology. On the other hand, in healthcare applications, the nature of printed biomolecular sensing elements[12], cells (including stem cells) [13], DNA microarrays [14], and tissues[15], and the precision in intermolecular interactions between the target elements decide the quality of the outcome[16]. The importance of applications has driven research in controlling the evaporation-induced particle depositions as have been achieved by varying temperature[17], humidity[18], viscosity[19], the roughness of the solid substrate[20], surfactants[21], size[20], and shape of the particles[22]. In this regard, printing of nanoscale particles and their functionalized counterparts into well-defined arrays is of great consequence in the current developments in droplet-based printing.[23,24] Thus, understanding the mechanisms of depositions of molecule functionalized nanoparticles and the nature of the depositions may reveal intriguing results that would be relevant not only to science but also technology.

Spectroscopic techniques offer potent means of pursuing nanoparticle and molecular level understanding of a dynamic system such as an evaporating droplet. A well-established method that could be utilized in order to pursue the nanoparticle deposition behavior at the pinned contact line is surface enhanced Raman spectroscopy (SERS).[25] The technique not only takes advantage of the enhancement of Raman scattering intensity due to the plasmon field of the nanoparticle but also of the hot-spots generated due to interacting nanoparticles.[26] Thus,

TH_3719_186122105

reaction kinetics between the molecules on the surface of a single nanoparticle could be differentiated from that occurring between molecules on the surfaces of adjacent and interactive nanoparticles.[4] In addition, the nature of the depositions could be studied using atomic force microscopic (AFM) techniques.[3] Although our recent results[4] suggest that intrananoparticle and internanoparticle reactions of 4-aminothiophenol (4-ATP) to 4,4´-dimercaptoazobenzene (DMAB) occur following depositions of the Ag nanoparticles on the substrate surface at the initial pH 7 of the droplet, the mechanism could be different at other pH especially under alkaline conditions. Thus, further studies could shed new lights on plasmon catalyzed reactions in an evaporating droplet and also on the nature of depositions of particle functionalized with the molecules.

4.2. Outline of the Present Work

We report that evaporation induced particle deposition at the TPCL of a sessile droplet, containing photochemically reactive Ag nanoparticles, involved multiple steps of reaction and deposition that varied across the deposited ring – depending on the initial pH of the medium. For example, at pH 7, the 4-ATP functionalized AgNPs (ATP@AgNPs) underwent (typically) single phase transition-based deposition that was followed by photochemical reaction to DMAB formation, when probed at the outer, middle and inner rings, respectively. On the other hand, at pH 8.4, the particles first reacted in the dispersion phase and were then deposited with both occurring in steps with the largest number of steps in the middle ring. Further, at pH 9.4, the reaction in the dispersion phase preceded deposition with virtually no steps of separation between them across the ring. The reactions and depositions were probed by SERS, that also helped in the photochemical reactions, and atomic force microscopy that clearly revealed changes in height and width profiles of the deposited rings especially in the case of step-wise depositions. The results indicated a rich interplay of physics and chemistry of particle reaction and deposition in droplet evaporation of reactive nanoparticles.

4.3. Experimental Section

4.3.1. Materials:

Silver nitrate, 99% ($AgNO_3$), tannic acid and 4-aminothiophenol, 97% (4-ATP) were bought from Sigma Aldrich. Trisodium citrate dihydrate, sodium hydroxide, acetone, methanol, nitric acid (98%) and hydrochloric acid (35%) were purchased from Merck India. Without further purification, all the chemicals were utilized as purchased. Milli-Q grade water was employed

TH_3719_186122105

for washing and all other experimental purposes. All the glass apparatuses were cleaned using aqua regia followed by rinsing and washing with Milli-Q water and acetone.

4.3.2. Instruments and Characterizations:

UV-Vis absorbance spectra were recorded using PerkinElmer® Lambda 365+ UV-Vis spectrometer. Transmission electron microscopic (TEM) images and selected-area electron diffractions (SAED) were obtained from JEOL JEM-2100F field emission transmission electron microscope (FETEM) instrument having acceleration voltage of 200 kV. FETEM samples were prepared by drop-casting 7 µL of AgNP dispersions on carbon-coated copper grids. Raman spectra were recorded using Horiba LabRAM HR Evolution Raman spectrometer attached with 633 nm laser source. Atomic force microscopic (AFM) measurements on the dried deposits were performed using Oxford Asylum Research Model: MFP-3D instrument. Zeta potential measurements were performed using Malvern Zetasizer Nano ZS-90 instrument and zeta potential value was averaged after six measurements each of which included 10 cycles. Reaction scheme was drawn using ChemDraw software. All the graphs were plotted and fitted in Origin 9.0 pro software.

4.3.3. Synthesis of citrate capped silver nanoparticles (Cit@AgNPs): Cit@AgNPs were synthesized using previously reported method.[27] Briefly, in two separate round bottom flasks, 40 mg of trisodium citrate dihydrate and 10 mg of $AgNO_3$ were dissolved in 20 mL and 80 mL Milli-Q water, respectively. 20 µL aqueous 3.0 (mM) tannic acid solution was added in the trisodium citrate solution. The two flasks were stirred and heated up to 65 °C. Then the hot mixture of trisodium citrate and tannic acid was added at a time to the stirring solution of $AgNO_3$ at 65 °C and stirred vigorously. When the color of the solution became yellowish in about 5 to 10 min, the temperature was increase to 110 °C and the mixture was boiled for 20 min. Appearance of dark reddish green color dispersion confirmed the completion of Cit@AgNPs synthesis. The mixture was then cooled to room temperature and stored at 4 °C in a refrigerator before further experiments. 10 mL of the as-synthesized Cit@AgNP was centrifuged first at 4000 rpm for 10 min at 10 °C to remove relatively larger particles and agglomerates. Then the supernatant was centrifuged at 15,000 rpm for 10 min at 10 °C and the precipitate was re-dispersed in 2 mL H_2O. The redispersed AgNPs were characterized by UV-vis spectroscopy and TEM measurements. Also, for further experiments, AgNPs were centrifuged beforehand in order to discard any impurities and unwanted chemicals.

TH_3719_186122105

4.3.4. Preparation of AgNP dispersions of pH 7.0, pH 8.4 and pH 9.4:

The pH of the centrifuged cit@AgNPs dispersion was 6.70 ± 0.05. In order to make the AgNPs dispersion of pH 7.0, 4.5 µL of 0.01 (M) NaOH was added in 1 mL of the AgNPs dispersion. 25 µL and 35 µL of 0.01 (M) NaOH were added in each of 1 mL of the AgNPs dispersions to make the final pH of the dispersions 8.4 and 9.4, respectively. All the three dispersions were kept undisturbed for 3 h to make the dispersions homogeneous.

4.3.5. AgNPs functionalization with 4-ATP:

Then each of the 4 µL of 34 µM 4-ATP solution in 1:1 methanol-H_2O was added to the 500 µL dispersion (being centrifuged beforehand) of Cit@AgNPs at pH 7.0, 8.4 and 9.4, respectively. Then the mixtures were ultrasonicated for 30 min to obtain homogeneous dispersion of 4-ATP functionalized AgNPs (ATP@AgNPs). After ultrasonication, the 4-ATP@AgNPs dispersions were centrifuged at 4000 rpm for 10 min at 10 °C to remove relatively larger agglomerates, which was confirmed by UV-vis spectroscopy.

4.3.6. Raman measurements and 4-ATP dimerization on AgNP surface:

5 µL of each ATP@AgNP dispersion was carefully dropped on cleaned glass slide to obtain a sessile droplet of circular base of 3 to 3.5 mm diameter. Raman measurements were carried out at every 15 s on a fixed spot of three-phase contact line (TPCL) while the sessile droplet was evaporating at 22 °C and 60-65% relative humidity. Raman spectra were recorded using 0.1% power of 16 mW 633 nm laser source at 600 gr/mm diffraction grating for 5 s acquisition time and accumulation number of 3 at the fixed spot of TPCL focused using 50x long distance objective lens. The diameter of laser beam was 1.0 µm.[28] Baseline corrections of all the spectra were done in the LabSpec 6.0 software equipped with the instrument. The 633 nm laser source also acted as photon source for the dimerization of 4-ATP into 4,4´-dimercaptoazobenzene (DMAB) over time. Recording of Raman spectra was carried out till the droplet was completely evaporated. It is worth mentioning here that the effect of geometry of droplet at TPCL was negligible as only the back-scattered radiations or the radiation which were scattered at zero degree angle were collected by the detector. The effect of interference by incident and scattered radiation on glass substrate, if any, was same for all the spectra recorded.

TH_3719_186122105

4.4. Results and Discussions

4.4.1. Characterization of AgNPs and ATP@AgNPs at different pH:

In our experiment. we used AgNPs for SERS measurements and heterogeneous plasmon catalyzed photochemical reaction because of sharp localized surface plasmon resonance (LSPR)[29] and strong near-field coupling between the particles[30]. UV-vis spectroscopic measurements of Cit@AgNPs showed the strong LSPR absorption peak at 397 nm as shown in **Figure 4.1A** and TEM measurements confirmed the presence of spherical AgNPs of ~28 nm diameter (**Figure 4.1B**). In our previous reports, ~25 nm gold nanoparticles[3] and ~28 nm AgNPs[4] offered satisfactory results in the similar kinds of studies which involved SERS measurements at TPCL and plasmon catalyzed reactions of 4-ATP. Hence, we chose the ~28 nm AgNPs dispersion for our experiments presented below. 4-ATP molecules can be easily functionalized onto the surface of AgNPs owing to the presence of soft thiol group. Additionally, aromatic 4-ATP acted as both the Raman probe and substrate for photochemical reaction on the surface of AgNPs. Absence of any additional peak at higher wavelength upon 4-ATP functionalization on Cit@AgNP surfaces (for all pH studied) implied the lack of any AgNP agglomeration in the aqueous dispersion containing 4-ATP functionalized AgNPs (ATP@AgNPs) as shown in **Figure 4.1D**, **Figure 4.1E** and **Figure 4.1F** at pH 7.0, pH 8.4 and pH 9.4, respectively.[4, 31]

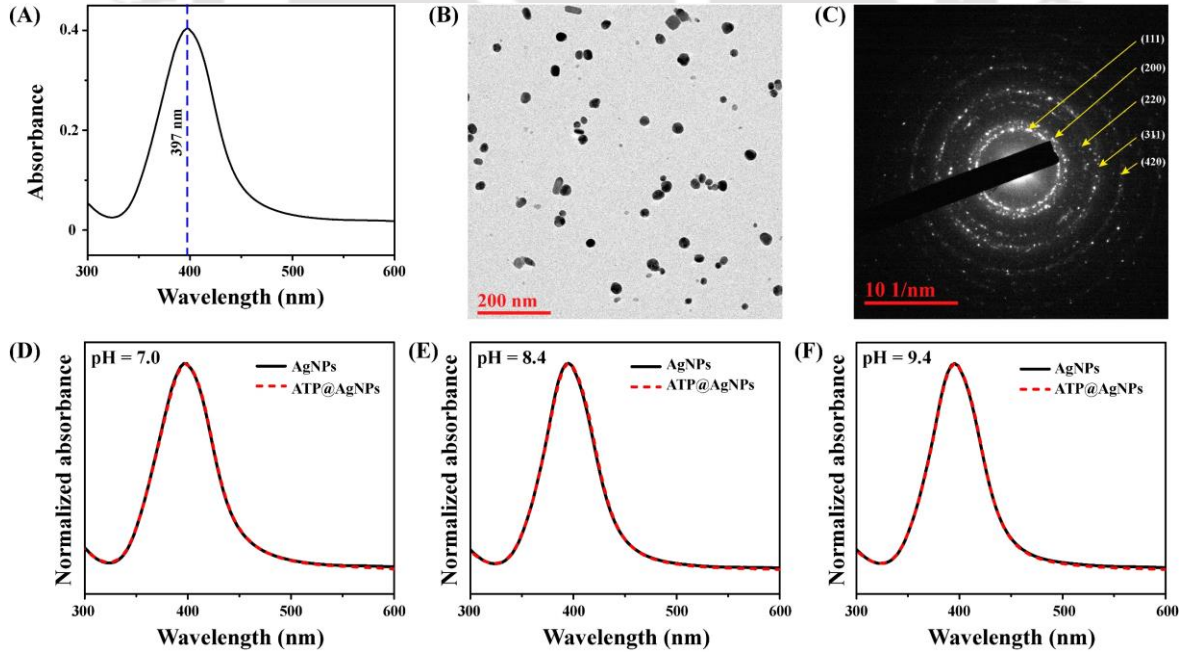

Figure 4.1: (A) UV-vis spectrum of Cit@AgNPs showing absorbance maximum at 397 nm. **(B)** TEM image and **(C)** SAED pattern of the synthesized Cit@AgNPs. UV-vis spectra of Cit@AgNPs and ATP@AgNPs at **(D)** pH 7.0, **(E)** pH 8.4 and **(F)** pH 9.4.

TH_3719_186122105

4.4.2. SERS measurements at TPCL:

Evaporation induced particle depositions of the AgNP dispersions at the TPCL were carried out at three different pH values, viz. 7.0, 8.4 and 9.4, at 22 °C and 60-65 % relative humidity. At first, we compared the deposition kinetics of ATP@AgNPs at the three different pH values by SERS at fixed spots on TPCL of the evaporating droplets. During droplet evaporation, the AgNPs will eventually move towards the TPCL and form assembly of ATP@AgNPs. Assembly of AgNPs generally showed additional absorbance in 600-650 nm range.[32] Therefore, 633 nm was best-suited for SERS measurement at the TPCL. Moreover, low laser power of 0.1% was used in order to avoid any effects due to heating caused by the intense laser source. 633 nm laser also acted as photon source to activate LSPR in the assembly of ATP@AgNPs for the photochemical dimerization of 4-ATP to DMAB as shown in the **Scheme 4.1**. In this case, the Raman probe areas were chosen carefully for each pH such that after complete deposition, the probing spot should be on the middle of the dried deposit as shown in the **Figure A4.1** in the Appendix of Chapter 4 (A4).

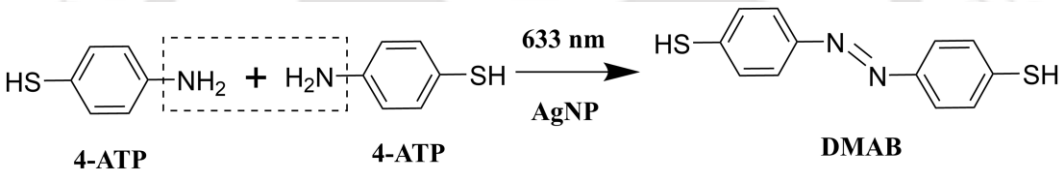

Scheme 4.1: Photochemical reaction of 4-ATP to DMAB.

At pH 7.0, there was no significant Raman signal of 4-ATP at TPCL until at 31.5 min. From 31.75 min, one characteristic peak of 4-ATP at 1078 cm^{-1} appeared (**Figure 4.2A**) and the intensity increased significantly until 34.25 min (**Figure 4.2B**). Another peak at 1434 cm^{-1}, that is the characteristic peak for dimerized product DMAB[33] was noticed from 32.75 min (**Figure 4.2A**) and the intensity rose in two steps as shown in **Figure 4.2B**. At first, the intensity of the 1434 cm^{-1} peak slightly increased until 33.25 min and then decreased until 34.0 min. In the second step, it started to increase again from 35.0 min to 40.0 min. On the other hand, after reaching the maximum at 34.25 min, the intensity of 1078 cm^{-1} peak decreased until 36.0 min and did not changed significantly from 36.0 min until the complete evaporation at 42.0 min. The initial sudden jump of 1078 cm^{-1} peak intensity was due to the plasmonic 'hot-spot' generation owing to phase transition of ATP@AgNPs from dispersion to deposit phase at the TPCL.[3] At the plasmonic 'hot-spot', the SERS enhancement can reach up to 10^7.[34] As evidenced from our previous report[3], most of the AgNPs were deposited during the phase transition time window and the remaining water continued to evaporate from the solid deposit.

TH_3719_186122105

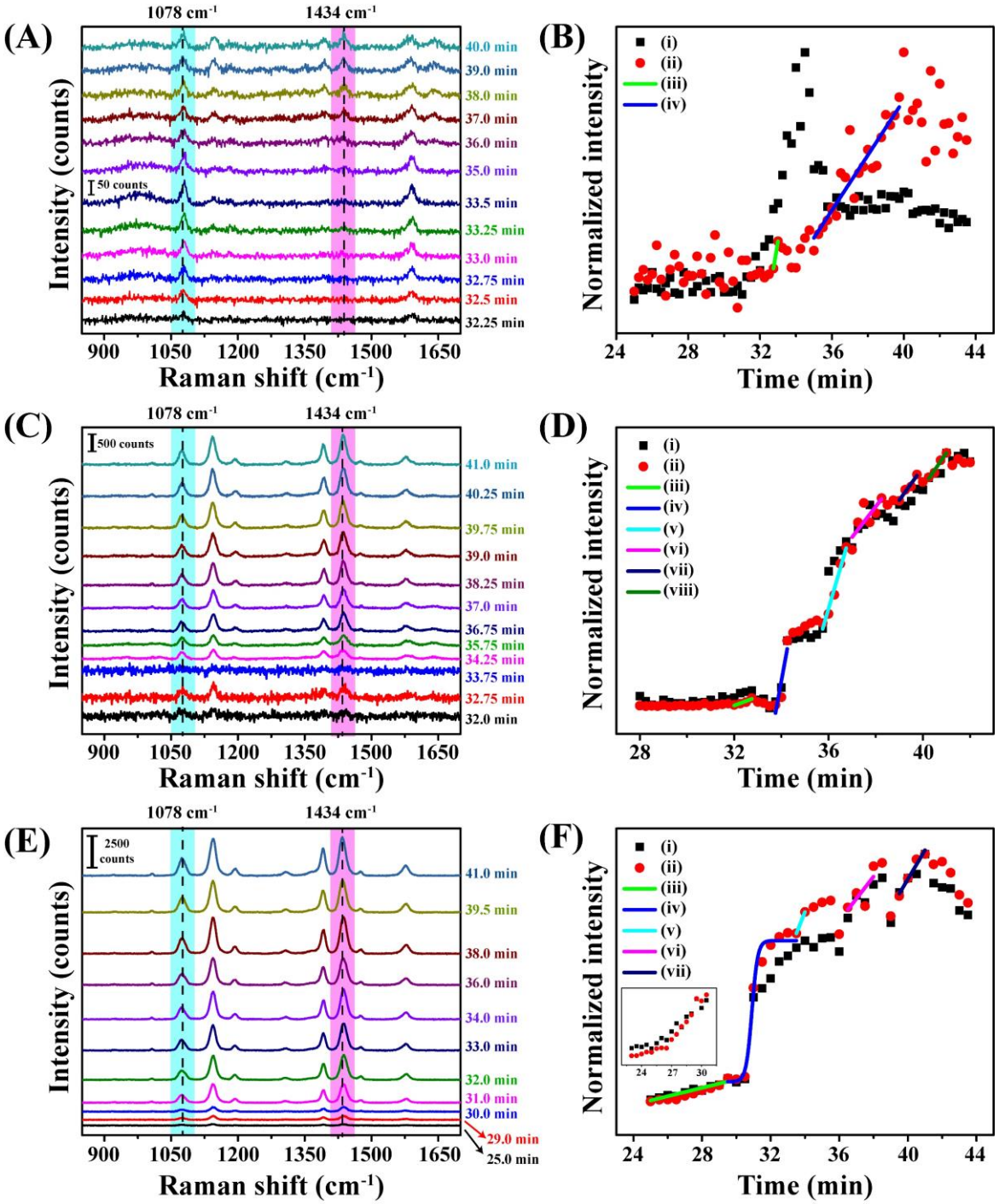

Figure 4.2: Raman spectra at different times recorded at the TPCL of evaporating droplets containing ATP@AgNP dispersions at **(A)** pH 7.0, **(C)** pH 8.4 and **(E)** pH 9.4, respectively. At **(B)** pH 7.0, **(D)** pH 8.4 and **(F)** pH 9.4, variation of (i) 1078 cm^{-1} and (ii) 1434 cm^{-1} Raman peak intensities with time for evaporating droplets containing ATP@AgNPs, respectively. The graphs (iii) and (iv) in **(B)**, (iii) to (viii) in **(D)** and (iii), (v) to (vii) in **(F)** are linear fittings of the variations of 1434 cm^{-1} Raman peak intensities with time. The graph (iv) in **(F)** is Boltzmann fitting of the variations of 1434 cm^{-1} Raman peak intensity with time. Inset in **(F)** is an expanded view for range 23 min to 30 min.

TH_3719_186122105

Therefore, H_2O molecules, which were hydrogen bonded with 4-ATP, move from the surface of ATP@AgNPs to the bulk H_2O resulting in change in the dielectric environment around AgNPs. Water acts as better dielectric environment to improve SERS intensity.[35] Thus, the decrease in the 1078 cm^{-1} peak intensity after 34.25 min was due to the change in dielectric environment of water to 4-ATP molecules on their surfaces. After 1 min of phase transition, the two-step rise of 1434 cm^{-1} peak signified the two-step formation of DMAB molecules at the plasmonic 'hot-spot' environment by intrananoparticle and internanoparticle 4-ATP dimerizations, as observed from linear fittings in **Figure 4.2B(iii)** and **Figure 4.2B(iv)**, respectively.[4]

In case of pH 8.4, there was no significant Raman signal at TPCL until 32.0 min of evaporation of the droplet having ATP@AgNPs dispersion. As shown in **Figure 4.2C** and **Figure 4.2D**, unlike for the pH 7.0, Raman signal intensity of both the 1078 cm^{-1} and 1434 cm^{-1} peaks were increasing simultaneously in six steps, from 32.0 min to 32.75 min (**Figure 4.2D(iii)**), 33.75 min to 34.25 min (**Figure 4.2D(iv)**), 35.75 min to 36.75 min (**Figure 4.2D(v)**), 37.0 min to 38.25 min (**Figure 4.2D(vi)**), 39.0 min to 39.75 min (**Figure 4.2D(vii)**) and 40.25 min to 41.0 min (**Figure 4.2D(viii)**), respectively. As mentioned earlier, similar sudden rise in the intensity during the coffee-ring formation is due to the transition from dispersion phase to deposit phase of nanoparticles at the TPCL.[3] Unlike the reported results in which only one such phase transitions were observed, for our system at pH 8.4, the coffee-ring formation might follow multistep deposition kinetics. The rates of DMAB formation at the 2nd and 3rd steps of the phase transitions were higher which might be due to larger deposition of AgNPs resulted in the greater increase of deposition height and thickness, which were confirmed later by performing AFM measurements.

Such single-phase transition or sudden jump in the Raman signal intensity was observed when Raman measurements were carried out for ATP@AgNP dispersion at pH 9.4. As shown in the **Figure 4.2F**, from 30.5 min to 33.5 min, sudden rise of both the 1078 cm^{-1} and 1434 cm^{-1} peak intensities were noticed. However, contrary to the pH 7.0 and 8.4, the DMAB product formation or the appearance of 1434 cm^{-1} peak started much earlier in the dispersion medium before such phase transition at 25.0 min to 29.0 min as shown in **Figure 4.2E** and **Figure 4.2F(iii)** as well as in the inset of **Figure4.2F**. At this pH value around 9.4, the plasmonic 4-ATP dimerization is fastest as reported earlier.[36-38] Therefore, the formation of DMAB before the phase transition in dispersed phase was due to the high pH of the medium. Thus, at pH 9.4, in the dispersion medium, 4-ATP molecules on the surface of AgNPs were already converted

TH_3719_186122105

to DMAB under the exposure of 633 nm laser over time and the first phase transition from 30.5 min to 33.5 min in **Figure 4.2F(iv)** was the deposition of DMAB attached AgNPs (DMAB@AgNPs) at TPCL instead of ATP@AgNPs. It is worth mentioning here that the phase transitions shown in **Figure 4.2F(v)**, **Figure 4.2F(vi)** and **Figure 4.2F(vii)** were due to the remaining DMAB@AgNP particles, which were converted first from ATP@AgNPs before deposition as solid. Vibration assignments of major Raman peaks of 4-ATP and DMAB were given in **Table A4.1** in Appendix. The time dependent Raman intensity plots starting from zero min of **Figure 4.2B**, **Figure 4.2D** and **Figure 4.2F** were given in **Figure A4.2**, **Figure A4.3** and **Figure A4.4**, respectively. As is evident from the zoomed view of the **Figure 4.2D** and **Figure 4.22F** shown in **Figure A4.5** and **Figure A4.6**, respectively, the SERS signal intensity after each phase transition step had slightly decreased due to the change in the dielectric environment while the droplet was evaporating.[35] The decrease in the intensity at pH 8.4 was lower as compared to that at pH 7.0 because smaller number of particles were depositing after each phase transition at the probe area. In other words, at pH 7.0, since all the particles were deposited at once the change in signal intensity due to release of water was significant and thus detected. On the other hand, at pH 8.4 since particles were deposited in six steps, their number in each step was low and signal intensity change due to release of water was either weak or could not be detected. Thus, changes in the intensity values were low for each step as that compared to the deposition in single step at pH 7.0.

4.4.3. Probe-area location dependent SERS measurements at TPCL:

For in-depth investigations of the deposition kinetics at all three pH, Raman spectroscopic measurements were carried out at three different locations of the deposits at TPCL while the droplets were evaporating. Raman probe areas were chosen in such a way that the three different probe areas were at the outer, the middle and at the inner boundaries of the ring deposits, as shown in **Figure A4.7**. At pH 7.0, when probed at the outer boundary, as shown in **Figure 4.3A**, appearance of 1078 cm^{-1} peak was observed after 27.75 min of the droplet evaporation and the signal intensity was increasing till 28.75 min showing phase transition behavior. DMAB formation at the probe area was completed in two steps, which started at 28.5 min and at 31.5 min, respectively. At the middle of the ring, phase transition started at 31.75 min and two-step DMAB formation occurred at 32.75 min and at 35.0 min, respectively (**Figure 4.3B**). Similar deposition characteristics were also observed when probed at the inner boundary of the deposit at which phase transition was noticed at 38.0 min (**Figure 4.3C**). At pH 7.0, the DMAB formation at three different locations of the deposit followed two-step

TH_3719_186122105

intrananoparticle and internanoparticle reaction kinetics as discussed earlier. The time for the occurrence of the phase transition time increased on going from outer boundary to the inner boundary. This might be because the particles were coming at the TPCL and depositing at the outer boundary first. After reaching the maximum height possible by the curvature of the droplet surface new particles started to deposit in the middle and then in the inner boundary at the TPCL.

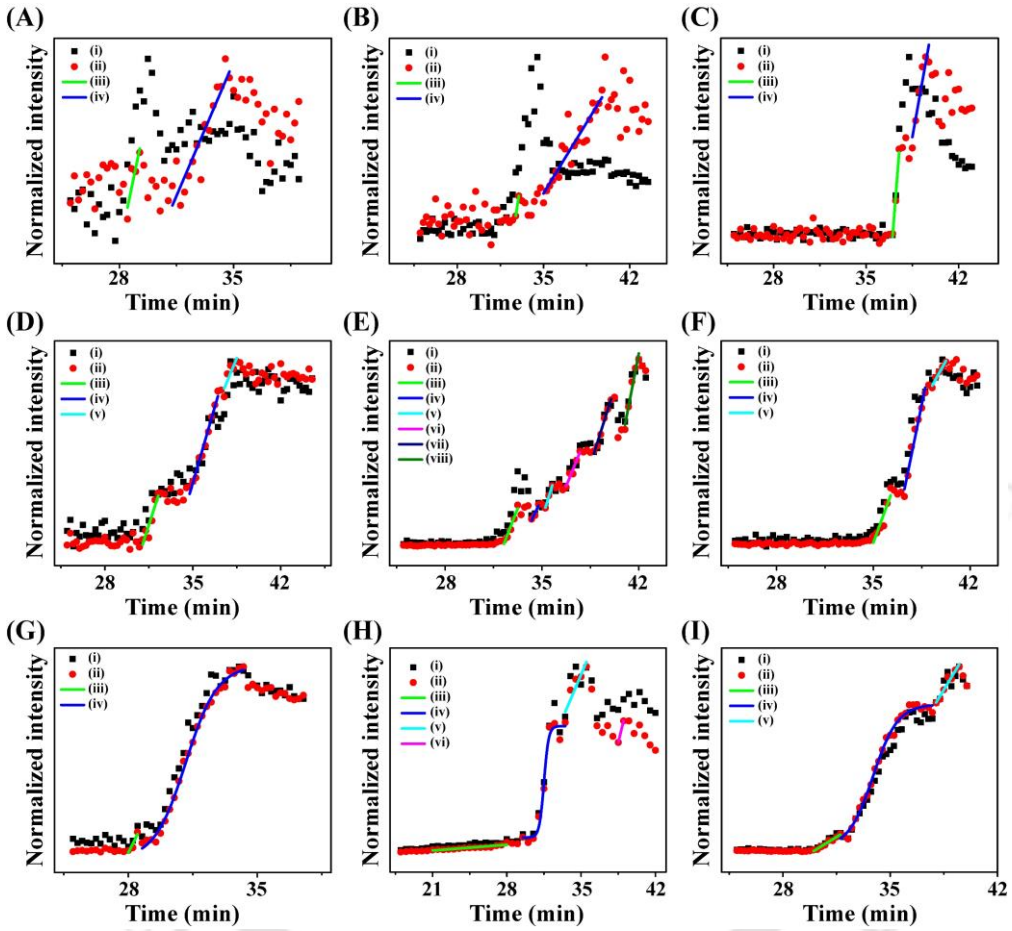

Figure 4.3: Variations of (i) 1078 cm^{-1} and (ii) 1434 cm^{-1} Raman peak intensities with time at the TPCL of evaporating droplets containing ATP@AgNP dispersion at **(A)** outer boundary of the deposit at pH 7.0, **(B)** middle of the deposit at pH 7.0, **(C)** inner boundary of the deposit at pH 7.0, **(D)** outer boundary of the deposit at pH 8.4, **(E)** middle of the deposit at pH 8.4, **(F)** inner boundary of the deposit at pH 8.4, **(G)** outer boundary of the deposit at pH 9.4, **(H)** middle of the deposit at pH 9.4, and **(I)** inner boundary of the deposit at pH 9.4. The graphs (iii) and (iv) in **(A)**, **(B)** and **(C)**; (iii) to (v) in **(D)**; (iii) to (viii) in **(E)**; (iii) to (v) in **(F)**; (iii) in **(G)**; (iii), (v) and (vi) in **(H)**; (iii) and (v) in **(I)** are linear fittings of the variations of 1434 cm^{-1} Raman peak intensities with time. The graphs in (iv) of **(G)**, **(H)** and **(I)** are Boltzmann fittings of the variations of 1434 cm^{-1} Raman peak intensity with time. The optical images of deposits indicating the probe areas are given in **Figure A4.7** in Appendix A4.

TH_3719_186122105

When Raman measurements were carried out at the outer boundary of the TPCL at pH 8.4, both the 1078 cm^{-1} and 1434 cm^{-1} peaks appeared after 31.0 min and only three number of steps of particle depositions were observed as shown in **Figure 4.3D**. Similar to the phenomenon exhibited in **Figure 4.2D**, at the middle of deposit at TPCL, we again noticed six-step phase transition behavior in **Figure 4.3E** from 31.25 min to 33.25 min, 34.25 min to 34.75 min, 35.25 min to 35.75 min, 36.75 min 37.75 min, 38.75 min to 40.0 min and 41.0 min to 42.0 min, respectively. But at the inner boundary of TPCL, both the 1078 cm^{-1} and 1434 cm^{-1} peaks started to appear at 35.0 min, which was much later compared to that for outer boundary and middle of the deposit (**Figure 4.3F**). At the inner boundary also, only three steps of increasing the intensity of Raman signal were noticed from 35.0 min to 36.25 min, 37.25 min to 38.75 min and 39.25 min to 40.25 min, respectively, as shown in **Figure 4.3F**. It is worth mentioning here that there were 0.5 min to 1.0 min delay between every step of rise of the intensity and during the delay time, intensity of both the peaks slightly decreased before being increased again. As reported earlier, ATP@AgNPs were surrounded by water molecules through hydrogen bonding and water molecules must leave from the surroundings of AgNPs in order for DMAB dimerization to occur. As DMAB formation was occurring at each step of the phase transition, water molecules around the nanoparticles were moving to the bulk water during the evaporation of droplet. Therefore, the surrounding plasmonic environment was changing from water to H-bonded networks of Ag bonded ATP molecules. As water act as a better dielectric medium in which Raman signal is higher compared to air, the lowering of the intensity after each step was because of the change in dielectric environment around AgNPs.[33] This was the same reason why intensities of Raman signals had decreased after complete drying too.

As discussed earlier, the rate of DMAB formation was the fastest at pH 9.4 in contrast to that at other two lower pH values. Therefore, as soon as particles reached at the Raman probe area at the outer boundary of TPCL, DMAB formation or the appearance of 1434 cm^{-1} peak started at 28 min in the dispersed medium before the phase transition or deposition, which started at 29.5 min and the intensity of both the peaks was increasing that lasted until 34.0 min (**Figure 4.3G**). Similarly, at the inner boundary, as shown in **Figure 4.3I**, DMAB formation started at 30.0 min and after that sudden jump of intensity of DMAB Raman signals was noticed from 32.25 min until 36.0 min. The remaining ATP@AgNPs moved towards the inner boundary of the deposit and we noticed another one step phase transition at that probe area from 38.0 min to 39.5 min as shown in **Figure 4.3I(v)**. At the middle of the deposit, DMAB formation started at 21.0 min to 28.0 min as shown in **Figure 4.3H(iii)**. This was followed by

TH_3719_186122105

major phase transition from 30.5 min to 32.5 min (**Figure 4.3H(iv)**). At this position, the remaining particles were deposited in two small steps after major single-phase transition. Raman spectra for the measurements at pH 7.0, pH 8.4 and pH 9.4 corresponding to **Figure 4.3** were given in **Figure A4.8**, **Figure A4.9** and **Figure A4.10**, respectively, in A4.

The above experiments suggested that at neutral pH 7.0, irrespective of the Raman probe area, particles deposited through single-phase transitions; however, the DMAB formation followed intrananoparticle and internanoparticle pathways as reported earlier.[4] At the high pH of 9.4, majority of DMAB formations took place in dispersed medium and most of the AgNPs having surface attached DMAB deposited in a single-phase transition. Interestingly, the droplets containing well-dispersed ATP@AgNPs in water at the moderate pH of 8.4 displayed step-by-step deposition kinetics involving multiple phase transition steps that has not been reported yet. Moreover, at the middle, the deposition steps were more than those at the inner and outer boundaries of the TPCL.

4.4.4. AFM measurements of the deposits after each step of phase transition at pH 8.4:

In order to further understand the step-by-step evolution of the particle deposits at pH 8.4, we performed AFM measurements of the dried deposits at each step of deposition or phase transition the results of which are shown in **Figure 4.4**. **Figure 4.4A** to **4.4F** revealed the Raman intensity profiles of 1078 cm^{-1} and 1434 cm^{-1} peaks as the evaporations were stopped after 1^{st}, 2^{nd}, 3^{rd}, 4^{th}, 5^{th} and 6^{th} phase transition steps in separate experiments. Raman spectra of these experiments were given in **Figure A4.11**. AFM images of the deposits are given in the inset of each plot. Interestingly, investigations of further revealed that height as well as width of the solid deposit was increasing with the number phase transitions (**Figure 4.4G**). Thus, the height profile diagram disclosed the step-by-step deposition of AgNPs at the TPCL of an evaporating droplet at pH 8.4. The increase in the height of the deposit till 4^{th} step was monotonous as shown in **Figure 4.4H**. But the increase in the height was less significant from 4^{th} to 6^{th} steps of the phase transition or solid deposition as observed from the fitted curve in **Figure 4.4H**. This was why we observed less increase in the Raman signal intensity after 4^{th} step compared to that for 1^{st} to 4^{th} steps as shown in **Figure 4.2D**. However, as is evident from **Figure 4.4I**, the width of the solid deposit was increasing linearly with the number of steps till the 6^{th} phase transition. Therefore, when we probed at the outer boundary of the deposit, we could only observe the change in deposit height, which was increasing till the 3^{rd} step of the deposition at that region marked in the **Figure 4.4G**.

TH_3719_186122105

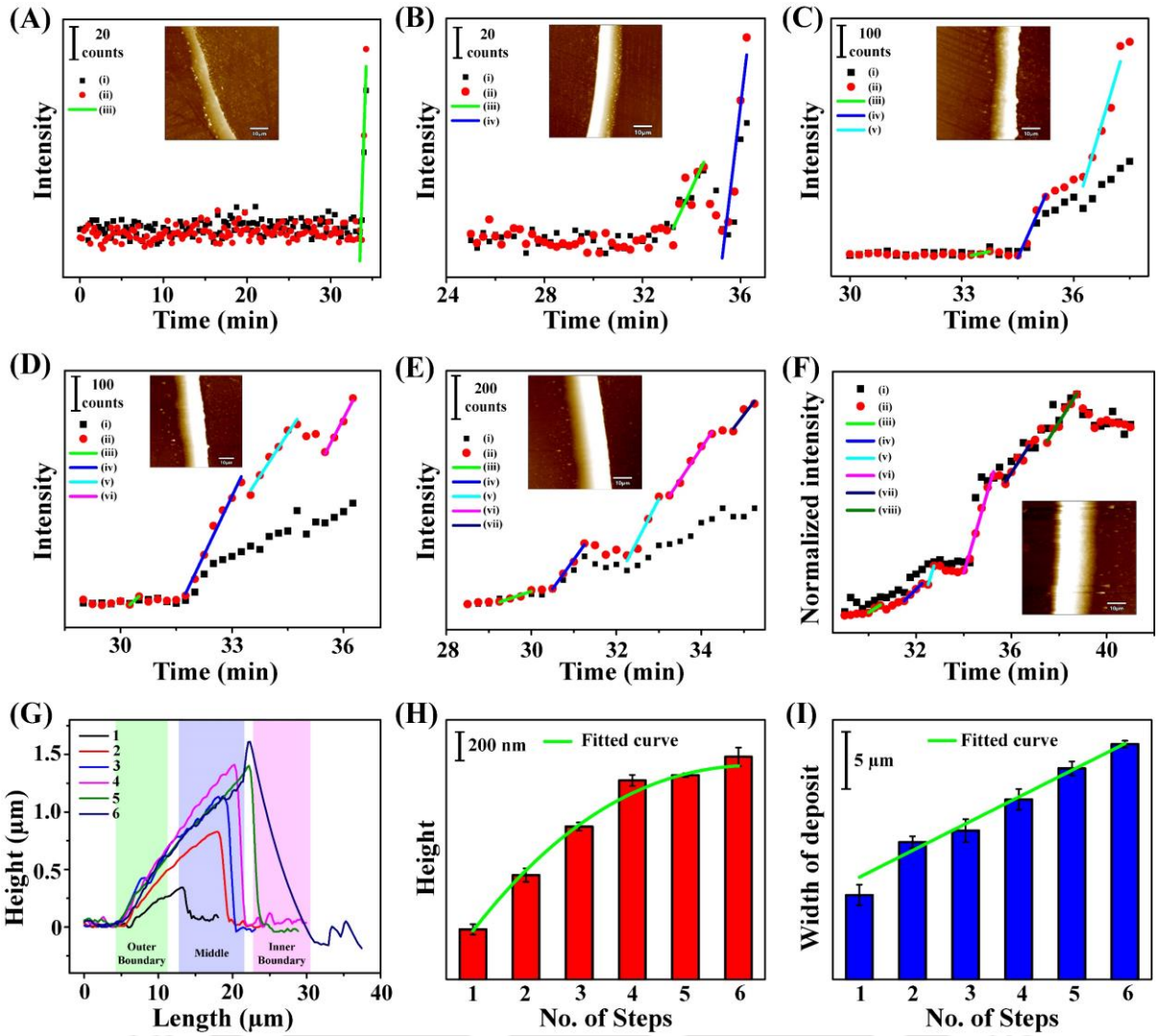

Figure 4.4: Variations of (i) 1078 cm^{-1} and (ii) 1434 cm^{-1} Raman peak intensities with time till **(A)** 1st, **(B)** 2nd, **(C)** 3rd, **(D)** 4th, **(E)** 5th and **(F)** 6th phase transitions for the droplets containing ATP@AgNP dispersions when probed in the middle of the deposits. The graphs (iii) to (viii) are linear fittings showing phase transitions. Insets are the AFM images of the dried deposits for the respective phase transition. Scalebar in each AFM image is 10 µm. **(G)** Height profile diagrams of the dried deposits for the number of phase transitions mentioned in the legends. Raman probe areas are highlighted. Bar diagrams with fitted curve of **(H)** height of the deposit and **(I)** width of the deposit plotted against the phase transition step number.

At the inner boundary, phase transitions for the last three steps led to deposition and consequent increase in the width of the deposits as could be seen in the highlighted region in **Figure 4.4G**. However, both the change in height and width could be measured well when probed at the middle of the deposit and consequently the six steps of phase transitions were experimentally identified in that region from the results of the SERS. Moreover, for the 2nd and 3rd steps of the depositions, both the height and width were increasing at the middle of the

TH_3719_186122105

deposit. This signified a larger number of AgNPs were depositing during these two phase transition time windows. As more and more plasmonic 'hot-spots' were getting generated due to depositions, the increase in the 1078 cm^{-1} peak and rate of DMAB formations were higher in these two steps as could be observed in the **Figure 4.2D**.

4.4.5. Mechanism of ATP@AgNP deposition and 4-ATP dimerization at three pH values:

Previous studies of coffee-ring formation by Deegan *et al*[1] and Boulogne *et al*[39] revealed that micro-particles deposit linearly with time at the TPCL while there is a sudden jump in deposition at the final leg of drying. However, our studies for nanoparticles forming coffee-ring revealed deposition kinetics via singular phase transition from the dispersion to deposit. The phase transition mechanism[3] has been discovered by us but the pH-dependent deposition kinetics has not been reported. Only one such phase transition step was observed at pH 7.0.[4] At pH of 8.4, ATP@AgNPs followed multistep phase transitions as observed from SERS and AFM measurements. Based on all the experimental evidences, it is now clear that the AgNP deposition kinetics at the TPCL depended on pH of the dispersions when the AgNPs were functionalized with photochemically reacting molecules such as 4-ATP. The deposition processes at the three pH values were schematically given in the Figure 5. The pH-dependent deposition and photochemical reaction involving ATP@AgNPs at the TPCL may be explained based on the following three factors: (i) the advective flow of ATP@AgNPs with time to the TPCL, (ii) the pH-dependent rate of dimerization reaction of 4-ATP into DMAB on the surface of AgNPs and (iii) the kinetic stability of ATP@AgNPs in the dispersion medium at different pH values. As is evident from **Figure 4.2**, significant AgNP depositions started at 31.75 min, 32.0 min and 30.5 min at pH 7.0, 8.4 and 9.4, respectively. Therefore, the time of starting of AgNP deposition at the TPCL was nearly the same at all three pH values. Hence, the pH of the medium had little influence on the advective flow of the AgNPs towards the TPCL. However, the rate of 4-ATP dimerization - that involves N-H bond cleavage of the amine group - is dependent on the pH. The rate of dimerization increases with the rise of pH of the reaction medium.[36-38] At the neutral pH of 7.0, the DMAB formation rate is slow. At pH 8.4 and 9.4, the rate of DMAB formation are moderate and fast, respectively. Further, our measurements revealed the zeta potential of the ATP@AgNP dispersions to have been -37.7±1.0 mV, -40.1±3.0 mV and -45.8±3.0 mV at pH 7.0, 8.4 and 9.4, respectively. Literature reports also suggest that with increasing pH of the dispersion, the negative zeta potential value of AgNPs increases and hence the dispersion become more stable at higher pH values.[40,41]

TH_3719_186122105

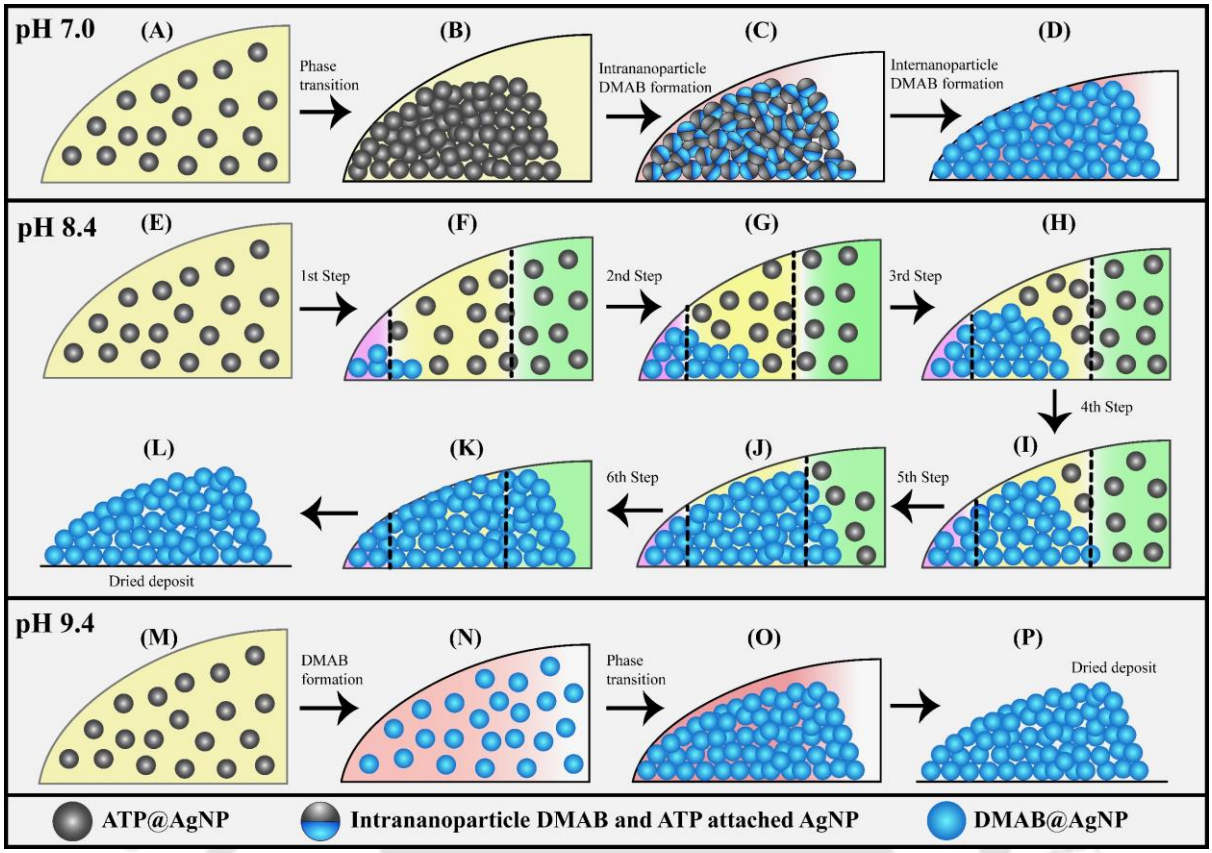

Figure 4.5: Two-dimensional schematic representations of the **(A)** dispersed of ATP@AgNPs at the TPCL at pH 7.0, **(B)** deposited ATP@AgNPs after phase transition at pH 7.0, **(C**) AgNP deposits after intrananoparticle DMAB formation at pH 7.0, **(D)** AgNP deposits after internanoparticle DMAB formation at pH 7.0, **(E)** dispersed ATP@AgNPs at the TPCL at pH 8.4. AgNP deposits after **(F)** 1st, **(G)** 2nd, **(H)** 3rd, **(I)** 4th, **(J)** 5th, and **(K)** 6th step of phase transition and simultaneous DMAB formation around AgNPs, respectively. Schematic of the **(L)** dried DMAB@AgNP deposit at pH 8.4. Two-dimensional schematic representations of the **(M)** dispersed ATP@AgNP at the TPCL at pH 9.4, **(N)** dispersed DMAB@AgNPs after photochemical reactions of ATP@AgNPs at the TPCL at pH 9.4, **(O)** Deposited DMAB@AgNPs at the TPCL after single phase transition at pH 9.4 and **(P)** dried DMAB@AgNPs deposit at pH 9.4.

At pH 7.0, the rate of 4-ATP dimerization as well as dispersion stability was comparatively low. Thus, once the particles reached the TPCL they were deposited via a phase transition (**Figure 4.5B**). This was followed by intrananoparticle H-bonded water release and photochemical dimerization of 4-ATP into DMAB (**Figure 4.5C**). Subsequently, following internanoparticle H-bonded water release, a second dimerization reaction took place that involved 4-ATP molecules from two different nanoparticles (**Figure 4.5D**). The loss of intrananoparticle and internanoparticle H-bonded water molecules and dimerization reactions

TH_3719_186122105

in two steps were evidenced by the changes in Raman signal intensity of DMAB at 1434 cm^{-1} that indicated both change in the dielectric environment and different reaction rates of formation DMAB. The results are consistent with our previous report.[4]

In the case of droplet evaporation at pH 8.4, the reaction between 4-ATP molecules involving the surfaces of AgNPs was faster than that at pH 7.0. On the other hand, zeta potential results implied that the ATP@AgNPs were highly dispersible at pH 8.4 as compared to that at 7.0. Thus, the ATP@AgNPs reaching the TPCL (**Figure 4.5E**) would remain in the dispersion phase for sufficient time to undergo photochemical dimerization. It is plausible that both intrananoparticle and internanoparticle reactions took place in the dispersion phase; however, due to lack of sufficient number of particles (as compared to layers of particles in the deposit phase) their distinction could not be made. This would be followed by deposition of the product assemblies (**Figure 4.5F**) as was evident from the sudden jump of 1078 cm^{-1} as well as 1434 cm^{-1} peak intensity as shown in **Figure 4.2D(iii)** that was further supported by AFM results discussed later. Interestingly, at the initial period of deposition (the first step here) the rise of the product peak was slow with the arrival of the particles at the TPCL and fast reaction leading to product formation and deposition in sequence. The final stage of deposition was indicated by the slight diminishing of the peak intensity as the water molecules around the DMAB@AgNPs had moved from the surface of AgNPs to the bulk, thus, altering the dielectric environment of the deposited NPs.[35] This was followed by steep rise in product peak intensity in five more steps (with the second and third steps corresponding to the fastest rise) as shown in **Figure 4.2D**, indicating the presence of larger number of particles at the TPCL that lead to faster reactions followed by depositions and release of water molecules defining the events of every step. The deposition steps are shown schematically in **Figure 4.5F** to **Figure 4.5K**. In other words, fast photochemical reactions at the TPCL led to agglomeration of the NPs causing the deposition of the particles. The successive steps indicated movement of newer particles from the surroundings to the illuminated (probe) area following depositions of the particles that were agglomerated upon reaction. The aforementioned peak intensities versus time plot clearly indicated step-wise reaction followed by deposition and release of water molecules as shown in **Figure 4.2D**.

Further, during the first three steps of phase transitions (**Figure 4.5F** to **Figure 4.5H**), both the height and width of the deposit significantly increased as observed from AFM measurements (**Figure 4.4G**). There were total six such steps of phase transitions that were observed at pH 8.4 (**Figure 4.2D**, **Figure 4.3E** and **Figure 4.4F**), which are represented

TH_3719_186122105

schematically in **Figure 4.5F** to **Figure 4.5K**, respectively. As mentioned earlier, the SERS signal intensity had decreased or remained the same after each step of deposition. However, each successive deposition resulted in the increase of intensity of the overall deposits. During the first three steps, a large number of AgNPs had deposited at the outer boundary and middle of the deposit. As monitored from AFM measurements (**Figure 4.4**), after the 4th step, the particles deposited at the middle and inner boundaries of the ring (**Figure 4.5I**) that had resulted in the slight increase in the height and greater increase in the width of the deposit. After 5th and 6th steps, as shown in **Figure 4.5J** and **Figure 4.5K**, few particles were deposited at the middle and majority of the AgNPs were deposited at the inner boundary increasing the width (only of the overall deposit).

At pH 9.4, as is obvious from **Figure 4.2F(iii)**, the rate of DMAB formation was so fast that nearly all the 4-ATP molecules on the ATP@AgNPs surface dimerized into DMAB forming DMAB@AgNPs in the dispersion medium as shown in **Figure 4.5N**. Here also, intrananoparticle and internanoparticle reactions could not be distinguished. Because of high dispersibility at pH 9.4, most of the particles deposited in one major phase transition after reaching a certain particle concentration. Hence, we observed one such major phase transition step in **Figure 4.2F(iv)**, which is represented schematically in **Figure 4.5O**. The other steps are due to the reaction and depositions of the remainder of the particles.

4.5. Conclusions

In summary, the deposition kinetics of ATP@AgNPs laden aqueous droplets were successfully identified at pH 7.0, 8.4 and 9.4 and across the ring by SERS and AFM measurements. The deposition kinetics were dependent on the pH of the evaporating droplets. AgNPs were deposited through single phase transition at both pH 7.0 and pH 9.4. Most importantly, multiple step-by-step depositions were observed when the pH of the evaporating droplet was 8.4. The difference in the DMAB formation time window was also monitored. At pH 7.0, DMAB formation started after phase transition led deposition of ATP@AgNPs and completed in two steps involving intrananoparticle and internanoparticle DMAB formations. At pH 9.4, DMAB formed on the surface of AgNPs in the dispersed phase followed by phase transition. At pH 8.4, both the DMAB formation and phase transition occurred simultaneously. These studies may be of significance in liquid printing technology where chemical or photochemical reactions in the course of depositions are key to the utility of the imprints in sensing, display or growth of device structures.

TH_3719_186122105

4.6. References

1. Deegan, R. D.; Bakajin, O.; Dupont, T. F.; Huber, G.; Nagel, S. R.; Witten, T. A. Contact line deposits in an evaporating drop. *Phys. Rev. E* **2000**, *62*, 756-765.
2. Deng, R.; Yang, L.; D, B. Colin. Combining Inkjet Printing with Emulsion Solvent Evaporation to Pattern Polymeric Particles. *ACS Appl. Mater. Interfaces* **2018**, *10*, 12317-12322.
3. Paul, S.; Chattopadhyay, A. Single Phase Transition Leads to the Nanoparticle Deposition in an Evaporating Sessile Droplet. *J. Phys. Chem. C* **2023**, *45*, 22401-22411.
4. Paul, S.; Chattopadhyay, A. Distinction of Plasmonic Intrananoparticle and Internanoparticle Molecular Reaction Rates at the Three-Phase Contact Line of an Evaporating Sessile Droplet. *J. Phys. Chem. Lett.* **2024**, *15*, 6812-6817.
5. Torrisi, F.; Hasan, T.; Wu, W.; Sun, Z.; Lombardo, A.; Kulmala, T. S.; Haieh, G.-W.; Jung, S.; Bonaccorso, F.; Paul, P. J.; *et al.* Inkjet-Printed Graphene Electronics. *ACS Nano* **2012**, *6*, 2992-3006.
6. Ye, X.; Ge, L.; Jiang, T.; Guo H.; Chen, B.; Liu, C.; Hayashi, K. Fully Inkjet-Printed Chemiresistive Sensor Array Based on Molecularly Imprinted Sol–Gel Active Materials. *ACS Sens.* **2022**, *7*, 1819-1828.
7. Pendyala, N. K.; Magdassi, S.; Etgar, L. Fabrication of Perovskite Solar Cells with Digital Control of Transparency by Inkjet Printing. *ACS Appl. Mater. Interfaces* **2021**, *13*, 30524-30532.
8. Xuan, T.; Shi, S.; Wang, L.; Kuo, H.-C.; Xie, R.-J. Inkjet-Printed Quantum Dot Color Conversion Films for High-Resolution and Full-Color Micro Light-Emitting Diode Displays. *J. Phys. Chem. Lett.* **2020**, *11*, 5184-5191.
9. Sajedi-Moghaddam, A.; Rahmanian, E.; Naseri, N. Inkjet-Printing Technology for Supercapacitor Application: Current State and Perspectives. *ACS Appl. Mater. Interfaces* **2020**, *12*, 34487-34504.
10. Gao, M.; Li, L.; Song, Y. Inkjet printing wearable electronic devices. *J. Mater. Chem. C* **2017**, *5*, 2971-2993.
11. Molina-Lopez, F.; Gao, T. Z.; Kraft, U.; Zhu, C.; Öhlund T.; Pfattner, R.; Feig, V. R.; Kim, Y.; Wang, S.; Yun, Y.; *et al.* Inkjet-printed stretchable and low voltage synaptic transistor array. *Nat Commun* **2019**, *10*, 2676.
12. Hussain, A.; Abbas, N.; Ali, A. Inkjet Printing: A Viable Technology for Biosensor Fabrication. *Chemosensors* **2022**, *10*, 103.

TH_3719_186122105

13. Derby, B. Bioprinting: inkjet printing proteins and hybrid cell-containing materials and structures. *J. Mater. Chem.* **2008**, *18*, 5717-5721.
14. Bietsch, A.; Henger, M.; Lang, H. P.; Gerber, C. Inkjet Deposition of Alkanethiolate Monolayers and DNA Oligonucleotides on Gold: Evaluation of Spot Uniformity by Wet Etching. *Langmuir* **2004**, *20*, 5119-5122.
15. Li, X.; Liu, B.; Pei, B.; Chen, J.; Zhou, D.; Peng, J.; Zhang, X.; Jia, W.; Xu, T. Inkjet Bioprinting of Biomaterials. *Chem. Rev.* **2020**, *19*, 10793-10833.
16. Gao, G.; Chu, X. Three-dimensional bioprinting in tissue engineering and regenerative medicine. *Biotechnol Lett.* **2016**, *38*, 203-211.
17. Zhang, W.; Yu, T.; Liao, L.; Cao, Z. Ring formation from a drying sessile colloidal droplet. *AIP Advances* **2013**, *3*, 102109.
18. Brutin, D. Influence of relative humidity and nano-particle concentration on pattern formation and evaporation rate of pinned drying drops of nanofluids. *Colloids and Surfaces A: Physicochemical and Engineering Aspects* **2013**, *429*, 112-120.
19. Wilkinson, J.; Tam, C.; Askounis, A.; Qi, S. Suppression of the coffee-ring effect by tailoring the viscosity of pharmaceutical sessile drops. *Colloids and Surfaces A: Physicochemical and Engineering Aspects* **2021**, *614*, 126144.
20. Lohani, D.; Basavaraj, M. G.; Satapathy, D. K.; Sarkar, S. Coupled effect of concentration, particle size and substrate morphology on the formation of coffee rings. *Colloids and Surfaces A: Physicochemical and Engineering Aspects* **2020**, *589* 124387.
21. Crivoi, A.; Duan, F. Effect of Surfactant on the Drying Patterns of Graphite Nanofluid Droplets. *J. Phys. Chem. B* **2013**, *117*, 5932-5938.
22. Yunker, P. J.; Still, T.; Lohr, M. A.; Yodh, A. G. Suppression of the coffee-ring effect by shape-dependent capillary interactions. *Nature* **2011**, *476*, 308-311.
23. Arango, J. C.; Pintro, C. J.; Singh, A.; Claridge, S. A. Inkjet Printing of Nanoscale Functional Patterns on 2D Crystalline Materials and Transfer to Soft Materials. *ACS Appl. Mater. Interfaces* **2024**, *16*, 8055-8065.
24. Sloma, M. 3D printed electronics with nanomaterials. *Nanoscale* **2023**, *15*, 5623-5648.
25. Langer, J.; Jimenez de Aberasturi, D.; Aizpurua, J.; Alvarez-Puebla, R. A.; Auguié, B.; Baumberg, J. J.; Bazan, G. C.; Bell, S. E. J.; Boisen, A.; Brolo, A. G., et al. Present and Future of Surface-Enhanced Raman Scattering. *ACS Nano* **2020,** *14*, 28-117.
26. Dutta, A.; Chattopadhyay, A. Surface and Tip-Enhanced Raman Spectroscopy at the Plasmonic Hot Spot of a Coordination Complex-Conjugated Gold Nanoparticle Dimer. *J. Phys. Chem. C* **2017**, *121*, 18854-18861.

TH_3719_186122105

27. Dadosh, T. Synthesis of uniform silver nanoparticle with a controllable size. *Materials Letters* **2009,** *63*, 2236-2238.
28. Mia, A. K.; Meyyappan, M.; Giri, P. K. Asymmetric contact-induced selective doping of CVD-grown bilayer WS_2 and its application in high-performance photodetection with an ultralow dark current. *Nanoscale* **2024**, *16*, 8583-8596.
29. Juma, M. W.; Birech, Z.; Mwenze, N. M.; Ondeiki, A. M.; Maaza, M.; Mokhotjwa, S. D. Localized surface plasmon resonance sensing of Trenbolone acetate dopant using silver nanoparticles. *Sci Rep* **2024**, *14*, 5721.
30. Pedersen, D. B.; Wang, S.; Paige, M. F.; Leontowich, A. F. G. Exploiting Near-Field Coupling between Closely Spaced, Gas-Phase, 10 ± 5 nm Ag Nanoparticles Deposited on NaCl To Observe the Quadrupolar Surface Plasmon Absorption. *J. Phys. Chem. C* **2007**, *111*, 5592-5598.
31. Pal, S.; Paul, S.; Chattopadhyay, A. Dual Role of Au nanoparticles in the Catalytic Formation of an Amorphous Polynuclear Peroxo Complex and Surface Enhanced Resonance Raman Scattering. *ChemistrySelect* **2022**, *7*, e202201569.
32. Dong, F.; Valsami-Jones, E.; Kreft, JU. New, rapid method to measure dissolved silver concentration in silver nanoparticle suspensions by aggregation combined with centrifugation. *J Nanopart Res* **2016**, *18*, 259.
33. Pal, S.; Paul, S.; Chattopadhyay, A. Enhanced solid-state plasmon catalyzed oxidation and SERS signal in the presence of transition metal cations at the surface of gold nanostructures. *Phys. Chem. Chem. Phys.* **2021**, *23*, 21808-21816.
34. Fang, Y.; Seong, N.-H.; Dlott, D. D. Measurement of the Distribution of Site Enhancements in Surface-Enhanced Raman Scattering. *Science* **2008**, *321*, 388-392.
35. de Barros, A.; Shimizu, F. M.; de Oliveira, C. S.; Sigoli, F. A.; dos Santos, D. P.; Mazali, I. O. Dynamic Behavior of Surface-Enhanced Raman Spectra for Rhodamine 6G Interacting with Gold Nanorods: Implication for Analyses under Wet versus Dry Conditions. *ACS Appl. Nano Mater.* **2020**, *3*, 8138-8147.
36. Sun, M.; Huang, Y.; Xia, L.; Chen, X.; Xu, H. The pH-Controlled Plasmon-Assisted Surface Photocatalysis Reaction of 4-Aminothiophenol to *p*,*p*′-Dimercaptoazobenzene on Au, Ag, and Cu Colloids. *J. Phys. Chem. C* **2011**, *115*, 9629-9636.
37. Zhang, Z.; Kneipp, J. Ligand-Supported Hot Electron Harvesting: Revisiting the pH-Responsive Surface-Enhanced Raman Scattering Spectrum of *p*-Aminothiophenol. *J. Phys. Chem. Lett.* **2021**, *12*, 1542-1547.

TH_3719_186122105

38. Huang, Y.; Dong, B. pH Dependent plasmon-driven surface-catalysis reactions of *p,p′*-dimercaptoazobenzene produced from *para*-aminothiophenol and 4-nitrobenzenethiol. *Sci. China Chem.* **2012**, *55*, 2567–2572.
39. Boulonge, F.; Ingremeau, F.; Stone, H. A. Coffee-stain growth dynamics on dry and wet surfaces. *J. Phys.: Condens. Matter* **2017**, *29*, 074001.
40. El Badawy, A. M.; Luxton, T. P.; Silva, R. G.; Scheckel, K. G.; Suidan, M. T.; Tolaymat, T. M. Impact of Environmental Conditions (pH, Ionic Strength, and Electrolyte Type) on the Surface Charge and Aggregation of Silver Nanoparticles Suspensions. *Environ. Sci. Technol.* **2010**, *44*, 1260–1266.
41. Bélteky, P.; Rónavári, A.; Igaz, N.; Szerencsés, B.; Tóth, IY.; Pfeiffer, I.; Kiricsi, M.; Kónya, Z. Silver nanoparticles: aggregation behavior in biorelevant conditions and its impact on biological activity. *Int J Nanomedicine*. **2019**, *14*, 667-687.

TH_3719_186122105

Appendix of Chapter 4 (A4):

A4.1. Optical images of the deposits at the TPCL (corresponding to the experimental results given in Figure 4.2 in Chapter 4):

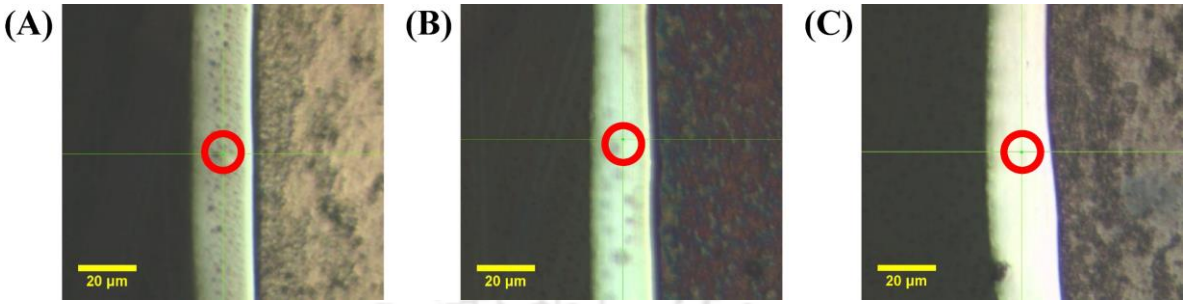

Figure A4.1: Optical images of the deposits at the TPCL after evaporation of droplets containing ATP@AgNPs dispersions of **(A)** pH 7.0, **(B)** pH 8.4 and **(C)** pH 9.4, respectively. The Raman probe areas are marked by red circles. The probing spots were chosen such that the areas were at the middle of the deposit after complete evaporation. The time dependent Raman measurements of these evaporating droplets are given in **Figure 4.2** in the Chapter 4.

A4.2. Table A4.1: Vibration assignment of major Raman peaks of 4-ATP and DMAB on AgNP surface:[1]

Raman peaks of 4-ATP (cm^{-1})	Raman peaks of DMAB (cm^{-1})	Vibration
1078	1078	$\nu(C{=}C)_{ring} + \nu(C{-}S)$
–	1140	$\nu(C{=}N) + \beta(C{-}H)$
–	1390	$\nu(N{=}N) + \nu(C{=}N)$
–	1434	$\nu(N{=}N) + \beta(C{-}H)$
–	1581	$\nu(C{=}C)_{ring}$
1590	–	$\nu(C{=}C)_{ring} + \delta NH_2$

TH_3719_186122105

A4.3. Time-dependent variation of 1078 cm^{-1} and 1434 cm^{-1} Raman peak intensities for pH 7.0 (corresponding to Figure 4.2B in Chapter 4):

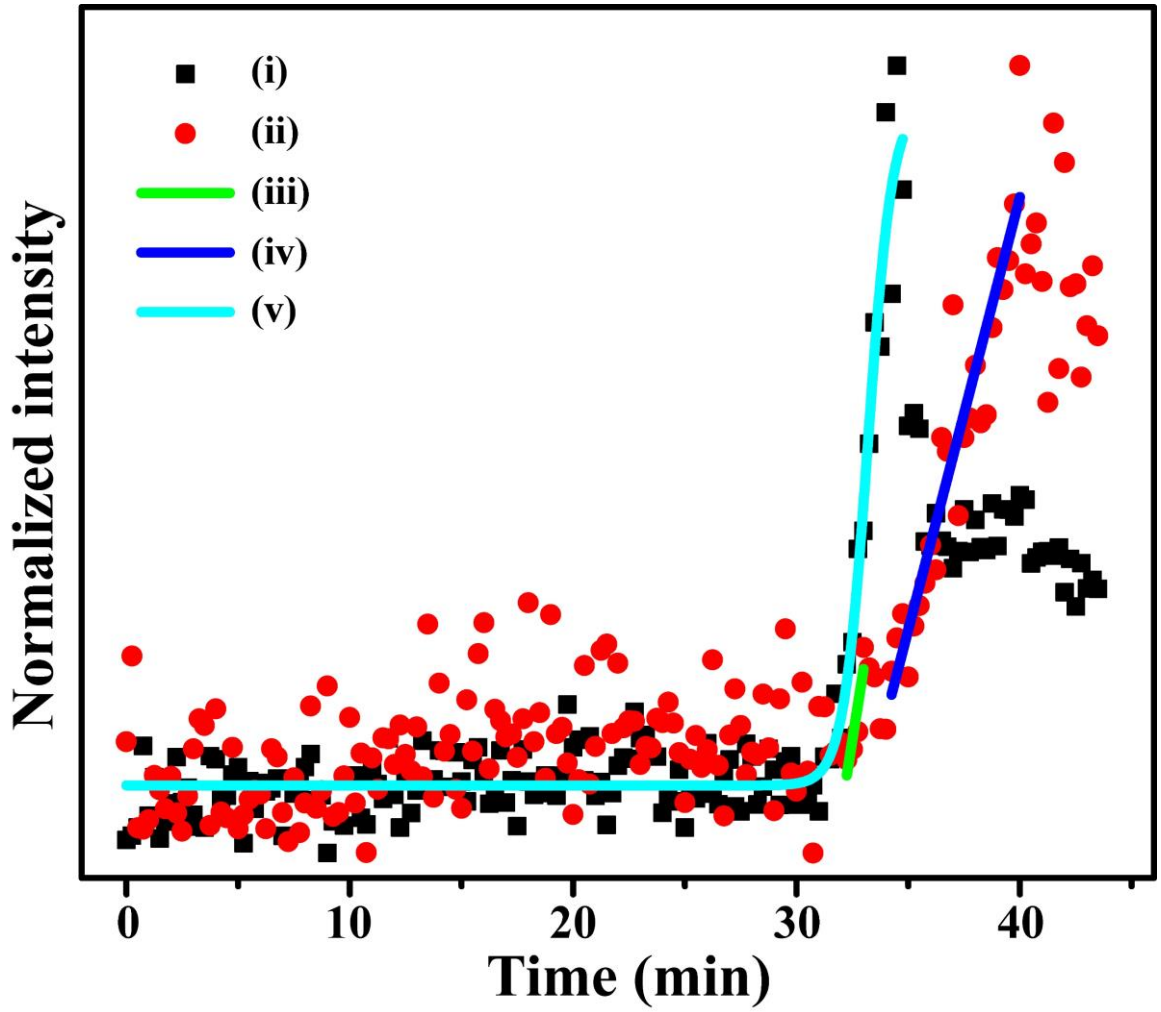

Figure A4.2: Variations of (i) 1078 cm^{-1} and (ii) 1434 cm^{-1} Raman peak intensities with time for the evaporating droplets containing ATP@AgNPs at pH 7.0 corresponding to the **Figure 4.2B** in the Chapter 4. The graphs in (iii) and (iv) are linear fittings of (ii). The graph in (v) is Boltzmann fitting of (i) showing phase transition.

TH_3719_186122105

A4.4. Time-dependent variation of 1078 cm^{-1} and 1434 cm^{-1} Raman peak intensities for pH 8.4 (corresponding to Figure 4.2D in Chapter 4):

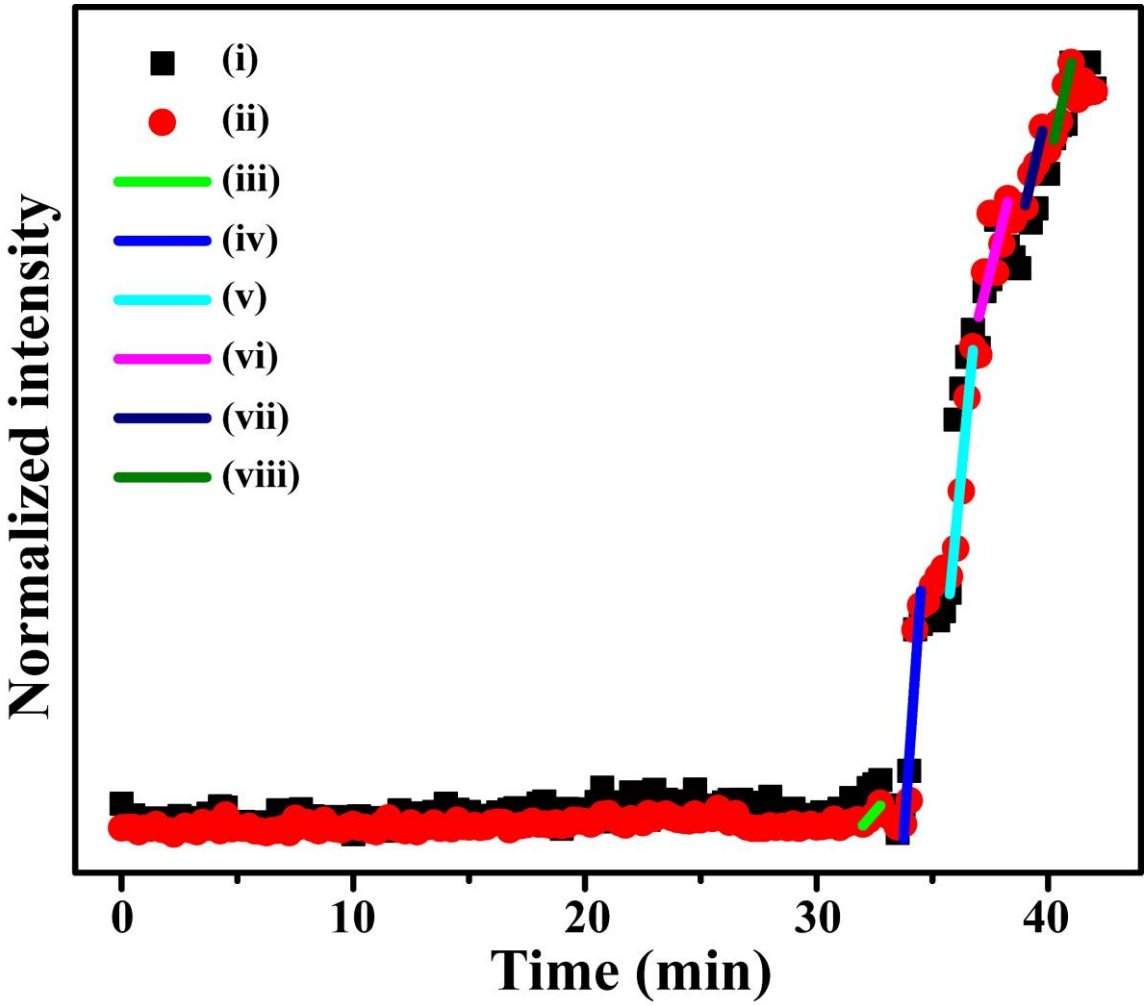

Figure A4.3: Variations of (i) 1078 cm^{-1} and (ii) 1434 cm^{-1} Raman peak intensities with time for the evaporating droplets containing ATP@AgNPs at pH 8.4 corresponding to **Figure 4.2D** in the Chapter 4. The graphs in (iii) to (viii) are linear fitting of (ii) showing six phase transition steps.

TH_3719_186122105

A4.5. Time-dependent variation of 1078 cm^{-1} and 1434 cm^{-1} Raman peak intensities for pH 9.4 (corresponding to Figure 4.2F in Chapter 4):

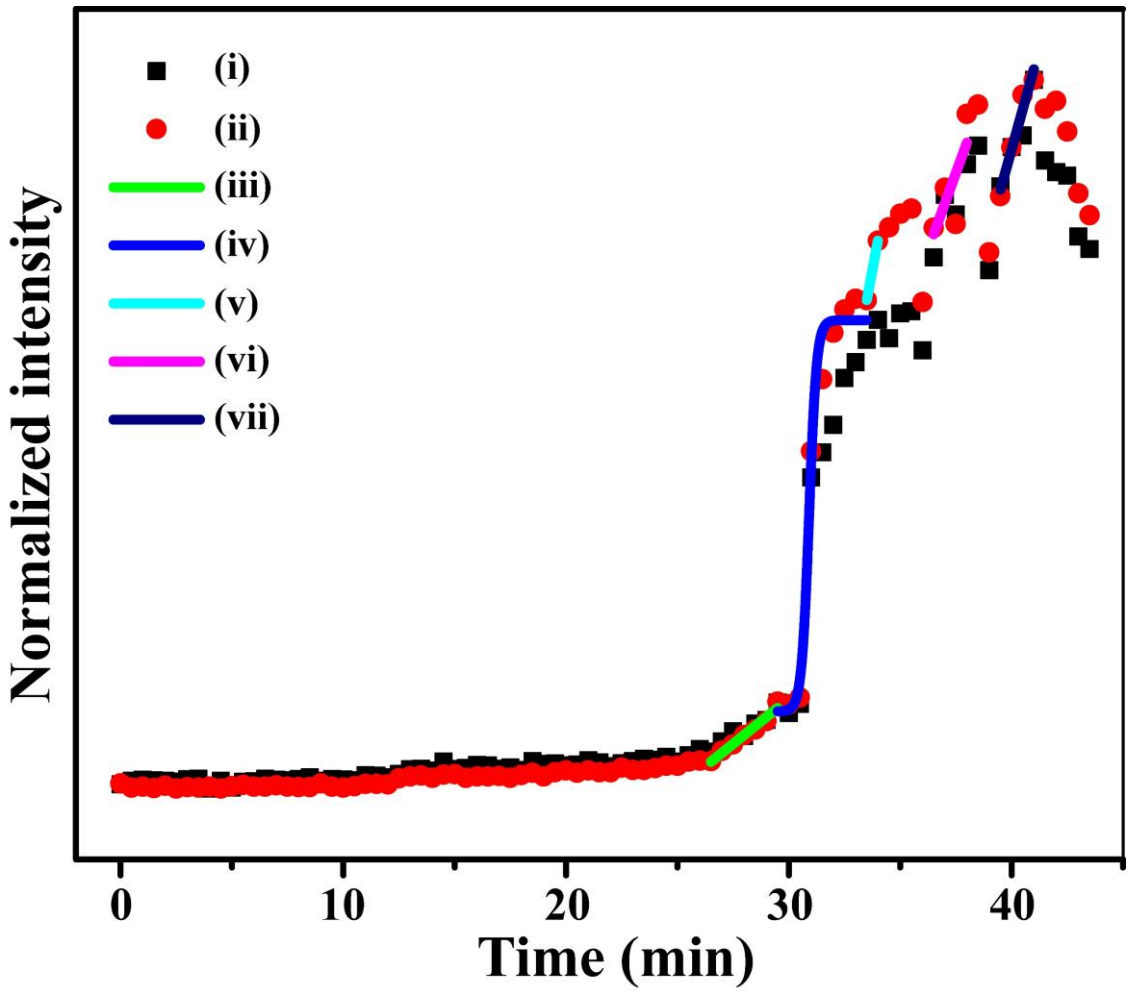

Figure A4.4: Variations of (i) 1078 cm^{-1} and (ii) 1434 cm^{-1} Raman peak intensities with time for the evaporating droplets containing ATP@AgNPs at pH 9.4 corresponding to **Figure 4.2F** in the Chapter 4. The graphs in (iii), (v) to (vii) are linear fitting of (ii). The graph in (iv) as Boltzmann fitting of (ii) showing single major phase transition.

TH_3719_186122105

A4.6. Zoomed view of time-dependent variation of 1078 cm^{-1} and 1434 cm^{-1} Raman peak intensities for pH 8.4 (corresponding to Figure 4.2D in Chapter 4):

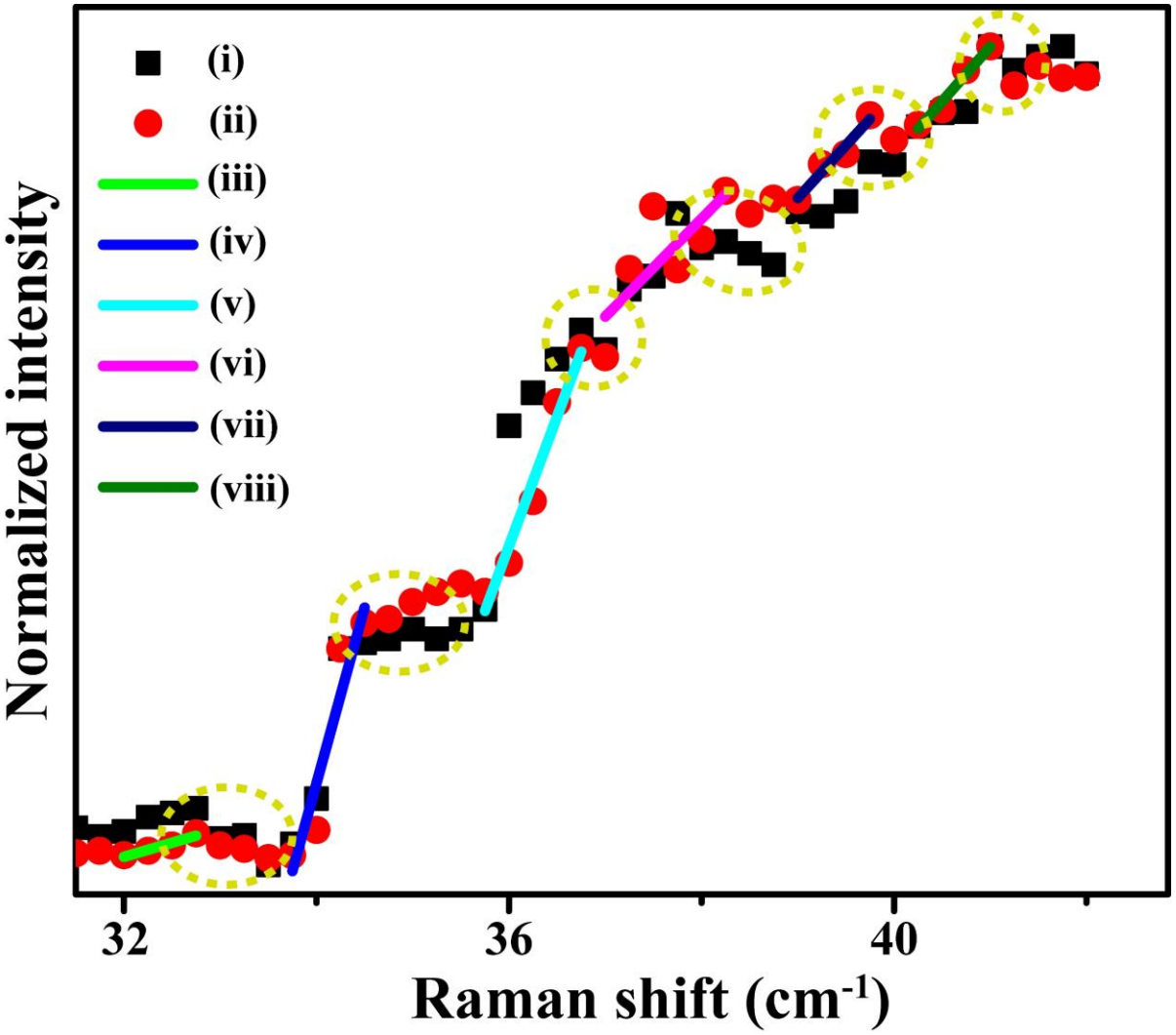

Figure A4.5: Zoomed view of the variations of (i) 1078 cm^{-1} and (ii) 1434 cm^{-1} Raman peak intensities with time for the evaporating droplets containing ATP@AgNPs at pH 8.4 corresponding to **Figure 4.2D** in the Chapter 4. The graphs in (iii) to (viii) are linear fittings of (ii) showing six phase transition steps. Decreases of signal intensity after each phase transition step are marked by yellow circles.

TH_3719_186122105

A4.7. Zoomed view of the time-dependent variation of 1078 cm^{-1} and 1434 cm^{-1} Raman peak intensities for pH 9.4 (corresponding to Figure 4.2F in Chapter 4):

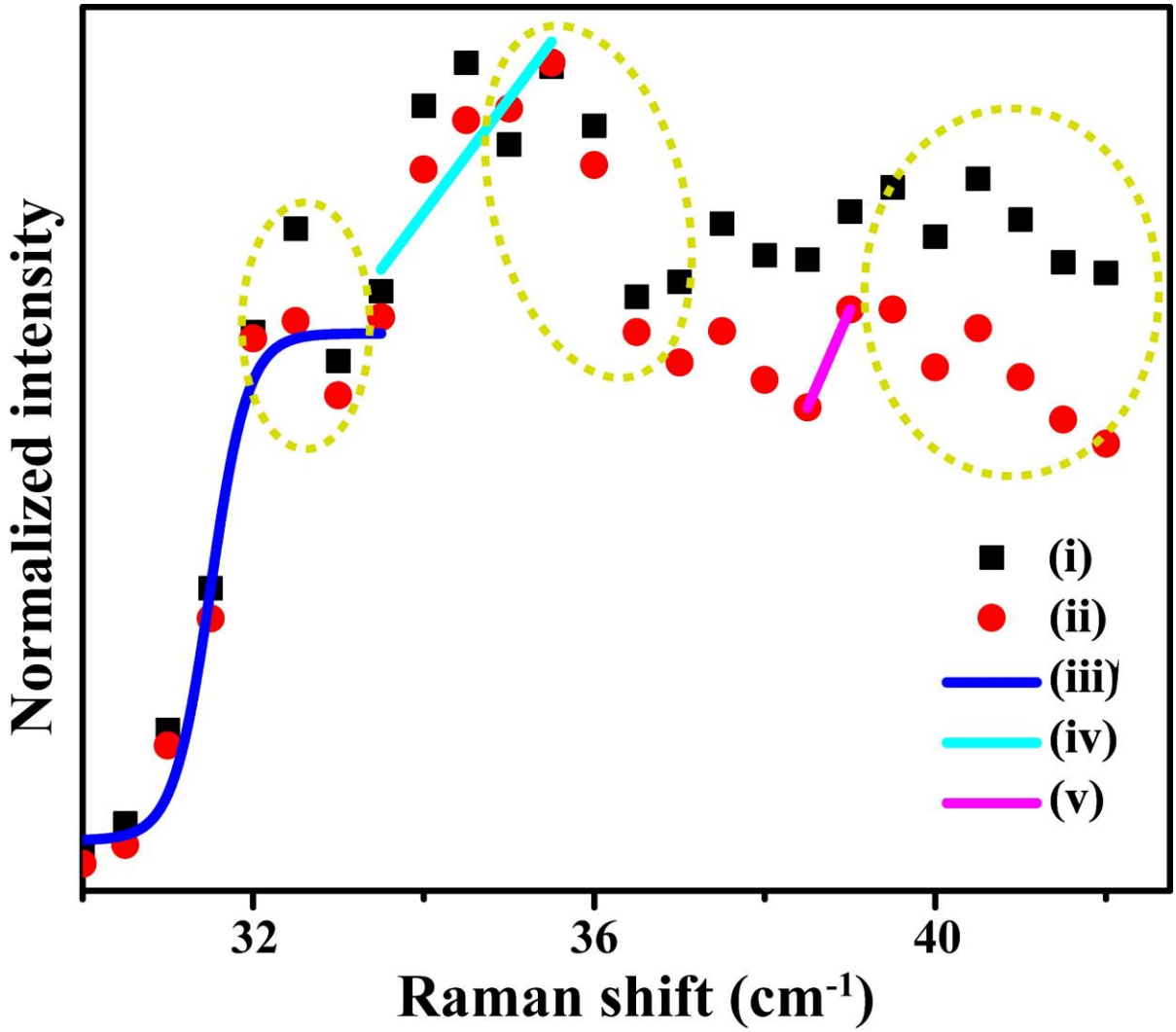

Figure A4.6: Zoomed view of the variations of (i) 1078 cm^{-1} and (ii) 1434 cm^{-1} Raman peak intensities with time for the evaporating droplets containing ATP@AgNPs at pH 9.4 corresponding to **Figure 4.2F** in the Chapter 4. The graphs in (iv) and (v) are linear fittings of (ii). The graph in (iii) is a Boltzmann fitting of (ii) showing single major phase transition. Decreases of intensity after phase transitions are marked by yellow circles.

TH_3719_186122105

A4.8. Optical images of the deposits at the TPCL after evaporation of droplets containing ATP@AgNP dispersions (corresponding to Figure 4.3 in the Chapter 4):

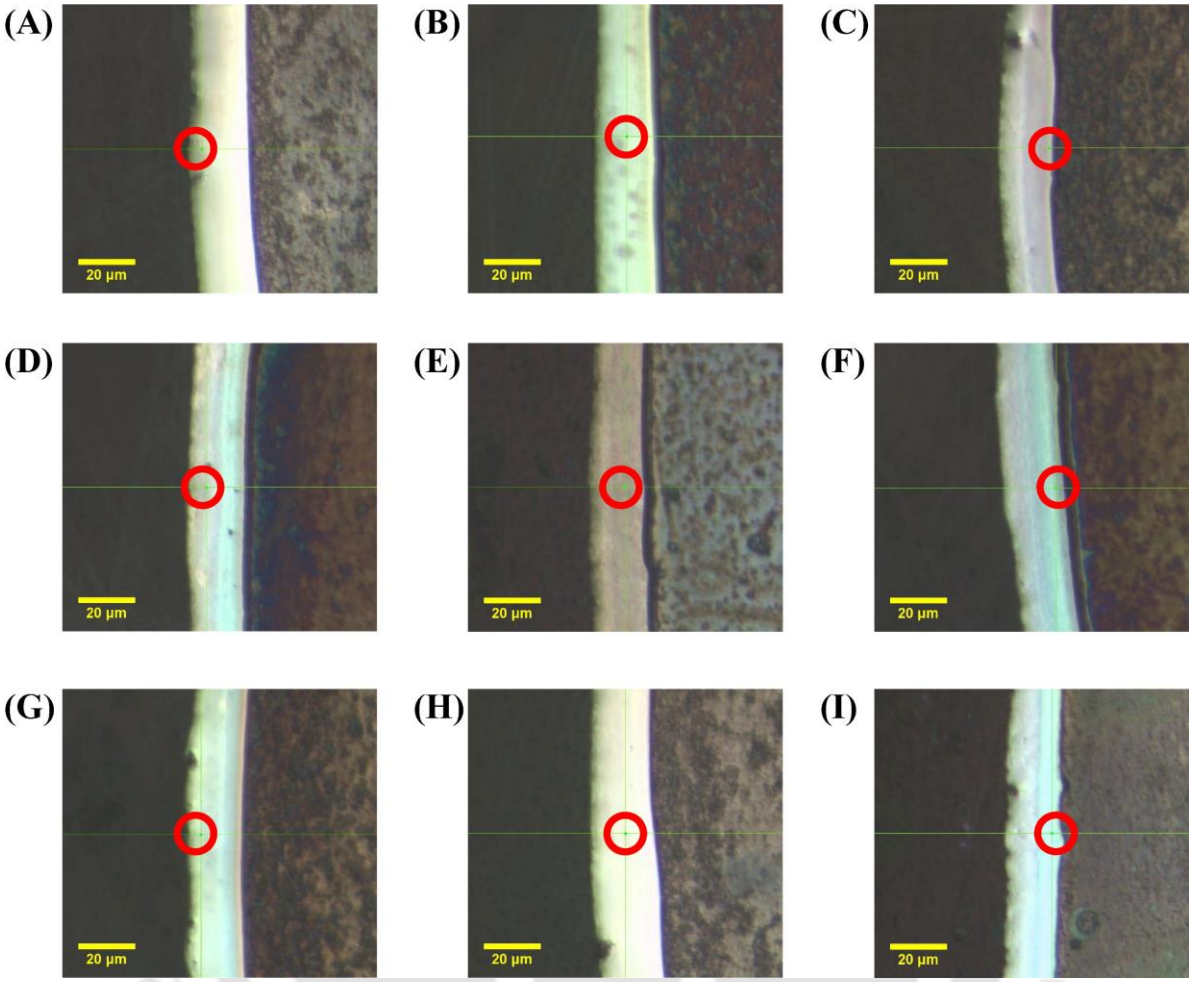

Figure A4.7: Optical images of the deposits at the TPCL after evaporation of droplets containing ATP@AgNPs dispersions at the **(A)** outer boundary of the deposit at pH 7.0, **(B)** middle of the deposit at pH 7.0, **(C)** inner boundary of the deposit at pH 7.0, **(D)** outer boundary of the deposit at pH 8.4, **(E)** middle of the deposit at pH 8.4, **(F)** inner boundary of the deposit at pH 8.4, **(G)** outer boundary of the deposit at pH 9.4, **(H)** middle of the deposit at pH 9.4, and **(I)** inner boundary of the deposit at pH 9.4. The Raman probe areas are marked by red circles. The time-dependent Raman peak intensities of these evaporating droplets are given in **Figure 4.3** in the Chapter 4.

TH_3719_186122105

A4.9. Raman spectra at different time of the evaporating droplets containing ATP@AgNP dispersions at pH 7.0 when probed at the outer boundary (corresponding to Figure 4.3A), middle (corresponding to Figure 4.3B) and inner boundary (corresponding to Figure 4.3C) of the deposits:

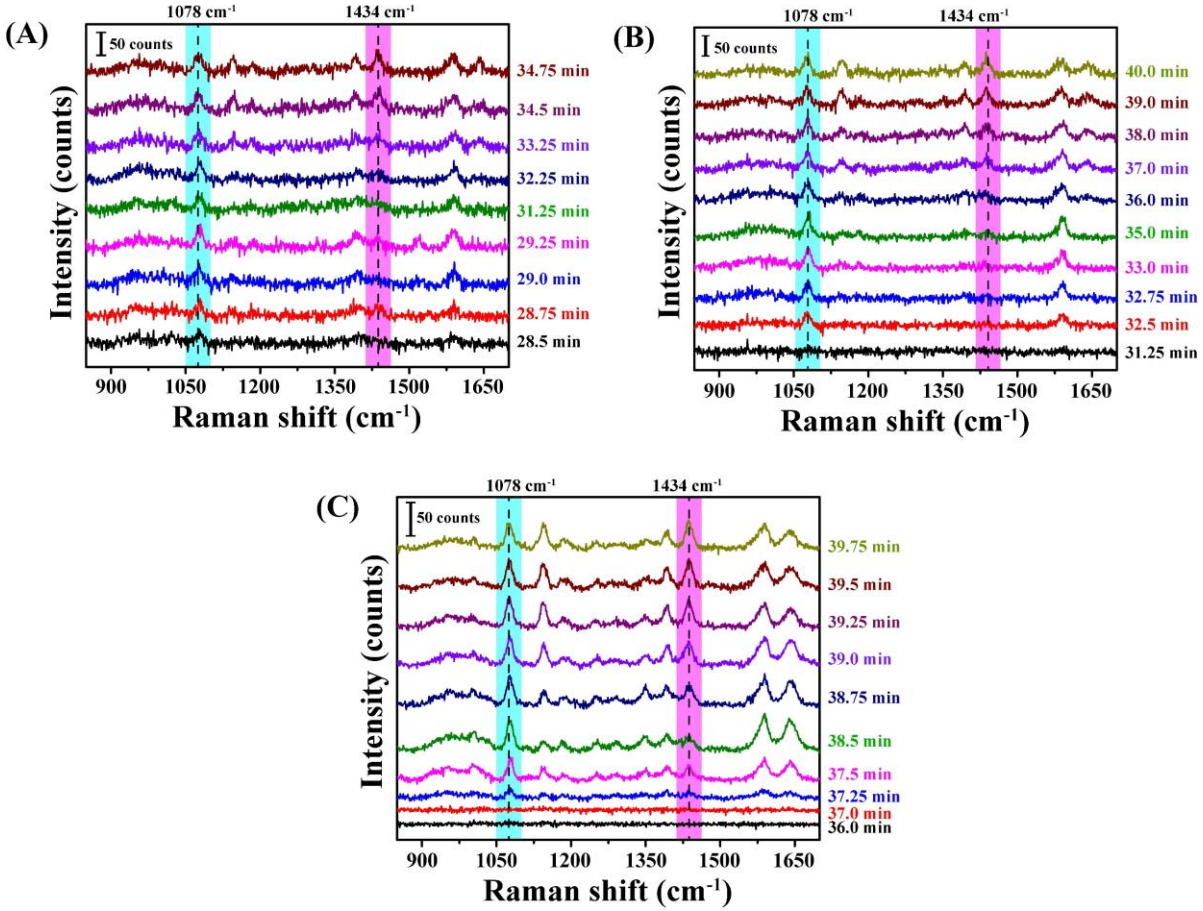

Figure A4.8: Raman spectra at different times of the evaporating droplets containing ATP@AgNP dispersions at pH 7.0 when probed **(A)** at the outer boundary of TPCL (corresponding to **Figure 4.3A** in Chapter 4), **(B)** at the middle of the deposit at TPCL (corresponding to **Figure 4.3B** in Chapter 4) and **(C)** at the inner boundary of the TPCL (corresponding to **Figure 4.3C** in Chapter 4), respectively.

TH_3719_186122105

A4.10. Raman spectra at different time of the evaporating droplets containing ATP@AgNP dispersions at pH 8.4 when probed at outer boundary (corresponding to Figure 4.3D), middle (corresponding to Figure 4.3E) and inner boundary (corresponding to Figure 4.3F) of the deposit:

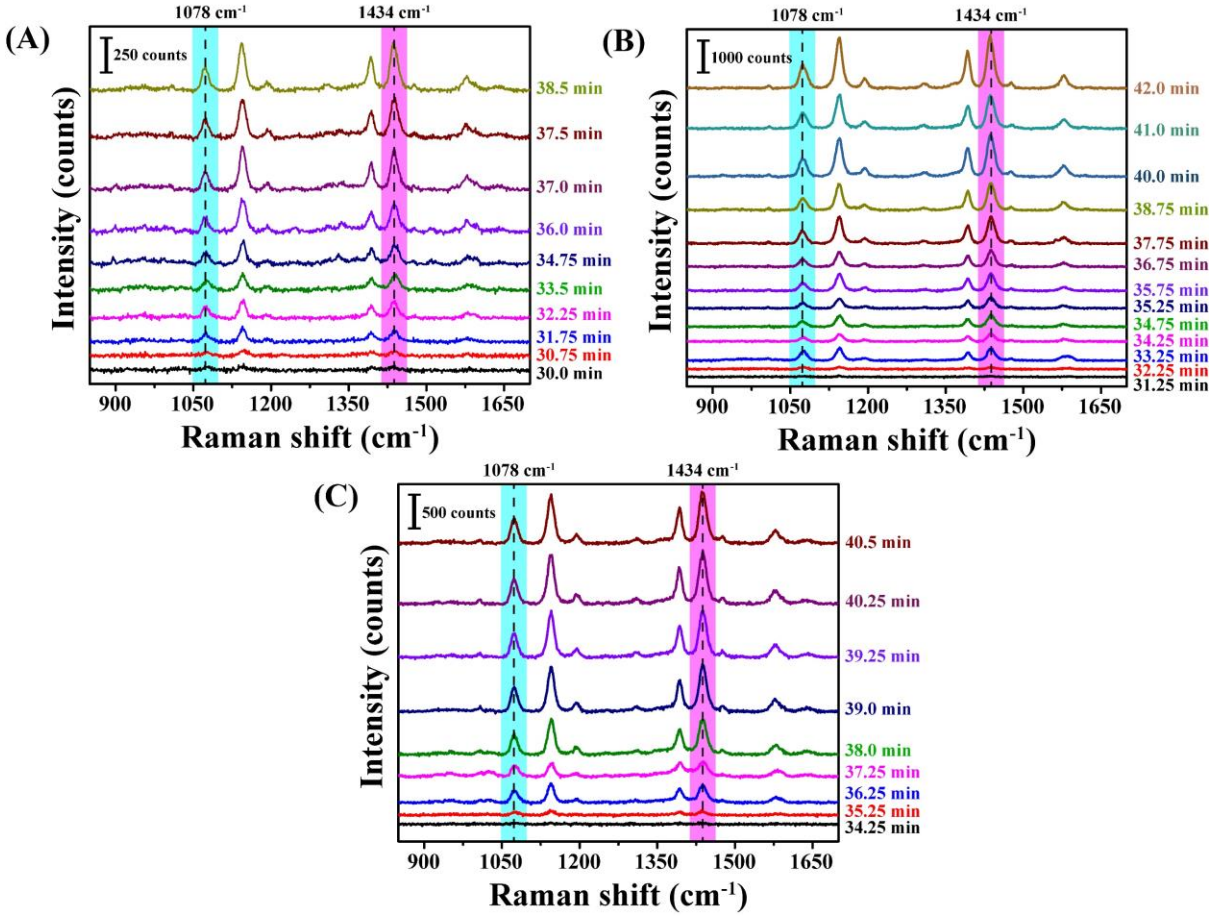

Figure A4.9: Raman spectra at different times of the evaporating droplets containing ATP@AgNP dispersions at pH 8.4 when probed **(A)** at the outer boundary of TPCL (corresponding to **Figure 4.3D** in Chapter 4), **(B)** at the middle of deposit at TPCL (corresponding to **Figure 4.3E** in Chapter 4) and **(C)** at the inner boundary of the TPCL (corresponding to **Figure 4.3F** in Chapter 4), respectively.

TH_3719_186122105

A4.11. Raman spectra at different time of the evaporating droplets containing ATP@AgNP dispersions at pH 9.4 when probed at outer boundary (corresponding to Figure 4.3G), middle (corresponding to Figure 4.3H) and inner boundary (corresponding to Figure 4.3I) of the deposit:

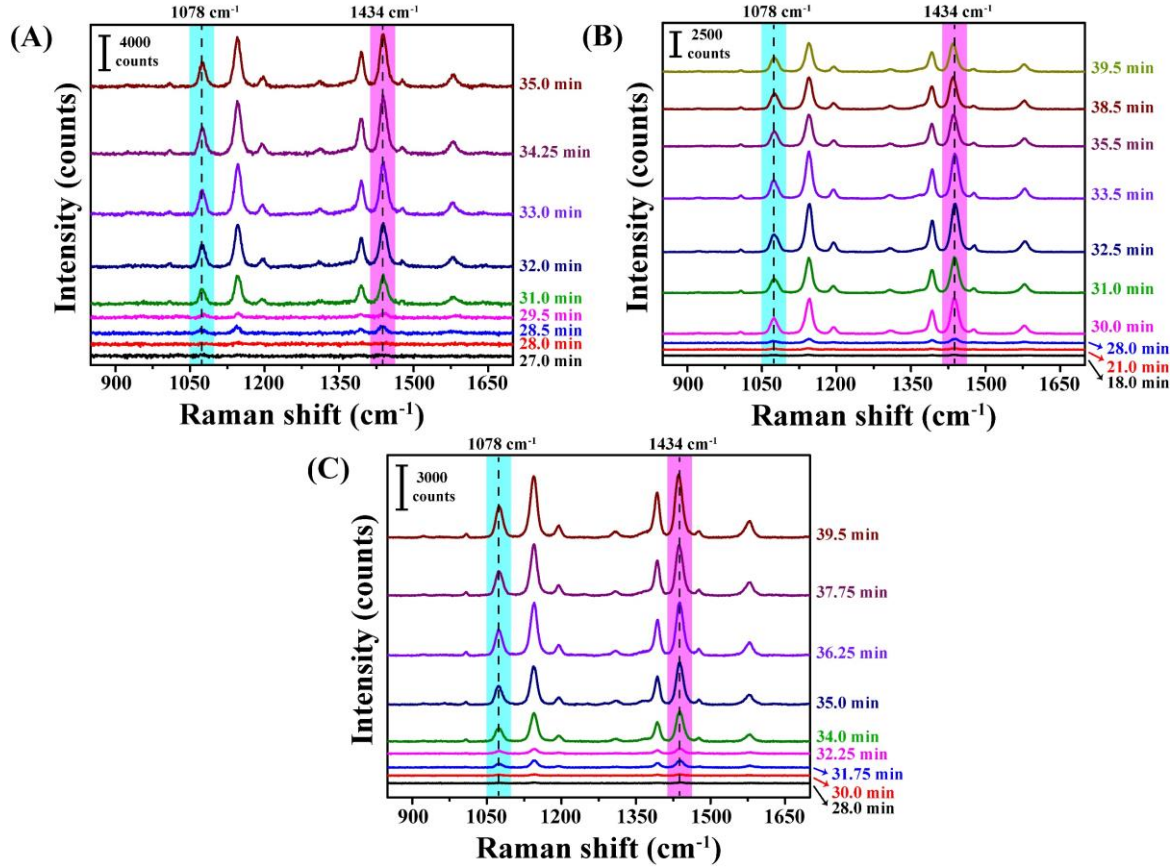

Figure A4.10: Raman spectra at different times of the evaporating droplets containing ATP@AgNP dispersions at pH 9.4 when probed **(A)** at the outer boundary of TPCL (corresponding to **Figure 4.3G** in Chapter 4), **(B)** at the middle of deposit at TPCL (corresponding to **Figure 4.3H** in Chapter 4) and **(C)** at the inner boundary of the TPCL (corresponding to **Figure 4.3I** in Chapter 4), respectively.

TH_3719_186122105

A4.12. Raman spectra at different times of the evaporating droplets containing ATP@AgNP dispersions at pH 8.4 after one to six steps of phase transitions (corresponding to Figure 4.4 in Chapter 4):

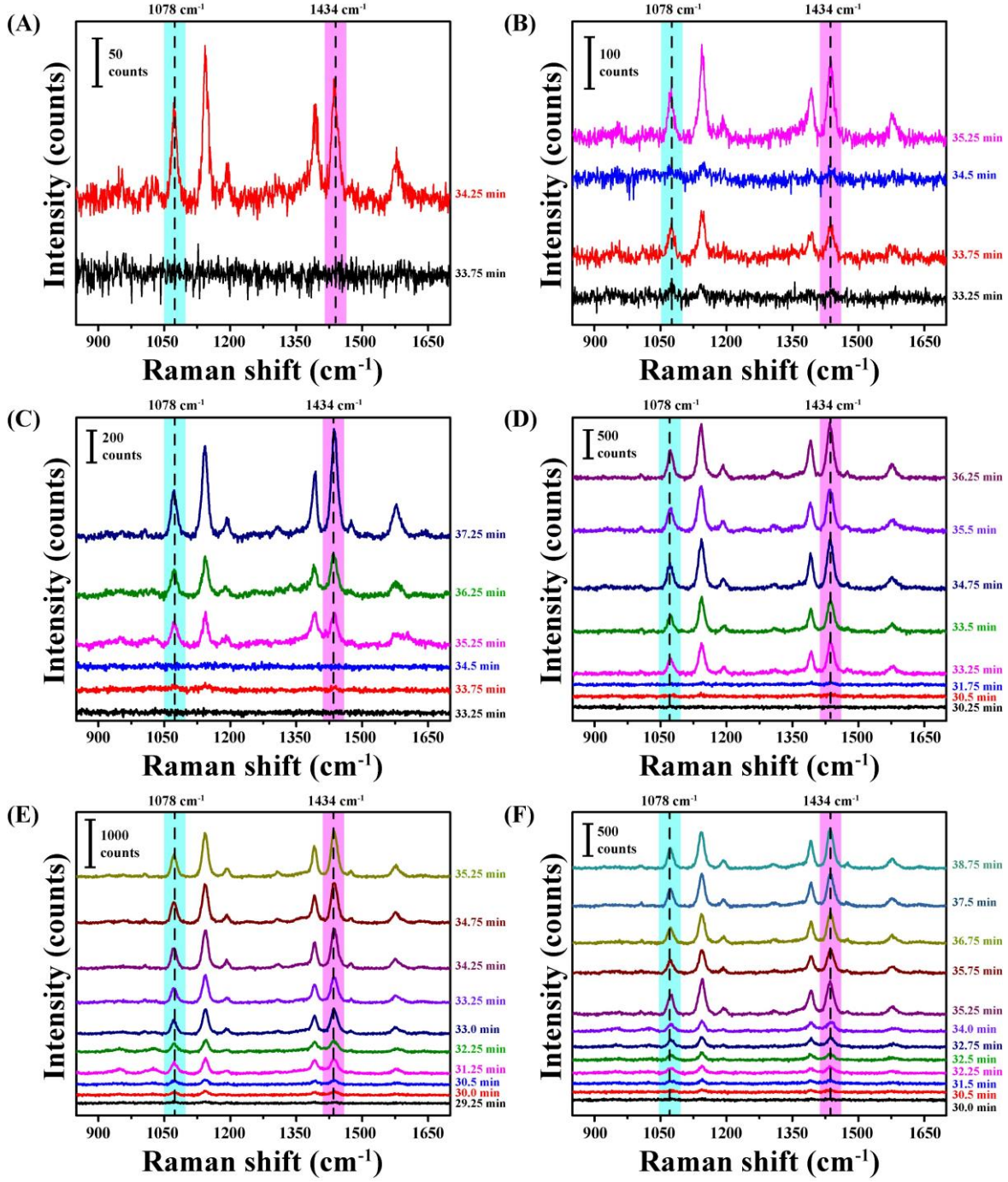

Figure A4.11: Raman spectra at different times at the TPCL of the evaporating droplets containing ATP@AgNP dispersions at pH 8.4 after **(A)** 1st, **(B)** 2nd, **(C)** 3rd, **(D)** 4th, **(E)** 5th, and **(F)** 6th phase transition steps (corresponding to **Figure 4.4** in the Chapter 4).

TH_3719_186122105

A4.13. Zeta potential measurements:

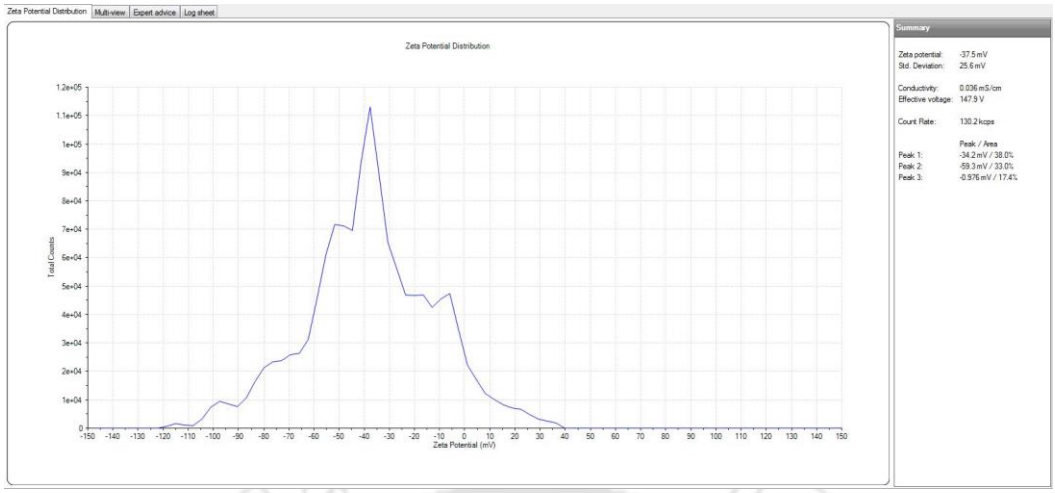

Figure A4.12: Zeta potential plot of the dispersion of ATP@AgNPs at pH 7.0.

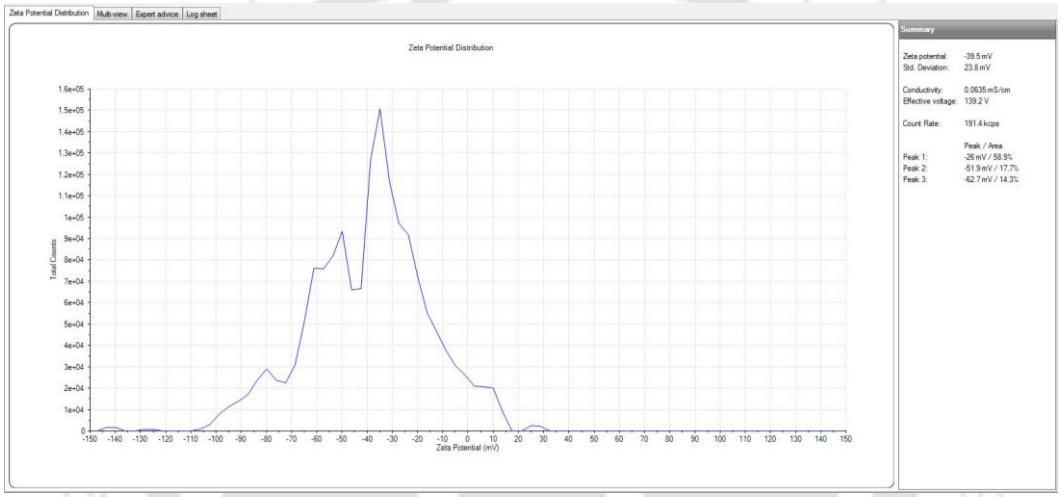

Figure A4.13: Zeta potential plot of the dispersion of ATP@AgNPs at pH 8.4.

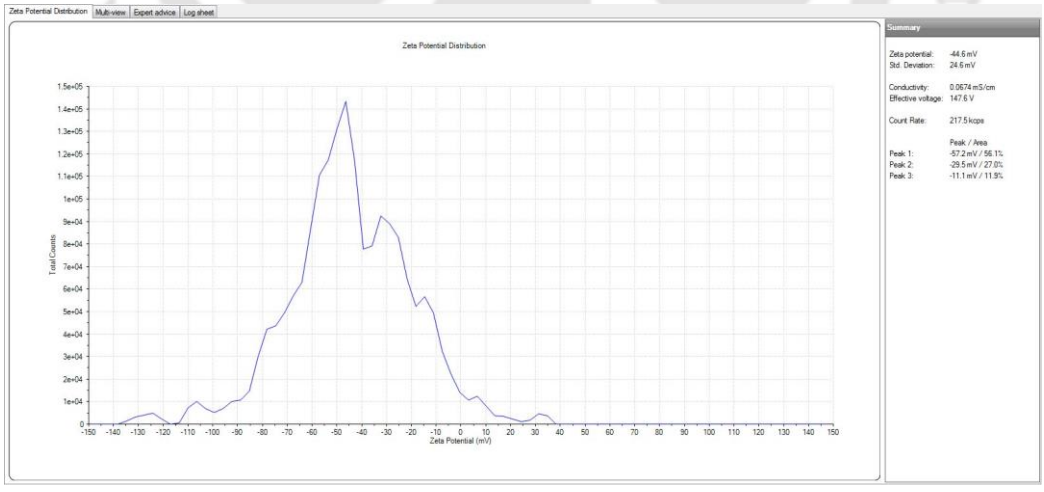

Figure A4.14: Zeta potential plot of the dispersion of ATP@AgNPs at pH 9.4.

One measurement at each pH is shown above. Zeta potential value was averaged after six measurements each of which included 10 cycles. Average zeta potential of the ATP@AgNP dispersions were found to be -37.7 ± 1.0 mV, -40.1 ± 3.0 mV and -45.8 ± 3.0 mV at pH 7.0, 8.4 and 9.4, respectively.

TH_3719_186122105

A4.14. References:

1. Huang, Y.-F.; Wu, D.-Y.; Zhu, H.-P., Zhao, L.-B.; Liu, G.-K.; Ren, B.; Tian, Z.-Q. Surface-enhanced Raman spectroscopic study of p-aminothiophenol. *Phys. Chem. Chem. Phys.* **2012**, *14*, 8485–8497.

TH_3719_186122105

Chapter-5

Anomalous Two-Dimensional Organic Molecular Crystal Formation in an Evaporating Droplet with Different Vibrational Characteristics of the Surface and the Bulk

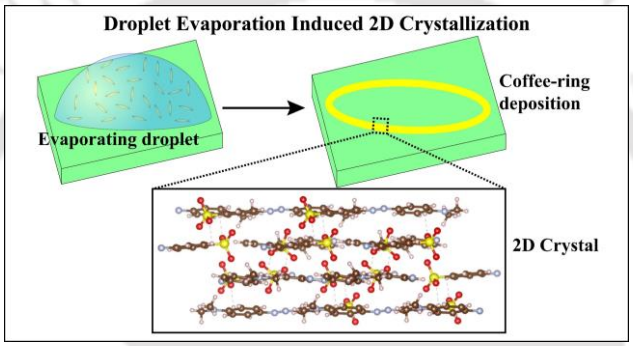

Chapter 5 *illustrates the evaporation of sessile droplet with dissolved organic molecules led to anomalous 2D crystallization at the three-phase contact line. Aqueous droplets containing methyl orange or methylene blue were evaporated into layer-by-layer deposited 2D single crystals, the structure and bonding of which were different from their 3D counterparts as probed by Raman scattering, X-ray diffraction and atomic force microscopy. Importantly, the vibrational characteristics of the surface molecules were different from those of the inner deposits. Such differences were also observed for the solution grown 3D crystals of the same molecules, indicating the general nature of the molecular crystal characteristics.*

The content of Chapter 5 has been published in *The Journal of Physical Chemistry Letters*, a journal of the American Chemical Society (ACS). *J. Phys. Chem. Lett* **2025**, *16*, 29, 7428–7435

TH_3719_186122105

https://pubs.acs.org/doi/10.1021/acs.jpclett.5c01659

5.1. Introduction

The ubiquitous solidification of molecules from a supersaturated solution into three-dimensional (3D) crystals has been fundamental to the knowledge of molecular structures and chemical bonding.[1-4] While there is a repertoire of techniques in designing and growth of crystals in 3D such ways of growing molecular single crystals in 2D and 1D from liquid solutions are yet to be systematically developed. Such crystals would not only pave the ways for new knowledge about molecular organizations but also act as essential components in applications such as low-dimensional molecule-based electronics that include flexible devices,[5] lasers,[6] quantum materials,[7] drug delivery,[8] surface enhanced Raman scattering (SERS)[9] and in chemical[10] and biological sensing.[11] Additionally, moiré superlattices of 2D molecular crystals have recently opened a new opportunity of their potential applications in sensing,[12] catalysis,[13] and as optical and quantum materials.[14] Current methods of growth of 2D organic crystals include physical or chemical vapor deposition,[15] solution techniques such as floating coffee ring driven assembly,[16] solution shearing,[17] Langmuir-Blodgett method,[18] self-assembly,[19] and coating.[20] Growing molecular crystals selectively in 2D starting with a solution remains a challenge.

Further, since the third dimension of a 2D crystal is necessarily in the nanometer scale range, the properties of the crystal would critically depend on integrity of arrangements of every layer of molecules. Thus, a question arises whether the surface molecules would keep the integrity of the crystal as the thinness of crystal becomes very small. This is important for practical applications as the molecules on the surface layer interact with external moieties for signal generation or transduction. There are generally two types of molecular environments possible in any crystalline materials. In the inside or bulk of a 3D crystal or in the inner layers of 2D crystals, all the non-bonding interactions are fully saturated. However, molecules on the surface of crystals have functional groups with unsaturated interactions and dangling bonds. Therefore, the molecular vibrational characteristics at the surface of any crystal is expected to be different from that in the bulk or inside. Modern X-ray crystallographic experiments decipher the exact structure and arrangements of molecules in the bulk of a crystal.[21] Surface crystallographic techniques such as low energy electron diffraction (LEED),[22] atomic force microscopy (AFM)[23] and scanning tunneling microscopy (STM)[24] can reveal surface defects, surface reconstruction and adsorbate interaction. However, these techniques do not provide information on the vibrational characteristics of the molecules at the surface. In these regard,

TH_3719_186122105

Raman spectroscopic technique of solid samples can reveal the properties of all the functional groups and molecular interactions at the surface of the crystals.[25] For example, it has been demonstrated that SERS techniques could be used to follow a newly discovered phase transition in an evaporating sessile aqueous droplet that contained organic molecule functionalized Au nanoparticles.[26] The same technique was used to pursue the distinction of intranaoparticle and internanoparticle reactions occurring in an evaporating sessile droplet.[27] Further, molecular specificity as well as cooperativity on the surface of a molecular crystal could be observed using SERS.[28] Thus, Raman spectroscopy could be a powerful technique in unveiling the differences in vibrational characteristics between the surface and bulk molecular species in a 2D as well as 3D crystal.

5.2. Outline of the Present Work

We report that under ambient conditions, aqueous sessile droplet evaporation induced solidifications of small organic molecules such as methyl orange (MO) and methylene blue (MB) - at the TPCL - led to the molecular 2D single crystal formations. Moreover, experiments also revealed significant differences in the vibrational characteristics of the surface molecular species when compared with those of the bulk in the same crystal. Thus, when an evaporating droplet containing aqueous MO or MB solution was subjected to Raman spectroscopic probe at the TPCL, a phase transition corresponding to dispersion to deposit phase was observed. Powder X-ray diffraction (XRD) patterns of the deposits indicated 2D single crystal formations following layer-by-layer growth of the molecules. TEM results also supported the stacking of 2D sheets and dot pattern SAED indicated single crystal formation at the TPCL. The experimental observations were further substantiated by simulations that revealed growth of crystalline molecular layers in 2D, with limited growth in the third dimension. Importantly, when the 2D crystals were etched with high power laser or scrapped off mechanically and then probed for Raman scattering, the results indicated substantial vibrational frequency differences between the top layers and that underneath. Similar results were obtained for solution grown 3D crystals of the same molecules, indicating the general nature of the differences in vibrational characteristics between the surface layers and those underneath in molecular crystals.

TH_3719_186122105

5.3. Experimental Section

5.3.1. Materials:

Methyl orange powder (MO) and methylene blue (MB) were purchased from Sigma-Aldrich. Nitric acid (98%) and hydrochloric acid (35%) were bought from Merck India. All the glass apparatus was pre-cleaned with aqua regia and water before being used in experiments. Milli-Q grade water was used for all the experiments.

5.3.2. Instruments and Characterizations:

Raman spectra were recorded using Horiba LabRAM HR Evolution Raman spectrometer attached with 532 and 633 nm laser source. Atomic force microscopic (AFM) measurements on the dried deposits were performed using Oxford Asylum Research Model: MFP-3D instrument. Powder X-ray diffractions were recorded using Rigaku TTRAX-III X-ray diffractometer instrument. The thin film samples were prepared by drop casting multiple small droplets containing solution of MO or MB. Transmission electron microscopic (TEM) images and selected-area electron diffractions (SAED) were obtained from JEOL JEM-2100F field emission transmission electron microscope (FETEM) instrument having acceleration voltage of 200 kV. FETEM samples were prepared by drop-casting 5 µL of solution on carbon-coated copper grids.

5.3.3. Raman measurements at three-phase contact line (TPCL):

5 µL of 1.53 mM aqueous solution of MO or 5 µL of 1.57 mM aqueous solution of MB was carefully dropped on a clean glass slide so that it formed a cylindrical capped drop with circular base. Then the glass slide was kept on the sample holder of Raman spectrometer and Raman measurements were carried out at the three-phase contact line (TPCL) at every 2.5 min until the droplet was completely evaporated. In order to probe the crystallization process, 5% laser power of 50 mW 532 nm laser i.e., 2.5 mW and 5% laser power of 16 mW 633 nm laser i.e., 0.8 mW for MO and MB, respectively, were used. Spectra were recorded for 5 s acquisition time, 3 accumulation number at 600 gr/mm diffraction grating focused under 50x objective lens.

In order to measure the Raman spectra of surface and interior of MO and MB crystals, 0.5 mW (1% of total power) of 532 nm laser and 0.16 mW (1% of total power) of 633 nm laser irradiations were used, respectively keeping all other parameters same. Surface of the MO and MB crystals were etched by using 5% of total power of each laser.

TH_3719_186122105

5.3.4. Computational calculations:

At first, the 2D and 3D crystal structures of MO and MB crystals of thin films were obtained by refinement of the powder XRD patterns using Endeavour 1.8 software of Crystal Impact.[29] Then from the crystal unit cell, interior and surface of each were constructed. The molecular structures in the constructed interior and surface were optimized by Quantum ESPRESSO program package[30] in 'relax' mode using optimized norm-conserving Vanderbilt (ONCV) pseudopotentials[31] constructed using the Perdew-Burke-Ernzerhof (PBE)[32] generalized gradient approximation (GGA).[33] In case of interior of the crystal, periodicity in all three directions were kept intact. In other words, the obtained unit cell after refinement was used for interior of crystal. To construct the surface of the crystal, 20 Å vacuum was given in the z-direction. This broke the periodicity along z-direction, however, periodicity along x and y-directions were kept intact such that it formed slab of surface. The kinetic energy cutoff was set at 340 eV. In order to reduce computational cost, the crystal structures were optimized only in 'gamma' Monkhorst-Pack *k*-point[34] mesh in the first Brillouin zone. The optimized structures of unit cells are given in **Figure A5.6, A5.8 and A5.16** in the appendix of Chapter 5 (A5). After that, Raman spectra were calculated from the optimized structure of MO or MB on the surface and interior of crystals using Gaussian 16 software.[35] Density functional theory (DFT) calculations were performed using B3LYP functional[36] and 6-31g(d,p) basis set,[37] which consists of both the diffused and polarization functions.

5.4. Results and Discussions

5.4.1. Raman measurements:

The 2D crystallization was pursued by placing droplets of aqueous solutions of MO or MB on a glass slide at 22 °C and 60 % relative humidity. Simultaneously, time-dependent Raman scattering intensity was recorded after focusing the laser beam at the TPCL as shown in **Scheme 5.1**. The reported UV-vis spectroscopic measurements revealed that MO and MB have absorption maxima at 500 nm and 664 nm, respectively.[38, 39] Therefore, during Raman measurements, excitation wavelengths of 532 nm and 633 nm were chosen for MO and MB, respectively, in order to obtain intense resonance Raman spectra. Results for MO are given in details here and those for MB are included in the **Appendix A5**. The results for MO are presented in **Figure 5.1**. Raman spectra with time are plotted in **Figure 5.1A** and time-dependent variation of 1394 cm^{-1} peak, which is the characteristic signal for collective vibrations - ν(N=N), ν(C–C) and δ(C–H), is plotted in **Figure 5.1B**. As is clear from **Figure**

TH_3719_186122105

5.1A, the signal intensity was poor from the beginning till 25.0 min; however, the signal intensity started to improve with time and at 30.0 min of evaporation, appearance of intense

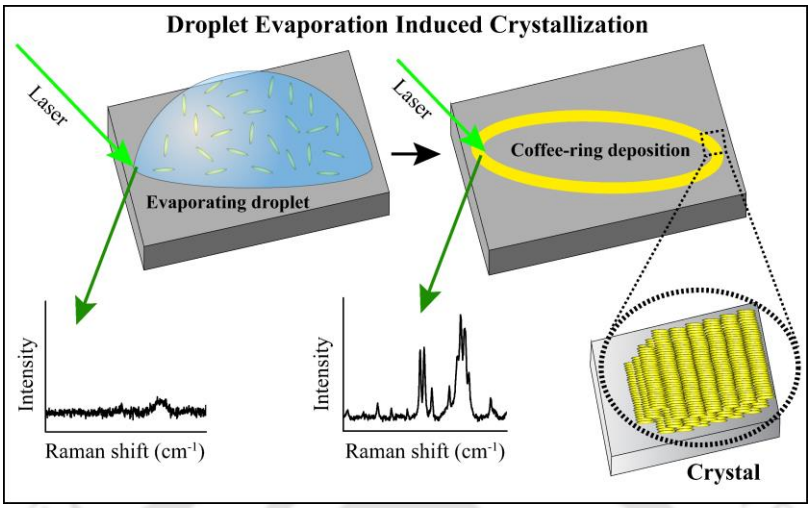

Scheme 5.1: A schematic of the Raman spectroscopic measurements at the TPCL of evaporating droplet, leading to evaporation induced crystallization of the dissolved molecules.

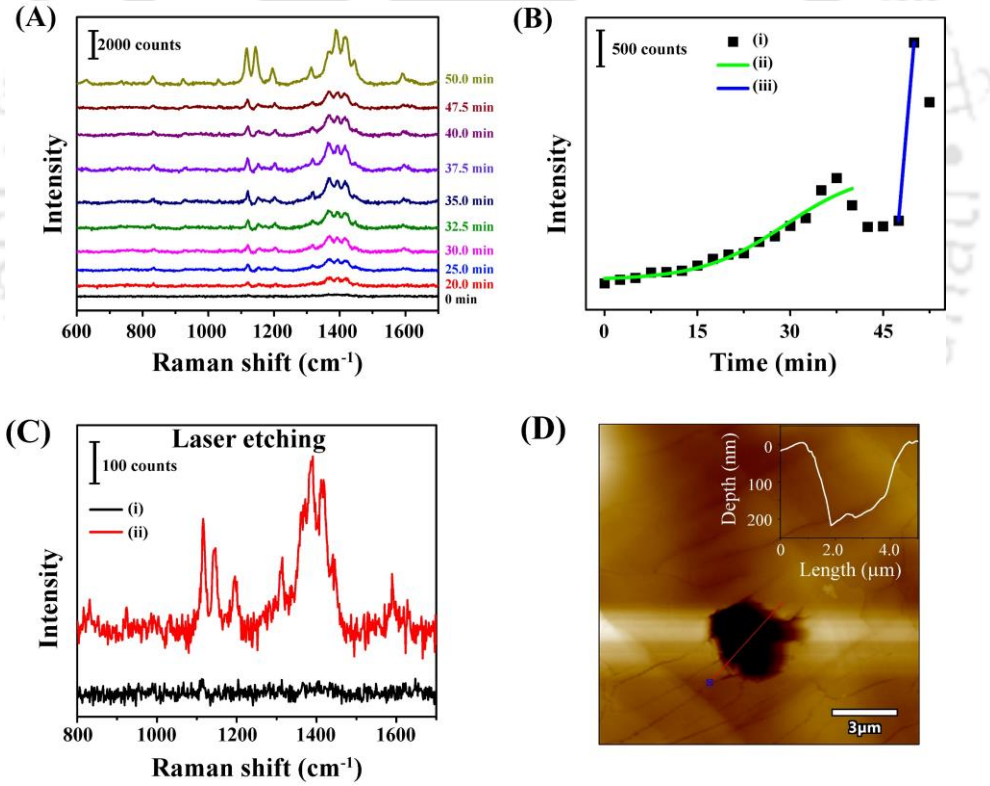

Figure 5.1: (A) Raman spectra at different times at the TPCL of evaporating droplet containing aqueous solution of MO using probed 2.5 mW laser power. (B)Variation of 1394 cm-1 peak intensity of MO with time while the droplet was evaporating. Traces (ii) and (iii) in (B) were nonlinear Boltzmann fitting and linear fitting, respectively. (C) Raman spectra (probed using 0.5 mW power) of MO on the (i) smooth surface and (ii) etched surface after etched by the laser and (D) corresponding AFM image of the etched area with depth profile in the inset.

TH_3719_186122105

peaks could be observed. The increase in intensity continued till 37.5 min. This was followed by decrease in intensity for the next 10 min. Starting at 47.5 min the signal intensity went up again and became intense when the deposit at the TPCL was completely dry. As is evident from **Figure 5.1B**, for the first 30 min of evaporation, there was indication of gradual depositions of the molecules. This was followed by faster depositions in a short window of time (30.0 min to 37.5 min). This is consistent with earlier observations of gradual depositions of colloidal particles of evaporating droplets, with accelerated depositions at the end and before complete drying.[40] The increase of the signal intensity was because of solidification of MO at the TPCL. The effects of shrinking of the droplet height with time and the laser refraction at the TPCL were negligible because the light scattered at zero degree angle with respect to incident beam i.e., perpendicular to the glass substrate was collected[41] and the laser light passed through the minimum length in the liquid medium at the outermost boundary of the droplet that is at the TPCL. Further, our earlier observations, with depositions of ligand-stabilized Au and Ag nanoparticles,[26, 27] suggest that the removal of water from the surface of MO solid depositions was the plausible cause of the intensity decrease following complete deposition. This was further confirmed by addition of water on top of the dried solid, which resulted in reversion of the intensity. The results in this regard are included in **Figure A5.1** in the appendix A5. Surprisingly, after complete drying of water at 47.5 min, signal intensity went up drastically at that same probe area. After analyzing the evaporated solid in the Raman microscope, as shown in **Figure A5.2**, the presence of a dark spot was found at the probe area, which was different from the smooth surface where laser was not shone.

In a separate experiment, after complete drying of the droplet having MO solution, at first Raman spectrum was recorded using a low power (0.5 mW) of the 532 nm laser light such that no similar spot on the surface could be observed. Under this condition, the Raman signal intensity was poor as shown in **Figure 5.1C(i)**. Then, the surface of the MO thin film was exposed to a high power (2.5 mW) of the 532 nm laser. Following that, when Raman spectrum was recorded on the spot using 0.5 mW laser power, an intense signal was observed as shown in **Figure 5.1C(ii)**. Later, the probe area was analyzed by atomic force microscopic (AFM) measurements and it was found that the surface of the deposit was etched by the intense laser power (**Figure 5.1D**) and the highly intense signal in **Figure 5.1C(ii)** was originating from the MO molecules located at bulk or inner layers of the thin film. The results indicated that the vibrational characteristics of the surface MO molecular depositions at the TPCL might be different from that of the bulk. Thus, the steep rise in the intensity following compete drying

TH_3719_186122105

of the droplet might be due to the exposition of the inner layers of the deposition in the presence of the intense probe laser light when the sample was fully dry. The final drop of the intensity as in **Figure 5.1B** may be due to burning of the sample under excessive laser exposure.

5.4.2. AFM measurements:

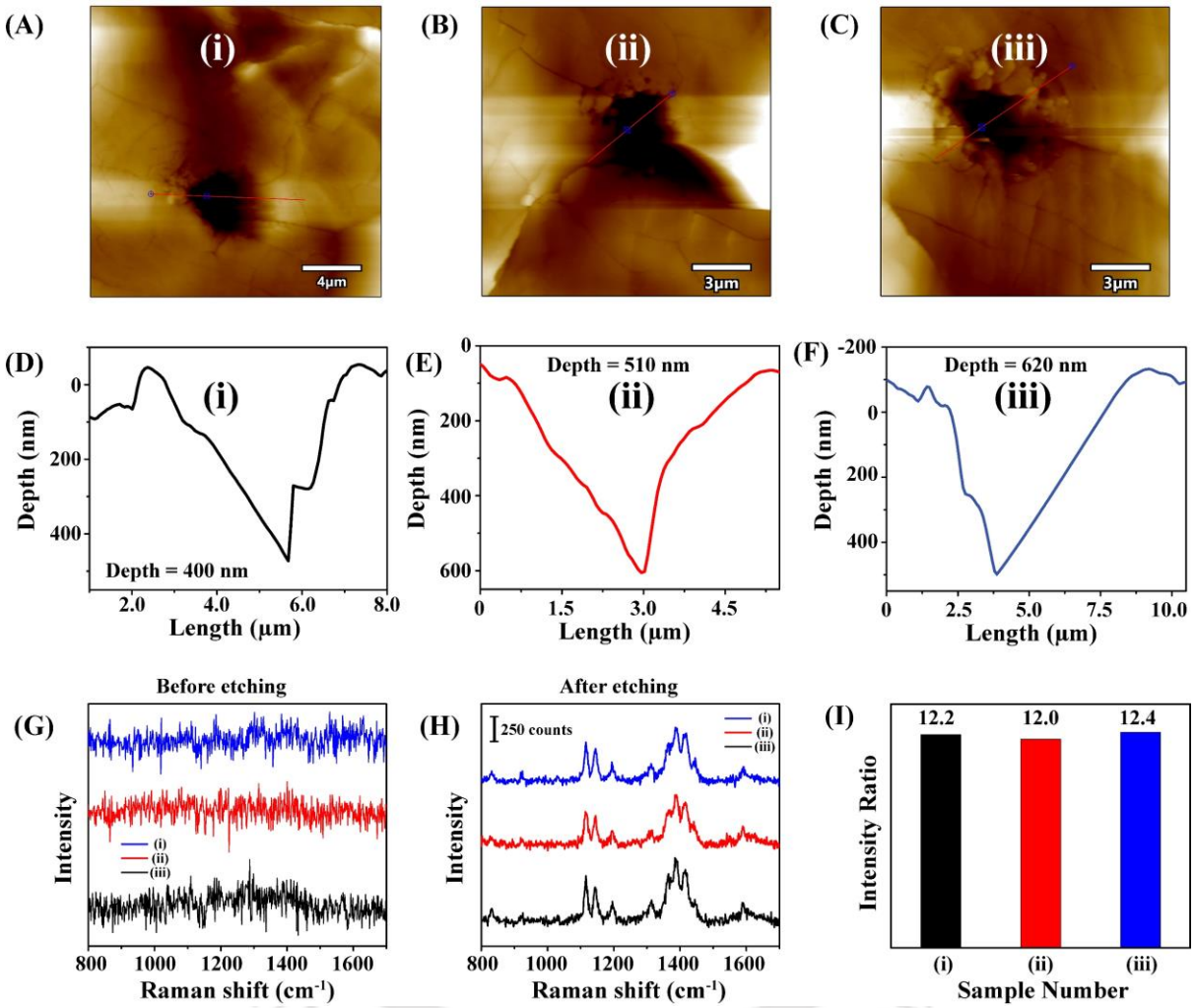

Figure 5.2: AFM images of the area on MO thin film etched with 2.5 mW 532 nm laser with exposure time of (A) 5 sec, (B) 9 sec and (C) 15 sec. (D), (E) and (F) Depth profile of the etched areas shown in (A), (B) and (C), respectively. Corresponding Raman spectra of MO on the areas (G) before etching and (H) after etching. Raman spectra were recorded using same parameters. (I) Ratio of the 1394 cm^{-1} peak intensity of the signals after etching to before etching.

Further experiments revealed that vibrational characteristics of the inner layers of the solid deposits were independent of the extent of etching. In this regard, three spots of MO thin film were irradiated with 2.5 mW of the 532 nm laser beam for 5, 9 and 15 s. This was followed by recording of Raman spectra and AFM measurements for the etched samples (**Figure 5.2**). As

TH_3719_186122105

shown in **Figure 5.2A, B, C**, the AFM images indicated increasing depth of etching as the exposure time was increased. Thus, for the 5, 9 and 15 s of exposures, the depths of etching were 400, 510 and 620 nm (**Figure 5.2D, E, F**). Importantly, the intensity of the Raman signals did not change with the extent of etching. As shown in **Figure 5.2I**, the ratios of 1394 cm^{-1} peak intensity after and before etching were nearly 12.2 ± 0.2 for each depth of 400 nm, 510 nm and 620 nm. The results indicated that the vibrational characteristics of the bulk molecules in the 2D solid that were deposited from the evaporation of the droplet were the same irrespective of their location in the matrix. Importantly, Raman scattering of the molecules in the bulk were strong as compared to those on the surfaces. Further experiments on the solid deposits of MO were performed by gently scrapping the surfaces mechanically using a tweezer. The results are included in the appendix (**Figure A5.3**), which suggest, even mechanical etching of the surfaces had improved the quality of Raman signal. For example, the Raman signal of MO at the mechanically etched area was nearly 20 times as intense as that recorded at the as-deposited (smooth) area (**Figure A5.3**).

5.4.3. Powder XRD measurements and molecular structure of thin film:

In order to further understand the molecular structure of the deposits vis-à-vis the difference between the surface molecular properties and bulk, their X-ray diffraction studies were pursed. The diffractions were recorded for the deposits obtained from several identically evaporated droplets placed next to each other. Typically, 15 such 3 mm diameter droplets containing MO solution were deposited with separation of one another of about 1-2 mm. In **Figure 5.3A**, the XRD pattern of the thin film recorded after complete evaporation of several droplets is shown in blue color. As is clear from the figure, MO thin film had a major diffraction at 4.2 ° (2θ). and a minor one at (2θ) 8.4 ° was also observed. The results indicated that crystalline films were formed at the TPCL following evaporation of the droplets containing MO solution. Further, the XRD pattern of the thin film formed after droplet evaporation was very different from those of the powder (red) and the 3D single crystals (black) of MO (**Figure 5.3A**), where several peaks of the crystals could be observed. The existence of a single major peak implied the selective growth of only one crystalline plane. After comparing the XRD data of the thin films with those of the bulk crystals, it was found that only (100) plane of the MO had grown in the solid deposits following evaporation of the droplets. In other words, at the TPCL, MO formed 2D crystal or planar crystal, as majority of the thin films consisted of only one crystal plane. Furthermore, theoretical refinement using the XRD of thin films of MO revealed that the 2D crystal also composed of layer by layer arrangements of MO molecules as shown in the

TH_3719_186122105

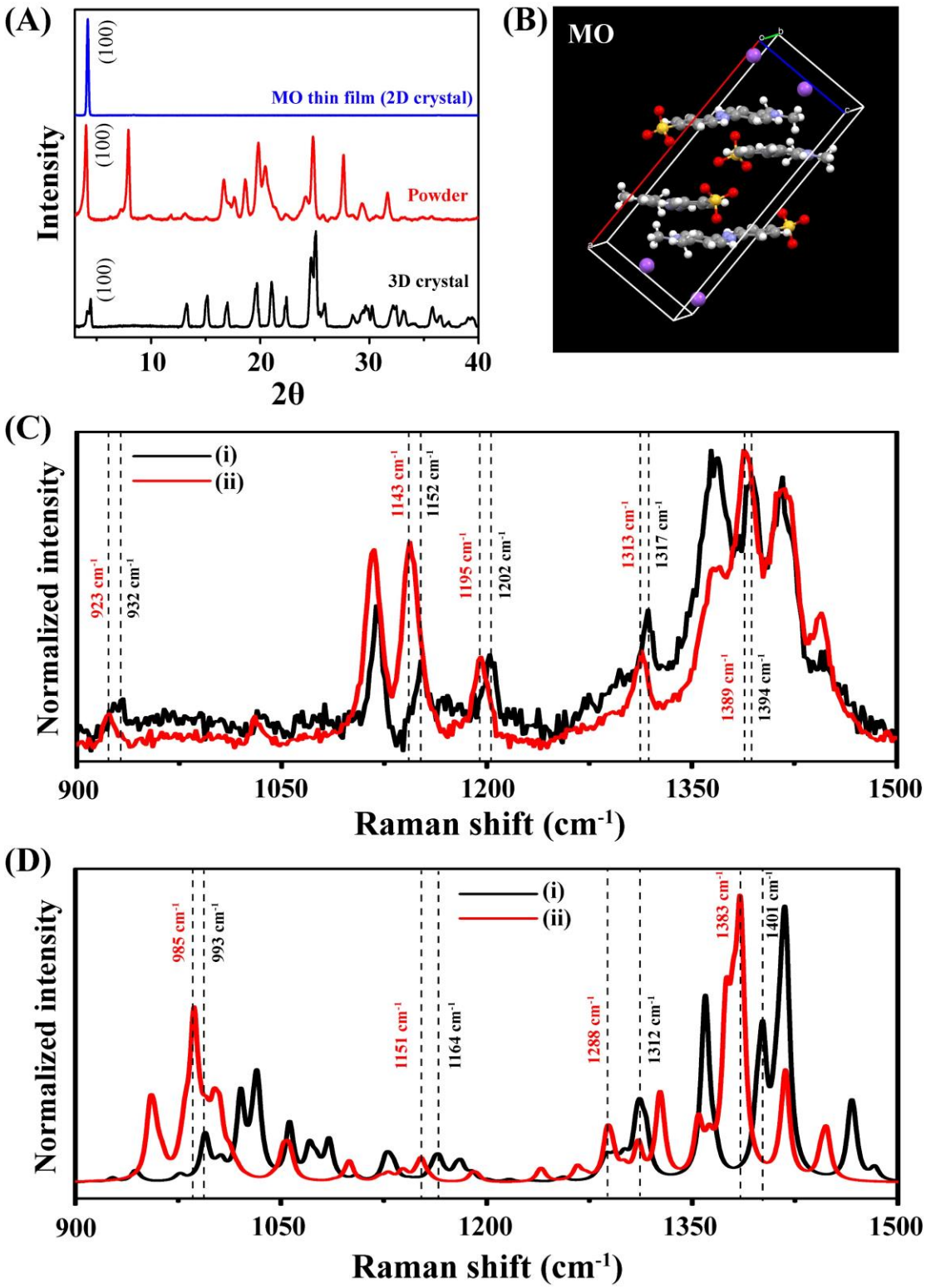

Figure 5.3: (A) Powder XRD pattern of the bulk MO crystal (black), MO powder (red) and the MO thin film (blue) obtained after evaporation of droplet having MO solution. (B) Crystal structure of MO after refinement of the powder XRD pattern of thin film. Gray, white, light blue, red, yellow and violet atoms are C, H, N, O, S and Na atoms, respectively. (C) Experimental Raman spectra and (D) calculated Raman spectra, showing different peak positions of MO on the (i) smooth surface of crystal and (ii) etched surface or inside the crystal.

TH_3719_186122105

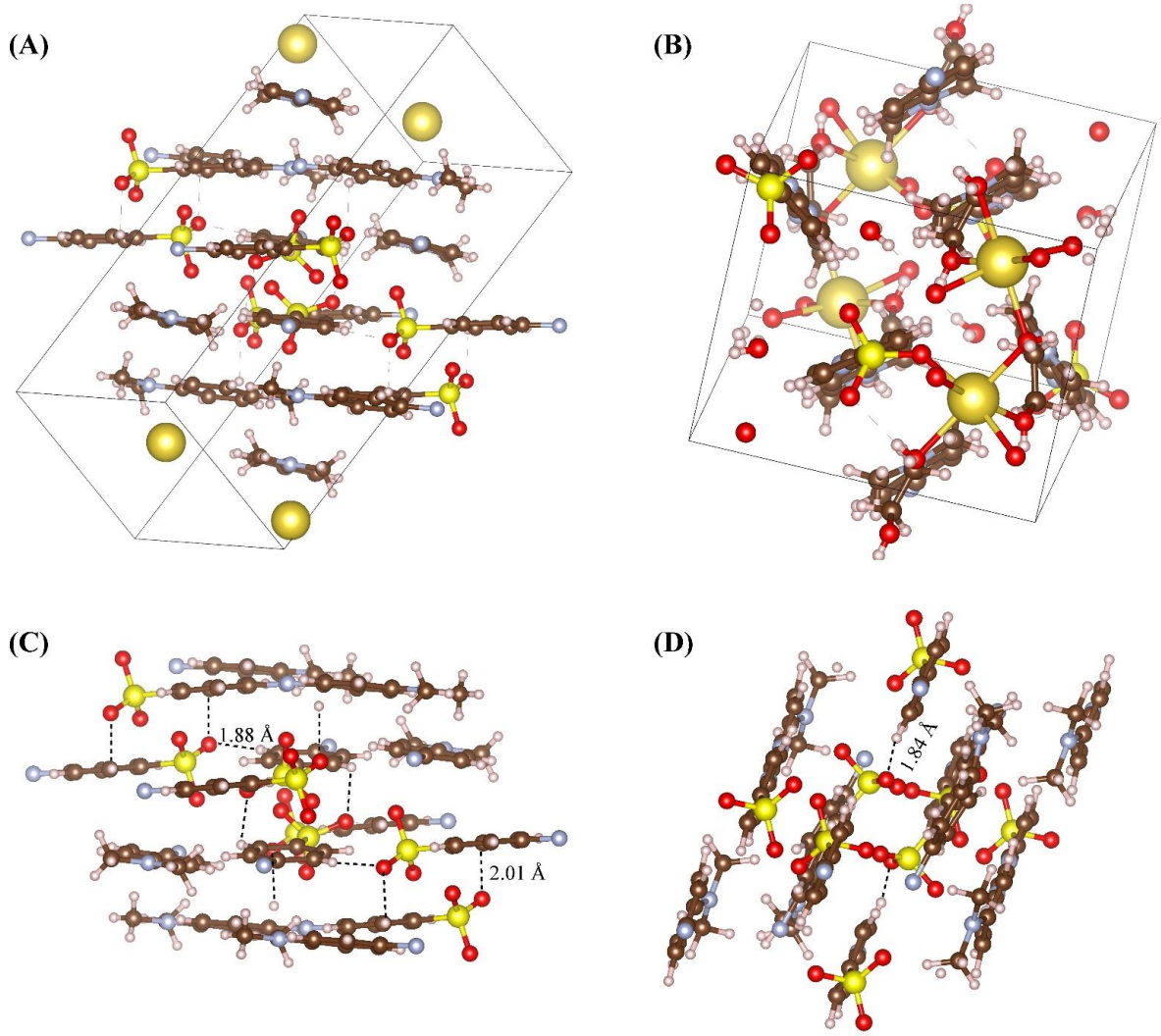

Figure 5.4: Single crystal structure of (A) MO thin film or 2D MO crystal and (B) MO 3D crystal (CCDC: 1209766). Optimized structure of few layers of MO 2D layers (C) inside the 2D MO crystal and (D) at the surface of the MO 2D crystal. These two structures were used to calculate Raman spectra shown in **Figure 5.3D**. Brown, white, pale blue, red, light yellow and dark yellow are C, H, N, O, S and Na atoms, respectively.

Figure 5.3B and **Figure A5.4**, respectively. A few layers of the MO sheets arranged in 2D fashion are shown in **Figure A5.4**. The MO 2D crystal consists of monoclinic unit cell belonging to the $P2_1/c$ space group having lattice parameters 20.0 Å (a), 9.3 Å (b) and 8.3 Å (c). As shown in **Figure 5.4A**, in the adjacent two layers, the MO molecules are antiparallel to each other. The molecules across the layers interact through weak hydrogen bonds involving aromatic C−H bond and O atom of sulfonic acid group (SO_3^-). There are two types of C−H···O interactions - one at 2.01 Å distance occurring between two different MO molecules from different layers and the other one is between two MO molecules in the same layer at 1.88 Å distance. It is worth mentioning here that although the 2D crystal composed of layer by layer

TH_3719_186122105

arrangements of MO, there is slight tilt of 8.5 ° between two MO molecules in the same layer. Although the space group of the theoretically obtained crystal of MO is the same as the reported 3D crystal (CCDC number: 1209766), the lattice parameters are slightly different with those of the 3D crystal having a, b and c of 22.11 Å, 10.34 Å and 8.3 Å, respectively (**Figure 5.4B**). Moreover, the 2D crystal diffracted at 4.2° (2θ) for the (100) plane that is slightly different from the 3D crystal of MO that occurred at 4.46°. Furthermore, there is no such parallel arrangements of MO molecules or layered structure in the 3D crystal. On the other hand, as shown in the **Figure 5.4B**, each MO molecule is perpendicular to the next MO molecule in the unit cell. Therefore, droplet evaporation induced solidification resulted in the formation of 2D molecular crystals, which is completely different from the 3D crystal. Transmission electron microscopy images indicated that thick 2D crystals were formed upon evaporation of MO solution on the grid (**Figure A5.5A**). As shown in the **Figure A5.5B**, the selected area electron diffraction also confirmed the formation of single crystalline MO thin film.

5.4.4. Raman measurement and DFT calculation at surface and inside of 2D crystals:

In addition to the observation of the enhanced Raman signal, shifts in several vibrational peak positions of MO were observed for the bulk as compared to the those on the surface of the 2D crystals. For example, major Raman peak positions of MO on the surface of the crystals at 932, 1120, 1152, 1202, 1317 and 1394 cm^{-1} were red-shifted to 923, 1117, 1143, 1195, 1313 and 1389 cm^{-1}, respectively, as shown in **Figure 5.3C**. Therefore, the results indicated that the surface vibrational characteristics of MO or MB molecules are different from those of the bulk crystals.

After obtaining the crystal structure through refinement, simulation studies were perused on the crystal systems to understand the Raman signal differences between the surface and the bulk molecules of the 2D crystalline deposits. We utilized Quantum Espresso program package to optimize the molecular structures and bonding at the surface and inside of the crystal. Then Raman spectra were calculated using Gaussian 16 software from the optimized structures. Detailed computational calculations are included the Experimental Section and the optimized structures are given in the **Figure 5.4C, D** and **Figure 5A.6**. The Raman signals on the surface of MO crystal appearing at 932, 1152, 1317 and 1394 cm^{-1} are corresponding to the ν(Ph–N) + δ(C–H), δ(C–H), ν(C–C) + δ(C–H) and ν(N=N) + ν(C–C) + δ(C–H) vibrational modes. Computationally calculated bands corresponding to these vibrations were positioned at 993, 1164, 1312 and 1401 cm^{-1} for the MO molecules located at the surface as shown **Figure**

TH_3719_186122105

5.3D(i). Similarly, the same Raman peaks were all red-shifted for the MO molecules, which were placed inside the bulk of crystal as shown in **Figure 5.3D(ii)**. The corresponding Raman peaks for bulk MO molecules were located at 985, 1151, 1288 and 1383 cm^{-1}, respectively. As mentioned in the previous section, there is weak hydrogen bond like interaction between aromatic C−H and O atom of SO_3^-. Literature reports also suggest that although C−H···O interaction seems very weak, it can significantly influence the vibrational characteristics of the molecule.[40] In the optimized structure of MO 2D crystal on the surface (**Figure 5.4D**), there is only one type of C−H···O interaction at 1.84 Å between two adjacent MO molecules in the same layer. However, there are two types of C−H···O interactions in the inner layers, one at 1.88 Å between two MO in same layer and another at 2.01 Å between two MO molecules in two different layers. As the distance between C−H in one layer and O atom of SO_3^- in another layer is 2.1 Å, which is longer than that in the inside of the crystal. Hence, the C−H···O interaction across the layer in the inside of MO 2D crystal is present in addition to C−H···O interaction along the layer as compared to the absence of that at the surface. The weak hydrogen bond affected the δ(C–H) vibration and red-shifted the frequency of vibrations, which involve the δ(C–H) mode. The overall effect has been observed in the red-shift of the vibrational frequencies on going from surface to the bulk or inside the crystal. Therefore, the computational calculations also confirmed that experimentally obtained red-shifting of Raman signal came from the MO molecules, which were located inside or bulk of the crystal.

5.4.5. Raman measurement and DFT calculation at surface and inside of 3D crystals:

In case of 3D crystal of MO, as shown in **Figure A5.7**, similar increase in the Raman signal intensity was observed after the surface had been etched by laser. The change in the frequencies or Raman peak positions was less significant compared to the 2D MO crystal. However, the Raman peak at 1116 cm^{-1} at surface was blue-shifted to 1119 cm^{-1} in the interior of MO 3D crystal (**Figure 5.5A**). The Raman peak corresponds to ν(Ph-N) + δ(C-H) vibration. After optimizing the MO molecular structures at surface and interior of 3D crystals, the DFT calculated Raman spectra implied similar blue shift of the corresponding ν(Ph-N) + δ(C-H) vibration from 1122 cm^{-1} to 1125 cm^{-1} (surface and interior), respectively (**Figure 5.5B**). The optimized crystal structures corresponding to the surface and interior are given the **Figure A5.8**. From **Figure 5.5C** and **Figure 5.5D**, it was found that the bond length of Ph-N at surface (1.407 Å) had decreased to 1.397 Å in the interior. The bond lengths of C=C, C-H and N=N did not change. Generally, with the lowering of bond length the vibrational peak position is shifted to higher wavenumber according to the relation $\nu = [a/(r\mu^{0.5}) + b]$, where ν, r, μ, a and

TH_3719_186122105

b are vibrational frequency, bond length, reduced mass, slope and intercepts, respectively.[43] Therefore, the decrease of the Ph-N bond length led to the blue shift of ν(Ph-N) + δ(C-H) vibration mode from surface to interior of MO 3D crystal. The differences in frequency and intensity between the experimental and calculated Raman spectra were due to a combination of factors such as approximations used in each step of calculations by the software program packages. Thus, in order to perform the calculations, smaller number of molecules were considered and anharmonic effect had been ignored to optimize the computational parameters.

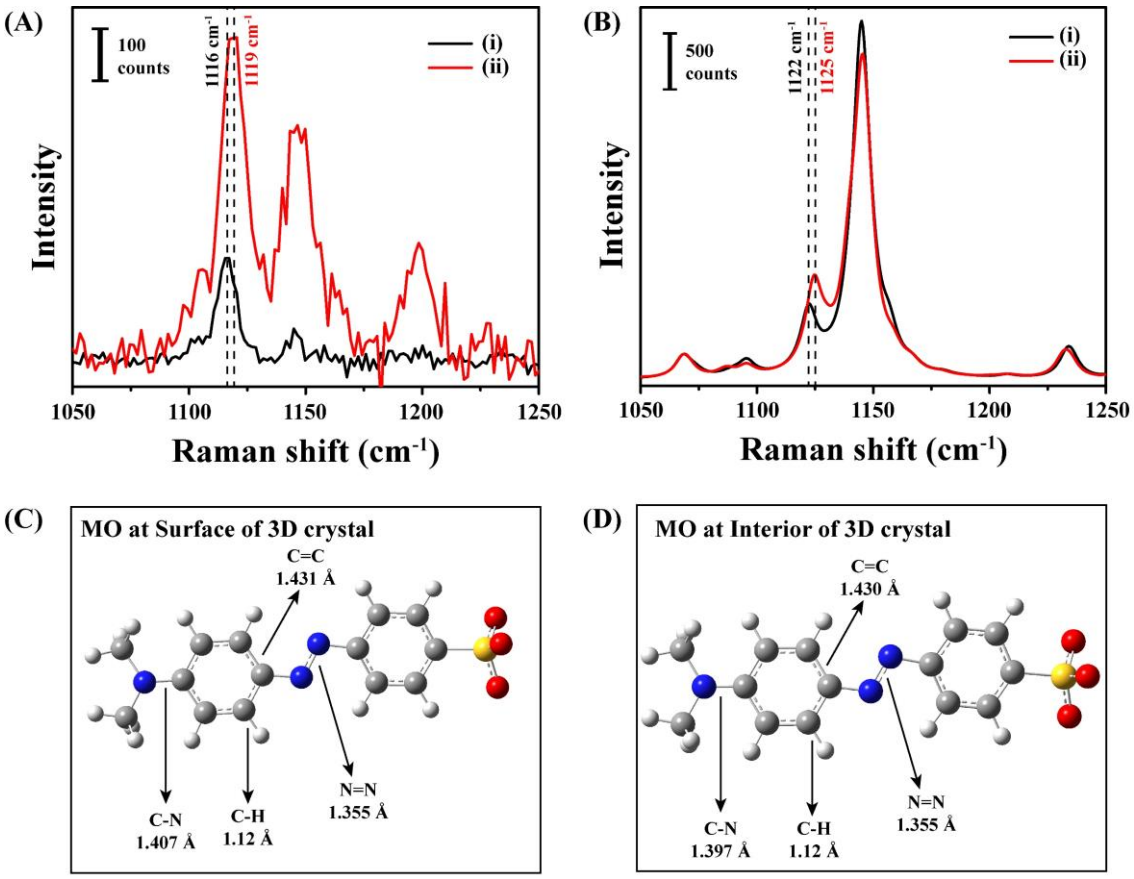

Figure 5.5: (A) Experimental Raman spectra of MO (i) at surface and (ii) in the interior of 3D MO crystal. **(B)** DFT calculated Raman spectra of MO (i) at surface and (ii) in the interior of 3D MO crystal. DFT Optimized structure of MO molecule **(C)** at surface and **(D)** in the interior of 3D MO crystal showing bond lengths. Gray, white, blue, red and yellow atoms are C, H, N, O and S, respectively.

Similar to MO, MB also formed 2D crystals upon evaporation of sessile droplet as found from XRD and theoretical refinement (**Figure A5.13**). Details of experimental and computational results shown in **Figure A5.9** to **A5.17** also suggest that the surfaces of the MB 2D and 3D crystals are different from the interior bulk. Thus, the vibrational characteristics of the molecules at the surface of MO or MB crystals, whether 2D or 3D, are different from those

TH_3719_186122105

of the bulk. The results also indicated that the chemical nature of molecules on the surface of a crystal is different from those in the bulk or inside the crystal.

Similar to MO, MB also formed 2D crystals upon evaporation of sessile droplet as found from XRD and theoretical refinement (**Figure A5.13**). Details of experimental and computational results shown in **Figure A5.9** to **A5.17** also suggest that the surfaces of the MB 2D and 3D crystals are different from the interior bulk. Thus, the vibrational characteristics of the molecules at the surface of MO or MB crystals, whether 2D or 3D, are different from those of the bulk. The results also indicated that the chemical nature of molecules on the surface of a crystal is different from those in the bulk or inside the crystal.

5.5. Conclusions

2D single crystals of organic molecules MO and MB have been prepared by 'coffee-ring' depositions at the TPCL of evaporating aqueous droplets. The crystallization process was monitored by the monotonous increase in the Raman signal intensity with time. The formation of 2D MO or MB single crystal was confirmed from XRD, AFM and TEM measurements. Only one diffraction peak at 4.2° (2θ) for MO or 5.7° (2θ) for MB indicated that the crystal grew in only one plane and theoretical refinements using the experimental XRD revealed 2D layer-by-layer arrangements of MO or MB molecules in the crystal structure. Moreover, the Raman signal intensity and peak positions at the surface and interior of the as-formed 2D as well as the 3D crystal have been found to be different. The interiors of the crystals were probed following etching the surface layer by laser irradiation or mechanically. In all cases, the Raman signal intensity was higher when measured inside the crystal compared to that at the surface. For MO 2D crystals, compared to the Raman signal intensity at the surface, the signal intensity at the interior was 12 times higher when etched by laser and was 20 times higher when etched mechanically. For MB crystal, the intensity rise was less compared to MO. The intensity rise was also similar for 3D crystals of MO and MB. Most significantly, representative Raman signals of MO at 932, 1152, 1202, 1317 and 1394 cm^{-1} measured at the surface, were red-shifted to 923, 1143, 1195, 1313 and 1389 cm^{-1}, respectively, when probed in the interior. The red-shift of the respective signals were governed by different extent of C−H···O interactions between the surface and interior of the crystals. Therefore, the vibrational characteristics of the surface and bulk of a crystal are fundamentally different at the molecular level.

TH_3719_186122105

5.6. References

1. Ahmed, J. Crystallization from a Supersaturated Solution of Sodium Acetate. *J. Chem. Educ.* **2000**, *77*, 11, 1446.
2. Watanabe, S.; Hayashida, T.; Iwai, M.; Inomata, Y.; Kunitake, M.; Kida, T. Single Crystallization of Cs_4PbBr_6 Perovskite from Supersaturated Organic Solutions Optimized Through Solubility Studies. *ACS Omega* **2023**, *8*, 2, 2455–2461.
3. Prymak, O.; Sokolova, V.; Peitsch, T.; Epple, M. The Crystallization of Fluoroapatite Dumbbells from Supersaturated Aqueous Solution. *Cryst. Growth & Des.* **2006**, *6*, 2, 498–506.
4. Korede, V.; Nagalingam, N.; Penha, F. M.; van der Linden, N.; Pedding, J. T.; Hartkamp, R.; Eral, H. B. A Review of Laser-Induced Crystallization from Solution. *Cryst. Growth Des*. **2023**, *23*, 5, 3873–3916.
5. Hoang, A. T.; Hu, L.; Katiyar, A. K.; Ahn, J.-H. Two-dimensional layered materials and heterostructures for flexible electronic. *Matter* **2022**, *5*, 4116–4132.
6. Luo, Z.; Wu, D.; Xu, B.; Xu, H.; Cai, Z.; Peng, J.; Weng, J.; Xu, S.; Zhu, C.; Wang, F.; Sun, Z.; Zhang, H. Two-dimensional material-based saturable absorbers: towards compact visible-wavelength all-fiber pulsed lasers. *Nanoscale* **2016**, *8*, 1066-1072.
7. Balandin, A. A.; Kargar, F.; Salguero, T. T.; Lake, R. K. One-dimensional van der Waals quantum materials. *Materials Today* **2022**, *55*, 74-91.
8. Mei, X.; Hu, T.; Wang, Y.; Weng, X.; Liang, R.; Wei, M. Recent advancements in two-dimensional nanomaterials for drug delivery. *WIREs Nanomed Nanobiotechnol*. **2020**, *12*, e1596.
9. Luo, W.; Xiong, W.; Han, Y.; Yan, X.; Mai, L. Application of two-dimensional layered materials in surface-enhanced Raman spectroscopy (SERS). *Phys. Chem. Chem. Phys.* **2022**, *24*, 26398-26412.
10. Zhang, Y.; Liu, J.; Rong, C.; Wang, D.; Li, W.; Gao. Z.; Chen, Y. Current Advances of CO Sensing Based on Low Dimensional Materials. *Langmuir* **2024**, *40*, 36, 18821–18836.
11. Rohaizad, N.; Mayorga-Martinez, C. C.; Fojtů, M.; Latiff, N. M.; Pumera, M. Two-dimensional materials in biomedical, biosensing and sensing applications. *Chem. Soc. Rev.* **2021**, *50*, 619-657.

TH_3719_186122105

12. Dey, U.; Chattopadhyay, A. Two-dimensional molecular moiré superlattices of tryptophan with visible photoluminescence for photo-activatable CO_2 sensing and storage. *J. Mater. Chem. C* **2024**, *12*, 5506-5516.
13. Wang, L.; Yin, S.; Yang, J.; Dou, S. X. Moiré Superlattice Structure in Two-Dimensional Catalysts: Synthesis, Property and Activity. *Small* **2023**, *19*, 2300165.
14. Dey, U.; Chattopadhyay, A. pH Controlled Twist-Angle Dependent Interfacial Quantum Tunneling in Multilayer Molecular Moiré Superlattices of p-Phenylenediamine. *Adv Quantum Technol.* 2025, 2400569.
15. Claire, F.J.; Solomos, M.A.; Kim, J.; et al. Structural and electronic switching of a single crystal 2D metal-organic framework prepared by chemical vapor deposition. *Nat Commun* **2020**, *11*, 5524.
16. Wang, Q.; Qian, J.; Li, Y.; Zhang, Y.; He, D.; Jiang, S.; Wang, Y.; Wang, X.; Pan, L.; Wang, J.; et al. 2D Single-Crystalline Molecular Semiconductors with Precise Layer Definition Achieved by Floating-Coffee-Ring-Driven Assembly. *Adv. Funct. Mater.* **2016**, *26*, 3191-3198.
17. Wang, C.; Fu, B.; Zhang, X.; Li, R.; Dong, H.; Hu, W. Solution-Processed, Large-Area, Two-Dimensional Crystals of Organic Semiconductors for Field-Effect Transistors and Phototransistors. *ACS Cent. Sci.* **2020**, *6*, 5, 636–652.
18. Gil, A.; Guitián, F. Formation of 2D colloidal crystals by the Langmuir–Blodgett technique monitored in situ by Brewster angle microscopy. *Journal of Colloid and Interface Science* 2007, 37, 304–307.
19. He, X.; He, Y.; Hsiao, M.-S.; Harniman, R. L.; Pearce, S.; Winnik, M. A.; Manners, I. Complex and Hierarchical 2D Assemblies via Crystallization-Driven Self-Assembly of Poly(l-lactide) Homopolymers with Charged Termini. *J. Am. Chem. Soc.* **2017**, *139*, 27, 9221–9228.
20. Yan, Y.; Yang, Y.; Liang, M. et al. Implementing an intermittent spin-coating strategy to enable bottom-up crystallization in layered halide perovskites. *Nat Commun* **2021**, *12*, 6603.
21. Goeta, A. E.; Howard, J. A. K. Low temperature single crystal X-ray diffraction: advantage, instrumentation and applications. *Chem. Soc. Rev.* **2004**, *33*, 490-500.
22. Firment, L. E.; Somorjai, G. A. Low Energy Electron Diffraction Studies of Organic Monolayers on Metal Surfaces. *Isr. J. Chem.* **1979**, *18*, 285-294.
23. Rydz, J.; Šišková, A.; Eckstein, A. A. Scanning Electron Microscopy and Atomic Force Microscopy: Topographic and Dynamical Surface Studies of Blends, Composites, and

TH_3719_186122105

Hybrid Functional Materials for Sustainable Future. *Advances in Materials Science and Engineering*, *2019*, 6871785.

24. Salmeron, M.; Eren, B. High-Pressure Scanning Tunneling Microscopy. *Chem. Rev.* **2021**, *121*, 2, 962–1006.
25. Bhakat, A.; Chattopadhyay, A. Molecular Cooperativity in the Intense Raman Scattering on the Surface of an Organic Molecular Microcrystal. *Adv. Optical Mater.* **2024**, *12*, 2301776.
26. Paul, S.; Chattopadhyay, A. Single Phase Transition Leads to the Nanoparticle Deposition in an Evaporating Sessile Droplet. *J. Phys. Chem. C* **2023**, *45*, 22401-22411.
27. Paul, S.; Chattopadhyay, A. Distinction of Plasmonic Intrananoparticle and Internanoparticle Molecular Reaction Rates at the Three-Phase Contact Line of an Evaporating Sessile Droplet. *J. Phys. Chem. Lett.* **2024**, *15*, 6812-6817.
28. Bhakat, A.; Paul, S.; Chattopadhyay, A. Molecular Specificity in the Intense Surface-Enhanced Raman Scattering on Copper(II) 8-Hydroxyquinoline Microcrystals. *J. Phys. Chem. C* **2023**, *127*, 10, 5169–5177.
29. Putz, H.; Schön, J. C.; Jansen, M. Combined Method for "Ab Initio" Structure Solution from Powder Diffraction Data. *J. Appl. Cryst.* **1999**, *32*, 864-870.
30. Giannozzi, P.; Andreussi, O.; Brumme, T.; Bunau, O.; Buongiorno Nardelli, M.; Calandra, M.; Car, R.; Cavazzoni, C.; Ceresoli, D.; Cococcioni, M. Advanced capabilities for materials modelling with Quantum ESPRESSO. *J. Phys.: Condens. Matter* **2017**, *29*, 465901.
31. Hamann, D. R. Optimized norm-conserving Vanderbilt pseudopotentials. *Phys. Rev. B* **2017**, *95*, 239906.
32. Ernzerhof, M.; Scuseria, G. E. Assessment of the Perdew–Burke–Ernzerhof exchange-correlation functional. *J. Chem. Phys.* **1999**, *110*, 5029–5036.
33. Perdew, J. P.; Burke, K.; Ernzerhof, M. Generalized Gradient Approximation Made Simple. *Phys. Rev. Lett.* **1997**, *78*, 1396.
34. Wisesa, P.; McGill, K. A.; Mueller, T. Efficient generation of generalized Monkhorst-Pack grids through the use of informatics. *Phys. Rev. B* **2016**, *93*, 155109.
35. Frisch, M. J.; Trucks, G. W.; Schlegel, H. B.; Scuseria, G. E.; Robb, M. A.; Cheeseman, J. R.; Scalmani, G.; Barone, V.; Mennucci, B.; Petersson, G. A.; *et al*. *Gaussian 16*, Revision C.01; Gaussian, Inc.: Wallingford CT, **2016**.
36. Becke, A. D. A new mixing of Hartree–Fock and local density-functional theories. *J. Chem. Phys.* **1993**, *98* (2), 1372-1377.

TH_3719_186122105

37. Ditchfield, R.; Hehre, W. J.; Pople, J. A. Self-Consistent Molecular Orbital Methods. 9. Extended Gaussian-type basis for molecular-orbital studies of organic molecules. *J. Chem. Phys.* **1971**, *54*, 724.
38. Garusinghe, U. M.; Raghuwanshi, V. S.; Batchelor, W. et al. Water Resistant Cellulose – Titanium Dioxide Composites for Photocatalysis. *Sci Rep* **2018**, *8*, 2306.
39. Dinh, V.-P.; Huynh, T.-D.-T.; Le, H. M.; Nguyen, V.-D.; Dao, V.-A.; Huang, N. Q.; Tuyne, L. A.; Lee, S.; Yi, J.; Nguyen, T. D. et al. Insight into the adsorption mechanisms of methylene blue and chromium(iii) from aqueous solution onto pomelo fruit peel. *RSC Adv.* **2019**, *9*, 25847-25860.
40. Deegan, R. D.; Bakajin, O.; Dupont, T. F.; Huber, G.; Nagel, S. R.; Witten, T. A. Contact line deposits in an evaporating drop. *Phys. Rev. E* **2000**, *62*, 756-765.
41. Paul, S.; Chattopadhyay, A. Multistep Phase Transition and Molecular Reaction of Plasmonic Nanoparticles at the Three-Phase Contact Line of an Evaporating Sessile Droplet. *J. Phys. Chem. C* **2025**, *129*, 8, 4250–4260.
42. Kolesov, B. A. Hydrogen Bonds: Raman Spectroscopic Study. *Int. J. Mol. Sci.* **2021**, *22*, 5380.
43. Zavitsas, A. A. Factors affecting the relation between stretching frequencies and bond lengths. Diatomic and polyatomic species without adjustable fitting parameters. *Spectrochimica Acta Part A: Molecular and Biomolecular Spectroscopy* **2015**, *151*, 553–565.

TH_3719_186122105

Appendix of Chapter 5 (A5):

A5.1. Effect of water addition on the Raman spectrum of MO crystal:

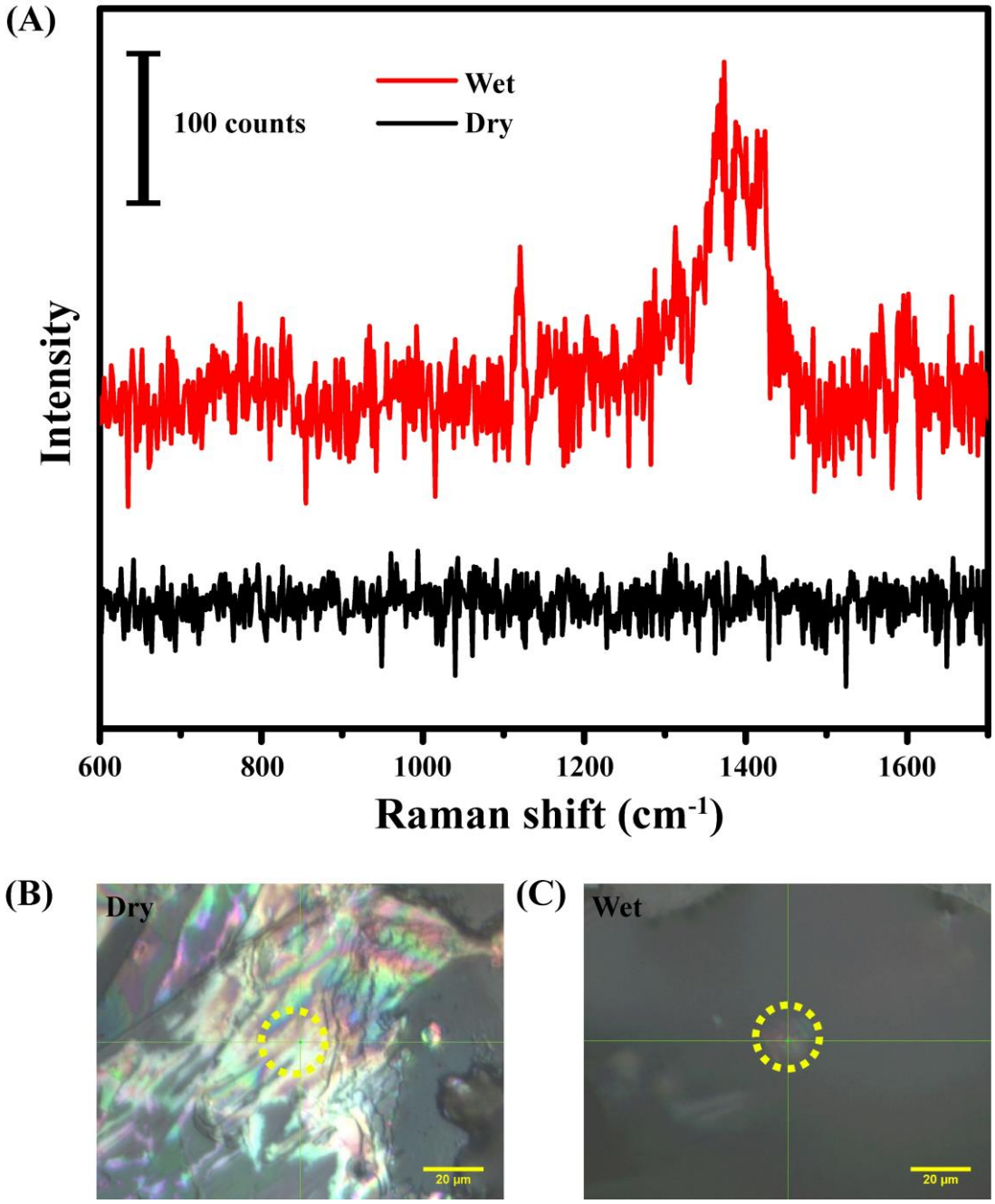

Figure A5.1: (A) Raman spectra of MO crystal in absence of water (dry) and in the presence of added water (wet). (B), (C) Optical images of MO crystal in dry and wet conditions, respectively. Raman probe areas are marked with yellow circles. Water in (C) was dropped on the dry MO thin film obtained through evaporation of droplet containing MO solution.

The experimental results of increase in Raman scattering following addition of water to the crystal, supported that the decrease in intensity after 37.5 min, during droplet evaporation as in **Figure 5.1B** in Chapter 5, was due to loss of water.

TH_3719_186122105

A5.2. Optical images of Raman probe area on MO thin film:

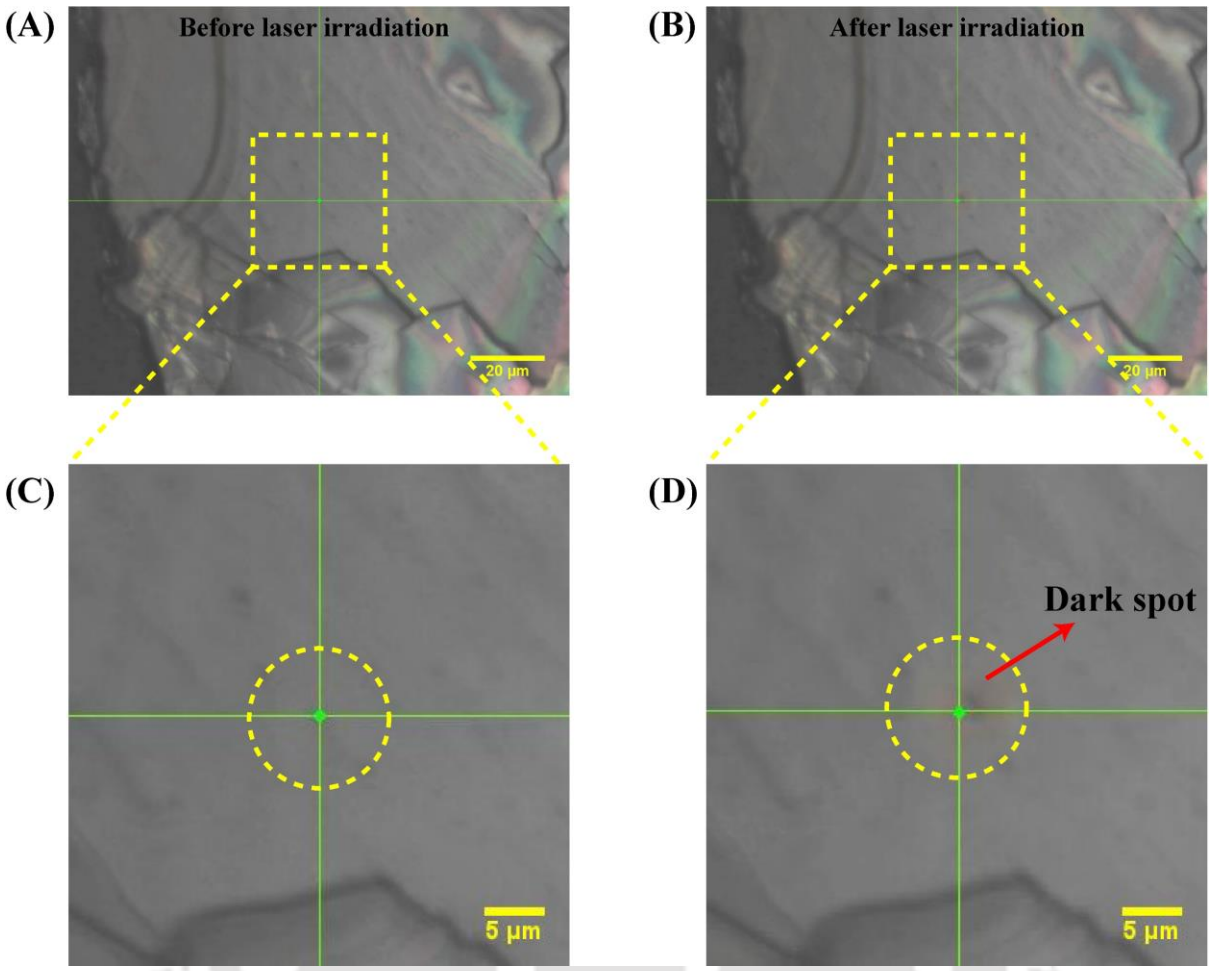

Figure A5.2: (A) and (B) Optical images of Raman probe area before and after irradiation of 2.5 mW 532 nm laser on MO thin film. (C) and (D) are magnified view of selected area in (A) and (B), respectively. The dark spot found in (D) implied etching of surface layer by intense laser power.

TH_3719_186122105

A5.3. Raman spectra of MO thin films before and after mechanical etching:

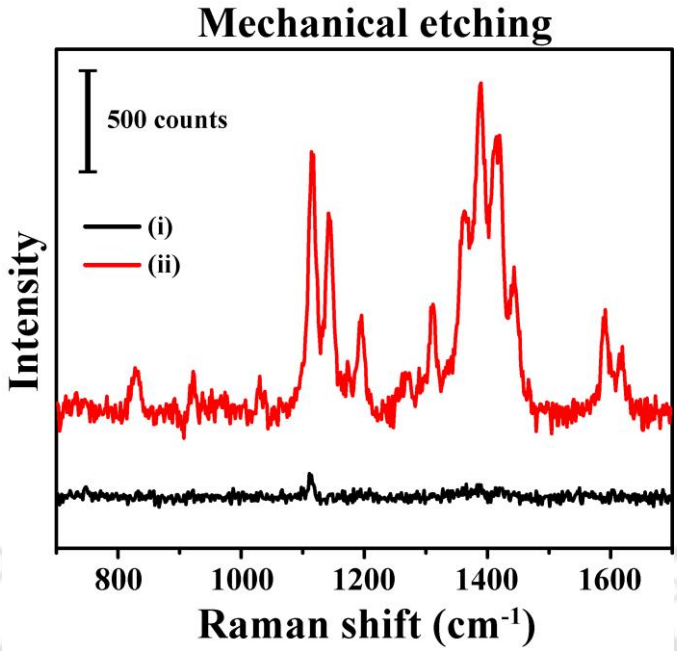

Figure A5.3: Raman spectra of MO thin film surface (i) before and (ii) after mechanical etching. The Raman signal of MO at the mechanically etched area was nearly 20 times as intense as that recorded at the as-deposited (smooth) area.

A5.4. 2D layer-by--layer arrangement of MO molecules:

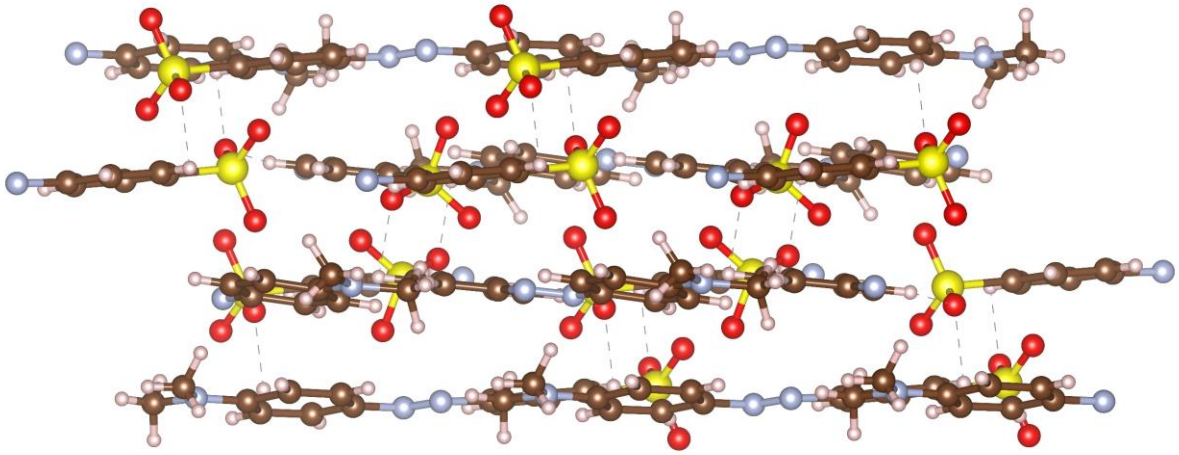

Figure A5.4: 2D layer-by-layer arrangement of MO molecules in the crystal structure obtained after refinement using powder XRD data. Brown, white, pale blue, red and light yellow atoms are C, H, N, O and S atoms, respectively.

TH_3719_186122105

A5.5. Results of TEM measurement of MO thin film:

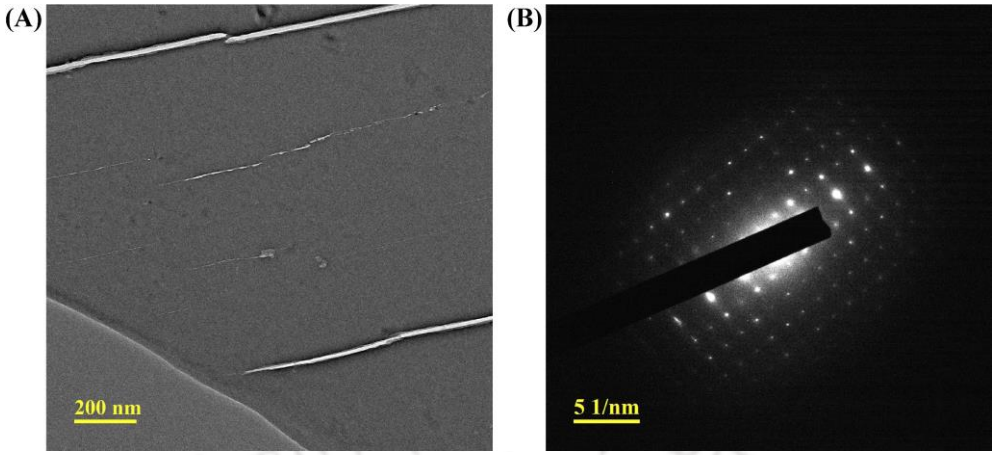

Figure A5.5: (A) TEM image and (B) SAED of MO thin film. TEM image confirmed the 2D layer formation and SAED supported the formation of signal crystal MO thin film.

A5.6. Optimized crystal structure of MO on the surface and in the interior of 2D crystal:

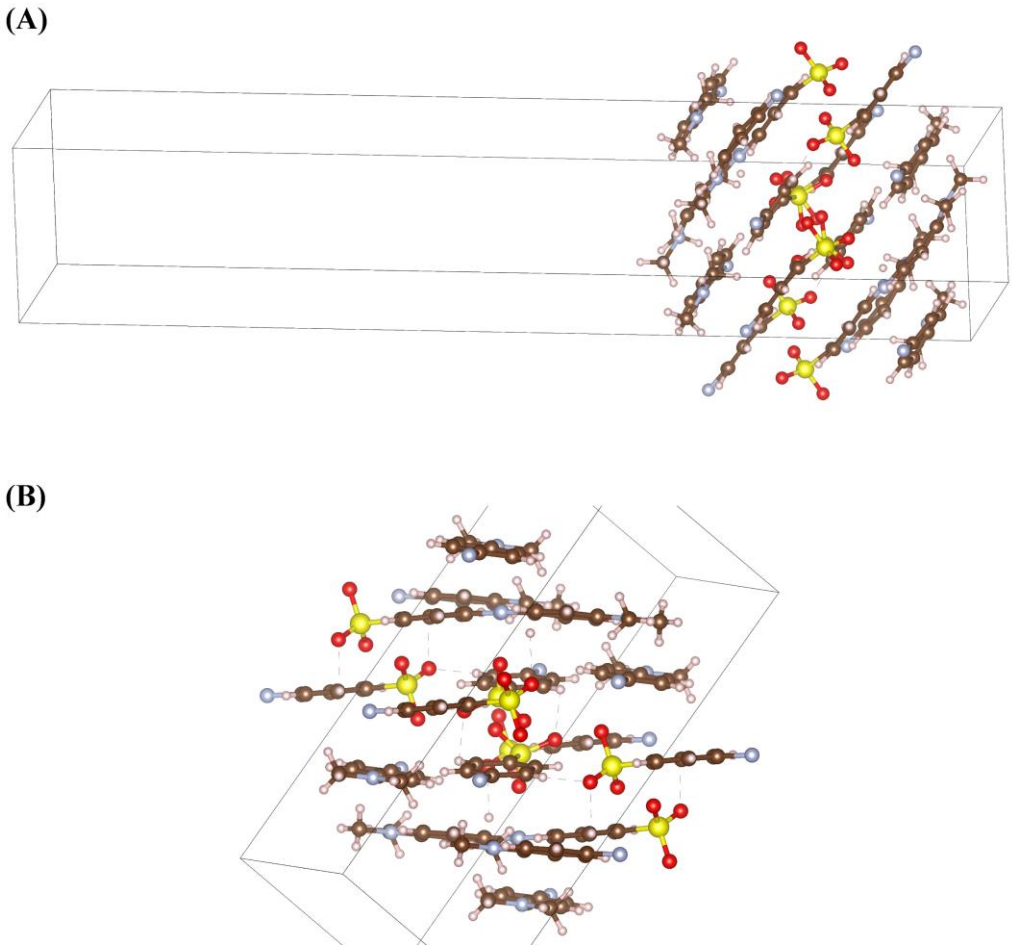

Figure A5.6: Optimized crystal structure of MO (A) on the surface and (B) in the interior of 2D crystal. The optimization methods used are mentioned in the experimental section. Brown, white, pale blue, red, light yellow and dark yellow are C, H, N, O, S and Na atoms, respectively.

TH_3719_186122105

A5.7. Raman spectra of 3D crystal of MO:

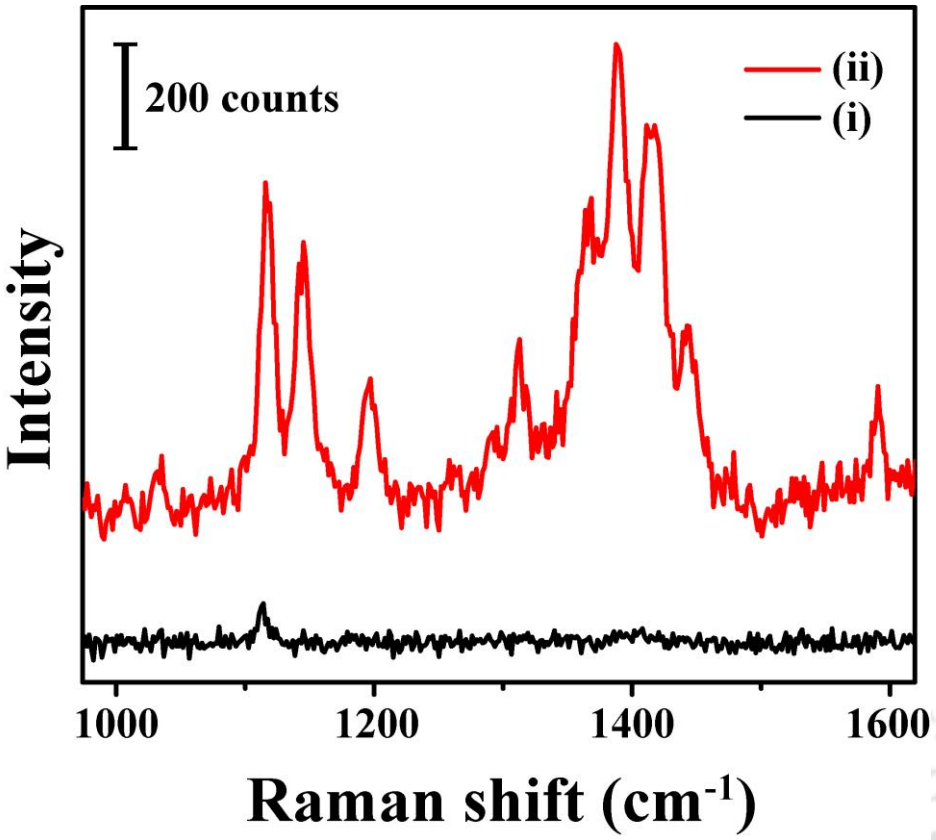

Figure A5.7: Raman spectra (recorded using 0.5 mW of the 532 nm laser) of MO 3D crystal on the (i) smooth surface and (ii) etched surface formed following exposure to 2.5mW 532 nm laser.

TH_3719_186122105

A5.8. Optimized crystal structure of MO on the surface and in the interior of 3D crystal:

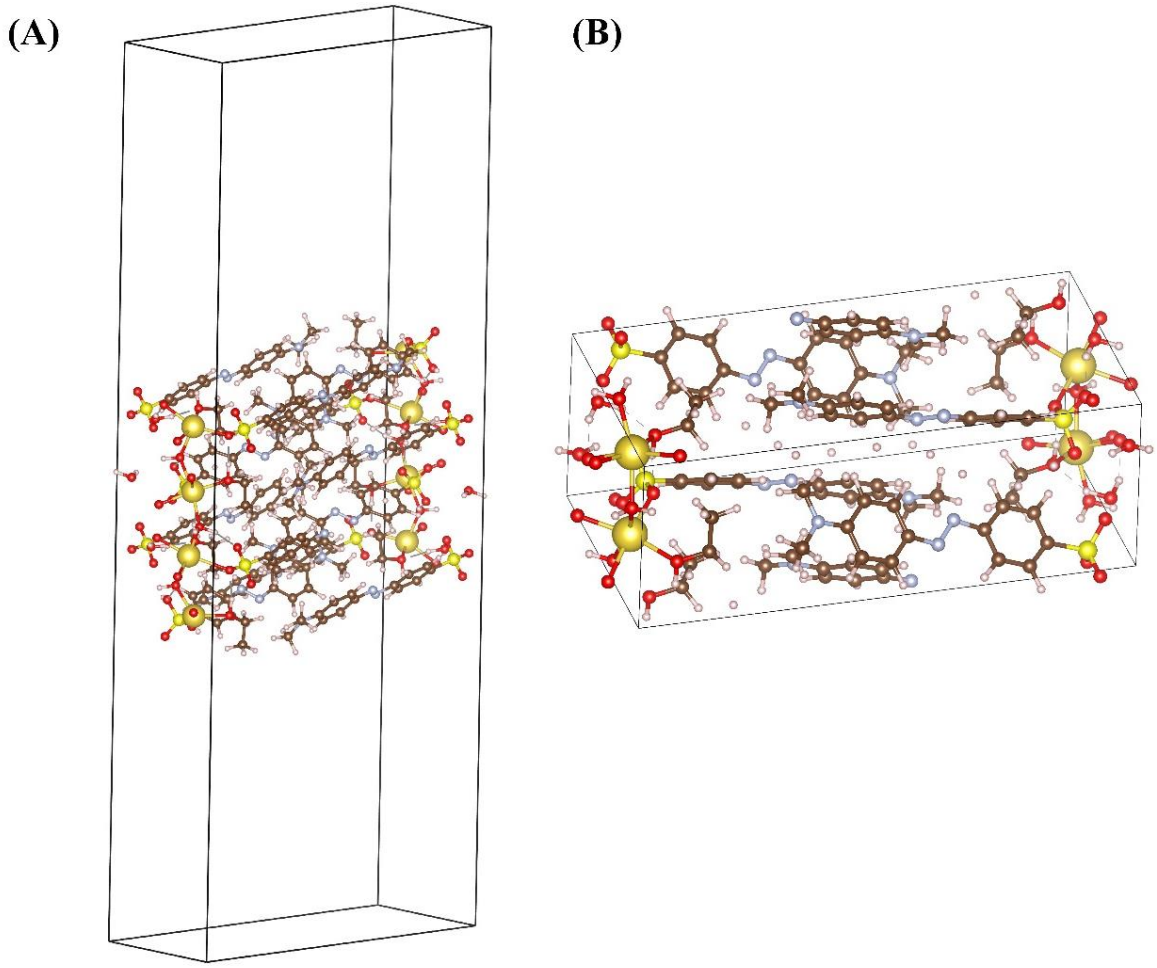

Figure A5.8: Optimized crystal structure of MO (A) on the surface and (B) in the interior of 3D crystal. The optimization methods used are mentioned in the experimental section. Brown, white, pale blue, red, light yellow and dark yellow are C, H, N, O, S and Na atoms, respectively.

TH_3719_186122105

A5.9. Results of the time-dependent Raman measurements at the TPCL of evaporating droplet containing 1.57 mM MB:

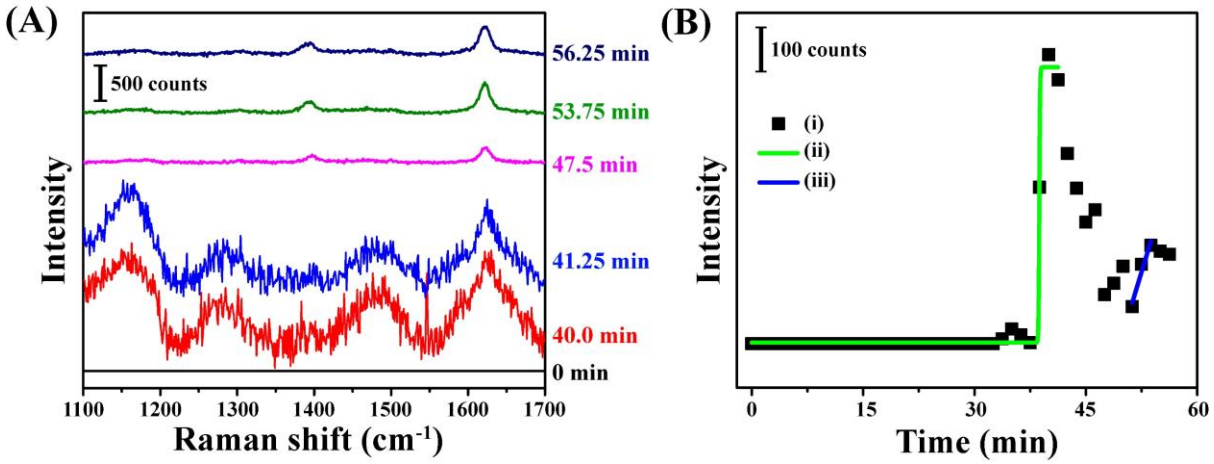

Figure A5.9: (A) Raman spectra at different times measured at the TPCL of evaporating droplet containing aqueous solution of MB recorded using 2.5 mW laser power. (B) Variation of 1624 cm^{-1} peak intensity of MB with time while the droplet was evaporating. (ii) and (iii) in (B) are nonlinear Boltzmann fitting and linear fitting, respectively.

When aqueous MB droplets were evaporated with probing for Raman scattering at the TPCL, a slow and monotonous increase in Raman signal intensity was observed till 37.5 min (Figure A5.9A, B). Then the intensity increased rapidly till 40.0 min. However, the intensity showed a decreasing trend till 51.25 min. In other words, the behavior of solid depositions of MB from the droplets was similar to that of MO. Further, the decrease in the signal intensity following complete deposition is similar to that of MO and possibly due to the release of water molecules from the solid deposits. Finally, here again the sharp rise in the signal following complete drying of the droplet was observed from 52.5 min and that was also due to the vaporization of the surface layers of the deposited molecules due the intense laser beam, which is similar to the observation in MO crystals.

TH_3719_186122105

A5.10. Raman spectra of MB thin films recorded before and after etching the surface layer:

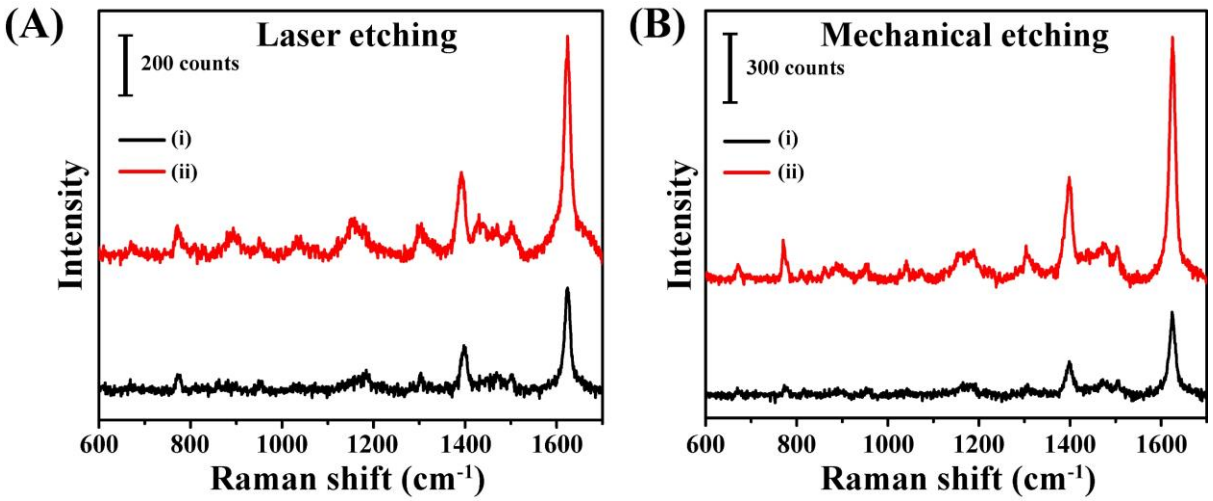

Figure A5.10: Raman spectra (recorded using 0.16 mW of the 633 nm laser) of MB thin film on the (i) smooth surface and (ii) etched surface formed following **(A)** exposure to 0.8 mW 633 nm laser and **(B)** etching mechanically by a tweezer.

Intensity of the MB Raman signal was enhanced nearly 2 times and 3 times, after the surfaces of MB thin film were etched by laser and mechanically, respectively. The result is similar to the etching experiment on the MO thin film.

A5.11. Raman peak shift of MB recorded after etching the surface layer by using laser:

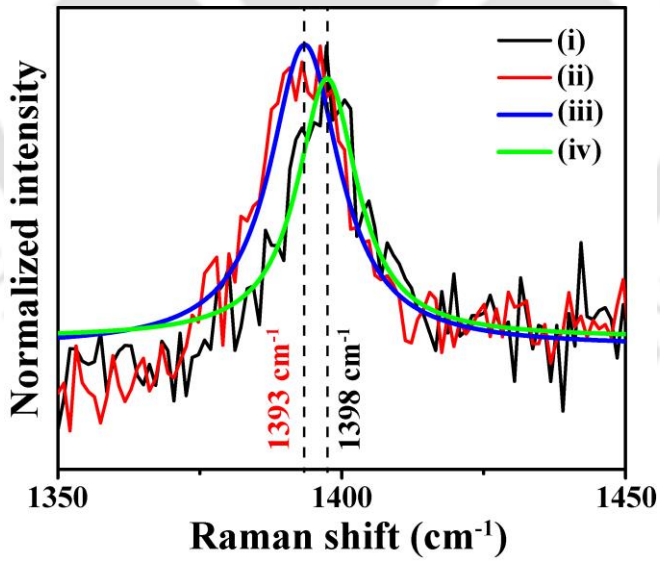

Figure A5.11: Zoomed view of Raman spectra showing peak shift on moving from (i) the smooth surface to (ii) the interior of the MB thin film. The graphs in (iii) and (iv) are Lorentzian fittings of (i) and (ii), respectively. In case of MB thin film, 1398 cm^{-1} peak was shifted to 1393 cm^{-1} on moving from surface to interior of thin film. However, peak position at 1624 cm^{-1}, which involves only aromatic C=C vibration did not change on moving from the surface to interior.

TH_3719_186122105

A5.12. AFM measurements of MB thin film etched by 0.8 mW 633 nm laser:

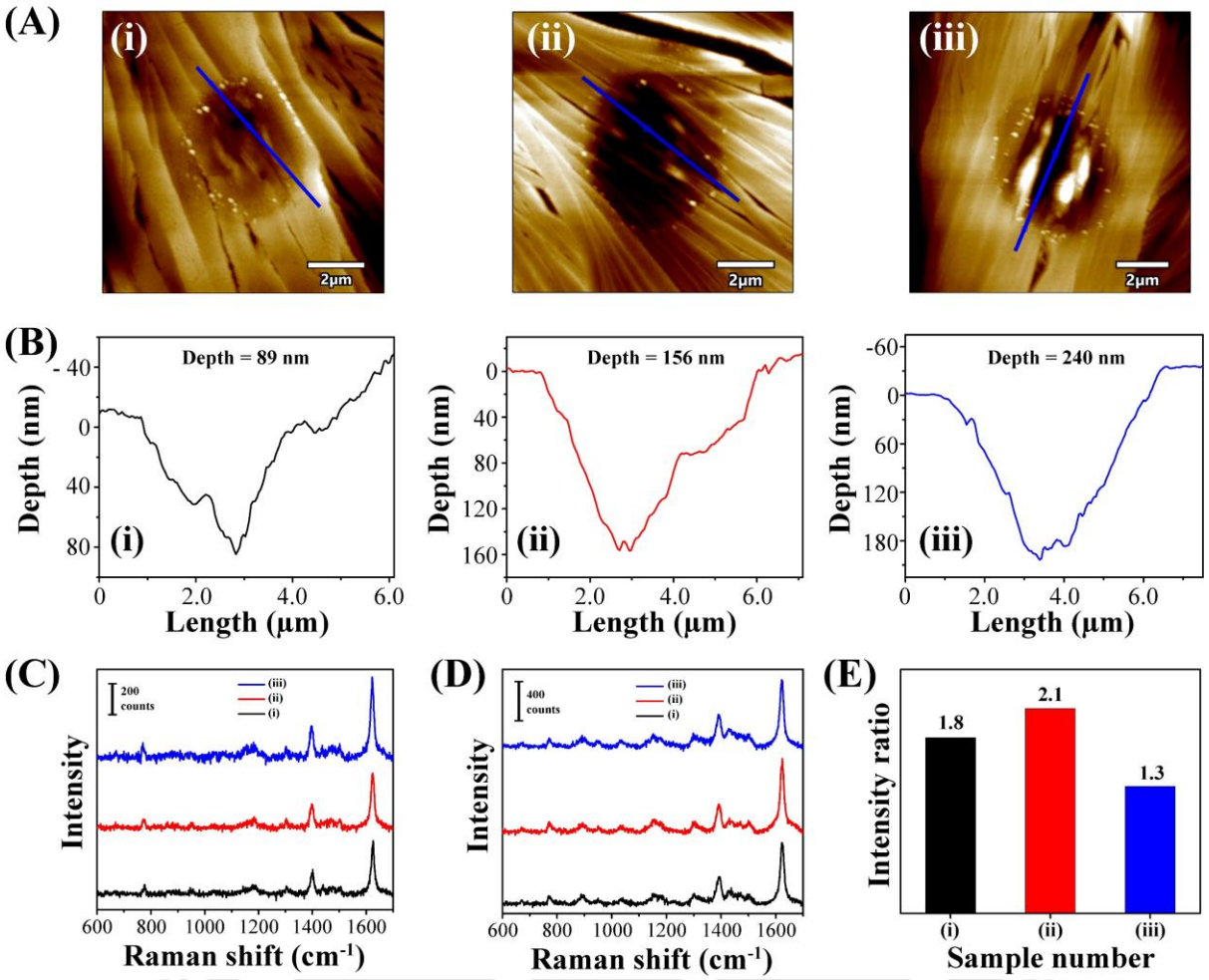

Figure A5.12: (A) AFM images of the area on MB thin film etched with 0.8 mW 633 nm laser with exposure time of (i) 5 s, (ii) 10 s and (iii) 15 s. **(B)** Depth profiles of the etched areas shown in **(A)**. Corresponding Raman spectra of MB on the areas recorded **(C)** before etching and **(D)** after etching, using a 0.16 mW 633 nm laser. Raman spectra were recorded using the same parameters. **(F)** Ratios of the 1624 cm^{-1} peak intensity of the signals after etching to before etching.

Similar to the MO thin films in Figure 5.2, Three different spots of the MB thin film were irradiated with 0.8 mW of the 633 nm laser for 5, 10 and 15 s. Raman spectra and AFM measurements, shown in Figure A5.12, were recorded for the etched samples. Figure A5.12B indicated increasing depth of etching as the exposure time was increased. Thus, for the 5, 10 and 15 s of exposures, the depths of etching were 89, 156 and 240 nm, respectively. Importantly, the intensity of the Raman signals did not vary that much with the extent of etching. As shown in Figure 5.12E, the ratios of 1624 cm^{-1} peak intensity after and before etching were nearly the same at 1.7 ± 0.3.

TH_3719_186122105

A5.13. Powder XRD and crystal structure of MB thin film:

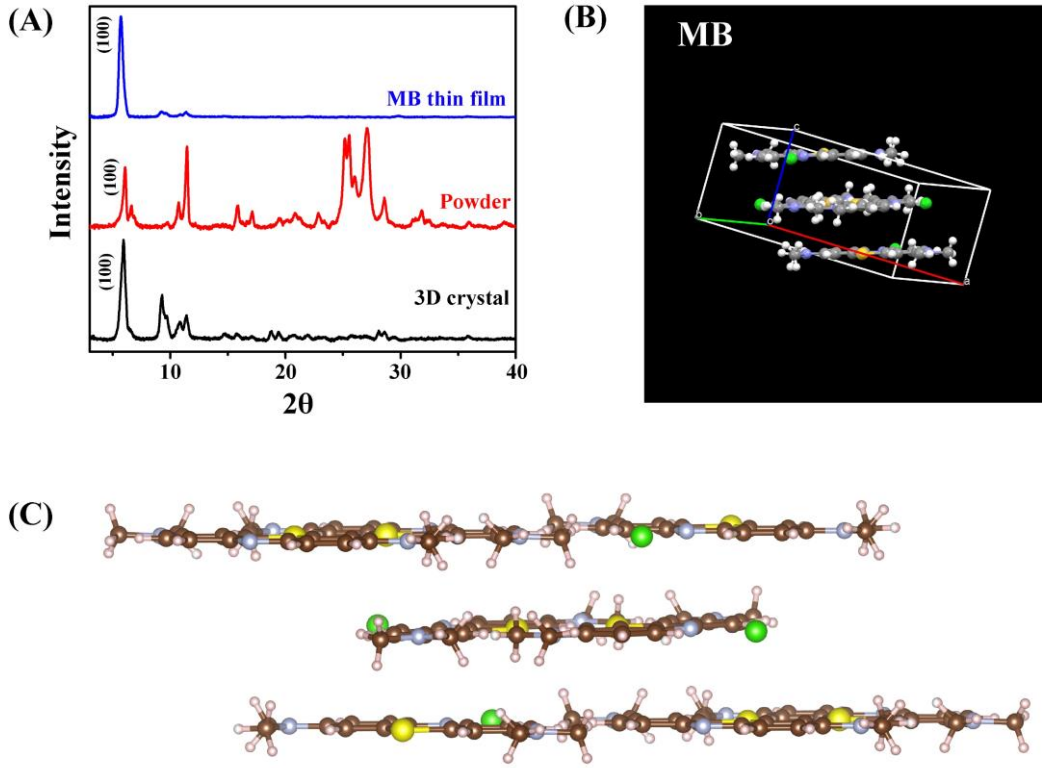

Figure A5.13: (A) Powder XRD pattern of the bulk MB crystal (black), MB powder (red) and the MB thin film (blue) obtained after evaporation of droplet having MB solution. (B) Crystal structure of MB after refinement of the powder XRD pattern of thin film. (C) 2D layer-by-layer arrangement of MB molecules in the crystal. Brown, white, pale blue, light yellow and green atoms are C, H, N, S and Cl atoms, respectively.

Powder XRD measurement of MB thin film revealed only one major diffraction peak at 5.7° (2θ) and two minor reflections at 9.3° and 11.3°. The existence of only one major peak at low angle implied the selective growth of only one crystalline plane. After comparing the powder XRD data of the thin films with the bulk crystals, it was found that only (100) plane for the MB thin films grew into 2D structure. In other words, at the TPCL, MB formed 2D crystal or planar crystal, as majority of the thin films consisted of only one crystal plane. This is also consistent with the 2D layer-by-layer arrangement of MB molecules in the crystal obtained after refinement of the powder XRD data. Therefore, the MB thin film obtained at the TPCL after evaporation of MB solution was composed 2D MB crystal.

After obtaining the MB 2D crystal structures, the surface and interior of the 2D crystal were optimized and Raman spectra were calculated to find out the reason behind the shift of

TH_3719_186122105

experimental Raman spectra shown in **Figure A5.11**. The optimized structure of 2D MB crystal and calculated Raman spectra on the surface and interior are given in **Figure A5.14**.

A5.14. Calculated Raman spectra of MB 2D crystal:

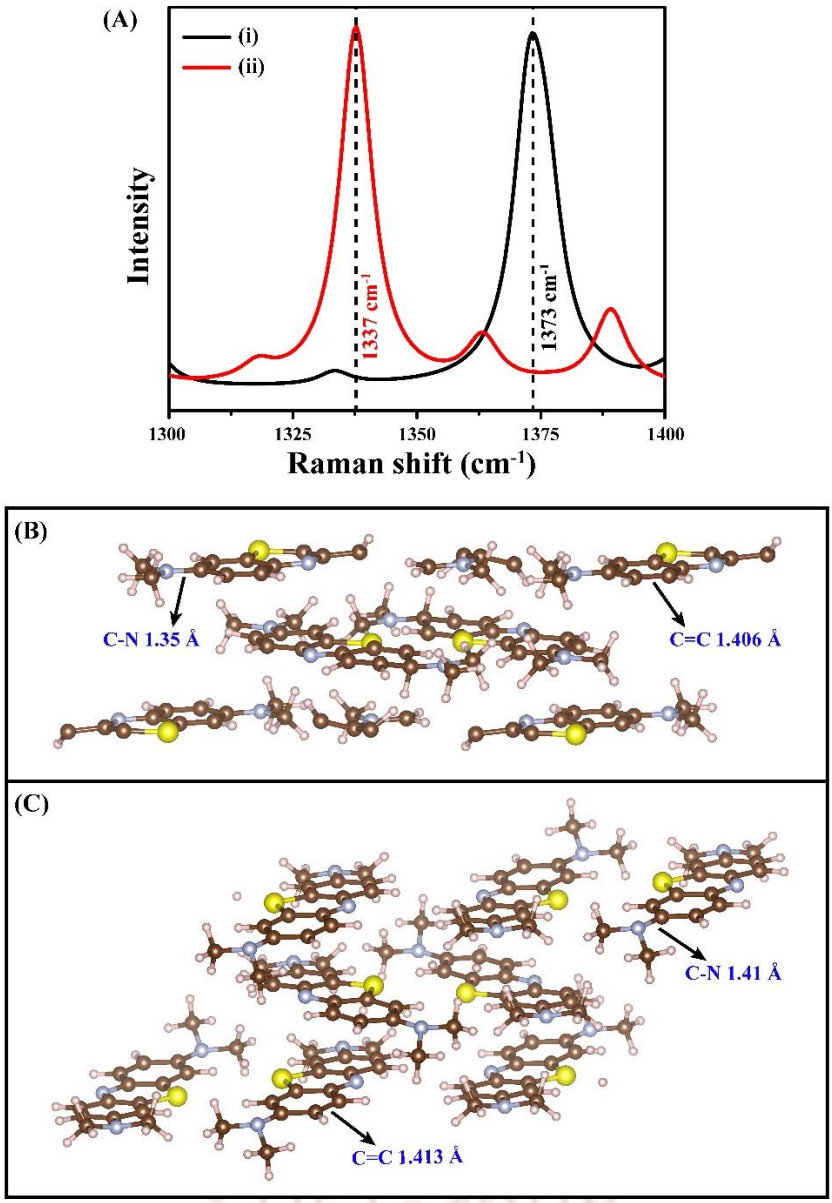

Figure A5.14: (A) DFT calculated Raman spectra of MB (i) at surface and (ii) in the interior of 2D MB crystal. DFT Optimized structure of MB molecules **(B)** at surface and **(C)** in the interior of 2D MB crystal showing bond lengths. Brown, white, pale blue and light-yellow atoms are C, H, N and S atoms, respectively.

In case of 2D crystal of MB, the Raman signal corresponding to ν(C–N) at 1398 cm^{-1} had been red shifted to 1393 cm^{-1} on moving from surface to interior (Figure A5.11). DFT calculated Raman spectra also suggested red-shift of ν(C–N) vibration from 1373 cm^{-1} to 1337 cm^{-1} in case of MB 2D crystal (Figure A5.14A) on moving from surface to inside of each crystal. From

TH_3719_186122105

the optimized structures on the surface (Figure A5.14B) and in the bulk (Figure A5.14C) of MB 2D crystal, the average bond length of aromatic C=C bond on the surface layer is calculated to be 1.406 Å, which is nearly identical to the 1.413 Å bond length of C=C in the interior of the MB 2D crystal. This is possibly the reason why the vibrational peak position at 1624 cm^{-1}, which involves only aromatic C=C vibration did not change on moving from the surface to the interior of MB 2D crystal. However, the C−N bond length (1.41 Å) in the inside of MB 2D crystal is higher than the C−N bond length of 1.35 Å at the surface of the crystal. Generally, with the lowering of bond length, the vibrational peak position is shifted to higher wavenumber according to the relation $\nu = [a/(r\mu^{0.5}) + b]$, where ν, r, μ, a and b are vibrational frequency, bond length, reduced mass, slope and intercepts, respectively.[1] Hence, the increase in the C−N bond length in the interior of crystal resulted in lowering of the Raman peak shift from 1398 cm^{-1} to 1393 cm^{-1} (Figure A5.11) upon moving from the surface to the interior of the MB 2D crystal.

A5.15. Experimental Raman spectra of MB 3D crystal:

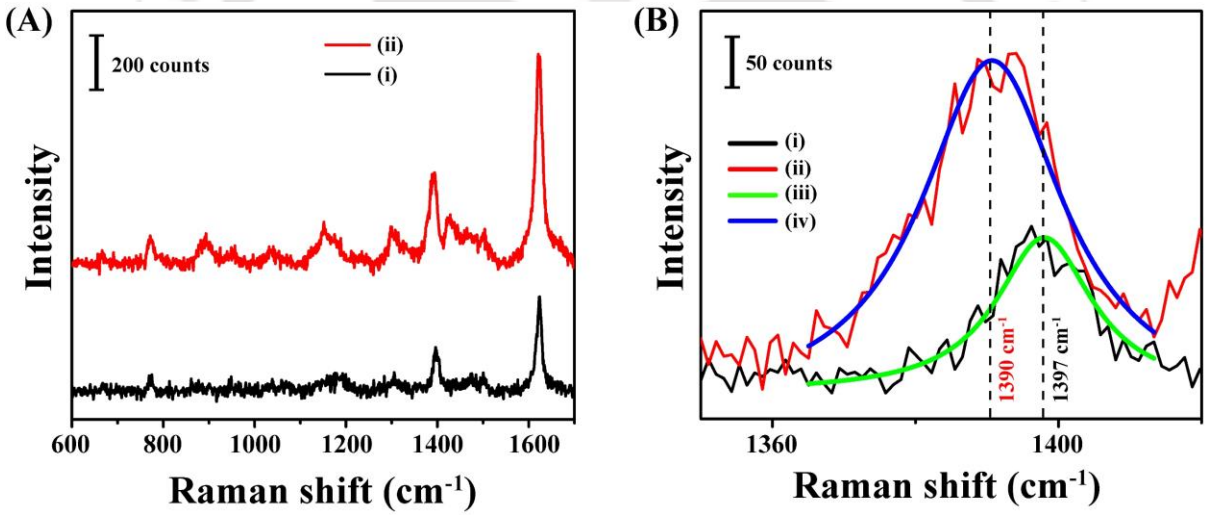

Figure A5.15: (A) Raman spectra (recorded using 0.16 mW of the 633 nm laser) of MB 3D crystal on the (i) smooth surface and (ii) etched surface formed following exposure to 0.8 mW 633 nm laser. **(B)** Zoomed view of Raman spectra showing peak shift on moving from (i) smooth surface to (ii) interior of the MB 3D crystal. The graphs (iii) and (iv) are Lorentzian fittings of (i) and (ii), respectively.

Similar to the MB 2D crystal, in case of MB 3D crystal, Raman signal intensity had been increased nearly 2 times on moving from surface to interior (Figure A5.15A). As shown in Figure A5.15B, Raman peak at 1397 cm^{-1} peak corresponding to ν(C–N) vibration was shifted to 1390 cm^{-1} on moving from surface to interior. However, peak position at 1624 cm^{-1}, which involves only aromatic C=C vibration did not change.

TH_3719_186122105

A5.16. Optimized structure of surface and interior of MB 3D crystal:

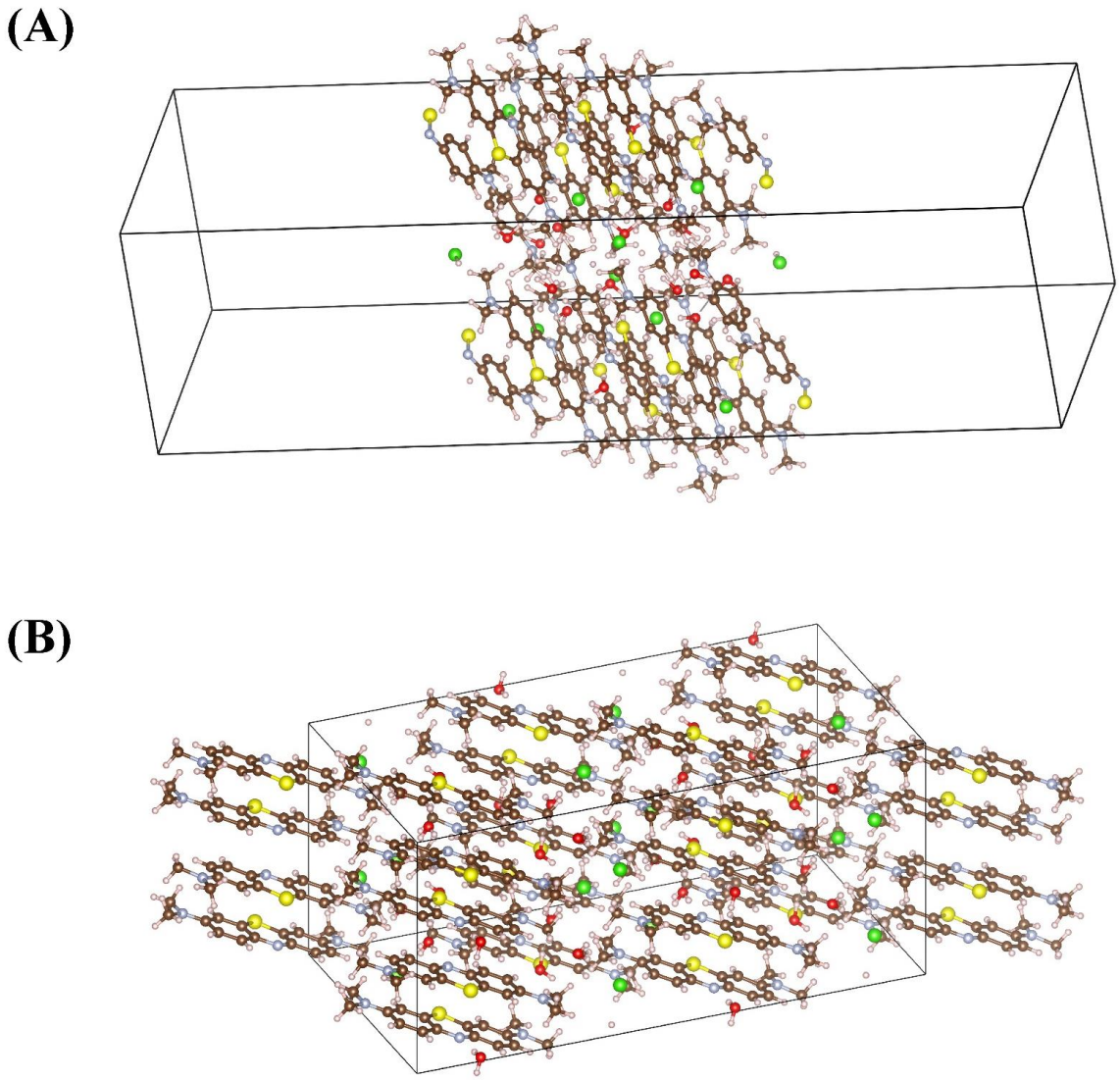

Figure A5.16: Optimized crystal structure of MB (A) on the surface and (B) in the interior of 3D crystal (CCDC number: 1811677). The optimization methods used are mentioned in the experimental section. Brown, white, pale blue, light yellow and green atoms are C, H, N, S and Cl atoms, respectively.

TH_3719_186122105

A5.17. Calculated Raman spectra of MB 3D crystal:

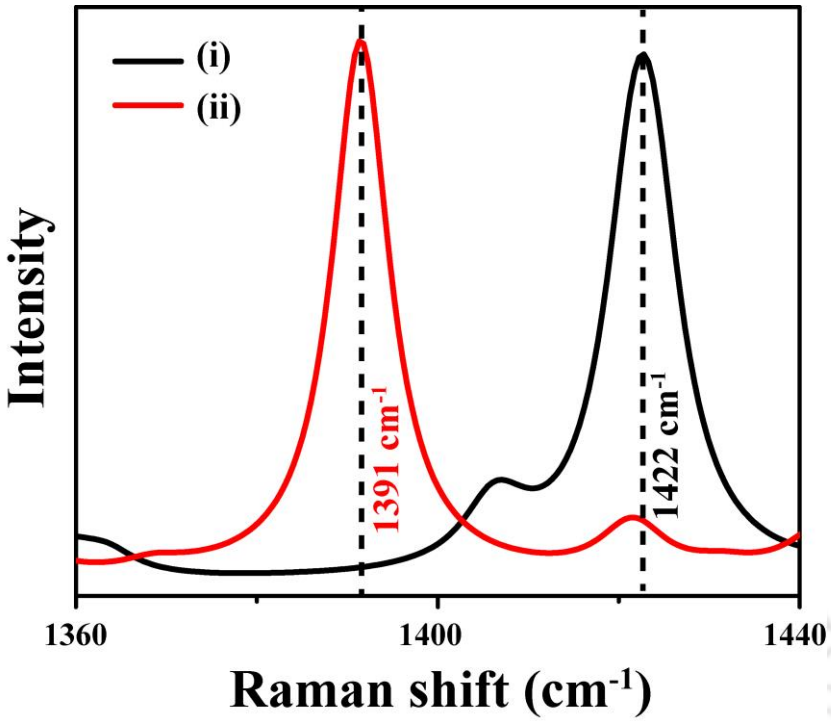

Figure A5.17: DFT calculated Raman spectra of MB (i) at surface and (ii) in the interior of 3D MB crystal shown in **Figure A5.16**.

DFT calculated Raman spectra also suggested red-shift of ν(C–N) vibration from 1422 cm^{-1} to 1391 cm^{-1} in case of MB 3D crystal (Figure A5.17), on moving from surface to inside of each crystal. From the optimized structures on the surface (Figure A5.16A) and in the bulk (Figure A5.16B) of MB 3D crystals (CCDC number: 1811677), the average bond length of aromatic C=C bond on the surface layer is calculated to be 1.43 Å, which is nearly identical to the 1.431 Å bond length of C=C in the interior of the MB 3D crystal. This is possibly the reason why the vibrational peak position at 1624 cm^{-1}, which involves only aromatic C=C vibration did not change on moving from the surface to the interior of MB 3D crystal as well. However, the C−N bond length (1.39 Å) in the inside of MB 3D crystal is higher than the C−N bond length of 1.35 Å at the surface of the crystal. Hence, the increase in the C−N bond length in the interior of crystal resulted in lowering of the Raman peak shift from 1397 cm^{-1} to 1390 cm^{-1} (Figure A5.15) upon moving from the surface to the interior of the MB 2D crystal.

A5.18 References:

1. Zavitsas, A. A. Factors affecting the relation between stretching frequencies and bond lengths. Diatomic and polyatomic species without adjustable fitting parameters. *Spectrochimica Acta Part A: Molecular and Biomolecular Spectroscopy* **2015**, *151*, 553–565

TH_3719_186122105

Chapter-6

Conclusions and Future Prospects

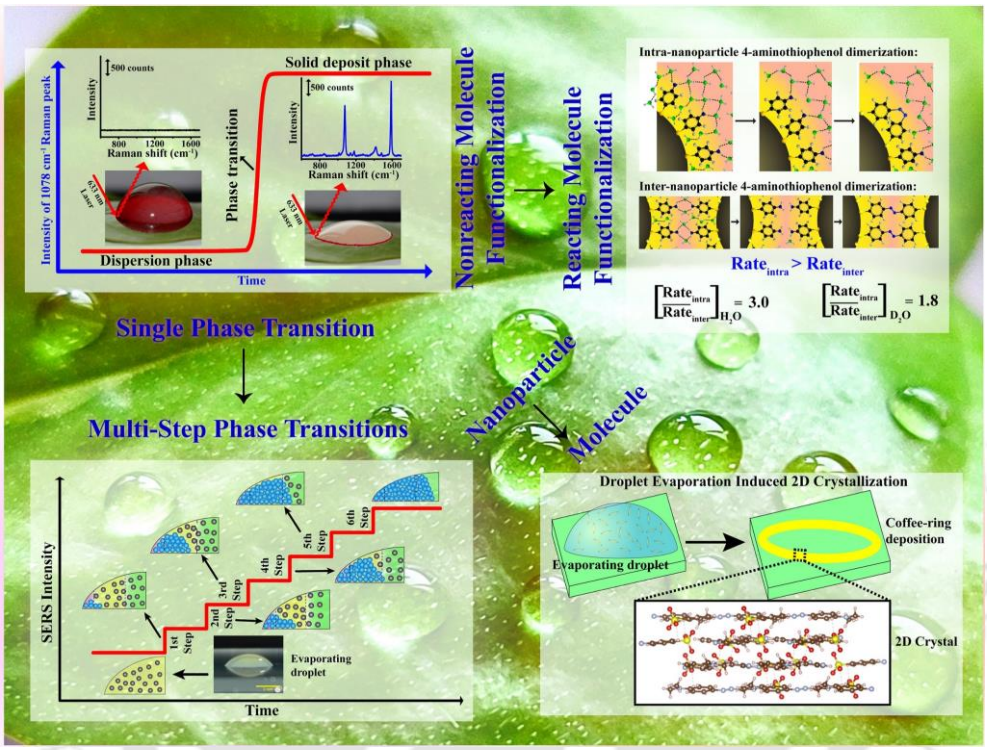

This chapter briefly presents the summary of the current studies and scope for the future.

TH_3719_186122105

6.1. Summary of the Thesis

Significant development in nanoscience and nanotechnology ushered the utilization of plasmonic nanoparticles in biomedical, sensing, chemical and energy applications. The evaporation induced deposition technique has gained notable attentions and has been employed for the fabrications of printed materials. The present thesis primarily focused on the deposition mechanism of nanoparticles, chemical interactions among plasmonic nanoparticles and the nature of crystal deposits of organic molecules. For the first time, we have reported the phase transition deposition behavior of nanoparticles from dispersion to deposit phase at the three-phase contact line (TPCL) of evaporating sessile droplets by using surface-enhanced Raman spectroscopy (SERS). This mechanism of deposition is distinct from the deposition of microparticles at the TPCL. Although particles were moving to the TPCL with time and during evaporation of solvent, atomic force microscopy (AFM) studies in conjugation with SERS also revealed that most of the nanoparticles were deposited in a short window of time during phase transition at the TPCL forming 'coffee-ring' pattern. The deposition kinetics of nanoparticles have not been reported earlier by any other method. Thus, we have developed a new technique to monitor the deposition process. Our studies indicated that for 15.4 nm, 25.3 nm and 36.4 nm spherical gold nanoparticles (AuNPs), the critical particle concentration for phase transition were 12.93±3.17 μM, 146.10±20.99 μM and 3.21±0.12 μM, respectively. In conjunction with the understanding of the nanoparticle deposition mechanism at the TPCL, we have for the first time successfully distinguished the intrananopaticle and internanoparticle reactions and their kinetics during the evaporation of sessile droplet. SERS measurements were carried out at the TPCL of evaporating droplet having dispersed 4-aminothiophenol (4-ATP) attached silver nanoparticle (AgNPs) (ATP@AgNPs) at pH 7.0. The intrananoparticle and internanoparticle dimerization of 4-ATP into 4,4´-dimercaptoazobenzene (DMAB) have different rates that depended on the solvent isotope effects. The ratio of intranaoparticle to internanoparticle reaction rates were found to be 3 and 1.8 in H_2O and in D_2O, respectively. The density functional theory (DFT) based calculations helped conclude that the elimination of hydrogen bonded water molecules before each step of the reactions was the major factor for the differential rates. Further, only one phase transition step was noticed at pH 7.0 for the dispersion of ATP@AgNPs. However, at slightly basic pH of 8.4 the deposition has been completed in six small phase transition steps distinguished by SERS measurements at the TPCL. Again, on moving to the higher pH of 9.4, a single phase transition has been observed.

TH_3719_186122105

The p- dependent deposition kinetics is governed by the higher dispersibility of ATP@AgNPs and faster 4-ATP dimerization rates at higher pH. Step by step growth of deposit height and width have been confirmed from AFM measurements as well. Therefore, Raman measurements of nanoparticle-laden evaporating sessile droplet is a crucial methodology, which deciphered various aspects of chemical and physical processes. The method when applied to the evaporating droplet having solution of common organic molecules, helped probe the formation of two-dimensional (2D) crystals of the molecules formed at the TPCL. The growth of 2D crystals of methyl orange (MO) and methylene blue (MB) and the layer-by-layer arrangements of the molecules in the crystals were also verified from powder X-ray diffraction and simulation studies. The discovery of the differences of the vibrational frequencies of the surface and interior species of molecular crystals - as characterized by Raman measurements - has been reported in the thesis.

6.2. Future Prospects

The future outlook and scopes of the current findings are mentioned below.

- The newly discovered phase transition mechanism of the deposition of nanoparticles may usher important consequences in printing technology, disease diagnostics and agriculture.
- The importance of critical concentrations for deposition of nanoparticles reported herein can be utilized for faster fabrications of devices and printed electronic structures.
- The monitoring of chemical reactions at the TPCL of evaporating droplets can be carried out for other heterogeneous plasmon-catalyzed reaction in order to obtain rich information about the reactions.
- The effect of pH can significantly influence the liquid printing methods in which photochemically active molecules are used or if any photochemical reaction occurs.
- The evaporation induced deposition method may be applied to any other molecules to make new types of 2D crystalline materials such as topographical insulators.
- The 3D crystal of MO can be exfoliated into 2D sheets which can further result in moiré superlattice under control condition. The newly formed moiré superlattice may bring about novel vibrational properties at molecular level.

TH_3719_186122105

Exfoliation of MO 3D crystal led to the formation of moiré superlattice with periodicity 22 nm as obtained from tapping mode AFM measurements. It has been calculated that the crystalline lattices have been rotated by ~5° with respect to the each other. The moiré pattern had been reconstructed from IFFT of the height mapping of the AFM image as shown in **Figure 6.1**.

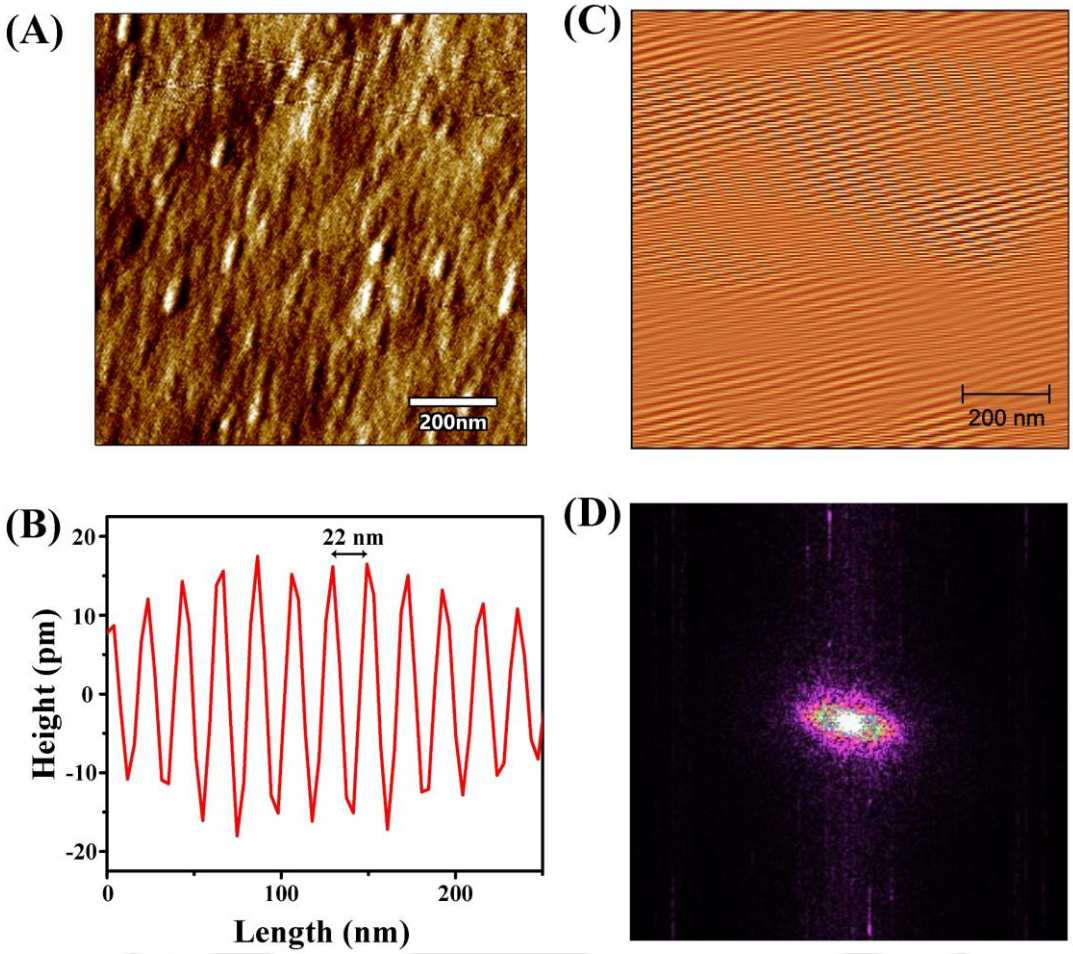

Figure 6.1: (A) AFM amplitude image of moiré superlattice of MO. **(B)** Reconstructed moiré pattern from IFFT of height mapping of the same measurement in **(A)**. **(C)** Height profile of moiré superlattice. **(D)** FFT of the height mapping from which the moiré superlattice in **(B)** is constructed.

Moreover, PXRD measurements of the MO moiré superlattice revealed that the diffraction peak at 4.2 ° (2θ) of (100) plane which was same for the MO 2D crystal discussed in Chapter 5 (**Figure 6.2B**). Therefore, after exfoliation, the 3D crystal of MO has been converted into the 2D sheets which stacked on top of other to form the moiré superlattice. However, the other diffraction peaks at higher 2θ were shifted to lower angle with reduced intensity compared to the PXRD of 3D crystal of MO (**Figure 6.2C**). This might be because of strain in the whole imperfect 3D crystal systems. Raman measurements of the moiré superlattice also revealed

TH_3719_186122105

red-shift of some vibrational peaks with respect to the original 3D crystal of MO as shown in **Figure 6.2D**. This experiments clearly pointed out different behavior of moiré superlattice in molecular level obtained experimentally by Raman and PXRD measurements. More experiments and computational calculations are going on to understand this behavior of moiré superlattice.

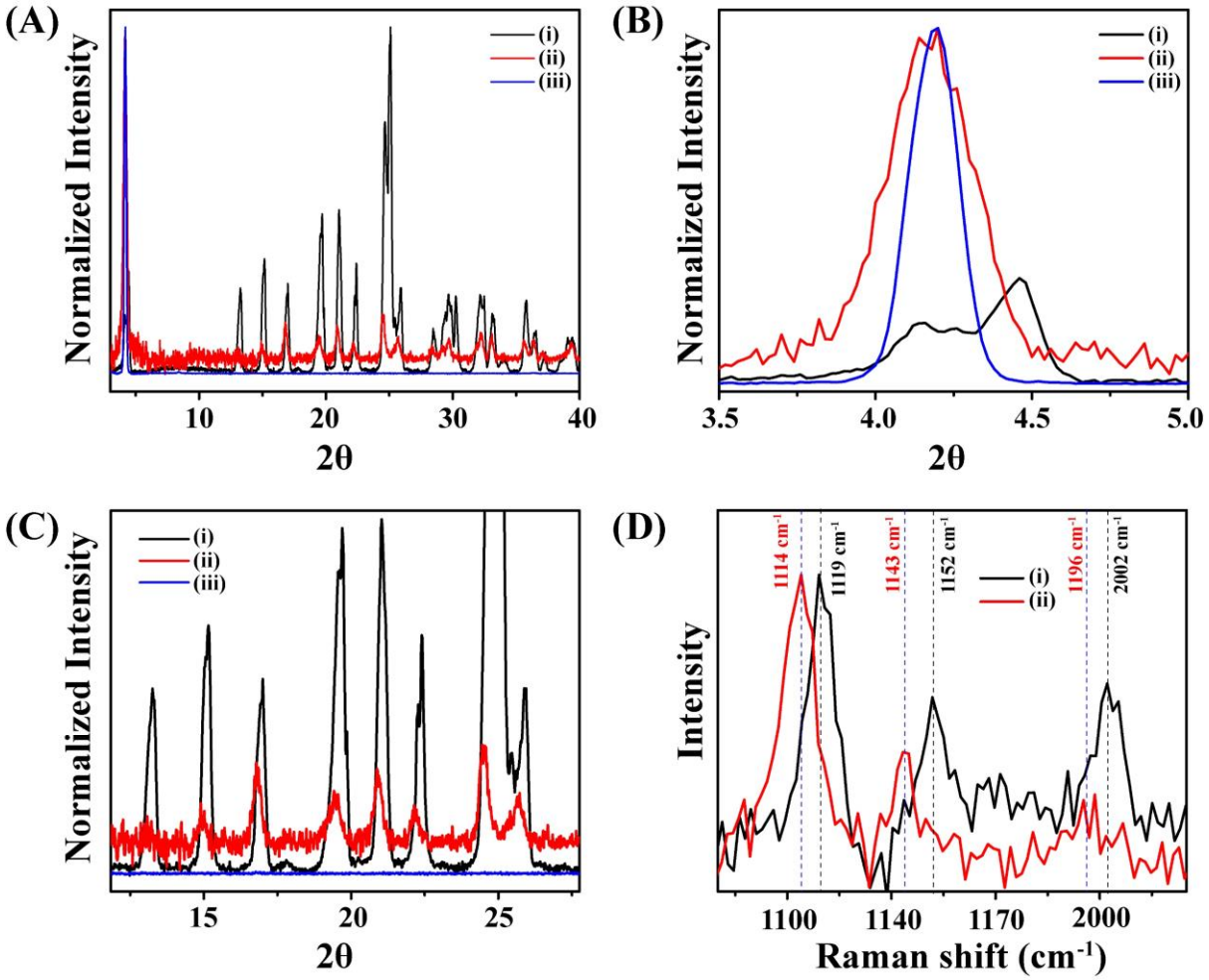

Figure 6.2: (A) PXRD patterns of (i) 3D crystal of MO, (ii) moiré superlattice of MO and (iii) 2D crystal of MO. **(B)** and **(C)** are zoomed view of the PXRD pattern shown in **(A)**. **(D)** Raman spectra on the surface of (i) 3D crystal of MO and (ii) moiré superlattice of MO showing red-shift of some peaks.

TH_3719_186122105

LIST OF PUBLICATIONS

Publications based on the works reported in the thesis

1. **Paul, S.**; Chattopadhyay, A. Single Phase Transition Leads to the Nanoparticle Deposition in an Evaporating Sessile Droplet. *J. Phys. Chem. C* **2023**, *45*, 22401-22411.
2. **Paul, S.**; Chattopadhyay, A. Distinction of Plasmonic Intrananoparticle and Internanoparticle Molecular Reaction Rates at the Three-Phase Contact Line of an Evaporating Sessile Droplet. *J. Phys. Chem. Lett.* **2024**, *15*, 6812-6817.
3. **Paul, S.**; Chattopadhyay, A. Multistep Phase Transition and Molecular Reaction of Plasmonic Nanoparticles at the Three-Phase Contact Line of an Evaporating Sessile Droplet. *J. Phys. Chem. C* **2025**, *129*, 8, 4250–4260.
4. **Paul, S.**; Chattopadhyay, A. Anomalous Two-Dimensional Organic Molecular Crystal Formation in an Evaporating Droplet with Different Vibrational Characteristics of the Surface and the Bulk. *J. Phys. Chem. Lett.* **2025**, *16*, 29, 7428–7435.

Publications from Collaborations

5. Pal, S.; **Paul, S.**; Chattopadhyay, A. Enhanced solid-state plasmon catalyzed oxidation and SERS signal in the presence of transition metal cations at the surface of gold nanostructures. *Phys. Chem. Chem. Phys.* **2021**, *23*, 21808-21816.
6. Pal, S.; **Paul, S.**; Chattopadhyay, A. Dual Role of Au nanoparticles in the Catalytic Formation of an Amorphous Polynuclear Peroxo Complex and Surface Enhanced Resonance Raman Scattering. *ChemistrySelect* **2022**, *7*, e202201569.
7. Bhakat, A.; **Paul, S.**; Chattopadhyay, A. Molecular Specificity in the Intense Surface-Enhanced Raman Scattering on Copper(II) 8-Hydroxyquinoline Microcrystals. *J. Phys. Chem. C* **2023**, *127*, 5169-5177.
8. Samanta, S.; **Paul, S.**; Debnath T. Obtaining Ligand-Free Aqueous Au-Nanoparticles Using Reversible $CsPbBr_3$ ↔ Au@$CsPbBr_3$ Nanocrystal Transformation. *Small* **2024,** *20*, 2311712.

TH_3719_186122105

CONFERENCES ATTENDED

1. Presented a Poster and gave an Oral Presentation in 8th International Conference on Advanced Nanomaterials and Nanotechnology - ICANN 2023, organized by the Centre for Nanotechnology, IIT Guwahati, from 29/11/2023 to 01/12/2023.
   Best Oral Presentation award has been received.
2. Presented a Poster in Research and Industrial Conclave 2024 (RIC-2024) at Indian Institute of Technology Guwahati, from 9 Aug, 2024 to 11 Aug, 2024.
3. Presented a Poster in Conference on Advances in Chemistry for Energy and Environment 2024 (CACEE 2024) at Tata Institute of Fundamental Research, Mumbai, from 16 Dec, 2024 to 20 Dec, 2024.

TH_3719_186122105

PERMISSIONS

Permission for Chapter 2

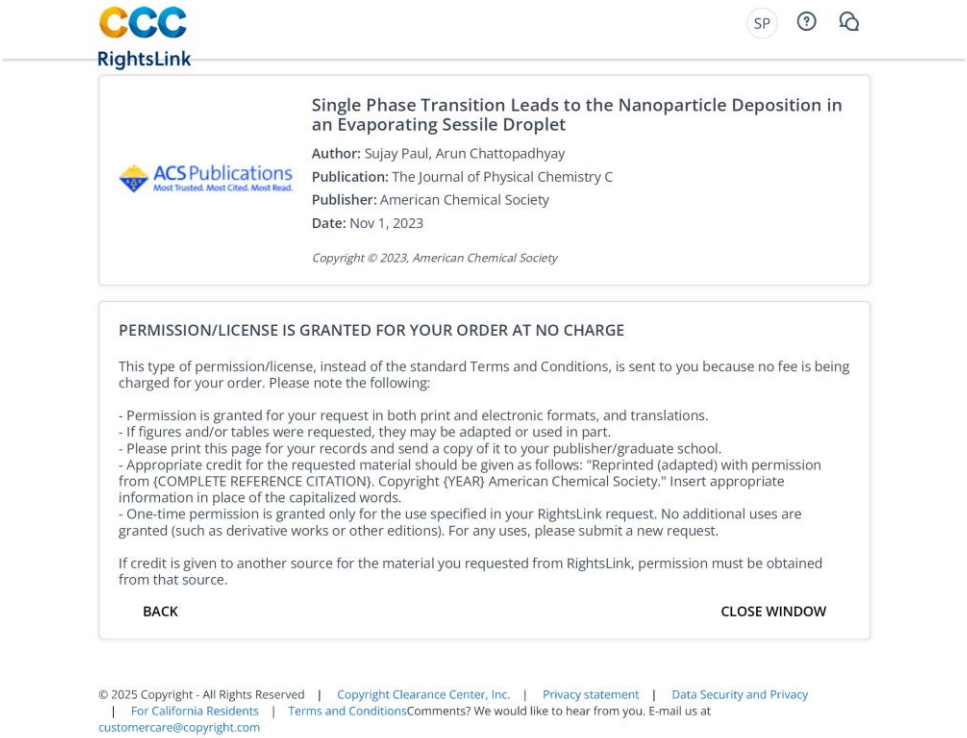

RightsLink

SP

ACS Publications
Most Trusted. Most Cited. Most Read.

Single Phase Transition Leads to the Nanoparticle Deposition in an Evaporating Sessile Droplet

Author: Sujay Paul, Arun Chattopadhyay
Publication: The Journal of Physical Chemistry C
Publisher: American Chemical Society
Date: Nov 1, 2023

Copyright © 2023, American Chemical Society

PERMISSION/LICENSE IS GRANTED FOR YOUR ORDER AT NO CHARGE

This type of permission/license, instead of the standard Terms and Conditions, is sent to you because no fee is being charged for your order. Please note the following:

- Permission is granted for your request in both print and electronic formats, and translations.
- If figures and/or tables were requested, they may be adapted or used in part.
- Please print this page for your records and send a copy of it to your publisher/graduate school.
- Appropriate credit for the requested material should be given as follows: "Reprinted (adapted) with permission from {COMPLETE REFERENCE CITATION}. Copyright {YEAR} American Chemical Society." Insert appropriate information in place of the capitalized words.
- One-time permission is granted only for the use specified in your RightsLink request. No additional uses are granted (such as derivative works or other editions). For any uses, please submit a new request.

If credit is given to another source for the material you requested from RightsLink, permission must be obtained from that source.

BACK CLOSE WINDOW

© 2025 Copyright - All Rights Reserved | Copyright Clearance Center, Inc. | Privacy statement | Data Security and Privacy | For California Residents | Terms and ConditionsComments? We would like to hear from you. E-mail us at customercare@copyright.com

Privacy - Terms

TH_3719_186122105

Permission for Chapter 3

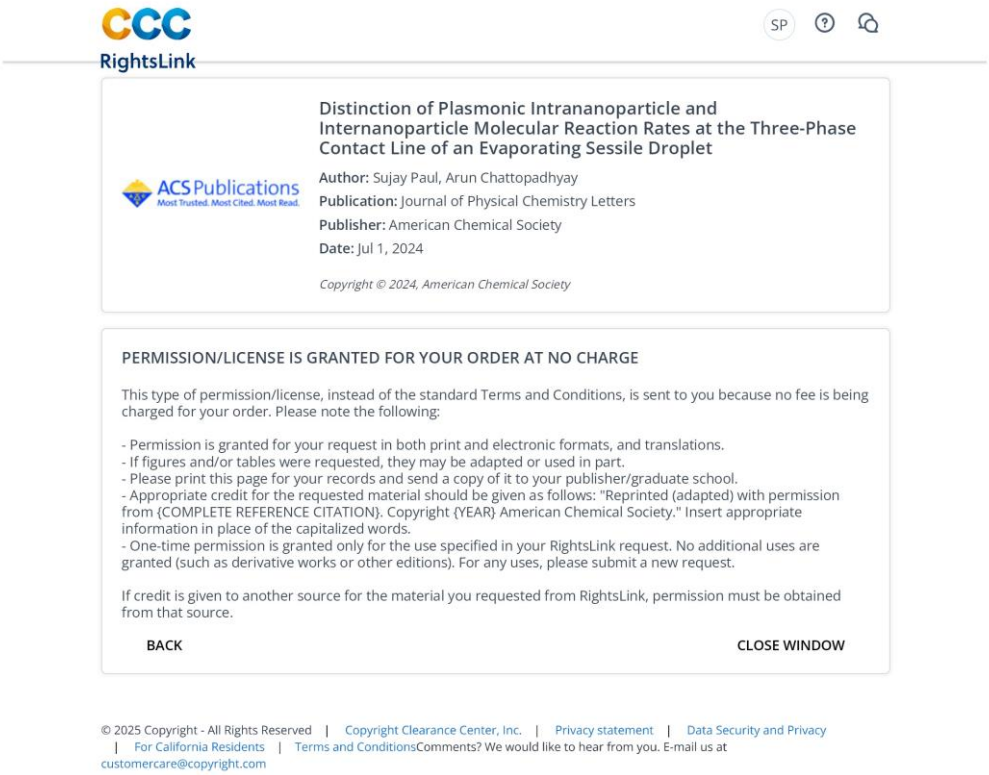

RightsLink

SP

Distinction of Plasmonic Intrananoparticle and Internanoparticle Molecular Reaction Rates at the Three-Phase Contact Line of an Evaporating Sessile Droplet

Author: Sujay Paul, Arun Chattopadhyay
Publication: Journal of Physical Chemistry Letters
Publisher: American Chemical Society
Date: Jul 1, 2024

Copyright © 2024, American Chemical Society

PERMISSION/LICENSE IS GRANTED FOR YOUR ORDER AT NO CHARGE

This type of permission/license, instead of the standard Terms and Conditions, is sent to you because no fee is being charged for your order. Please note the following:

- Permission is granted for your request in both print and electronic formats, and translations.
- If figures and/or tables were requested, they may be adapted or used in part.
- Please print this page for your records and send a copy of it to your publisher/graduate school.
- Appropriate credit for the requested material should be given as follows: "Reprinted (adapted) with permission from {COMPLETE REFERENCE CITATION}. Copyright {YEAR} American Chemical Society." Insert appropriate information in place of the capitalized words.
- One-time permission is granted only for the use specified in your RightsLink request. No additional uses are granted (such as derivative works or other editions). For any uses, please submit a new request.

If credit is given to another source for the material you requested from RightsLink, permission must be obtained from that source.

BACK CLOSE WINDOW

© 2025 Copyright - All Rights Reserved | Copyright Clearance Center, Inc. | Privacy statement | Data Security and Privacy | For California Residents | Terms and ConditionsComments? We would like to hear from you. E-mail us at customercare@copyright.com

Privacy - Terms

TH_3719_186122105

Permission for Chapter 4

RightsLink

SP

Multistep Phase Transition and Molecular Reaction of Plasmonic Nanoparticles at the Three-Phase Contact Line of an Evaporating Sessile Droplet

ACS Publications
Most Trusted. Most Cited. Most Read.

Author: Sujay Paul, Arun Chattopadhyay
Publication: The Journal of Physical Chemistry C
Publisher: American Chemical Society
Date: Feb 1, 2025

Copyright © 2025, American Chemical Society

PERMISSION/LICENSE IS GRANTED FOR YOUR ORDER AT NO CHARGE

This type of permission/license, instead of the standard Terms and Conditions, is sent to you because no fee is being charged for your order. Please note the following:

- Permission is granted for your request in both print and electronic formats, and translations.
- If figures and/or tables were requested, they may be adapted or used in part.
- Please print this page for your records and send a copy of it to your publisher/graduate school.
- Appropriate credit for the requested material should be given as follows: "Reprinted (adapted) with permission from {COMPLETE REFERENCE CITATION}. Copyright {YEAR} American Chemical Society." Insert appropriate information in place of the capitalized words.
- One-time permission is granted only for the use specified in your RightsLink request. No additional uses are granted (such as derivative works or other editions). For any uses, please submit a new request.

If credit is given to another source for the material you requested from RightsLink, permission must be obtained from that source.

BACK CLOSE WINDOW

© 2025 Copyright - All Rights Reserved | Copyright Clearance Center, Inc. | Privacy statement | Data Security and Privacy | For California Residents | Terms and ConditionsComments? We would like to hear from you. E-mail us at customercare@copyright.com

Privacy - Terms

TH_3719_186122105

Permission for Chapter 5

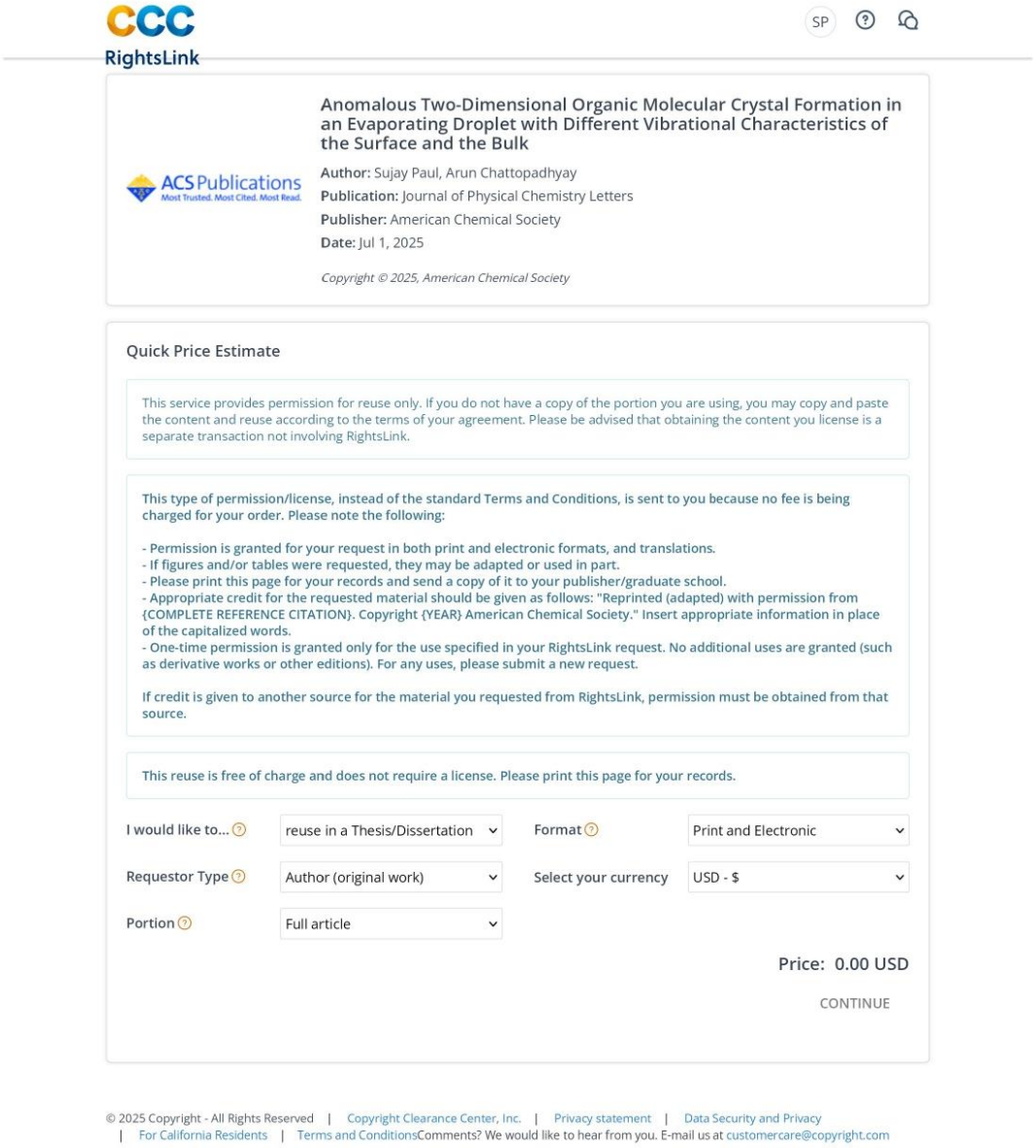

RightsLink

SP

Anomalous Two-Dimensional Organic Molecular Crystal Formation in an Evaporating Droplet with Different Vibrational Characteristics of the Surface and the Bulk

ACS Publications
Most Trusted. Most Cited. Most Read.

Author: Sujay Paul, Arun Chattopadhyay
Publication: Journal of Physical Chemistry Letters
Publisher: American Chemical Society
Date: Jul 1, 2025

Copyright © 2025, American Chemical Society

Quick Price Estimate

This service provides permission for reuse only. If you do not have a copy of the portion you are using, you may copy and paste the content and reuse according to the terms of your agreement. Please be advised that obtaining the content you license is a separate transaction not involving RightsLink.

This type of permission/license, instead of the standard Terms and Conditions, is sent to you because no fee is being charged for your order. Please note the following:

- Permission is granted for your request in both print and electronic formats, and translations.
- If figures and/or tables were requested, they may be adapted or used in part.
- Please print this page for your records and send a copy of it to your publisher/graduate school.
- Appropriate credit for the requested material should be given as follows: "Reprinted (adapted) with permission from {COMPLETE REFERENCE CITATION}. Copyright {YEAR} American Chemical Society." Insert appropriate information in place of the capitalized words.
- One-time permission is granted only for the use specified in your RightsLink request. No additional uses are granted (such as derivative works or other editions). For any uses, please submit a new request.

If credit is given to another source for the material you requested from RightsLink, permission must be obtained from that source.

This reuse is free of charge and does not require a license. Please print this page for your records.

I would like to... reuse in a Thesis/Dissertation
Format Print and Electronic
Requestor Type Author (original work)
Select your currency USD - $
Portion Full article

Price: 0.00 USD

CONTINUE

© 2025 Copyright - All Rights Reserved | Copyright Clearance Center, Inc. | Privacy statement | Data Security and Privacy | For California Residents | Terms and ConditionsComments? We would like to hear from you. E-mail us at customercare@copyright.com

TH_3719_186122105

PLAGIARISM REPORTS

Plagiarism Report of Abstract

Sujay PhD Thesis Abstract

by Sujay PAUL

Submission date: 03-Mar-2025 04:53PM (UTC+0530)
Submission ID: 2603907475
File name: SP_Thesis_Abstract_02032025.docx (17.31K)
Word count: 699
Character count: 4182

TH_3719_186122105

Sujay PhD Thesis Abstract

ORIGINALITY REPORT

0%	0%	0%	0%
SIMILARITY INDEX	INTERNET SOURCES	PUBLICATIONS	STUDENT PAPERS

PRIMARY SOURCES

Exclude quotes	On	Exclude matches	Off
Exclude bibliography	On		

TH_3719_186122105

Plagiarism Report of Chapter 1

Sujay PhD Thesis Chapter 1

by Sujay PAUL

Submission date: 03-Mar-2025 04:45PM (UTC+0530)
Submission ID: 2603907475
File name: SP_Thesis_Chapter-1_Introduction_02032025.docx (1.74M)
Word count: 5537
Character count: 31496

TH_3719_186122105

Sujay PhD Thesis Chapter 1

ORIGINALITY REPORT

5%	1%	4%	0%
SIMILARITY INDEX	INTERNET SOURCES	PUBLICATIONS	STUDENT PAPERS

PRIMARY SOURCES

1	Sujay Paul, Arun Chattopadhyay. "Single Phase Transition Leads to the Nanoparticle Deposition in an Evaporating Sessile Droplet", The Journal of Physical Chemistry C, 2023 Publication	2%
2	Vincenzo Amendola, Roberto Pilot, Marco Frasconi, Onofrio M Maragò, Maria Antonia Iatì. "Surface plasmon resonance in gold nanoparticles: a review", Journal of Physics: Condensed Matter, 2017 Publication	1%
3	Tamitake Itoh, Marek Procházka, Zhen-Chao Dong, Wei Ji, Yuko S. Yamamoto, Yao Zhang, Yukihiro Ozaki. "Toward a New Era of SERS and TERS at the Nanometer Scale: From Fundamentals to Innovative Applications", Chemical Reviews, 2023 Publication	<1%
4	Xingying Zhang, Ben Liu, Chenglong Hu, Shaoyun Chen, Xueqing Liu, Jiyan Liu, Fang Chen, Jian Chen, Fangyan Xie. "A facile method in removal of PVP ligands from silver nanowires for high performance and reusable SERS substrate", Spectrochimica Acta Part A: Molecular and Biomolecular Spectroscopy, 2020 Publication	<1%
5	publishup.uni-potsdam.de Internet Source	<1%

TH_3719_186122105

6	Submitted to Higher Education Commission Pakistan Student Paper	<1%
7	Lalji Dixit. "An Integrated Spectroscopic Approach for the Characterization of Petroleum Reforming Catalysts", Applied Spectroscopy Reviews, 1998 Publication	<1%
8	docslib.org Internet Source	<1%
9	www.mdpi.com Internet Source	<1%
10	Maryam Nayeri, Parisa Akherati. "The influence of intrinsic atomic defects on the electronic and optical properties of the single layer AlN", Physica Scripta, 2020 Publication	<1%

Exclude quotes	On	Exclude matches	Off
Exclude bibliography	On		

TH_3719_186122105

Plagiarism Report of Chapter 5

Turnitin Sujay PhD Thesis Chapter 5

by Sujay PAUL

Submission date: 03-Mar-2025 04:50PM (UTC+0530)
Submission ID: 2603907475
File name: SP_Thesis_Chapter-5_2D_Crystal_02032025.docx (3.23M)
Word count: 4367
Character count: 22680

TH_3719_186122105

Turnitin Sujay PhD Thesis Chapter 5

ORIGINALITY REPORT

4%	2%	3%	0%
SIMILARITY INDEX	INTERNET SOURCES	PUBLICATIONS	STUDENT PAPERS

PRIMARY SOURCES

1	SUJAY PAUL, ARUN CHATTOPADHYAY. "Differing Plasmonic Intra-nanoparticle and Inter-nanoparticle Molecular Reaction Rates at the Three-Phase Contact Line of an Evaporating Sessile Droplet", American Chemical Society (ACS), 2024 Publication	1%
2	www.science.gov Internet Source	1%
3	Thomas Steiner. "C–H···O hydrogen bonding in crystals", Crystallography Reviews, 2003 Publication	<1%
4	Submitted to (school name not available) Student Paper	<1%
5	Linglong Zhang, Md Mehedi Hasan, Yilin Tang, Ahmed Raza Khan et al. "2D organic single crystals: Synthesis, novel physics, high-performance optoelectronic devices and integration", Materials Today, 2021 Publication	<1%
6	www.ncbi.nlm.nih.gov Internet Source	<1%
7	patents.google.com Internet Source	<1%
8	Fardous A. Mohamed, Pakinaz Y. Khashaba, Reem Y. Shahin, Mohamed M. El-Wekil. "Tunable ternary nanocomposite prepared by	<1%

TH_3719_186122105

	electrodeposition for biosensing of centrally acting reversible acetyl cholinesterase inhibitor donepezil hydrochloride in real samples", Colloids and Surfaces A: Physicochemical and Engineering Aspects, 2019 Publication	
9	dx.doi.org Internet Source	<1 %
10	worldwidescience.org Internet Source	<1 %
11	SUJAY PAUL, ARUN CHATTOPADHYAY. "Single Phase Transition Leads to the Coffee Ring Deposition of Nanoparticles in an Evaporating Sessile Droplet", American Chemical Society (ACS), 2023 Publication	<1 %
12	Weiping Cai, Guotao Duan, Yue Li. "Hierarchical Micro/Nanostructured Materials - Fabrication, Properties, and Applications", CRC Press, 2019 Publication	<1 %

Exclude quotes	On	Exclude matches	Off
Exclude bibliography	On		

TH_3719_186122105

Plagiarism Report of Chapter 6

Turnitin Sujay PhD Thesis Chapter 6

by Sujay PAUL

Submission date: 03-Mar-2025 04:57PM (UTC+0530)
Submission ID: 2603907475
File name: SP_Thesis_Chapter-6_Summary_02032025.docx (16.61K)
Word count: 705
Character count: 4155

TH_3719_186122105

Turnitin Sujay PhD Thesis Chapter 6

ORIGINALITY REPORT

0%	0%	0%	0%
SIMILARITY INDEX	INTERNET SOURCES	PUBLICATIONS	STUDENT PAPERS

PRIMARY SOURCES

Exclude quotes	On	Exclude matches	Off
Exclude bibliography	On		

TH_3719_186122105